

# **TOWARDS MODELING THE MAGNETOSPHERIC SPACE PLASMA ENVIRONMENT**

**Michael Silevitch  
Elena Villalon**

**Northeastern University  
360 Huntington Ave  
Boston, MA 02115**

**July 1999**

**Final Report**

<p><b>APPROVED FOR PUBLIC RELEASE; DISTRIBUTION UNLIMITED.</b></p>
--



**AIR FORCE RESEARCH LABORATORY  
Space Vehicles Directorate  
29 Randolph Rd  
AIR FORCE MATERIEL COMMAND  
Hanscom AFB, MA 01731-3010**

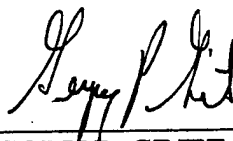
---

**20010720 043**

This Technical Report has been reviewed and is approved for publication.



Paul L. Rothwell  
Contract Manager



GREGORY P. GINET  
Chief, Space Weather Center of Excellence

This report has been reviewed by the ESC Public Affairs Office (PA) and is releasable to the National Technical Information Service.

Qualified requestors may obtain additional copies from the Defense Technical Information Center (DTIC). All others should apply to the National Technical Information Service (NTIS).

If your address has changed, if you wish to be removed from the mailing list, or if the address is no longer employed by your organization, please notify AFRL/VSIM, 29 Randolph Rd., Hanscom AFB, MA 01731-3010. This will assist us in maintaining a current mailing list.

Do not return copies of this report unless contractual obligations or notices on a specific document require that it be returned.

REPORT DOCUMENTATION PAGE			Form Approved OMB No. 0704-0188	
Public reporting burden for this collection of information is estimated to average 1 hour per response, including the time for reviewing instructions, searching existing data sources, gathering and maintaining the data needed, and completing and reviewing the collection of information. Send comments regarding this burden estimate or any other aspect of this collection of information, including suggestions for reducing this burden, to Washington Headquarters Services, Directorate for Information Operations and Reports, 1215 Jefferson Davis Highway, Suite 1204, Arlington, VA 22202-4302, and to the Office of Management and Budget, Paperwork Reduction Project (0704-0188), Washington, DC 20503.				
1. AGENCY USE ONLY (Leave blank)		2. REPORT DATE July 1999		3. REPORT TYPE AND DATES COVERED FINAL REPORT (Oct 1995 - December 1998)
4. TITLE AND SUBTITLE Towards Modeling the Magnetospheric Space Plasma Environment			5. FUNDING NUMBERS PE: 62101F PR: 2311 TA: GB WU: NE  Contract: F19628-95-C-0212	
6. AUTHOR(S) Michael Silevitch and Elena Villalon				
7. PERFORMING ORGANIZATION NAME(S) AND ADDRESS(ES) Northeastern University 360 Huntington Avenue Boston, MA 02115			8. PERFORMING ORGANIZATION REPORT NUMBER	
9. SPONSORING/MONITORING AGENCY NAME(S) AND ADDRESS(ES) Air Force Research Laboratory 29 Randolph Road Hanscom AFB MA 01731-3010  Contract Manager: William Burke/VSBP			10. SPONSORING/MONITORING AGENCY REPORT NUMBER  AFRL-VS-TR-2000-1507	
11. SUPPLEMENTARY NOTES				
12a. DISTRIBUTION AVAILABILITY STATEMENT Approved for Public Release; Distribution Unlimited			12b. DISTRIBUTION CODE	
13. ABSTRACT (Maximum 200 words) The research described in this report was focused into three related areas: a) A study of nonadiabatic particle orbits and the electrodynamic structure of the coupled magnetosphere-ionosphere arc system. b) An examination of electron acceleration and pitch angle scattering due to wave-particle interaction in the ionosphere and radiation belts. c) A study of ionospheric modification research and the experimental results of Oedipus C satellite.				
14. SUBJECT TERMS Radiation belts Auroral arc  Oedipus C experiment Ionospheric wave particle interactions			15. NUMBER OF PAGES	
			16. PRICE CODE	
17. SECURITY CLASSIFICATION OF REPORT  UNCLASSIFIED	18. SECURITY CLASSIFICATION OF THIS PAGE  UNCLASSIFIED	19. SECURITY CLASSIFICATION OF ABSTRACT  UNCLASSIFIED	20. LIMITATION OF ABSTRACT  SAR	

	<b>Contents</b>
<b>Introduction</b>	1
<b>Description of Research</b>	1
<b>Publications:</b>	
Inertial Currents and Substorm Onsets	5
O <sup>+</sup> Phase Bunching, Oblique Alfven Waves and Auroral Arcs	11
O <sup>+</sup> Phase Bunching as a Source for Stable Auroral Arcs	17
Pitch Angle Scattering of Diffuse Auroral Electrons by Whistler Mode Waves	43
Theory of Quasi-Monochromatic Whistler Wave Generation in the Inner Plasma Sheet	52
Electron Acceleration by MHz Waves During OEDIPUS C	67
Theory of Plasma Wave Propagation and Electron Heating in a Tenuous Ionospheric Plasma	102

## **1. Introduction**

This document is a final report describing the research performed under contract F19628-95-C-0212, on "Towards Modeling the Magnetospheric Space Plasma Environment." The proposed research program initially incorporated the efforts of two scientists who were eliminated from the contract due to Air Force budgetary constraints and reallocation strategies. This program modification impacted Dr. Jay Albert (a co-Principal Investigator) and Dr. Steve Anderson (a Post-Doctoral Research Associate). The modified program was implemented during the early stages of the funding period. Prof. Michael Silevitch and Dr. Elena Villalon redefined the research program in concert with the priorities articulated by the contract monitor. The research was focused into three different related areas. These were:

- (A) A study of nonadiabatic particle orbits and the electrodynamic of the coupled magnetosphere-ionosphere auroral arc system.
- (B) The generation of VLF chorus in the inner plasma sheet, and its relevance to the precipitation of the electrons that form the diffuse aurora.
- (C) A study of ionospheric modification research and the experimental results from the Oedipus C satellite.

The next section describes the three research areas. Following this are copies of the publications that resulted from the research investigations.

## **2. Description of Research**

This section gives more detailed synopses of the research areas that were investigated during the period of the contract.

- (A) A study of nonadiabatic particle orbits and the electrodynamic of the coupled magnetosphere-ionosphere auroral arc system.

In this area, we investigated the characteristics of oxygen ion orbits in the presence of spatially varying electric and magnetic fields. Specifically, we compared analytical and numerical solutions for field structures characterized by spatial variations in a direction corresponding to latitudinal variations near the Harang Discontinuity Region. In developing our ideas, we have continued to incorporate the effects of spatial magnetic field gradients into our study of the oxygen ion orbits. Moreover, we have shown that the large scale gradients in both the magnetic and electric fields can create density striations due to phase bunching effects.

During this contract, Professor Silevitch has been working with Paul Rothwell at the Air Force Research Laboratory and with Lars Block and Carl-Gunne Falthammar at the Royal

Institute of Technology in Stockholm, Sweden. As a result of this collaboration, a new theoretical description of the magnetospheric generator and its subsequent coupling to the ionosphere has been developed. Papers and an accepted manuscript related to this work and included in this report are as follows:

1. P.L. Rothwell, M.B. Silevitch, L.P. Block and C-G. Falthammar, "Inertial Currents and Substorm Outsets," Proc. Third international Conference on Substorm (ICS-3), ESA SP - 389, pp. 447-452 (1996).
2. P.L. Rothwell, M.B. Silevitch, L.P. Block, and C-G. Falthammar, "O<sup>+</sup> Phase Bunching, Oblique Alfvén Waves and Auroral Arcs," Physics of Space Plasmas, Number 15, pp. 289-294 (1998).
3. M.B. Silevitch, P.L. Rothwell, L.P. Block, and C-G. Falthammar, "O<sup>+</sup> Phase Bunching as a Source for Stable Auroral Arcs," J. Geophys. Res., Manuscript accepted for publication.

(B) The Generation of VLF chorus in the inner plasma sheet, and its relevance to the precipitation of the electrons that form the diffuse aurora.

The plasma sheet is a region of low plasma density where linear and non-linear waves and particle dynamics are very important. Quasi-electrostatic waves are believed to be responsible for the diffuse aurora precipitation. There exist two kinds of waves that can effectively interact with electrons. They are the electron cyclotron harmonic waves (ECH) and the electromagnetic whistler waves. Whistler waves that propagate near the resonance cone can satisfy the resonance conditions interacting with electrons in the energy range from about 1 to 10 keV.

In the article by Villalon and Burke, J. Geophys. Res. (1995) we proved the efficiency of the interactions between the electrons and a broad coherent frequency spectrum of waves such as the one found in the hiss-triggered chorus emissions. This was due to second-order resonant interactions that compensate the inhomogeneities of the magnetic field with the frequency variations. Thus waves and electrons stay in gyroresonance for extended distances along geomagnetic field lines. This is to be contrasted with the more traditional theory of first-order resonant interactions, which does not compensate for the inhomogeneities with the frequency variations. For first-order interactions, the changes in the particle's physical parameters such as pitch-angles and energies are linear with the electric field's amplitudes. For second-order resonances we were able to prove that due to the frequency variations, the changes of the particles' physical parameters were proportional to the square root of the electric field amplitudes. This is an important result that can effectively account for the formation of the diffuse aurora, since the field amplitudes that are known in the plasma sheet from CREES and other experiments, are small.

Because of the relevance of our theory of second-order interactions, we investigated the generation of chorus emissions near equatorial regions of the inner plasma sheet. In our article, Villalon and Burke, *J. Geophys. Res.*, (1997) nonlinear interactions between plasma sheet electrons and nearly monochromatic whistler wave packets were extensively studied. For electric fields that exceed those of the background plasmaspheric hiss, electrons become bunched in phase space and wavelets are generated by second-order resonant interactions that have frequency spreads that depend on inhomogeneities and plasma parameters.

(C) A study of ionospheric modification research and the experimental results of the Oedipus C satellite.

This third area of research was not part of the original 1995 proposal. It was motivated by the ionospheric observations of the recent Oedipus C rocket experiment. In our discussions with our contract monitor it was concluded that it was of high interest to the Air Force to work with the data generated from this experiment. Oedipus C was a tethered double subpayload satellite that was launched over the auroral ionosphere and that reached a maximum of about 800 km. The forward and aft payloads have electron detectors from about 20 eV to 20 keV. The transmitter swept frequencies from below 25 kHz to 8 MHz. Sounded accelerated electrons were observed by both sub-payloads for frequencies at and below the plasma frequency, and between the electron gyro- and upper hybrid frequencies. Those two frequency intervals are within the range of propagation of the quasi-electrostatic whistler and Z-eigenmodes. In our paper (Huang, et al.) *J. Geophys. Res.* (1999) there is a very extensive description of the experiments and the results on sounded accelerated electrons (SAE), which were observed by both payloads over large frequency and pitch angle ranges. To explain the experimental observations a second paper has been written and submitted to *Radio Science*, which contains analytical models on wave propagation and electron acceleration. The quasi-electrostatic W- and Z-modes are treated in a warm plasma, and their dispersion characteristics are described as functions of plasma parameters that require that the frequency of the plasma be smaller than that of the electron cyclotron waves. The W- and Z- plasma eigenmodes can efficiently interact with the secondary electron population and with the primary auroral electrons. A model for electron acceleration is presented and described within the context of non-linear plasma theory.

Papers and manuscripts related to this work and included in this report are as follows:

1. E. Villalon and W.J. Burke, Pitch Angle Scattering of Diffuse Auroral Electrons by Whistler Mode Waves, *J. Geophys. Res.*, Vol. 100, No. A10, pp. 19,631-19,369. October 1, 1995.
2. E. Villalon and W.J. Burke, Theory of Quasi-Monochromatic Whistler Wave Generation in the Inner Plasma Sheet, *J. Geophys. Res.*, Vol. 102, No. A7, p. 14,381-14,395, July 1, 1997

3. C.Y. Huang, W.J. Burke, D.A. Hardy, M.P. Gough, H.G. James, E. Villalon, and L.C. Gentile, Electron Acceleration by MHz Waves during OEDIPUS C, *J. Geophys. Res.*, 1999
4. E. Villalon, Theory of Plasma Waves Propagation and Electron Heating in a Tenuous Ionospheric Plasma, submitted to *Radio Science*, 1999



## INERTIAL CURRENTS AND SUBSTORM ONSETS

P. L. Rothwell

Geophysics Research Directorate, Phillips Laboratory,  
Hanscom AFB, Bedford, Massachusetts, 01731  
phone: (617) 377-9664, fax: (617) 377-3160

M. B. Silevitch

Center for Electromagnetics Research,  
Northeastern University, Boston, Massachusetts, 02115  
phone: (617) 373-5110, fax: (617) 373-8627

Lars P. Block and Carl-Gunne Fälthammar

Division of Plasma Physics, Alfvén Laboratory,  
Royal Institute of Technology, S 100 44, Stockholm 70, Sweden  
phone: 46-8-790-7686, fax: 46-8-245-431, e-mail: playfys:falthammar

## ABSTRACT

When magnetic field lines are sufficiently stretched during the substorm growth phase, in the equatorial plane the earthward  $E \times B$  ion drift velocity can become comparable to the ion gyration velocity. Under these conditions inertial currents can become quite important. Using a two-dimensional model we find that  $O^+$  ions injected from the ionosphere into the equatorial plane at high latitudes will drift eastward at radial distances less than  $-10 R_E$  because the inertial drift dominates and westward at distances closer to the earth because the magnetic gradient drift dominates. The inertial eastward drift gives rise to a current which in terms of  $J \times B$  is consistent with the convective deceleration of the earthward drift velocity due to higher values of  $B$ . Similarly, momentum balance requires that the convective acceleration of the westward drift velocity should be consistent with a tailward inertial current. Therefore, an equatorial current wedge system with eastward and tailward current components naturally arises from the ion dynamics. In a future paper a three-dimensional treatment will determine whether curvature drift masks the eastward inertial drift of the oxygen ions.

## 1. INTRODUCTION

Daglis and Axford [Ref. 1] have emphasized the importance of  $O^+$  in the substorm process. Their detection of a correlation between the enhancement of upward flowing oxygen ions in the auroral zone and magnetic activity is intriguing. Here we theoretically explore this result utilizing the fact that the higher mass of the  $O^+$  is more likely to give rise to inertial effects. These effects become important in the magnetotail where the drift velocity ( $E/B$ ) is comparable to the particle's gyrovelocity.

Parker [Ref. 2] showed, given the validity of the usual assumptions for MHD, that particle dynamics lead to transverse currents that depend only on the gradient of the pressure associated with those particles. This important result allowed the replacement of the single particle equations with the thermodynamic equation of state in determining the perpendicular currents. Vasyliunas [Ref. 3] in a seminal paper applied these results to magnetospheric-ionospheric coupling which has formed the basis for much of recent magnetospheric research. It may, however, be questioned whether the required assumptions of MHD in the near-earth magnetospheric environment are satisfied

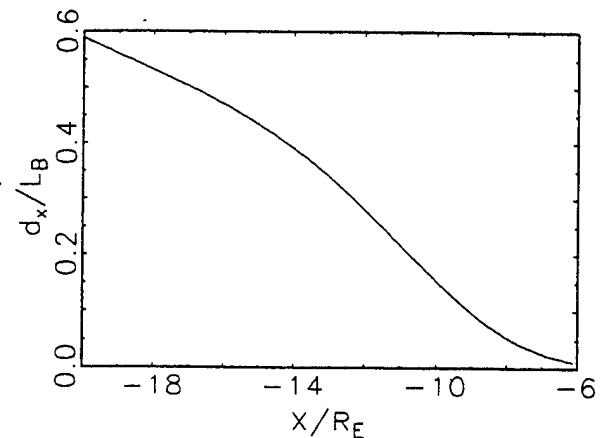


Figure 1. The  $E \times B$  drift distance traveled in one gyroperiod divided by the scale size of the magnetic field as determined from Ref. 7. This ratio increases linearly with  $E_y$ .

in the presence of  $O^+$ ? If the conditions for MHD are satisfied and magnetic field lines convect with the particles then the stability of steady-state convection is questionable [Refs. 4, 5]. If the conditions for MHD are not satisfied then

particle effects may mitigate the instability as shown by Kivelson and Spence [Ref. 6].

We have used the simple analytic model of Rostoker-Skone [Ref. 7] for the near tail region equatorial magnetic field. This model is based on satellite measurements during magnetically active times. The equatorial magnetic field is assumed to point in the z-direction and varies in the x-direction (toward the earth). A cross-tail electric field  $E_y$  points westward which cause's particles to drift toward the earth. We first address the slow flow assumption. This is the assumption that the particle undergoes numerous gyrations while drifting one scale length in B. The local scale size of the magnetic field  $L_B$  is defined by  $B/\nabla B$ . The ion drift distance in one gyroperiod is  $d_x = 2\pi E_y / (B\omega)$  where  $\omega$  is the  $O^+$  gyrofrequency. The ratio  $d_x/L_B$  is shown in Fig. 1 where the value of  $E_y = 1$  mV/m is used. Note that this ratio is larger than 0.1 for  $X \leq -10 R_E$  indicating that at these distances the flow velocity is not "very small" and that the slow flow approximation does not apply for  $O^+$  ions.

## 2. INERTIAL CURRENTS-THEORY

Here we derive the inertial current terms from the single particle equations following an analysis somewhat different from that of Parker [Ref. 2]. We find two first order nonlinear differential equations for the drift velocity components  $V_{xd}$  and  $V_{yd}$ . We then show that these equations give the correct form for the drift velocity for known cases. The equations of motion are

$$\frac{dV_x(x(t),t)}{dt} = \frac{e}{M} E_x + \omega V_y(x(t),t) \quad (1)$$

and

$$\frac{dV_y(x(t),t)}{dt} = \frac{e}{M} E_y - \omega V_x(x(t),t) \quad (2)$$

The system is assumed to be homogeneous in y, and e and M denote the charge and mass of the ion, respectively, and  $\omega = e B/M$ . The cross-tail electric field  $E_y$  is treated as constant. The velocity components are assumed to consist of two parts, a purely time-dependent gyrating part  $V_g$  and a space-dependent drift velocity ( $V_{xd}$  and  $V_{yd}$ ). Expanding the derivatives on the LHS of (1) and (2) and taking an orbit average we find that

$$\begin{aligned} V_{xd} \frac{\partial V_{xd}}{\partial x} &= \left\langle \frac{e}{M} E_x + \omega V_y \right\rangle \\ V_{yd} \frac{\partial V_{yd}}{\partial x} &= \left\langle \frac{e}{M} E_y - \omega V_x \right\rangle \end{aligned} \quad (3)$$

where the symbol  $\langle \rangle$  denotes orbit average. As  $\langle V_{xd} \rangle = V_{xd}$ ,  $\langle V_{yd} \rangle = V_{yd}$  equations (3) can be expressed as

$$V_{xd} = \frac{E_y}{B} \frac{1}{1 + \frac{1}{\omega} \frac{\partial V_{yd}}{\partial x}} \quad (4a)$$

$$V_{yd} = -\frac{E_x}{B} + \frac{1}{2} \frac{V_g^2}{B\omega} \frac{\partial B}{\partial x} + \frac{V_{xd}}{\omega} \frac{\partial V_{xd}}{\partial x} \quad (4b)$$

where the first term on the RHS of the first equation of (4b) is the standard  $E \times B$  drift and the second term describes the magnetic gradient drift [Ref. 8]. Orbit-averaged quantities are understood. The third term corresponds to an inertial drift effect which will be examined in detail below. We now consider these equations for specific cases.

Case I:  $dE_x/dx = \text{const.}$ ,  $B = \text{const.}$ ,  $V_{xd} = \text{const.}$

$$\begin{aligned} V_{xd} &= \frac{\omega^2}{\Omega^2} \frac{E_y}{B} \\ V_{yd} &= -\frac{E_x}{B} \\ \Omega^2 &= \omega^2 - \frac{e}{M} \frac{dE_x}{dx} \end{aligned} \quad (5)$$

Case I agrees with the drift velocity obtained by solving the equations of motion explicitly [Ref. 9] and will not be repeated here.

Case II:  $E_x = 0$ ,  $B=B(x)$ . This case is of primary interest

$$\begin{aligned} V_{xd} &\approx \frac{E_y}{B} \\ V_{yd} &= \frac{M}{e} \frac{V_g^2}{2B^2} \frac{\partial B}{\partial x} - \frac{M}{e} \frac{E_y^2}{B^4} \frac{\partial B}{\partial x} \\ \frac{1}{\omega} \frac{\partial V_{yd}}{\partial x} &\ll 1 \end{aligned} \quad (6)$$

here in dealing with the outer magnetosphere. Weak inertial currents in the  $x$  direction can arise from the deviation of  $\Delta V_{xd}$  from  $E_y/B$  and is given by the following expression

$$J_x = ne \left( V_{xd} - \frac{E_y}{B} \right) = - \frac{\rho E_y}{B^2} \frac{\partial V_{yd}}{\partial x} \quad (7)$$

where  $\rho$  is the mass density. Implications of equations (6) and (7) for the Rostoker-Skone model will be examined below. There we find that  $\partial V_{yd}/\partial x \approx 0.01\omega$  consistent with the assumption stated in equation (6).

Case III:  $dE_x/dx = \text{const.}$ ,  $B=B(x)$ . This is the most complicated case and applies where there is a radial electric field component in the magnetosphere, such as when the Harang discontinuity maps to the equatorial plane.

$$\begin{aligned} V_{xd} &= \frac{\omega^2}{\Omega^2} \frac{E_y}{B} \\ \Omega^2 &= \omega^2 - \omega \frac{\partial \left( \frac{E_x}{B} \right)}{\partial x} \end{aligned} \quad (8)$$

Case III is analogous to Case II. Now where we have assumed that the main contribution to  $\partial V_{yd}/\partial x$  comes from the first term in equation (9). See equation (4a).

$$\begin{aligned} V_{yd} &= -\frac{E_x}{B} - \frac{\omega^5 E_y^2}{B^3 \Omega^6} \left[ \frac{\partial B}{\partial x} \left( 1 + 2 \frac{M}{e} \frac{1}{B} \frac{\partial \left( \frac{E_x}{B} \right)}{\partial x} \dots \right. \right. \\ &\quad \left. \left. + \frac{M}{e} \frac{E_x}{B^2} \frac{\partial^2 B}{\partial x^2} \right] + \frac{1}{2} \frac{M}{e} \frac{V_g^2}{B^2} \frac{\partial B}{\partial x} \end{aligned} \quad (9)$$

The above cases show that as the electric and magnetic field structure becomes more complicated that the analytic expressions for the ion drift velocities also become more complex which reflects their enhanced departure from  $E \times B$  drift. This departure results in inertial currents that balance the change in momentum of the convective flow. In the nightside near-earth magnetosphere these currents may form current wedges that are related to the substorm onset. They also, as is well known, must be consistent with the expression

$$\rho \mathbf{V} \cdot (\nabla \mathbf{V}) = \mathbf{J} \times \mathbf{B} - \nabla P \quad (10)$$

By subtracting the  $E \times B$  drift from equations (4a) and (4b) one can easily show that this is the case.

### 3. INERTIAL CURRENTS -NUMERICS

We now want to determine the drift velocities by a numerical integration of equations (1) and (2). The method should be valid even if the conditions for MHD are not met. The most direct approach is to integrate a velocity component over one gyroperiod. However, this technique is not very accurate if the orbit shape and/or size changes significantly during one gyroperiod. For example, the gyroradius decreases upon entering a region with a positive  $B$ -field gradient. Integration over velocity components gives good agreement (one part in  $10^{5-6}$ ) with theory provided either  $E_y$  or  $dB/dx$  is zero. When both  $E_y$  and  $dB/dx$  are nonzero then the  $y$ -drift velocity is too high by 20% using the velocity averaging technique. Another method for determining the drift velocity is to define the orbit center by integrating over either  $x$  and  $y$  for one gyroperiod. One then numerically determines the velocity of this center. This method works but is noisy due to dividing by the gyroperiod twice. One division is for finding the position average and the other for determining the drift velocity. However it is noted that one turning point drifts at a different speed than the other turning point. We find that the most accurate technique for determining the net drift velocity is to average the drift speed of the two turning points for each velocity component.

Figure 2 shows the  $y$  component of the drift speed for  $H^+$  and  $O^+$  using the Rostoker-Skone magnetic field model for Case II. For purposes of illustration a 500 eV ion is injected at  $-30 R_E$  with  $E_y = 1$  mV/m. Note that at larger distances from the earth this velocity is strongly eastward for  $O^+$  implying an eastward current. The solid line represents the drift velocity as determined by the numerics with the

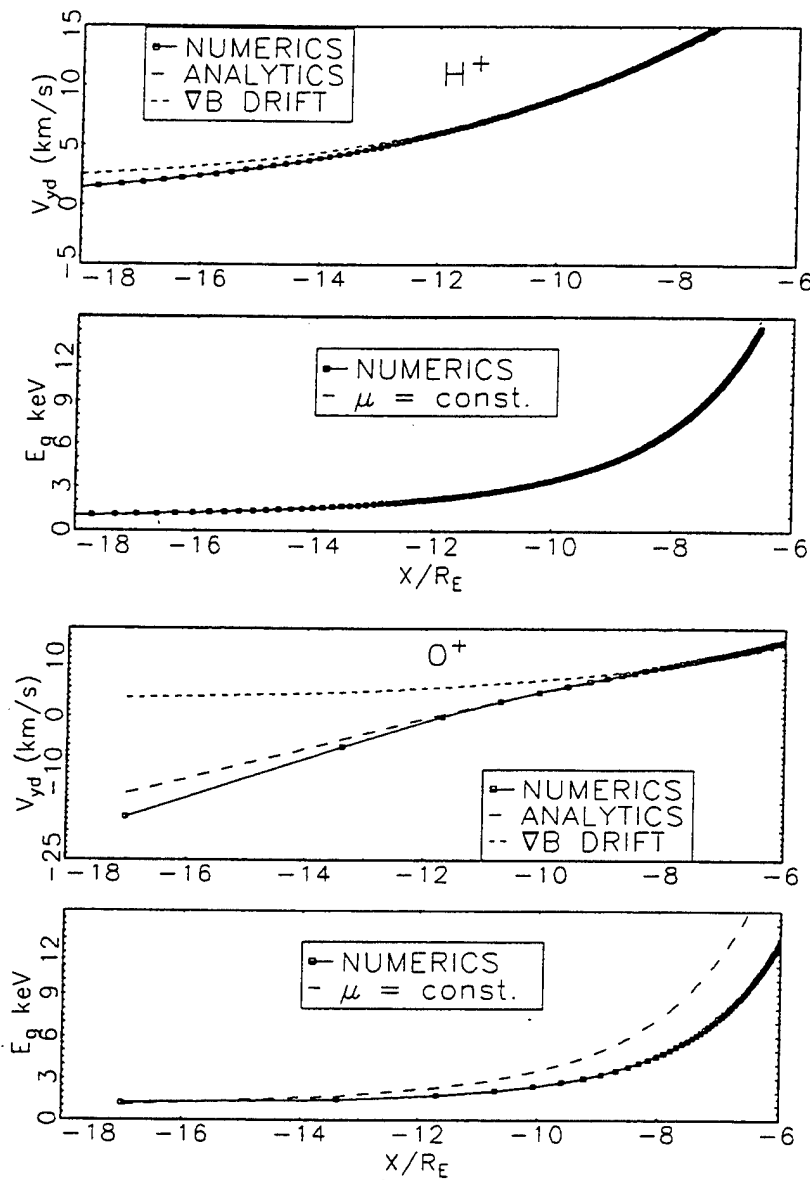


Figure 2. The importance of the  $E_y^2$  inertial term (equation (6)) for oxygen at larger distances from the earth is illustrated. The short-dashed line represents the expected drift velocity due to the magnetic gradient. The bottom portion of each figure is the gyroenergy as a function of  $X$  in comparison with that expected from the conservation of the first adiabatic invariant.

distance between the small squares denoting a gyroperiod. The dashed line (lower) represents the drift velocity as determined from equation (6). The upper line (short dashes) represents the drift speed as expected by the magnetic gradient drift. It is clear that magnetic gradient drift does not by itself adequately describe the  $y$  drift velocity for oxygen at larger distances from the earth. Protons, due to their smaller mass, contribute far less to the

inertial currents. The physical picture is that the cross tail current is maintained by gradient-curvature drifting protons but is locally weakened by the injection of ionospheric oxygen that mirrors in equatorial plane. The degree of weakening is proportional to  $E_y^2$  as seen from equation (6). This feature could provide a mechanism for local current interruption that is required for a substorm onset. The bottom part of Figure 2 for each of the ions denotes the

gyroenergy as determined from the numerics and conservation of the first adiabatic invariant. The violation of the first adiabatic invariant at smaller  $X$  leads to a substantial discrepancy closer to the earth. From equation

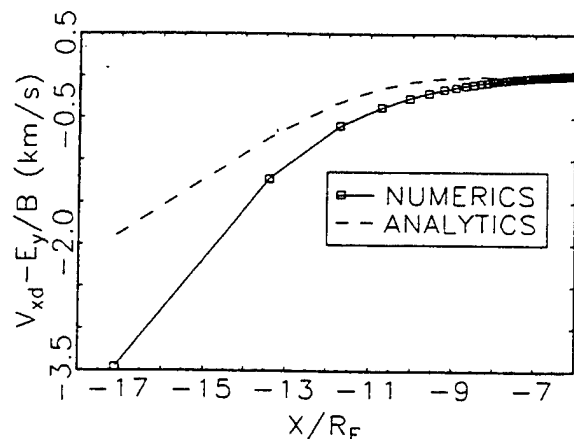


Figure 3. The oxygen ions drift earthward at a speed less than  $E_y/B$  consistent with equation (6).

(4a) we note that the positive slope of  $V_{yd}$  vs.  $X$  curve as seen in Figure 2 should lead to values of  $V_{xd}$  which are less than  $E_y/B$ . This is indeed the case as seen in Figure 3. This

feature implies a weak tailward current which could close off the region I and region II currents in the premidnight equatorial plane.

As seen from Figure 2 the oxygen ions drift eastward and then westward. This occurs because as the ions drift earthward their gyroenergy increases. The westward magnetic gradient drift is proportional to the gyroenergy so at some point the drift reverses and becomes strongly westward. This effect produces a polarization that tends to lessen the west-east polarization field due to the charge separation of  $H^+$  and  $e^-$  caused by gradient-curvature drift. A sufficiently strong eastward drift of oxygen ions could cause a local enhancement of  $E_y$ . This, of course, would cause the polarization to spread earthward as the subsequent ions experience an enhanced eastward drift. The weakening of the westward neutral sheet current by eastward flowing  $O^+$  would lead to dipolarization. Therefore, the presence of ionospheric oxygen in the equatorial plane could play a direct role in the onset process. In this picture the current wedge structure is naturally closed in the equatorial plane by single ion dynamics and becomes intensified during magnetically active periods when ionospheric oxygen becomes more plentiful. [Ref. 1].

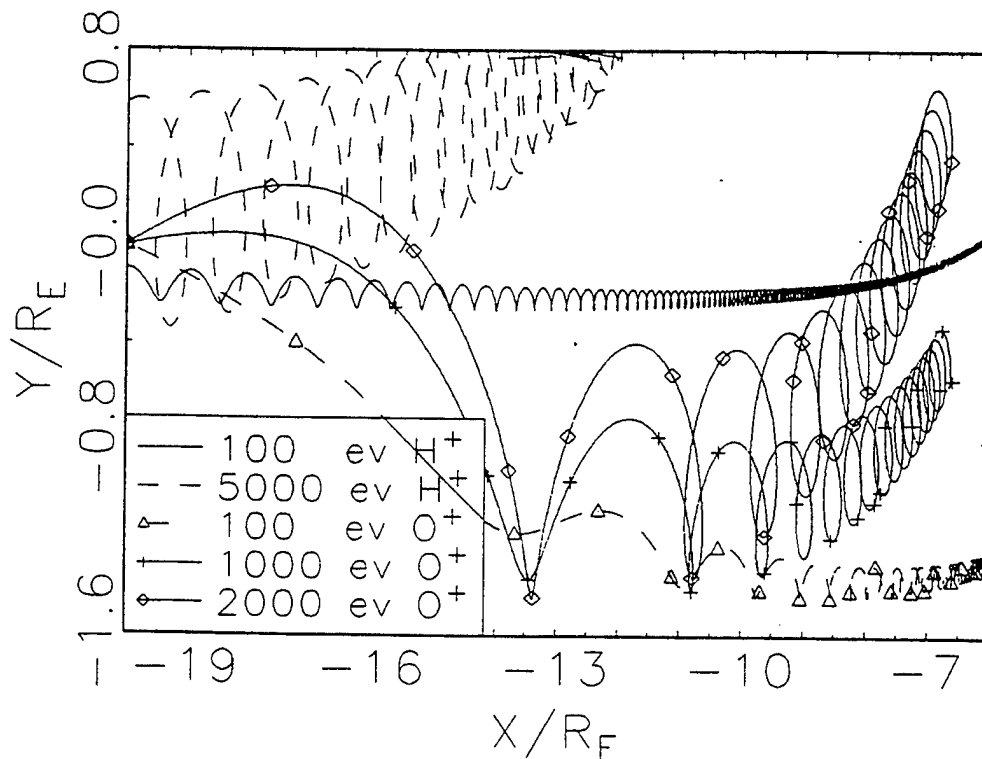


Figure 4. Proton and oxygen trajectories in the near-earth magnetosphere using the Rostoker-Skone magnetic field model with  $E_y = 2/mV/m$ . Note the preferential displacement of oxygen in the eastward (-y) direction.

In order to demonstrate the polarization effect we plot proton and oxygen trajectories for a number of initial energies as shown in Figure 4. All the ion trajectories shown in this figure start at  $-20 R_E$  with  $E_y$  set to 2 mV/m to emphasize the electric polarization. The initial phase angle in all cases equals  $90^\circ$ .

#### 4. DISCUSSION

As shown above the enhanced presence of oxygen ions during a substorm can lead to magnetospheric-ionospheric current structures. In particular, the eastward motion of the oxygen ions forms an equatorial generator that could partially power the westward electrojet. Huang and Frank [Ref. 10] measured the bulk flow of ions in the plasma sheet and found that for  $AE > 600$  nT the bulk flow became progressively eastward. See their figure 2. This noticeable effect is consistent with the enhanced population of oxygen during active periods [Ref. 1] and its eastward motion as discussed above. Another feature found by Huang and Frank was that the earthward bulk flow was smaller than 20 km/s regardless of the value of  $AE$ . This latter result has been used by others [Refs. 5] as verifying the slow flow condition required by ideal MHD.

This apparent paradox may be explained by identifying a more adiabatic proton population with a flux tube that moves according to the formulation of Erickson and Wolf [Refs. 4,5]. On the other hand, energetic oxygen ions mirroring near the equatorial plane are unlikely to remain identified with a single flux tube and, as shown, can contribute to the formation of a substorm current wedge. Thus, it may be the substorm onset itself marks the transition from an ideal MHD configuration to one in which single particle effects become important. The current arising from the heavy ion drifts must contribute to the overall pressure balance through  $J \times B$  and also allow particle leakage through the tail boundaries [Ref. 6].

During substorm onsets the east-west electric field may be significantly higher than 1 mV/m [Ref. 11]. The inertial effects described above are enhanced under such circumstances. In the future we will look at the localized injection of oxygen during a substorm onset and define where the resulting current wedge structures should exist. Also, it should be noted that the two-dimensional nature of our analysis has ignored curvature drift which could dominate in the near-earth regions discussed here. Whether curvature drift is important or not depends on the magnetic field geometry and the pitch angle distribution of the ions. This important point is left for a future analysis.

#### 5. REFERENCES

1. Daglis I A & W I Axford 1996, Fast ionospheric response to enhanced activity in geospace: ion feeding of the inner magnetotail, *J. Geophys. Res.*, 101, 5047-5065
2. Parker E N 1957, Newtonian development of the dynamical properties of ionized gases at low density, *Phys. Rev.* 107, 924-933
3. Vasyliunas V 1970, Mathematical models of magnetospheric convection and its coupling to the ionosphere, *Particles and Fields in the Magnetosphere*, ed. B. M. McCormac, *D. Reidel publ.*, 60-71
4. Erickson G M & R A Wolf 1980, Is steady convection possible in the earth's magnetotail, *Geophys. Res. Letts.*, 7, 897
5. Erickson G M & al 1991, The physics of the Harang discontinuity, *J. Geophys. Res.*, 96, 1633-1645
6. Kivelson M G & H E Spence 1988, On the possibility of quasi-static convection in the quiet magnetotail, *Geophys. Res. Letts.*, 15, 1541-1544
7. Rostoker G & S Skone 1993, Magnetic flux mapping considerations in the auroral oval and the earth's magnetotail, *J. Geophys. Res.*, 98, 1377-1384
8. Chen F F 1990, Introduction to Plasma Physics and Controlled Fusion, vol. 1, Plasma Physics, *Plenum*, New York
9. Rothwell P L & al, 1994,  $O^+$  phase bunching and auroral arc structure, *J. Geophys. Res.*, 99, 2461-2470
10. Huang C Y & L A Frank 1986, A statistical study of the central plasma sheet : implications for substorm models, *Geophys. Res. Letts.*, 13, 652-655
11. Maynard N C & et al 1996, Dynamics of the inner magnetosphere near times of substorm onset, *J. Geophys. Res.*, 101, 7705-7736

# O<sup>+</sup> Phase Bunching, Oblique Alfvén Waves and Auroral Arcs

Paul L. Rothwell

Air Force Research Laboratory, Hanscom AFB, Bedford, Massachusetts, 01731

Michael B. Silevitch

Center for Electromagnetics Research, Northeastern University, Boston, Massachusetts, 02115

Lars P. Block and Carl-Gunne Fälthammar

Division of Plasma Physics, Alfvén Laboratory, Royal Institute of Technology, S 100 44, Stockholm 70, Sweden

**Abstract.** In the earthward drifting magnetotail plasma, phase bunching of O<sup>+</sup> ions (but to a much lesser extent of the H<sup>+</sup> ions) can be caused by, for example, a weak ( $\sim 1 \times 10^{-9}$  V/m<sup>2</sup>) electric field gradient [Rothwell *et al.*, 1994]. This leads to density striations in the (non-rotating) earthfixed "lab" frame. In this scenario the O<sup>+</sup> density striations are seen as a tailward propagating source of magnetospheric Alfvén waves in the moving frame where the hydrogen ions provide the polarization current of the wave. If the generated Alfvén waves in this frame are entrained moving tailward then a transformation to the lab frame will yield a static, oblique wave structure similar to that discussed by Maltsev *et al.* [1977] and Mallinckrodt and Carlson [1978]. The waves propagate from the equatorial region to both ionospheres where they are reflected. The ionospheric boundary conditions when combined with a magnetospheric boundary condition allows a solution of the wave amplitudes in terms of the striation driver. The frequency of the Alfvén wave and the associated wavelengths are also determined by the striation driver. We find that the magnitude of the parallel current at the ionosphere has a spatial resonance when the distance between the ionosphere and the equatorial plane is equal to a quarter wavelength along B. In that case, the magnitude of the parallel current at the ionosphere is on the order of 10  $\mu$ A/m<sup>2</sup> and peaks for striation wavelengths (as mapped to the ionosphere) of 10-40 km consistent with observations.

## 1. Introduction

There has been many studies of oblique Alfvén waves in which the propagation and reflection of Alfvén waves have been intensively examined [Maltsev *et al.*, 1977; Mallinckrodt and Carlson, 1978; Lysak, 1985, 1986, 1990; Haerendel, 1983; Borovsky, 1993; Seyler, 1990, 1995; Knudsen, 1996]. A few studies have also identified a magnetospheric source. For example, the coupling of a compressional wave in the equatorial region with a shear Alfvén wave could produce a Field Line Resonance (FLR) [Chen and Hasegawa, 1974; Southwood, 1974; Miura and Sato, 1980; Samson and Rankine, 1994; Samson *et al.*, 1996]. In this work we

investigate density striations in the near-earth nightside magnetosphere as a possible magnetospheric source of an oblique Alfvén waves. The basic idea is that the magnetic field near local midnight can become quite extended near the equatorial plane such that the oxygen ions exhibit nonadiabatic behavior while the hydrogen ions remain adiabatic. See Rothwell *et al.* [1994]. In the present model density striations are assumed to be produced by the phase bunching of the O<sup>+</sup> ions as they enter a region of an extended electric field gradient as shown by Rothwell *et al.* [1994]. Other mechanisms can also be operative. For example, local acceleration occurring over short time scales by magnetic dipolarization can cause a similar effect [Delcourt *et al.*, 1996]. Associated with the density striations is a periodic static spatial variation of the radial current which when viewed in the drift frame of the adiabatic hydrogen ions is seen as tailward moving current wave. In this frame the current wave has a wavelength given by the distance between striations and a frequency given by the corresponding wavenumber times the drift velocity. This defines the frequency of the oblique wave in the drift frame. It also defines the wavelength of the Alfvén wave along the field line through the dispersion relation. If one doppler shifts the wave frequency in the moving frame to that in the laboratory (non-rotating) frame one finds the latter to be zero consistent with the static nature of the source. The oblique Alfvén wave forms a static wave pattern in the spirit of Maltsev *et al.* [1977] and Mallinckrodt and Carlson [1978].

There are two boundary conditions. One boundary condition requires  $j_z$  to be zero at the equatorial plane ( $z = 0$ ) consistent with symmetry of the two ionospheres. The other boundary condition determines the reflection coefficient of the oblique Alfvén waves at the two ionospheres. Together they fully determine the wave amplitude in terms of the striation driver and the wave phase at the ionosphere. By imposing a current node at the equatorial plane and having the wavelength fixed we find that the parallel current is a maximum at the ionosphere if the ionosphere is located a quarter wavelength from the equatorial plane. This is a well known resonant relation seen in resonant cavities.

The goal of the present work is to determine whether the proposed mechanism can lead to reasonable values of the

parallel current at the ionosphere given reasonable values for the magnetospheric input parameters. In this paper we have used several assumptions that should be stated. The difference in dynamical behavior between the oxygen and hydrogen has already been mentioned. The treatment here is not self-consistent in that the effect of the wave fields on the striations has not been taken into account. Also, we assume that the Alfvén speed is constant along the field line and that the static wave structure has time to form. Finally, we do not consider wavelengths below or at the electron inertial length (6 km) because of the evanescent property of these waves in the ionosphere [Borovsky, 1993]. Therefore, kinetic Alfvén waves as described by Goertz and Boswell [1979] are not treated here.

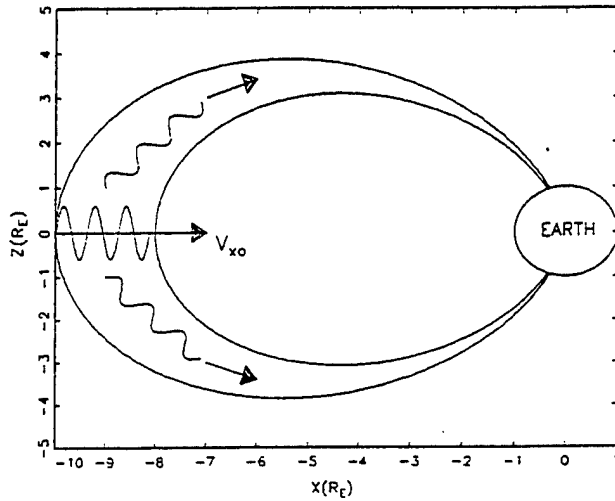


Figure 1. Cartoon of the concepts involved.  $O^+$  ions drifting earthward with a drift speed  $V_{x0}$  can create density striations through phase bunching. This acts as a source of oblique Alfvén waves that propagate to the two ionospheres.

Figure 1 illustrates the concepts described above. The  $O^+$  density striations are represented by a sinusoid along the equatorial plane. The waves emanate towards each ionosphere creating density (conductivity) perturbations as shown. If the ionospheres are symmetrically located relative to the equatorial plane then the magnetospherically generated waves at each ionosphere will be at the same phase and the conductivity perturbations will be conjugate.

In the coordinate system used here  $x$  points earthward,  $y$  towards the west and  $z$  is parallel to the earth's magnetic field. With  $z=0$  denoting the equatorial plane the northern ionosphere is located at  $z = L_m$  and the southern ionosphere at  $z = -L_m$ .

## 2. Magnetospheric Theory

With the above scenario in mind let us now analyze the generation of the oblique Alfvén wave. We found in Rothwell et al. [1994] that in the presence of an electric field gradient the drift speed can be much faster for the heavier ions. This feature elongates the separation of the turning points as seen in the laboratory (non-rotating) frame and enhances the presence of

the density striations due to phase bunching. The protons remain adiabatically trapped and  $E \times B$  drift through the  $O^+$  striations that form the wave source.

The presence of ion density striations leads to an additional  $x$ -component of the current that is carried by electrons. This can be understood as follows. In regions of enhanced ion density charge neutrality requires that electrons flow up the field line to neutralize the additional positive charge. To make the problem tractable we assume that the ions originated outside the striation region and are not gained or lost along the magnetic field lines. This means that their flux in the  $x$ -direction is conserved. If  $N_{O^+}$  is the ambient  $O^+$  density outside the striation region and  $\delta n_{O^+}$  the density perturbation due to the striations we have

$$j_{xO^+} = e [N_{O^+} - (N_{O^+} + \delta n_{O^+})] \frac{E_y}{B} = -e \delta n_{O^+} \frac{E_y}{B} \quad (1)$$

Note that in Eq. (1) electrons are the current carriers forming a spatially varying current structure which maintains charge neutrality with the  $O^+$  density striations. The density perturbation exponentially decreases from the equator with a scale length  $L_z$  and has a wavenumber in the  $x$  direction equal to  $k_x$ . (In Rothwell et al. [1994]  $k_x$  is determined by the drift speed of  $O^+$  ions as they enter a region of a large scale electric field gradient.) There are other mechanisms, such as that reported by Delcourt et al. [1996], that can also produce density striations. With these assumptions Eq. (1) becomes in the lab frame

$$j_{xsource} = -e \delta n_{O^+} V_{x0} \exp(-z/L_z) \exp(ik_x x) \quad (2)$$

where  $\delta n_{O^+}$  is the amplitude of the  $O^+$  number density amplitude and  $V_{x0}$  is the drift speed ( $E_y/B$ ).

Now let us recast Eq. (2) in terms of the moving plasma coordinate frame. As the plasma convects towards the earth at a speed  $V_{x0}$  a current wave is seen in the moving frame moving tailward at the drift velocity and with a frequency  $\omega_i = k_x V_{x0}$ . This current wave is a source of Alfvén waves in the moving frame and may be rewritten in this frame as

$$j_{xsource} = -e \delta n_{O^+} V_{x0} \exp(-z/L_z) \exp(\omega_i t + k_x x') \quad (3)$$

While the incipient untrapping of the oxygen ions provides the source current for the Alfvén waves the protons remain adiabatic and provide the polarization current that allows the Alfvén wave to propagate. Details are given in the Appendix.

If we now doppler shift the wave field, as derived in the Appendix, to the lab frame the wave is seen as static. This should hold for any spatially periodic current driver. Therefore, as a general rule a drifting plasma through a spatially periodic current structure produces Alfvén waves in the moving plasma



frame such that when doppler shifted ( $x' = x - V_{so}t$ ,  $\omega_i = k_o V_{so} = k_z V_A$ ) to the lab frame these waves will be preceived as static *Haerendel* [1983]. The result is

$$E_x = E_{xi} \exp i(k_o x - k_z z) + E_{xr} \exp i(k_o x + k_z z) - \dots$$

$$i \frac{e \mu_o k_o \delta n_o V_{so}^2 \exp(-z/L_z)}{\frac{1}{L_z^2} + \frac{k_o^2 V_{so}^2}{V_A^2}} \exp i(k_o x) \quad (4)$$

In the lab frame the wave magnetic field will also be static. Now the drifting of the moving plasma past a stationary  $B_y$  will induce an  $E_z = -V_{so} E_x / V_A$  in the lab frame that doesn't exist in the moving frame. This electric field component is necessary for the total electric field to be perpendicular to the total magnetic field in both the laboratory and moving frames as is required by the well known invariance of  $\mathbf{E} \cdot \mathbf{B}$  between moving frames [Landau and Lifshitz, 1959]. Therefore, the total magnetic field is an equipotential and trapped electrons cannot be accelerated along  $B$  by the wave unless the electron's inertia is considered.

It can be shown that [Maltsev et al., 1977]

$$j_z = -\frac{1}{\mu_o V_{so}} \frac{\partial E_x}{\partial z} \quad (5)$$

and the inhomogeneous solution can be recast in terms of  $E_{xi}$  and  $E_{xr}$  through an equatorial boundary condition.

The equatorial boundary condition arises from the source wave propagating to both ionospheres. We also assume in this model that the wave structure in one hemisphere is decoupled from the wave structure in the other. They are related only in that they have a common source. In that case the  $j_z$  in each hemisphere, as defined by Eqs. (4) and (5), is zero at  $z = 0$ . This leads to

$$E_i - E_r = \overline{E_{in}} = \frac{E_{in}}{k_z L_z}$$

$$E_{in} = \frac{k_o \mu_o V_{so} L_z^2 V_A^2}{V_A^2 + k_o^2 V_{so}^2 L_z^2} (e \delta n_o V_{so}) \quad (6)$$

where  $E_{in}$  is the inhomogeneous part of the solution shown in Eq. (A3). At larger distances from the equator the inhomogeneous solution goes to zero and the density perturbation source on the Alfvén wave is effected by the constraint Eq. (6) on the incident and reflected amplitudes.

### 3. The Northern Ionosphere

The ionosphere defines another relation between  $E_i$  and  $E_r$  through the conservation of current at the reflecting surface. Here we use coordinates consistent with the northern ionosphere. We equate the  $j_{zo}$  of the wave to the gradient of  $\Sigma_{po}$   $E_x$  in the ionosphere where  $E_x$  is determined from the homogeneous solution Eq. (A4). The result is

$$E_r = \frac{\Sigma_{\omega} - \Sigma_{po}}{\Sigma_{\omega} + \Sigma_{po}} E_i \exp(-2 i k_z L_i) \quad (7)$$

The symbol  $\Sigma_{po}$  denotes the background Pedersen conductivity. The exponential term takes into account the phase of the wave as it impinges on the ionosphere. The symbol  $\Sigma_{\omega} = (\mu_o V_A)^{-1}$  represents the conductivity of the Alfvén wave. By combining Eqs. (6) and (7) one obtains a solution for the wave that depends on both magnetospheric and ionospheric parameters.

Insight can be gained by looking at the wave electric field and parallel current at  $z = L_m$  (northern ionosphere).

$$E_x(x, L_{in}) = \frac{\Sigma_{\omega} \overline{E_{in}} \exp(i k_o x)}{\Sigma_{po} \cos(k_z L_{in}) + i \Sigma_{\omega} \sin(k_z L_{in})} \quad (8)$$

$$j_{zw}(x, L_{in}) = \frac{i k_o \Sigma_{\omega} \Sigma_{po} \overline{E_{in}} \exp(i k_o x)}{F_x(L_{in}) [\Sigma_{po} \cos(k_z L_{in}) + i \Sigma_{\omega} \sin(k_z L_{in})]}$$

The parallel wave current at the ionosphere is dependent on the phase at which the wave reflects off the ionosphere. For example, if  $k_z L_m = \pm \pi/2$  then  $j_{zo}$  is proportional to the ionospheric conductivity. If  $k_z L_m = \pm \pi$  then  $j_{zo}$  is proportional to the Alfvén conductivity along  $B_z$ . Inspection of Eq. (8) reveals the resonant nature of the phase relation due to the ionosphere being much more conductive than the wave medium. The reason for this was stated above. That is, with the wavelength and one boundary condition fixed in the equatorial region the wave amplitude is sensitive to the location of the second boundary condition in analogy with a resonant cavity. The condition  $k_z L_m = \pm \pi/2$  is, of course, the usual quarter wavelength criterion.  $F_x$  is a scale factor between the ionosphere and the equatorial plane.

A similar analysis can be done for the southern ionosphere.

### 4. Self-Consistent Ionospheric Reflection

So far we have investigated the production of oblique Alfvén waves by density striations in the equatorial plane. These waves produce also conductivity perturbations in the two ionospheres. When coupled to the background ionospheric electric fields these perturbations provide an additional source of parallel current in the manner suggested by Maltsev et al. [1977]. The parallel current carried by the waves at the northern ionosphere is given by Eq. (8). The positive conductivity perturbation produced by this current is given by

$$\delta \Sigma_p(L_{in}) = -G j_{z\omega}$$

$$G = \frac{(Qh)eh}{2\sigma_r \Sigma_{po} B_i^2} \quad (9)$$

which results from a balance between the recombination and ionization rates. We use  $Qh = .5$  ion/incident electron for the ionization rate produced by  $j_{z\omega}$ . The ionospheric integration height  $h$  equals 20 km, the recombination rate  $\sigma_r = 1 \times 10^{-13} \text{ m}^3/\text{s}$ ,  $\Sigma_{po} = 20 \text{ S}$  and the magnetic field value at the ionosphere,  $B_i = 4 \times 10^{-5} \text{ T}$ . This gives  $G = 2.5 \times 10^5 \text{ S}/(\text{A}/\text{m}^2)$ . The  $z$  axis is parallel to the ambient magnetic field so that a positive  $j_{z\omega}$  corresponds to an incident current in the northern ionosphere while a positive  $j_{z\omega}$  corresponds to an exiting current in the southern ionosphere. For the sake of simplicity we also assume Eq. (9) holds for currents into the ionospheres (upward moving electrons) although this is not strictly valid.

$$\delta \Sigma_p(L_{in}) = -G j_{z\omega}(L_{in}) \quad \text{Northern Ionosphere}$$

$$\delta \Sigma_p(-L_{is}) = +G j_{z\omega}(-L_{is}) \quad \text{Southern Ionosphere} \quad (10)$$

In the two ionospheres we have a height integrated current.

$$J_x = \mp [E_{x\omega} - R_\Sigma E_{y\omega}] G j_{z\omega} \quad (11)$$

where the minus corresponds to the northern ionosphere and the plus sign to the southern ionosphere. Here  $E_{x\omega}$  is the southward component of the ambient ionospheric electric field and  $E_{y\omega}$  is the westward component. Following Maltsev *et al.* [1977] current continuity at the northern ionosphere is given by

$$E_x = [E_i^n \exp(-ik_z z) + E_r^n \exp(+ik_z z)] \exp(ik_o x)$$

$$j_{z\omega}(L_{in}) = \Sigma_{po} \frac{\partial E_x}{\partial x} - i\eta j_{z\omega}(L_{in}) \quad (12)$$

$$\eta = G k_{\alpha} [E_{x\omega} - R_\Sigma E_{y\omega}] (\text{dimensionless})$$

where  $k_{\alpha}$  is the striation wavenumber as scaled to the ionosphere with a scale factor  $F_x = .032$ .  $R_\Sigma$  is the ratio of the Hall to Pedersen conductivities. From Eq. (12) we calculate  $E_r^n$

$$E_r^n = E_i^n \exp(-2ik_z L_{in}) \left[ \frac{\Sigma_{\omega}(1+i\eta) - \Sigma_{po}}{\Sigma_{\omega}(1+i\eta) + \Sigma_{po}} \right] \quad (13)$$

where 'n' denotes the northern ionosphere. Note that the self-consistent reflection adds an imaginary component to the Alfvén conductivity which is equivalent to an additional phase shift in the reflected amplitude. We can determine when this

effect becomes important by using the above values. We find from Eq. (12)  $\eta = 10^4 k_{\alpha}$  when the background ionospheric electric fields contribute a factor of  $4 \times 10^{-2} \text{ V/m}$ . The ionospheric wavelength at which  $\eta \Sigma_{\omega}$  becomes comparable to  $\Sigma_{po}$  is 1.25 km which is significantly shorter than the scale size stated in our assumptions.

## 5. Numerical Results

The key numerical requirement of our model is that the distance  $L_z$  between the equatorial plane and the ionospheres is consistent with the quarter wavelength criterion. This is consistent with the distance between the ionosphere and the equatorial plane in the auroral region being about  $10 R_E$ .

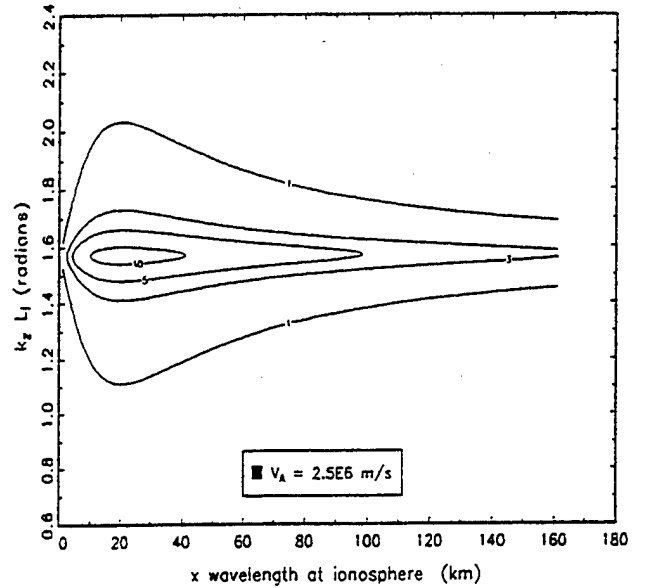


Figure 2. A contour plot of the parallel current ( $\mu\text{A}/\text{m}^2$ ) carried by the oblique Alfvén wave as seen at the ionosphere. The abscissa denotes the equatorial source wavelength as mapped to the ionosphere. Note the maximum values occur at the quarter wavelength criterion and for 10-40 km wavelengths.

Now let us look at the numerical viability of our model. First, we calculate the value of  $E_m$  as defined in Eq. (6) as a function of wavelength in the ionosphere for various values of the Alfvén speed. The chosen parameter values are  $V_{\omega} = 20 \text{ km/s}$ ,  $\delta n_0 = 1 \times 10^5 \text{ O}^+ \text{ ions}/\text{m}^3$  and  $L_z = 2 R_E$ . In this model the wave amplitude and, hence, the strength of the magnetosphere-ionosphere interaction scales as the Alfvén speed. This implies more intense wave fields exist on field lines where the particle density has been depleted and may imply a stronger magnetospheric-ionospheric coupling during substorm growth periods when there is a substantial flux of upflowing  $\text{O}^+$  [Daglis *et al.*, 1998].

Figure 2 shows a contour plot of the resulting parallel wave current at the ionosphere for  $V_A = 2.5 \times 10^6 \text{ m/s}$ . We use a scaling factor of  $F_x = 0.032$  which corresponds to a dipole field model at  $L = 6.5$ . The ordinate denotes the  $z$  phase of the wave

at the ionosphere in radians and the abscissa denotes the striation wavelength as transformed to the ionosphere. The contours are in units of  $\mu\text{A}/\text{m}^2$ . Note that for the parameter values used that we obtain a maximum parallel current of some tens of microamps per meter squared. These maximum values are obtained at the quarter wavelength condition and for ionospheric wavelengths of tens of kilometers consistent with larger auroral forms. Therefore, we argue that even quite conservative values of the magnetospheric parameters leads to realistic values for the parallel current at the two ionospheres.

Now let us look at the resonant nature of the Alfvén wave. Recall that the oblique Alfvén wave amplitude is determined by the striation source as well as the magnetospheric and ionospheric boundary conditions in a manner equivalent to that of a resonant cavity. Figure 3 dramatically demonstrates this effect. This is a plot of the parallel current for  $x=0$  at the ionosphere as a function of the wave phase at the ionosphere denoted in units of  $\pi$ . See Eq. (8).

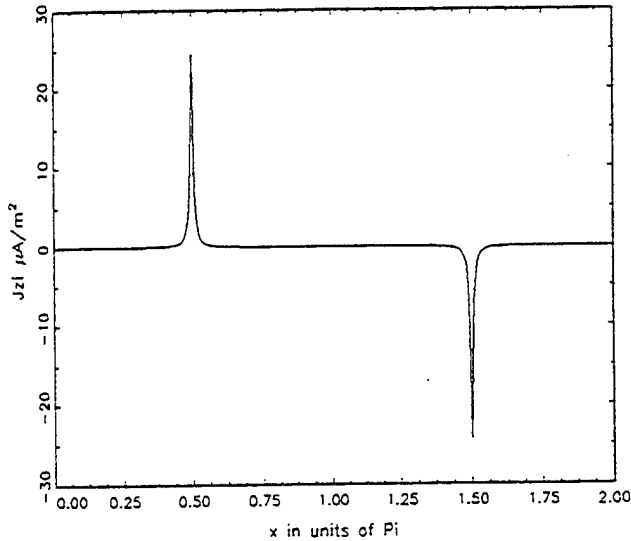


Figure 3. The resonant nature of the magnetosphere-ionosphere coupling by the oblique Alfvén wave is demonstrated. The resonance occurs when the distance between the ionosphere and the equatorial plane satisfies the quarter wavelength criterion. It arises from the ionospheric conductivity being much larger than the Alfvén (wave) conductivity.

Clearly, the quarter wavelength resonance can be seen. The resonance at  $k_{\perp} L_1 = 3\pi/2$  requires that  $V_A$  be one third the value necessary for the  $k_{\perp} L_1 = \pi/2$  resonance for constant  $V_{\infty}$ . Alternately the same criterion is satisfied if  $V_A$  remains constant but  $V_{\infty}$  increases by a factor of three. Note that the parallel current outside the resonance regions is not zero but differs by a factor of  $\Sigma_p/\Sigma_{\omega} \approx 50$  from the parallel current at resonance. The width of the resonance is determined by  $\Sigma_{\omega}$ . The creation of an 10 - 40 km arc structures, such as those observed by Marklund *et al.* [1984], by oblique Alfvén waves depends on the length of the field line, the plasma density along the field line, the  $x$  wavelength of the magnetospheric driver and the drift speed of the plasma. One obvious effect is that

any increase in  $k_z$  would cause the resonance criterion to be satisfied on field lines closer to the earth. This could be related to the observed equatorial motion of auroral arcs under substorm growth conditions when there is a substantial  $\text{O}^+$  population in the near earth magnetosphere [Daglis *et al.*, 1998].

## 6. Summary and Conclusions

We have identified density striations formed by nonadiabatic oxygen ions as a possible magnetospheric source for oblique Alfvén waves. It was found that magnetospheric and ionospheric boundary conditions lead to a resonant type behavior. Reasonable input parameter values imply  $10 \mu\text{A}/\text{m}^2$  parallel currents at the ionosphere with the maximum values occurring for structures on the order of 10 - 40 km, a width consistent with observations of auroral arcs [Marklund *et al.*, 1984]. Thus, even with the stated simplifications results consistent with observations are obtained.

## 7. Appendix

Here we derive the Alfvén wave in the plasma frame. In addition to the usual polarization current we also now have a time-dependent source term due to the striations. We assume that the  $\text{O}^+$  striations can be approximated by a sine dependency in  $x$  and an exponential dependence in  $z$  i.e.

$$\delta j_x = -e V_{\infty} \delta n_o \exp(i(\omega_r t' + k_o x')) \exp(-z'/L_z) \quad (\text{A1})$$

where  $\omega_r = k_o V_{\infty}$  is the frequency of the current source as seen in the plasma (moving) frame. The primed variables denote quantities in the moving frame. Eq. (A1) represents the oscillating source current in the moving frame that is formed by the nonadiabatic  $\text{O}^+$  ions. These ions do not participate in the propagation of the Alfvén wave near the equatorial plane. In this region, according to our model, the wave is carried by adiabatic (cold) protons.

The equation for the Alfvén wave is

$$\frac{\partial^2 E_x}{\partial z^2} - \frac{1}{V_A^2} \frac{\partial^2 E_x}{\partial t'^2} = \quad (\text{A2})$$

$$-i \mu_o e \omega_r V_{\infty} \delta n_o \exp(i(\omega_r t' + k_o x')) \exp(-z'/L_z)$$

where the LHS of Eq. (A2) is derived in the usual manner. The density in  $V_A$  is assumed equal to the proton mass density. This leads to an inhomogeneous solution for  $E_x$  of the form

$$E_{x\text{in}} = E_{\infty} \exp(i(\omega_r t' + k_o x')) \exp(-z'/L_z) \quad (\text{A3})$$

which leads to the solution shown in the second term on the RHS of Eq. (4) in the text. The homogeneous solution is

$$E_{x\text{ho}} = E_i \exp[i(k_o x - k_z z)] + E_r \exp[i(k_o x + k_z z)] \quad (\text{A4})$$

where  $k_x$  and  $k_z = V_{\infty} k_y / V_A$  are the wavenumbers in the  $x$  and  $z$  direction respectively. The latter relation is equivalent to setting the frequency of the Alfvén wave equal to the frequency of the source wave.

The generated Alfvén waves are entrained by the source wave and also move tailward with a phase velocity  $V_{\infty}$  and wavenumber  $k_x$ . From Eq. (A2) we find a total solution in the lab frame as given by Eq. (4).

## References

- Borovsky, Joseph E., Auroral arc thicknesses as predicted by various theories, *J. Geophys. Res.*, **98**, 6101, 1993.
- Chen, L. and A. Hasegawa, A theory of long period pulsations, 1, Steady excitation of field line resonances, *J. Geophys. Res.*, **79**, 1024, 1974.
- Daglis, I. A., et al., Ion composition in the inner magnetosphere: its importance and its potential role as a discriminator between storm-time substorms and non-storm substorms, *Proceedings of the Fourth International Conference on Substorms (IC4)*, to be published, 1998.
- Delcourt, D. C., et al., Centrifugally driven phase bunching and related current sheet structures in the near-earth magnetotail, *J. Geophys. Res.*, **101**, 19,839, 1996.
- Goertz, C. K., and R. W. Boswell, Magnetosphere-ionosphere coupling, *J. Geophys. Res.*, **84**, 7239, 1979.
- Haerendel, Gerhard, An Alfvén wave model of auroral arcs, in *High-Latitude Space Plasma Physics*, edited by B. Hultquist and T. Hagfors, 515, Plenum, New York, 1983.
- Knudsen, David J., Spatial modulation of electron energy and density by nonlinear stationary inertial waves, *J. Geophys. Res.*, **101**, 10,761-10,772, 1996.
- Landau L. and Lifshitz, *The Classical Theory of Fields*, Translated by Morton Hamermesh, Addison-Wesley Publ., Reading, Massachusetts, 1959.
- Lysak, Robert L., Auroral electrodynamics with current and voltage generators, *J. Geophys. Res.*, **90**, 4178, 1985.
- Lysak, Robert L., Coupling of the dynamical ionosphere to auroral flux tubes, *J. Geophys. Res.*, **91**, 7047, 1986.
- Lysak, Robert L., Electrodynamical coupling of the magnetosphere and ionosphere, *Space Sci. Revs.*, **52**, 33, 1990.
- Mallinicrodt, A. J. and C. W. Carlson, Relations between transverse electric fields and field-aligned currents, *J. Geophys. Res.*, **83**, 1426, 1978.
- Maltsev, Yu. P., W. B. Lyatsky and L. M. Lyatskaya, Currents over an auroral arc, *Planet. Space Sci.*, **25**, 53, 1977.
- Marklund, G., I. Sandahl and H. Opgenoorth, A study of the dynamics of a discrete auroral arc, *Planet. Space Sci.*, **30**, 79, 1982.
- Miura, Akira, and Tetsuya Sato, Numerical simulation of global formation of auroral arcs, *J. Geophys. Res.*, **85**, 73, 1980.
- Rothwell, Paul L., et al., O<sup>+</sup> phase bunching and auroral arc structure, *J. Geophys. Res.*, **99**, 2461, 1994.
- Samson, J. C. and R. Rankin, The coupling of solar wind energy to MHD cavity modes, waveguide modes, and field line resonances in the Earth's magnetosphere, in *Solar Wind Sources of Magnetospheric Ultra-Low-Frequency Waves*, Geophys. Monogr. Ser., vol 81, edited by M. J. Engebretson, K. Takahashi, and M. Scholer, p. 253, AGU, Washington, D.C., 1994.
- Samson, J. C., L.L. Cogger, and Q. Pao, Observations of field line resonances, auroral arcs, and auroral vortex structures, *J. Geophys. Res.*, **101**, 17,373, 1996.
- Seyler, C. E., A mathematical model of the structure and evolution of small-scale discrete auroral arcs, *J. Geophys. Res.*, **95**, 17,199, 1990.
- Seyler, C. E., J. E. Wahlund, and B. Holback, Theory and simulation of low-frequency plasma waves and comparison to Freja satellite observations, *J. Geophys. Res.*, **100**, 21,453, 1995.
- Southwood, D. J., Some features of field line resonances in the magnetosphere, *Planet. Space Sci.*, **22**, 483, 1974.

# O<sup>+</sup> PHASE BUNCHING AS A SOURCE FOR STABLE AURORAL ARCS

by

Michael B. Silevitch  
Center for Electromagnetics Research,  
Northeastern University, Boston, Massachusetts, 02115  
phone: (617) 373-5110, fax: (617) 373 -8627

Paul L. Rothwell  
Space Vehicles Division  
Air Force Research Laboratory  
Hanscom AFB, Bedford, Massachusetts, 01731  
phone: (617) 377-9664, fax: (617) 377-3160

Lars P. Block and Carl-Gunne Fälthammar  
Division of Plasma Physics, Alfvén Laboratory,  
Royal Institute of Technology, S 100 44, Stockholm 70, Sweden  
phone: 46-8-790-7686, fax: 46-8-245-431

February 25, 1999

## ABSTRACT

We propose a model to explain how ion dynamics create an Alfvén wave generator in the equatorial region that can be applied to the stable arc problem. For example, in the earthward drifting magnetotail plasma, phase bunching of  $O^+$  ions (and to a much lesser extent of the  $H^+$  ions) can be caused by, for example, a weak ( $\sim 1 \times 10^{-9}$  V/m<sup>2</sup>) electric field gradient [Rothwell *et al.* 1994]. This leads to density striations in the GSM frame.  $O^+$  density striations in the earthward drifting plasma frame are seen as a tailward propagating source of Alfvén waves where the hydrogen ions provide the polarization current of the wave. A transformation to the GSM frame will yield a static, oblique wave structure similar to that discussed by Maltsev *et al.* [1977] and Mallinckrodt and Carlson [1978]. The waves propagate from the equatorial region to both ionospheres where they are reflected. The ionospheric boundary condition when combined with a magnetospheric boundary condition allows a solution of the wave amplitudes in terms of the striation structure. The frequency of the Alfvén wave and the associated wavelengths are also determined by the striation driver. We find that the magnitude of the parallel current density at the ionosphere has a spatial resonance when the distance between the ionosphere and the equatorial plane is equal to a quarter wavelength along  $B_0$ . In that case, the magnitude of the parallel current density at the ionosphere is on the order of  $10 \mu\text{A}/\text{m}^2$  and peaks for striation wavelengths (as mapped to the ionosphere) of 10-40 km which is comparable to the transverse scale of auroral arcs. The associated Poynting flux incident on the ionosphere is found to be  $\sim 2 \text{ mW}/\text{m}^2$  and represents a net transfer of energy from the magnetosphere to the ionosphere as observed by Maynard *et al.* [1996]. The energy source of our wave mechanism is  $O^+$  convective flow, a conclusion similar to that reached by Maynard *et al.* [1996] and Shiowaka *et al.* [1998] in studying substorm onsets. However, we find that in the steady state the power extracted from the bulk flow to power the arc is balanced by energy provided by the solar wind through the cross tail electric field and not the braking of the plasma as was found in the onset studies.

## Introduction

Recently *Maynard et al.* [1996] and *Shiowaka et al.* [1998] using satellite and ground observations have concluded that Alfvén waves (Pi2's) observed during substorm onsets arise from braking earthward convective flow. In this paper we deal with the stable arc problem rather than the dynamical situation that characterizes substorm onsets. This is done by joining the single ion dynamics of  $O^+$  ions (*Rothwell et al.* [1994]) with the theory of oblique Alfvén waves. In Appendix C we show how the solar wind through the cross tail electric field provides the necessary energy to maintain arc stability. Based on this arc model we suggest that substorm onsets can arise when the equatorial generator is overdriven by an increase of energetic  $O^+$  ions such as observed by *Daglis and Axford* [1996] and *Daglis and Sarris* [1998].

There have been many studies of oblique Alfvén waves in which the propagation and reflection of Alfvén waves have been examined [ *Maltzev et al.* 1977; *Mallinicrodt and Carlson* 1978; *Lysak* 1985, 1986, 1990; *Haerendel* 1983; *Borovsky* 1993; *Seyler* 1990, 1995; *Knudsen* 1996; *Kan*, 1998]. A few studies have also identified a magnetospheric source. For example, the coupling of a compressional wave in the equatorial region with a shear Alfvén wave could produce a Field Line Resonance (FLR) [ *Chen and Hasegawa* 1974; *Southwood* 1974; *Samson and Rankin* 1994; *Samson et al.* 1996]. In this work we investigate density striations in the near earth night side magnetosphere as a possible magnetospheric source of oblique Alfvén waves. The basic idea is that the magnetic field near local midnight can become quite weak near the equatorial plane such that oxygen ions exhibit nonadiabatic behavior while hydrogen ions remain adiabatic. In the present model density striations are assumed to be produced by the phase bunching of the  $O^+$  ions as they enter a region of an extended electric field gradient as shown by *Rothwell et al.* [1994]. Associated with the density striations is a periodic static spatial variation of the earthward current density which when viewed in the drift frame of the adiabatic hydrogen ions is seen as a tailward moving current wave. In this frame the current wave has a wavelength given by the distance between striations and a frequency given by the corresponding wavenumber times the drift velocity. This defines the frequency of the oblique wave in the drift frame. It also defines the wavelength of the Alfvén wave along the field line through the dispersion relation. If one Doppler shifts the wave frequency in the moving frame to that in the GSM frame one finds the latter to be zero consistent with the static nature of the source. The oblique Alfvén wave forms a static wave pattern in the spirit of *Maltzev et al.* [1977] and *Mallinicrodt and Carlson* [1978].

There are two boundary conditions. One boundary condition requires  $j_z$  to be zero at the equatorial plane ( $z = 0$ ) consistent with symmetry of the two ionospheres. The other boundary condition determines the reflection coefficient of the oblique Alfvén waves at the two ionospheres. Together they fully determine the wave amplitude in terms of the striation driver and the wave phase at the ionosphere. By imposing a current density node at the equatorial plane and having the wavelength fixed we find that the parallel current density is a maximum at the ionosphere if the ionosphere is located a quarter wavelength from the equatorial plane. This is a well known resonant relation as seen in resonant cavities.

The goal of the present work is to determine whether the proposed mechanism can lead to

reasonable values of the parallel current density at the ionosphere given reasonable values for the magnetospheric input parameters. In this paper we have used several assumptions that should be stated. The difference in dynamical behavior between the oxygen and hydrogen has already been mentioned. Also, we assume that the Alfvén speed is constant along the field line and that the static wave structure has time to form. Finally, we do not consider wavelengths below or at the electron inertial length because of the evanescent property of these waves in the ionosphere [Borovsky 1993]. Therefore, kinetic Alfvén waves as described by Goertz and Boswell [1979] are not treated here. The wave equation is solved analytically for a parallel field geometry. The appropriate scale factors are then applied to estimate the parallel currents at the ionosphere. A more precise approach is to include the scale factors in the wave equation which is solved numerically (Singer *et al.* [1981]).

Figure 1 illustrates the concepts described above. The  $O^+$  density striations are represented by a sinusoid along the equatorial plane. The waves emanate toward each ionosphere creating density (conductivity) perturbations. If the ionospheres are symmetrically located relative to the equatorial plane then the magnetospherically generated waves at each ionosphere will be at the same phase and the conductivity perturbations will be conjugate.

In the coordinate system used here  $x$  points earthward,  $y$  towards the west and  $z$  is parallel to the earth's magnetic field. With  $z=0$  denoting the equatorial plane, the northern ionosphere is located at  $z = L_{in}$  and the southern ionosphere at  $z = -L_{is}$ .

#### $O^+$ Density Striations

With the above scenario in mind let us now analyze the proposed source of oblique Alfvén waves. First, previous work (Rothwell *et al.* [1994]) that motivates the present effort will be briefly reviewed. In that paper we analytically solved the equation of motion of a particle  $\mathbf{E} \times \mathbf{B}$  drifting through an electric field gradient. For an electric field gradient  $dE_x/dx$ , the particle drift velocity is

$$V_d = \left[ 1 - \frac{M}{e} \frac{dE_x}{B^2} \right]^{-1} \frac{E_y}{B} \quad (1)$$

where  $M$  denotes particle's mass,  $E_y$  the cross tail electric field and  $B$  the magnetic field. Note from the denominator in (1) that  $V_d$  is highly mass selective and nonlinear, which causes the drift speed for heavier ions to be faster. A computer simulation was performed that took a uniform distribution of  $O^+$  ions outside the gradient region and followed them as they  $\mathbf{E} \times \mathbf{B}$  drifted through the electric field gradient ( $\sim 1 \times 10^{-9}$  V/m<sup>2</sup>). Note that the  $H^+$  remained adiabatic. In the gradient region the  $O^+$  ions were not uniformly distributed in gyrophase while  $H^+$  remained uniform. This feature caused the formation of spatially periodic density striations in the GSM frame of the  $O^+$  ions but not that of the  $H^+$  ions. The protons adiabatically drifted through the  $O^+$  striations. The electric field in (1) is large-scale and should not be confused with the electric field of the generated Alfvén wave as discussed below.

The presence of ion density striations leads to an additional  $x$ -component of the current density that is carried by electrons. This can be understood as follows. In regions of enhanced ion density charge neutrality requires that electrons flow up the field line to neutralize the additional positive



charge. We assume that the ions originated outside the striation region and are not gained or lost along the magnetic field lines. This means that their flux in the x-direction is conserved. If  $N_{o+}$  is the average  $O^+$  density and  $\delta n_{o+}$  the density perturbation due to the striations we have for the perturbed earthward current density

$$j_x = e [N_{o+} - (N_{o+} + \delta n_{o+})] \frac{E_y}{B} = -e \delta n_{o+} \frac{E_y}{B} \quad (2)$$

Note that in (2) electrons are the current carriers forming a spatially varying current density structure which maintains charge neutrality with the  $O^+$  density striations. The  $O^+$  density perturbation  $\delta n_{o+}$  is assumed to exponentially decrease from the equator with a scale length  $L_z$  and has a wavenumber in the x direction equal to  $k_o$ . In *Rothwell et al.* [1994]  $k_o$  is determined by the drift speed of  $O^+$  ions as they enter a region of a large scale electric field gradient. For simplicity we assume a sinusoidal structure for the density striations. With these assumptions (2) becomes in the GSM frame

$$j_x = -e \delta n_o V_{xo} \exp(-z/L_z) \exp(i k_o x) \quad (3)$$

where  $\delta n_o$  is the amplitude of the  $O^+$  number density amplitude and  $V_{xo}$  is the drift speed ( $E_y/B$ ). In the moving frame (3) becomes

$$j_x = -e \delta n_o V_{xo} \exp(-z'/L_z) \exp(\omega_r t' + k_o x') \quad (4)$$

As the plasma convects towards the earth at a speed  $V_{xo}$  a current density wave is seen in the moving frame moving tailward at the drift velocity and with a frequency  $\omega_r = k_o V_{xo}$ . While the incipient untrapping of the oxygen ions (1) provides the source current for the Alfvén waves, the protons remain adiabatic and provide the polarization current that allows the Alfvén wave to propagate. Details are given in Appendix A.

If we now Doppler shift the wave field derived in Appendix A to the GSM frame then (4) becomes a static wave structure. This should hold for any spatially periodic current driver. Therefore, as a general rule a drifting plasma through a spatially periodic current structure produces Alfvén waves in the moving plasma frame such that when Doppler shifted ( $x' = x - V_{xo}t$ ,  $\omega_r = k_o V_{xo} = k_z V_A$ ) to the GSM frame these waves will be perceived as static (compare with *Haerendel* [1983]). The result in the GSM frame is

$$E_x = E_{xi} \exp i(k_o x - k_z z) + E_{xr} \exp i(k_o x + k_z z) - \dots \\ i E_{in} \exp(-z/L_z) \exp i(k_o x) \quad (5)$$

where  $E_{xi}$  and  $E_{xr}$  denote the amplitude of the incident and reflected waves respectively and  $E_{in}$  is the

inhomogeneous component as defined in (7). Note that the third term on the RHS of (5), which results from (4), goes to zero far outside the density perturbation region. Therefore, only the first two terms need be considered at the ionosphere. Note in addition that in the GSM frame the wave magnetic field will also be static.

It can be shown (see Appendix B) that the solution (5) gives rise to a current density along the ambient magnetic field [Maltsev *et al.* 1977] which is given by

$$j_z = - \frac{1}{\mu_o V_{xo}} \frac{\partial E_x}{\partial z} \quad (6)$$

Using (6)  $E_{xi}$  and  $E_{xr}$  can be related to the inhomogeneous term (the third term on the RHS of (5)) through an equatorial boundary condition. The equatorial source region couples via Alfvén waves to the ionosphere in each hemisphere. This implies a natural asymmetry that requires  $j_z$  to be zero at the equatorial plane (i.e.  $z = 0$ ). Using expressions in (5) and (6) we have

$$\begin{aligned} E_{xi} - E_{xr} &= \overline{E_{in}} = \frac{E_{in}}{k_z L_z} \\ E_{in} &= \frac{k_o \mu_o V_{xo} L_z^2 V_A^2}{V_A^2 + k_o^2 V_{xo}^2 L_z^2} (e \delta n_o V_{xo}) \end{aligned} \quad (7)$$

where  $E_{in}$  is the coefficient of the inhomogeneous term in the solution shown in (5). At larger distances from the equator the inhomogeneous solution goes to zero and the effect of the density perturbation source on the Alfvén wave is seen through the modification of the incident and reflected amplitudes as defined by (7).

#### The Northern Ionosphere

The ionosphere defines another relation between  $E_{xr}$  and  $E_{xi}$  through the conservation of current at the reflecting surface. Here we use coordinates consistent with the northern ionosphere and set  $L_{in} = L_i$ . We equate the  $j_{zw}$  of the wave to the gradient of  $\Sigma_{po} E_x$  in the ionosphere where  $E_x$  is determined from the homogeneous part of (5) since the ionosphere is well outside the striation region. The result is

$$E_{xr} = \frac{\Sigma_\omega - \Sigma_{po}}{\Sigma_\omega + \Sigma_{po}} E_{xi} \exp(-2 i k_z L_i) \quad (8)$$

The symbol  $\Sigma_{po}$  denotes the background Pedersen conductivity and the exponential term takes into account the phase of the wave as it impinges on the ionosphere. The symbol  $\Sigma_\omega = (\mu_o V_A)^{-1}$  represents

the conductivity of the Alfvén wave. By combining (7) and (8) one obtains a solution for the wave that depends on both magnetospheric and ionospheric parameters.

$$E_x(x,z) = \overline{E}_{in} \exp(ik_o x) \frac{\Sigma_\omega \cos[k_z(z - L_i)] - i \Sigma_{po} \sin[k_z(z - L_i)]}{\Sigma_{po} \cos(k_z L_i) + i \Sigma_\omega \sin(k_z L_i)} \quad (9)$$

Note that the wave amplitude is very sensitive to the phase at the ionosphere which depends on the length of the magnetic field line. The maximum magnitude of the wave electric field at the ionosphere occurs when  $k_z L_i = \pm\pi/2$  and the minimum when  $k_z L_i$  is equal to an integral multiple of  $\pi$ . The ratio of the maximum to minimum wave amplitudes is  $\Sigma_{po}/\Sigma_\omega$  which is usually greater than 10.

The parallel current density carried by the wave can easily be found by using (6) and (9).

$$j_{zw} = \overline{E}_{in} \Sigma_\omega k_o \exp(ik_o x) \frac{\Sigma_\omega \sin(k_z(z - L_i)) + i \Sigma_{po} \cos(k_z(z - L_i))}{\Sigma_{po} \cos(k_z L_i) + i \Sigma_\omega \sin(k_z L_i)} \quad (10)$$

Insight can be gained by looking at the wave electric field and parallel current density at  $z=L_i$  (northern ionosphere).

$$E_x(x, L_i) = \frac{\Sigma_\omega \overline{E}_{in} \exp(ik_o x)}{F_x(L_i) (\Sigma_{po} \cos(k_z L_i) + i \Sigma_\omega \sin(k_z L_i))} \quad (11)$$

$$j_{zw}(x, L_i) = \frac{ik_o \Sigma_\omega \Sigma_{po} \overline{E}_{in} \exp(ik_o x)}{F_x(L_i) F_y(L_i) [\Sigma_{po} \cos(k_z L_i) + i \Sigma_\omega \sin(k_z L_i)]}$$

where  $F_x$  and  $F_y$  are the scaling factors that arise from the convergence of the magnetic field lines. Singer et al. [1981] noted that the wave equation should be solved including the spatial dependence of the scale factors. This requires a numerical treatment which is beyond the scope of the present paper. We assume that the local, equatorial nature of our wave source makes (11) a reasonable approximation. The parallel wave current density at the ionosphere is also dependent on the phase at which the wave reflects off the ionosphere. For example, if  $k_z L_i = \pm\pi/2$  then  $j_{zw}$  is proportional to the ionospheric conductivity. If  $k_z L_i = \pm\pi$  then  $j_{zw}$  is proportional to the Alfvén conductivity along  $B_o$ . Inspection of (11) reveals the resonant nature of the phase relation due to the ionosphere being much more conductive than the wave medium. The reason for this was stated above. That is, with the wavelength and one boundary condition fixed in the equatorial region the wave amplitude is sensitive to the location of the second boundary condition in analogy with a resonant cavity. The condition  $k_z L_i = \pm\pi/2$  is, of course, the usual quarter wavelength criterion.

#### Self-Consistent Ionospheric Reflection

So far we have investigated the production of oblique Alfvén waves by density striations in the equatorial plane. These waves also produce conductivity perturbations in the two ionospheres. When coupled to the background ionospheric electric fields these perturbations provide an additional source of parallel current in the manner suggested by *Maltzev et al.* [1977]. The parallel current density carried by the waves at the northern ionosphere is given by (11). When the current is away from the ionosphere the incoming electrons provide a source of ionization that causes a localized conductivity enhancement. A time-independent positive conductivity enhancement results from the balance of this source with the electron-ion recombination rate  $\sigma_r$ . This enhancement can modify the reflection properties of the wave itself. The positive conductivity perturbation produced by this effect is given by

$$\delta \Sigma_p(L_i) = -G j_{z\omega}$$

$$G = \frac{(Qh + 1)eh}{2\sigma_r \Sigma_{po} B_i^2} \quad (12)$$

which results from a balance between recombination and ionization rates. The 'one' in the G variable arises from local charge neutrality in the ionosphere caused by the parallel flowing electrons stopping. In the upward current region we also have the ionization rate produced by  $j_{z\omega}$  denoted by  $Qh = .5$  ion/incident electron. This value of  $Qh$  corresponds to an incident electron energy of  $\sim 200$  eV. The ionospheric integration height  $h$  equals 20 km, the recombination rate  $\sigma_r = 1 \times 10^{-13}$  m<sup>3</sup>/s,  $\Sigma_{po} = 20$  S and the magnetic field value at the ionosphere,  $B_i = 4 \times 10^{-5}$  T. This gives  $G = 2.5 \times 10^5$  S/(A/m<sup>2</sup>). The  $z$  axis is parallel to  $B$  so that a positive  $j_{z\omega}$  corresponds to an downward current density in the northern ionosphere while a positive  $j_{z\omega}$  corresponds to an upward current density in the southern ionosphere. For the sake of simplicity we also assume (12) holds for currents into the ionosphere (upward moving electrons).

$$\delta \Sigma_p(L_{in}) = -G j_{z\omega}(L_{in}) \quad \text{Northern Ionosphere}$$

$$\delta \Sigma_p(-L_{is}) = +G j_{z\omega}(-L_{is}) \quad \text{Southern Ionosphere} \quad (13)$$

In each of the two ionospheres we have a height integrated current.

$$\delta J_x = \mp [E_{xo} - R_\Sigma E_{yo}] G j_{z\omega} \quad (14)$$

where the minus corresponds to the northern ionosphere and the plus sign to the southern ionosphere. Here  $E_{xo}$  is the equatorward component of the ambient ionospheric electric field and  $E_{yo}$  is the westward component. Following *Maltzev et al.* [1977] current continuity at the northern ionosphere is given by

$$E_x = [E_{xi}^n \exp(-ik_z z) + E_{xr}^n \exp(+ik_z z)] \exp(ik_o x)$$

$$j_{z\omega}(L_{in}) = \Sigma_{po} \frac{\partial E_x}{\partial x} - i \eta j_{zw}(L_{in}) \quad (15)$$

$$\eta = G k_{oi} [E_{xo} - R_\Sigma E_{yo}] (\text{dimensionless})$$

where  $k_{oi}$  is the striation wavenumber as scaled to the ionosphere with a scale factor  $F_x = .032$ .  $R_\Sigma$  is the ratio of the Hall to Pedersen conductivities. From (15) we calculate  $E_r^n$ .

$$E_r^n = E_i^n \exp(-2 i k_z L_{in}) \left[ \frac{\Sigma_\omega (1 + i \eta) - \Sigma_{po}}{\Sigma_\omega (1 + i \eta) + \Sigma_{po}} \right] \quad (16)$$

where again  $n$  denotes the northern ionosphere. Note that the self-consistent reflection adds an imaginary component to the Alfvén conductivity which is equivalent to an additional phase shift in the reflected amplitude. We can determine when this effect becomes important by using the above values for equations (12) and (15). With the ionospheric electric field factor in (15) set to  $4 \times 10^{-2}$  V/m we find that  $\eta$  can be approximated by  $10^4 k_{oi}$ . The ionospheric wavelength at which  $\eta \Sigma_\omega$  becomes comparable to  $\Sigma_{po}$  in (16) is 1.25 km which is significantly shorter than the scale size stated in our assumptions.

## Numerical Results

The key numerical requirement of our model is that the distance  $L_i$  between the equatorial plane and the ionospheres is consistent with the quarter wavelength criterion. Now the relation  $k_z = V_{xo} k_o / V_A$  is constant along the field line since we have assumed  $V_A$  is constant and the product  $V_{xo} k_o$  is independent of the scaling factor. As shown in Figure 2 we have chosen three arc sizes of 10, 20 and 30 km in the ionosphere. These values are mapped to the equatorial plane using a mapping factor of .032. Having thus defined  $k_o$  we define  $k_z$  by setting the corresponding wavelength to  $40 R_E$ . This is consistent with the distance between the ionosphere and the equatorial plane in the auroral region being about  $10 R_E$ . Figure 2 shows that the quarter wavelength criterion is satisfied for a drift speed of some tens of kilometers per second and an Alfvén speed of some a few thousand kilometers per second. This is consistent with observations [Huang and Frank 1986] for the drift speed and theoretical estimates for the Alfvén speed [Lysak 1990].

Now let us look at the numerical viability of our model. First, we calculate the value of  $E_{in}$  as defined in (7) as a function of wavelength in the ionosphere for various values of the Alfvén speed. The chosen parameter values are  $V_{xo} = 20$  km/s,  $\delta n_o = 1 \times 10^4$  O<sup>+</sup> ions/m<sup>3</sup> and  $L_z = 2 R_E$ . Figure 3 shows the results for three values of  $V_A$ ,  $1 \times 10^6$ ,  $2.5 \times 10^6$  and  $5 \times 10^6$  m/s. Note the peaking of the inhomogeneous electric field at higher Alfvén speeds and at wavelengths of 10-20 km. In this model the wave amplitude and, hence, the strength of the magnetosphere-ionosphere interaction scales as

the Alfvén speed. This implies more intense wave fields exist on field lines where the particle density has been depleted. Figure 4 shows a contour plot of the parallel wave current density at the ionosphere for  $V_A = 2.5 \times 10^6$  m/s. We use scaling factors of  $F_x = 0.032$ ,  $F_y = 0.078$  which corresponds to a dipole field model at  $L = 6.5$ . The ordinate denotes the  $z$  phase of the wave at the ionosphere in units of  $\pi$  and the abscissa denotes the striation wavelength as transformed to the ionosphere. The contours are in units of  $\mu\text{A}/\text{m}^2$ . Note that we obtain a maximum parallel current density at the ionosphere of some tens of microamps per meter squared using an oxygen density perturbation amplitude of  $1 \times 10^4$   $\text{O}^+$  ions/ $\text{m}^3$ . The maximum current values are obtained at the quarter wavelength condition and for ionospheric wavelengths of tens of kilometers consistent with larger auroral forms. Therefore, we argue that even quite conservative values of the magnetospheric parameters are consistent with observed values of the parallel current density at the ionosphere.

Now let us look at the resonant nature of the Alfvén wave. Recall that the oblique Alfvén wave amplitude is determined by the striation source as well as the magnetospheric and ionospheric boundary conditions in a manner equivalent to that of a resonant cavity. Figure 5 dramatically demonstrates this effect. This is a plot of the parallel current density for  $x=0$  at the ionosphere as a function of the wave phase at the ionosphere denoted in units of  $\pi$ . See (11). Clearly, the quarter wavelength resonance can be seen. The resonance at  $k_z L_i = 3\pi/2$  requires that  $V_A$  be one third the value necessary for the  $k_z L_i = \pi/2$  resonance for constant  $V_{xo}$ . Alternately the same criterion is satisfied if  $V_A$  remains constant but  $V_{xo}$  increases by a factor of three. Note that the parallel current density outside the resonance regions is not zero but differs by a factor of  $\Sigma_{po}/\Sigma_{\omega} \approx 10$  from the parallel current density at resonance. The width of the resonance is determined by  $\Sigma_{\omega}$ . Of course, any scattering of the wave, such as partial reflections, should significantly broaden the width of the resonance.

The creation of an 10 - 40 km arc structure, such as those observed by *Marklund et al.* [1984], by oblique Alfvén waves depends on the length of the field line, the plasma density along the field line, the  $x$  wavelength of the magnetospheric driver and the drift speed of the plasma. One obvious effect is that any increase in  $k_z$  would cause the resonance criterion to be satisfied on field lines closer to the earth. This could be related to the observed equatorial motion of auroral arcs under substorm growth conditions [*Tanskanen et al.* 1987].

## Discussion

We have developed here an idealized model for a magnetospheric generator of oblique Alfvén waves. This is in contrast with the treatments of *Maltsev et al.* [1977]; *Mallinicrodt and Carlson* [1978]; and *Miura and Sato* [1980] that consider an ionospheric wave source. The dependence of the wave amplitude on both magnetospheric and ionospheric parameters have been obtained. It was found that parallel current density values comparable to those measured in auroral arcs can be obtained. Therefore, we maintain that magnetospheric wave sources play a major role in the formation of 10-40 km arc structures and imply a net Poynting flux from the magnetosphere to the ionosphere (*Maynard et al.* [1996]).

We will now show that the Poynting flux values, as calculated from our model, are reasonable. The creation of wave energy requires a generator in the magnetospheric striation (source) region. In Appendix C we calculate  $\mathbf{j} \cdot \mathbf{E}$  and show that such a generator exists. Using Poynting's Theorem and

integrating over the source region we find a net Poynting flux incident on the ionosphere of  $2 \text{ mW/m}^2$ , a value consistent with observations. The same parameter values are used in calculating this flux as the parallel currents shown in Fig. 4.

The presence of an electrical generator requires the extraction of equal kinetic power from the oxygen ions' bulk flow. In Appendix C we show that the presence of the wave generator causes the ions to drift as to gain energy from the cross tail electric field  $E_y$ . In this way the kinetic energy of the perturbed oxygen component is replenished from the external energy source that sustains  $E_y$ . Moreover, the additional current due to the new drift creates an earthward  $j \times B$  force that exactly balances the drag force associated with the presence of the electrical generator. The details of how this is accomplished are shown in Appendix C. *Maynard et al.* [1996] and *Shiowaka et al.* [1998] have concluded from satellite measurements that substorm onsets are related to the creation of Alfvén waves that have as their energy source the braking of earthward convection. In contrast, we have found that the presubstorm stable arcs are powered by a steady state transfer of solar wind energy via earthward convection to a magnetospheric wave generator. This transfer of energy implies that the generated wave energy does not degrade the striations. They are stable in this sense. We do not believe that the variation of  $V_A$  along the field line will change the conclusions here but will add new features such as those described by *Haerendel* [1983], *Seyler* [1990, 1995] and *Lysak* [1985, 1986, 1990].

Although a finite  $E_z$  exists in the GSM frame it cannot accelerate electrons parallel to  $B_z$  as the total electric field is perpendicular to the total magnetic field. Field aligned acceleration would have to arise in this model from instabilities created by the field aligned current associated with the wave.

*Daglis and Axford* [1996] and *Daglis and Sarris* [1998] have shown that the energy density of 17 keV to 300 keV  $O^+$  ions increases dramatically ( $\sim$  a factor of 40) during the expansion phase of substorms. The corresponding  $H^+$  energy density increases only about a factor of 3. During the growth phase the ratio of  $O^+$  to  $H^+$  is estimated to be 0.1 from Fig. 1 of *Daglis and Sarris* [1998]. If one takes the  $H^+$  number density to be  $0.3\text{--}1.0 \times 10^6 \text{ ions/m}^3$  then the  $O^+$  number density  $N_{O^+}$  is  $0.3\text{--}1.0 \times 10^5 \text{ ions/m}^3$ . From Fig. 7 of *Rothwell et al.* [1994] one finds that  $\delta n_o \sim 0.3 N_{O^+}$ . Any turbulence present *Delcourt et al.* [1996] could reduce  $\delta n_o$  further. However, even with turbulence present we expect sufficient  $O^+$  ions to sustain the stable arc structure proposed in this model. Based on these arguments we took a value of  $\delta n_o = 1 \times 10^4 \text{ ions/m}^3$  for the amplitude of the  $O^+$  striation density which we believe is consistent with the results of *Daglis and Sarris* [1998] for the near earth plasma sheet during the growth phase. This value for  $\delta n_o$  also yields parallel current and Poynting flux values at the ionosphere consistent with observations.

An interesting feature arises here. If the convective flow of the  $O^+$  ions are the source of the Alfvén wave then it follows that an increase in the  $O^+$  ion density increases the Poynting flux to the ionosphere as  $(\delta n_o)^2$ . See Eqns. ((7) and (C5)). If part of this flux heats the ionospheric oxygen and causes them to form conics and flow upwards towards the equatorial plane then we have a feedback mechanism that could play a major role in substorm onsets. *Maynard et al.* [1996] note that a large spike of Poynting flux is injected from the equatorial region towards the ionosphere at substorm onset.

After onset there is less order in the background flow and less intensity in the Poynting flux (*Maynard et al.* [1996]). This could be a manifestation of the saturation of the suggested feedback

mechanism that depends on ordered flow. Note from Fig. 1 of *Daglis and Sarris* [1998] that substorm onsets occur when the energy density of the more energetic ions (17-300 keV) in the near earth plasma sheet is increasing. We speculate that substorm onsets occur when the  $O^+$  bulk flow energy is converted to wave energy by our mechanism at a rate such as to trigger the suggested feedback mechanism. For more information on Alfvén waves and substorm onsets see *Lui and Murphee* [1998].

At first glance it may appear that the resonances shown in Fig. 5 are unphysically too narrow and, therefore, difficult to realize. However, one must remember that resonances by their nature tend to be broadened rather than narrowed by external factors. Here we are dealing with an idealized model with the neglect of partial reflections along the field line and other effects that should tend to contribute to the broadening. Also, the width of the resonance in our model is dependent on the numerical value of the Alfvén conductivity along the field line. If this were to be significantly higher then the resonance curves shown in Fig. 5 would be broader.

The structure of the wave electric field at the ionosphere may cause vortices. From (11) the maximum wave electric field at the ionosphere occurs when the quarter wavelength criterion is satisfied. In this case the electric field lags  $j_{\omega}$  by  $90^\circ$  in  $x$  at the ionosphere. This means that in both ionospheres there is a diverging electric field ( $E_x$ ) where the parallel current enters the ionosphere and a converging electric field where the parallel current exits the ionosphere. This implies a reversal in the  $y$  drift velocity as either parallel current region is traversed. If our assumption of uniformity in the  $y$  direction is now relaxed to allow for variation in  $E_x$  along  $y$  then the ionospheric plasma will twist about the magnetic field at locations where  $E_x$  is large. This will cause the stable arc structure that is envisioned in the present model to form vortices along the  $y$  direction and is, no doubt, related to the stability of our arc model. Further investigation of this feature is beyond the scope of the present paper.

## Summary and Conclusions

We have identified density striations formed by nonadiabatic oxygen ions as a possible magnetospheric source for oblique Alfvén waves. It was found that magnetospheric and ionospheric boundary conditions lead to a resonant type behavior. Reasonable input parameter values imply  $10 \mu A/m^2$  parallel current densities and  $2 mW/m^2$  Poynting flux intensities at the ionosphere are attainable with the maximum values occurring for arc structures on the order of 10 - 40 km, a width consistent with observations of inverted-V events (*Marklund et al.* [1984]). Energy from the cross tail electric field is transferred as required to the wave generator (see Appendix C) to maintain the stability of the arc structure. The additional tail current in the  $+y$  (westward) direction causes a local stretching of the magnetic field lines in the equatorial region which correlates in our model with the corresponding Poynting flux incident on the ionosphere and, hence, the brightness of the auroral arcs. It is noted that substorm onsets occur during periods of significant increases in the  $O^+$  population (*Daglis and Axford* 1996; *Daglis and Sarris* 1998). Such a feature would enhance the intensity of the Alfvén waves generated by our mechanism and suggests a possible feedback connection that may play a role in substorm onsets.



## APPENDIX A:

Here we derive the equations for the Alfvén wave in the plasma frame. In addition to the usual polarization current we also now have a time-dependent source term due to the striations. We assume that the  $O^+$  striations can be approximated by a sine dependency in  $x$  and an exponential dependence in  $z$ . i.e.

$$\delta j_{x'} = -e V_{xo} \delta n_o \cdot \exp i (\omega_r t' + k_o x') \exp(-z'/L_z) \quad (A1)$$

where  $\omega_r = k_o V_{xo}$  is the frequency of the current source as seen in the plasma (moving) frame. The primed variables denote quantities in the moving frame. (A1) represents the oscillating source current in the moving frame that is formed by the nonadiabatic  $O^+$  ions. These ions do not participate in the propagation of the Alfvén wave near the equatorial plane. In this region the wave is carried by adiabatic (cold) protons.

The equation for the Alfvén wave is derived from (B1) below and

$$\begin{aligned} -\frac{\partial B_y}{\partial z'} &= \mu_o j_x = \frac{\mu_o \rho}{B_o^2} \frac{\partial E_x}{\partial t'} + \mu_o \delta j_{x'} \\ \frac{\partial^2 E_x}{\partial z'^2} - \frac{1}{V_A^2} \frac{\partial^2 E_x}{\partial t'^2} &= -i \mu_o e \omega_r V_{xo} \delta n_o \cdot \exp i (\omega_r t' + k_o x') \exp(-z'/L_z) \end{aligned} \quad (A2)$$

This leads to an inhomogeneous solution for  $E_x$  of the form

$$E_{xin} = E_{in} \exp(i \omega_r t' + k_o x') \exp(-z'/L_z) \quad (A3)$$

where  $E_{in}$  is explicitly shown in (7) in the text.

The homogeneous solution in the moving frame is

$$E_{xho} = E_{xi} \exp[i(\omega_r t' + k_o x' - k_z z')] + E_{xr} \exp[i(\omega_r t' + k_o x' + k_z z')] \quad (A4)$$

where  $k_o$  and  $k_z = V_{xo} k_o / V_A$  are the wavenumbers in the  $x$  and  $z$  direction respectively. The latter relation is equivalent to setting the frequency of the Alfvén wave equal to the frequency of the source wave.

The generated Alfvén waves are entrained by the source wave and also move tailward with a phase velocity  $V_{xo}$  and wavenumber  $k_o$ . From (A2) we find a total solution to be

$$E_{x'} = E_{xi} \exp i(\omega_r t + k_o x' - k_z z) + E_{xr} \exp i(\omega_r t + k_o x' + k_z z) - ..$$

$$i \frac{e \mu_o \omega_r \delta n_{o+} V_{xo} \exp(-z/L_z)}{\frac{1}{L_z^2} + \frac{\omega_r^2}{V_A^2}} \exp i(\omega_r t + k_o x') \quad (A5)$$

in the moving frame where  $E_{xi}$  and  $E_{xr}$  are the amplitudes of the incident and reflected waves respectively. Note that the third term on the RHS of (A5) becomes negligible far from the equatorial plane.

#### APPENDIX B:

In this Appendix we derive expressions for  $E_z$  and  $j_{z\omega}$  from Maxwell's equations. In the moving (plasma) frame we have

$$\frac{\partial E_{x'}}{\partial z'} = -\frac{\partial B_{y'}}{\partial t'} \quad (B1)$$

The RHS of (B1) can be written as  $-i\omega_r B_y$ , where  $\omega_r = k_o V_{xo}$ . The  $E_z$  component in the GSM frame is then given by

$$E_z = -V_{xo} B_y = -\frac{i}{k_o} \frac{\partial E_x}{\partial z} \quad (B2)$$

In both coordinate frames  $j_{z\omega}$  is given by

$$j_{z\omega} = \frac{1}{\mu_o} \frac{\partial B_y}{\partial x} = -\frac{1}{\mu_o V_{xo}} \frac{\partial E_x}{\partial z} \quad (B3)$$

where the x derivative of  $B_y$  is given by  $ik_o B_y$ . Equation (B3) is the same as equation (7) in the text.

#### APPENDIX C:

According to our model the cross tail electric field and, hence, the resulting earthward plasma drift is the source of the wave's Poynting flux into the ionosphere. In this appendix we first calculate

the electrical power per  $m^3$  extracted from the earthward drift of the  $O^+$  ions that form the striations. Next, using Poynting's Theorem, we integrate over the magnetospheric source region to find the net wave energy flowing towards the ionosphere. Scaling this energy flux consistent with magnetic field line convergence gives us the wave energy incident on the ionosphere. Finally, we show that the tailward drag on the striation ions from the electrical generator is balanced by an earthward  $j \times B$  force that sustains the steady state nature of the striations and, hence, stabilizes the arc structure in our model.

First, we take the real parts of  $E_x$  from (9) and  $j_x$ . Note that  $L_i$  denotes the location of the ionosphere.

$$\begin{aligned}
 Re(E_x) &= \eta_1 (A(z) \cos(k_o x) - B(z) \sin(k_o x)) + E_{in} \sin(k_o x) e^{-z/L_z} \\
 A(z) &= \sum_o \sum_\omega \cos(k_z z) \\
 B(z) &= -\sum_\omega^2 \sin(k_z L_i) \cos(k_z (z - L_i)) - \sum_{po}^2 \cos(k_z L_i) \sin(k_z (z - L_i)) \\
 \eta_1 &= \frac{\overline{E_{in}}}{[\sum_{po}^2 \cos(k_z L_i)^2 + \sum_\omega^2 \sin(k_z L_i)^2]}
 \end{aligned} \tag{C1}$$

The earthward current density is given by the following expression.

$$Re(j_x) = \frac{V_{xo}}{\mu_o V_A^2} \frac{\partial (Re(E_x))}{\partial x} - e \delta n_o V_{xo} \cos(k_o x) e^{-z/L_z} \tag{C2}$$

Using (C1) in (C2) and averaging over one wavelength in  $x$  it is found that only the product of the first term on the RHS of (C1) and the second term on the RHS of (C2) is nonzero.

$$\langle Re(E_x) Re(j_x) \rangle_x = -\frac{\eta_1}{2} A(z) e \delta n_o V_{xo} e^{-z/L_z} \tag{C3}$$

This is a generator that represents the rate at which electrical wave energy is being created per unit volume. The Poynting Theorem relates the wave energy flux  $S$  ( $W/m^2$ ) to the electrical power.

$$\nabla \cdot S = -j \cdot E \tag{C4}$$

Integrating (C3) over the source region from  $z=0$  to  $z \gg L_z$  one finds an expression for  $S$  as it leaves the magnetospheric source region along the magnetic field lines. It is

$$S = \overline{E_{in}} \frac{\sum_{po} e \delta n_o V_{xo} L_z}{\sum_\omega 2(1 + k_z^2 L_z^2)} \tag{C5}$$

where we have used the condition  $k_z L_i = \pi/2$ . This implies  $k_z L_z = 0.3$ . We use the following magnetospheric values to calculate  $S$ ,  $V_A = 2.5 \times 10^6$  m/s,  $L_z = 2R_E$ ,  $\delta n_o = 10^4$  O<sup>+</sup> ions/m<sup>3</sup>,  $V_{xo} = 2 \times 10^4$  m/s and  $k_o = 10^{-5}$  m<sup>-1</sup>. The ratio of  $\Sigma_{po}/\Sigma_o$  is taken as 10. With these input values we have  $E_{in} = 0.7$  mV/m,  $\bar{E}_{in} = 2.3$  mV/m and the Poynting flux  $S$  emanating from the magnetospheric source region towards the ionosphere is  $4.7 \times 10^{-6}$  W/m<sup>2</sup>. Multiplying by a factor of 400 for the convergence of the magnetic field lines gives a value of  $\sim 2$  mW/m<sup>2</sup> flowing into the ionosphere which is consistent with values observed inside auroral arcs.

We will now show that in the steady state the energy tapped from the striation ions to power the arcs is balanced by energy provided by the solar wind through the cross tail electric field. The wave generator acts as a constant drag force in the -x direction so that the oxygen ion's equation of motion (see equation (3) in *Rothwell et al.* 1994) is modified as follows.

$$\begin{aligned} \frac{dV_x(t)}{dt} &= \frac{\omega_c}{B} E_{xo}[x(t)] + \omega_c V_y(t) - \gamma V_{xo} \\ \frac{dV_y(t)}{dt} &= \frac{\omega_c}{B} E_y - \omega_c V_x(t) \end{aligned} \quad (C6)$$

where  $E_{xo}$  is the large scale electric field,  $\omega_c$  is the oxygen ion's gyrofrequency,  $V_{xo}$  is the x component of the drift velocity and  $\gamma$  is to be determined from  $\mathbf{j} \cdot \mathbf{E}$ . Now we can simply transform the y component of the velocity

$$V_y(t)' = V_y(t) - \frac{\gamma}{\omega_c} V_{xo} \quad (C7)$$

so that the equations in (C6) reduce to those in *Rothwell et al.* (1994). There we found

$$\begin{aligned} V_{xo} &= \frac{\omega_c^2}{\Omega^2} \frac{E_y}{B} \\ \Omega^2 &= \omega_c^2 - \frac{\omega_c}{B} \frac{dE_x}{dx} \end{aligned} \quad (C8)$$

From (C7) we see that there is an additional drift in the y direction of

$$V_{yd} = \frac{\gamma}{\omega_c} V_{xo} \quad (C9)$$

and the kinetic power per unit volume transferred to the drifting oxygen ions is given by

$$P_{KE} = \delta n_o e E_y \frac{\gamma}{\omega_c} V_{xo} = j \cdot E = \frac{\overline{E_{in}}}{2} \frac{\Sigma_{po}}{\Sigma_\omega} e \delta n_o V_{xo}$$

or

(C10)

$$\frac{\gamma}{\omega_c} = \frac{\overline{E_{in}}}{2 E_y} \frac{\Sigma_{po}}{\Sigma_\omega}$$

where (C3) has been used. The y component of the drift  $V_{yd}$  can be expressed in terms of the wave amplitude using (C8), (C9) and (C10).

$$V_{yd} = \frac{1}{2} \frac{\overline{E_{in}}}{B} \frac{\Sigma_{po}}{\Sigma_\omega} \frac{\omega_c^2}{\Omega^2}$$
(C11)

Recall that  $\overline{E_{in}}$  is the amplitude of the generated oblique Alfvén wave ( See equation (7)). It can also be shown that (C9) implies a current  $j_y$  such that the earthward force  $j_y B$  balances the tailward drag force  $\delta n_o \gamma M V_{xo}$  where  $M$  is the mass of the oxygen ion. This implies a steady state such that the drift velocity of the striation  $O^+$  ions in the y direction will adjust according to the power extracted by the wave generator. Note that only the oxygen ions forming the striations supply energy to the wave. Therefore, it is these ions that contribute to  $j_y$ .

Figure Captions:

Fig. 1 Cartoon of the concepts involved.  $O^+$  ions drifting earthward with a drift speed  $V_{xo}$  can create density striations through phase bunching. This acts as a source of oblique Alfvén waves that propagate to the two ionospheres.

Fig. 2 We find the magnetosphere-ionosphere system to be analogous to a resonant cavity with the resonance occurring at the quarter wavelength criterion. The quantity  $\lambda_{xc}$  denotes the arc size  $\lambda/2$  at the ionosphere as mapped to the equatorial plane. The symbol  $\lambda_z$  denotes the wavelength along the magnetic field. This figure shows the required relation between the Alfvén and drift speeds for the quarter wavelength to be equal to the distance between the ionosphere and the equatorial plane in the auroral region.

Fig. 3 The wave electric field amplitude  $E_{in}$  as defined in (7). This is the driver electric field that defines the amplitude of the Alfvén waves.

Fig. 4 A contour plot of the parallel current density carried by the oblique Alfvén wave as seen at the ionosphere. The abscissa denotes the equatorial source wavelength as mapped to the ionosphere. Note the maximum values occur at the quarter wavelength criterion and for 10-40 km wavelengths.

Fig. 5 The resonant nature of the magnetosphere-ionosphere coupling by the oblique Alfvén wave is demonstrated as a function of  $k_z L_i$  where  $L_i$  is the distance between the ionosphere and the equatorial plane. The resonance occurs when the distance between the ionosphere and the equatorial plane satisfies the quarter wavelength criterion as shown in Figure 2. It arises from the ionospheric conductivity being much larger than the Alfvén (wave) conductivity. It is expected that other effects, such as partial wave reflections, would broaden the resonance curves and extend the parameter space over which arc structure exists.

## REFERENCES

- Borovsky, Joseph E., Auroral arc thicknesses as predicted by various theories, *J. Geophys. Res.*, 98, 6101-6138, 1993.
- Chen, L. and A. Hasegawa, A theory of long period pulsations , 1, Steady excitation of field line resonances, *J. Geophys. Res.*, 79, 1024, 1974.
- Daglis, I. A., and W. I. Axford, Fast ionospheric response to enhanced activity in geospace: Ion feeding of the inner magnetotail, *J. Geophys. Res.*, 101, 5047-5065, 1996.
- Daglis, Iannis A., and Emmanuel T. Sarris, Comments on "Statistical investigation of IMF  $B_z$  effects on energetic (0.1- to 16-keV) magnetospheric  $O^+$  ions" by O. W. Lennartsson, *J. Geophys. Res.*, 103, 9357-9359, 1998.
- Delcourt, D. C., G. Belmont, J.-A. Sauvaud, T. E. Moore and R. F. Martin Jr., Centrifugally driven phase bunching and related current sheet structures in the near-earth magnetotail, *J. Geophys. Res.*, 101, 19,839-19847, 1996.
- Goertz, C. K., and R. W. Boswell, Magnetosphere-ionosphere coupling, *J. Geophys. Res.*, 84, 7239, 1979.
- Haerendel, Gerhard, An Alfvén wave model of auroral arcs, in *High-Latitude Space Plasma Physics*, edited by B. Hultquist and T. Hagfors, 515, Plenum, New York, 1983.
- Huang, C. Y., and L. A. Frank, A statistical study of the central plasma sheet: implications for substorm models, *Geophys. Res. Ltrs.*, 13, 652-655, 1986.
- Kan, J. R., A globally integrated substorm model: Tail reconnection and magnetosphere-ionosphere coupling, *J. Geophys. Res.*, 103, 11,787-11,795, 1998.
- Knudsen, David J., Spatial modulation of electron energy and density by nonlinear stationary inertial waves, *J. Geophys. Res.*, 101, 10,761-10,772, 1996.
- Lui, A.T. Y., and J.S. Murphree, A substorm model with onset location tied to an auroral arc, *Geophys. Res. Ltrs.*, 1269-1272, 1998.
- Lysak, Robert L., Auroral electrodynamics with current and voltage generators, *J. Geophys. Res.*, 90, 4178-4190, 1985.
- Lysak, Robert L., Coupling of the dynamical ionosphere to auroral flux tubes, *J. Geophys. Res.*, 91, 7047-7056, 1986.

- Lysak, Robert L., Electrodynamic coupling of the magnetosphere and ionosphere, *Space Sci. Revs.*, 52, 33-87, 1990.
- Mallinicrodt, A. J. and C. W. Carlson, Relations between transverse electric fields and field-aligned currents, *J. Geophys. Res.*, 83, 1426-1432, 1978.
- Maltzev, Yu. P., W. B. Lyatsky and L. M. Lyatskaya, Currents over an auroral arc, *Planet. Space Sci.*, 25, 53-57, 1977.
- Marklund, G., I. Sandahl and H. Opgenoorth, A study of the dynamics of a discrete auroral arc, *Planet. Space Sci.*, 30, 179-197, 1982.
- Maynard, N. C., W. J. Burke, E. M. Basinka, G. M. Erickson, W. J. Hughes, H. J. Singer, A. G. Yahnin, D. A. Hardy, and F. S. Mozer, Dynamics of the inner magnetosphere near times of substorm onsets, *J. Geophys. Res.*, 101, 7705-7736, 1996.
- Miura, Akira, Tetsuya Sato, Numerical simulation of global formation of auroral arcs, *J. Geophys. Res.*, 73-91, 1980.
- Rothwell, Paul L., Michael B. Silevitch, Lars P. Block and Carl-Gunne Fälthammar, O<sup>+</sup> phase bunching and auroral arc structure, *J. Geophys. Res.*, 99, 2461-2470, 1994.
- Seyler, Charles E., A mathematical model of the structure and evolution of small-scale discrete auroral arcs, *J. Geophys. Res.*, 95, 17,199-17,215, 1990.
- Seyler, C. E., J. E. Wahlund, and B. Holback, Theory and simulation of low-frequency plasma waves and comparison to Freja satellite observations, *J. Geophys. Res.*, 100, 21,453, 1995.
- Samson, J. C. and R. Rankin, The coupling of solar wind energy to MHD cavity modes, waveguide modes, and field line resonances in the Earth's magnetosphere, in *Solar Wind Sources of Magnetospheric Ultra-Low-Frequency Waves*, Geophys. Monogr. Ser., vol 81, edited by M. J. Engbretson, K. Takahashi, and M. Scholer, p. 253, AGU, Washington, D.C., 1994.
- Samson, J. C., L.L. Cogger, and Q. Pao, Observations of field line resonances, auroral arcs, and auroral vortex structures, *J. Geophys. Res.*, 101, 17,373, 1996.
- Singer, H. J., D. J. Southwood, R. J. Walker, and M. G. Kivelson, Alfvén wave resonances in a realistic magnetospheric magnetic field geometry, *J. Geophys. Res.*, 86, 4589-4596, 1981.
- Shiokawa, K., W. Baumjohann, G. Haerendel, G. Paschmann, J.F. Fennell, E. Friis-Christensen, H. Lühr, G. D. Reeves, C. T. Russell, P. R. Sutcliffe and K. Takahashi, High speed ion flow, substorm current wedge, and multiple Pi 2 pulsations, *J. Geophys. Res.*, 103, 4491-4507, 1998.



Southwood, D. J., Some features of field line resonances in the magnetosphere, *Planet. Space Sci.*, 22, 483, 1974.

Tanskanen, P. , J. Kangas, L. Block, G. Kremser, A. Korth, J. Woch, I. B. Iversen, K. M. Torkar, W. Riedler, S. Ullaland, J. Stadnes, and K.-H. Glassmeier, Different phases of a magnetospheric substorm on June 23, 1979, *J. Geophys. Res.*, 92, 7443-7457, 1987.

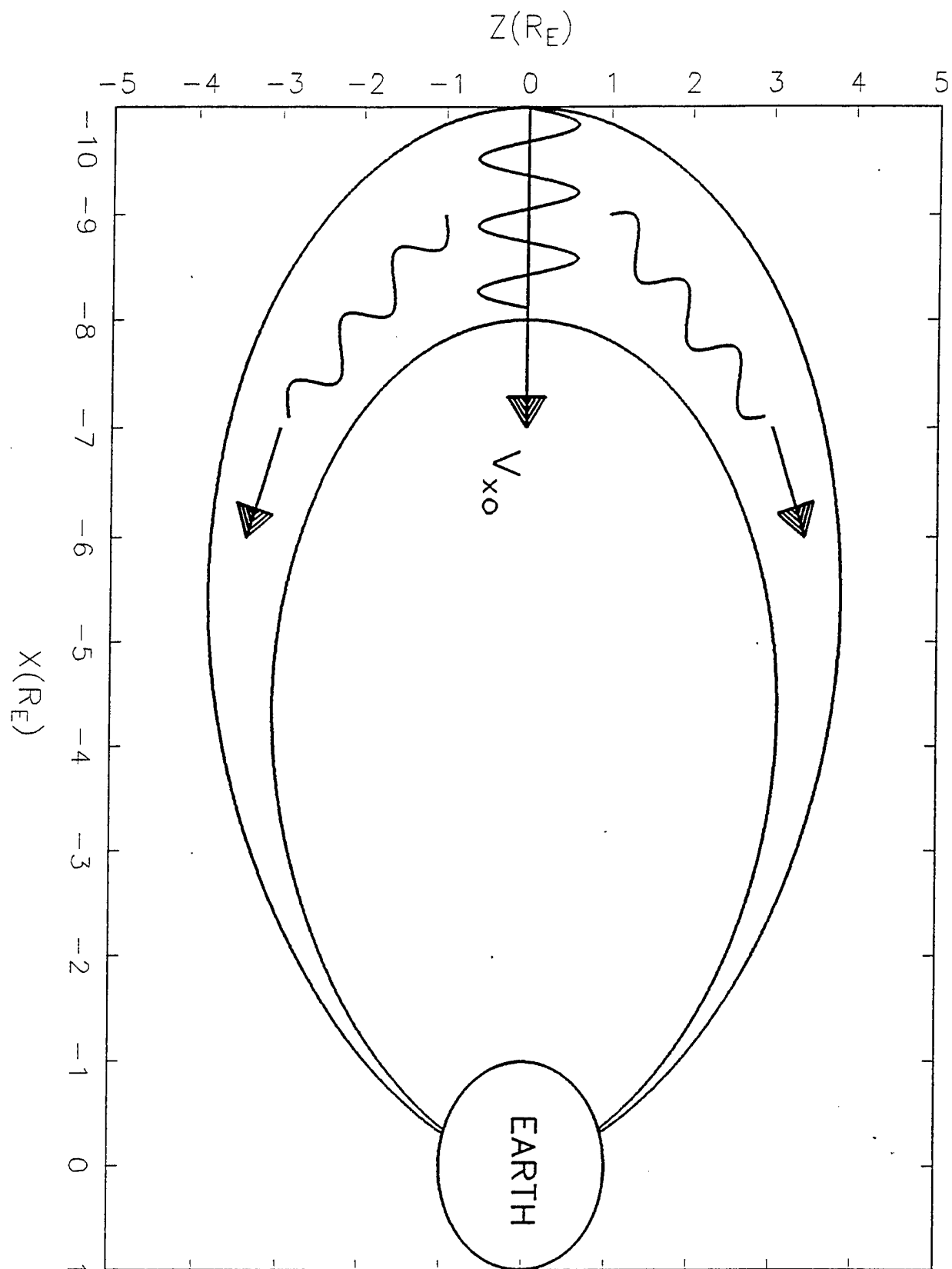


Fig. 1

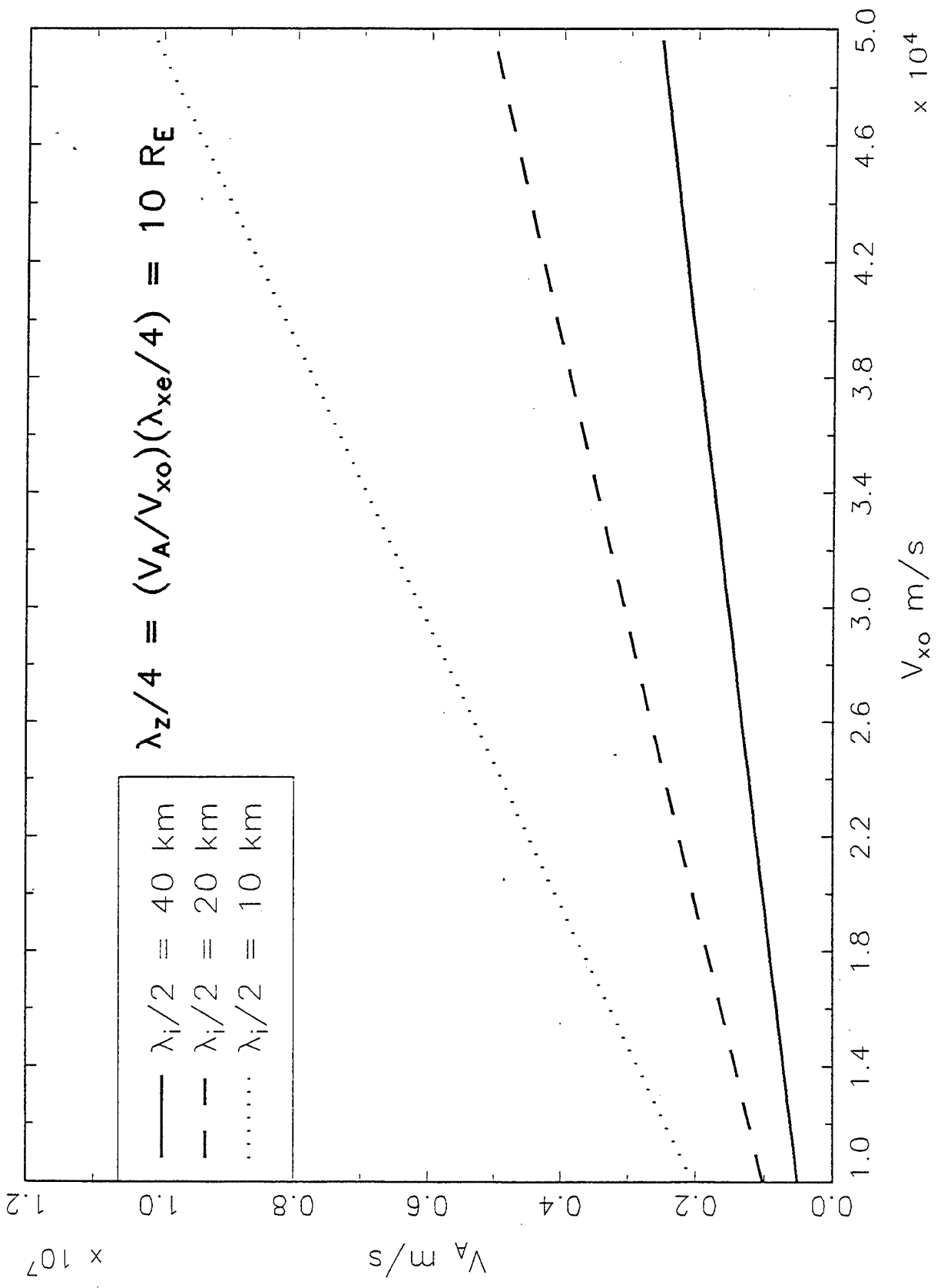


Fig. 2

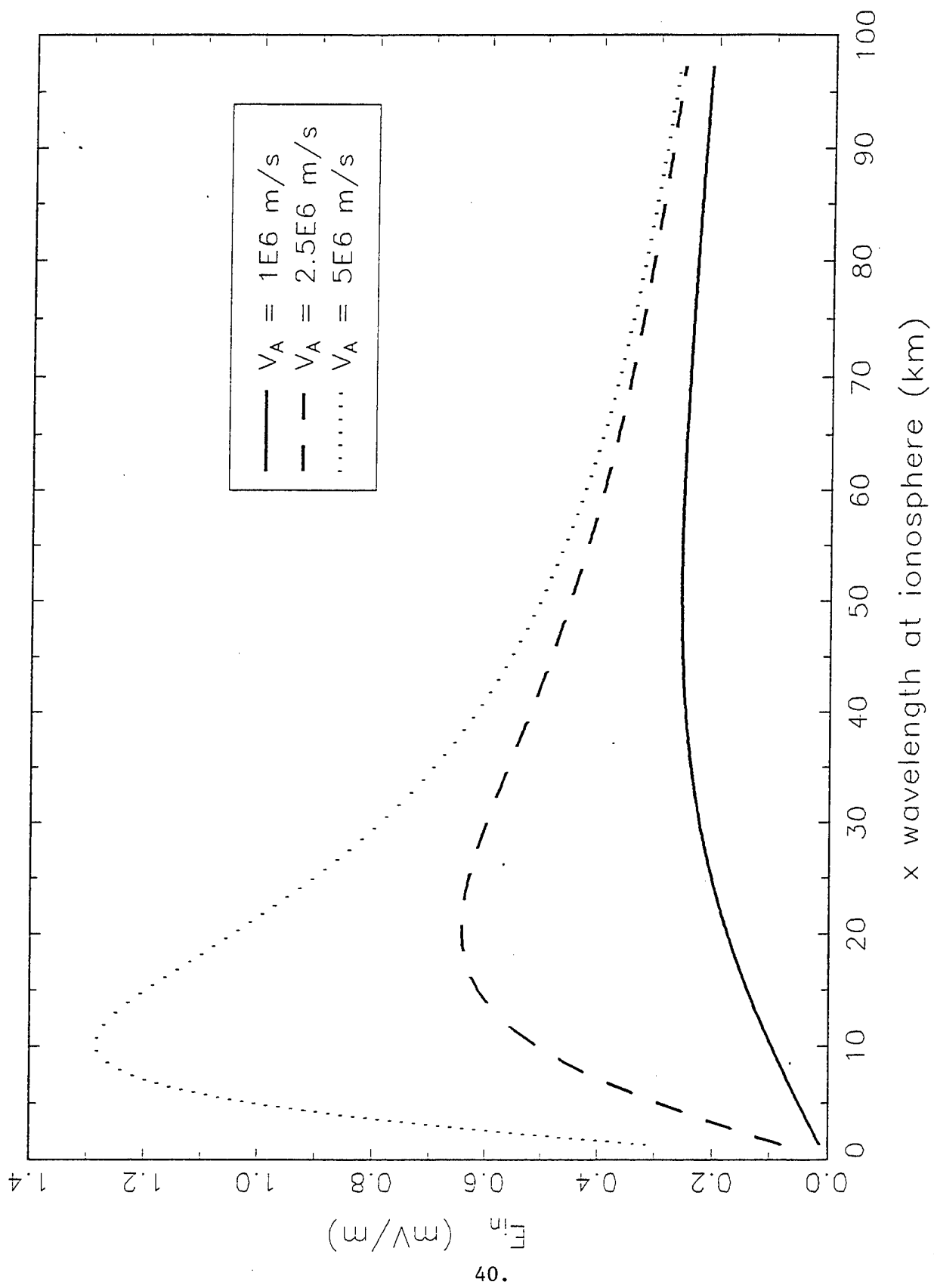


Fig. 3

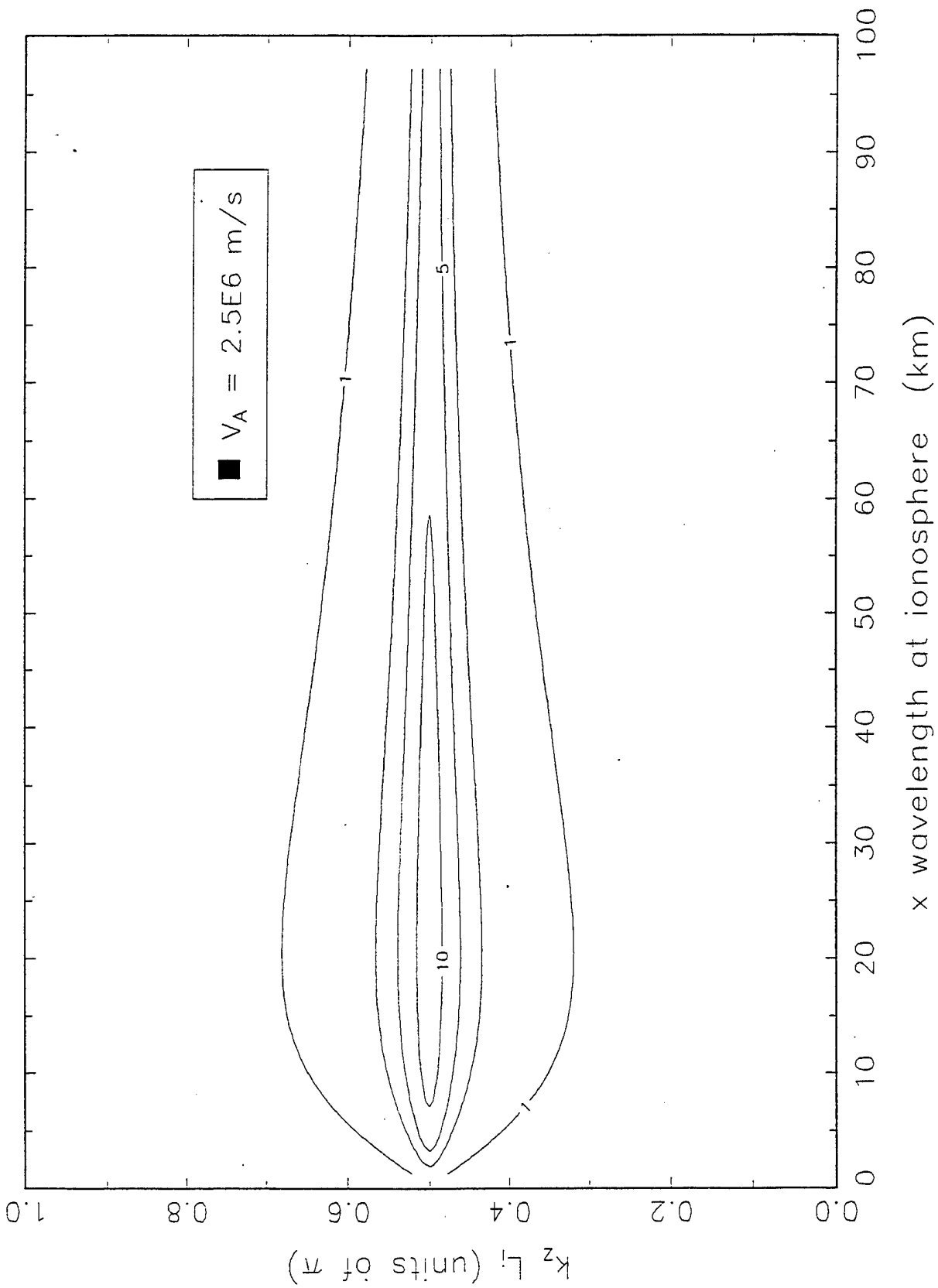


Fig. 4

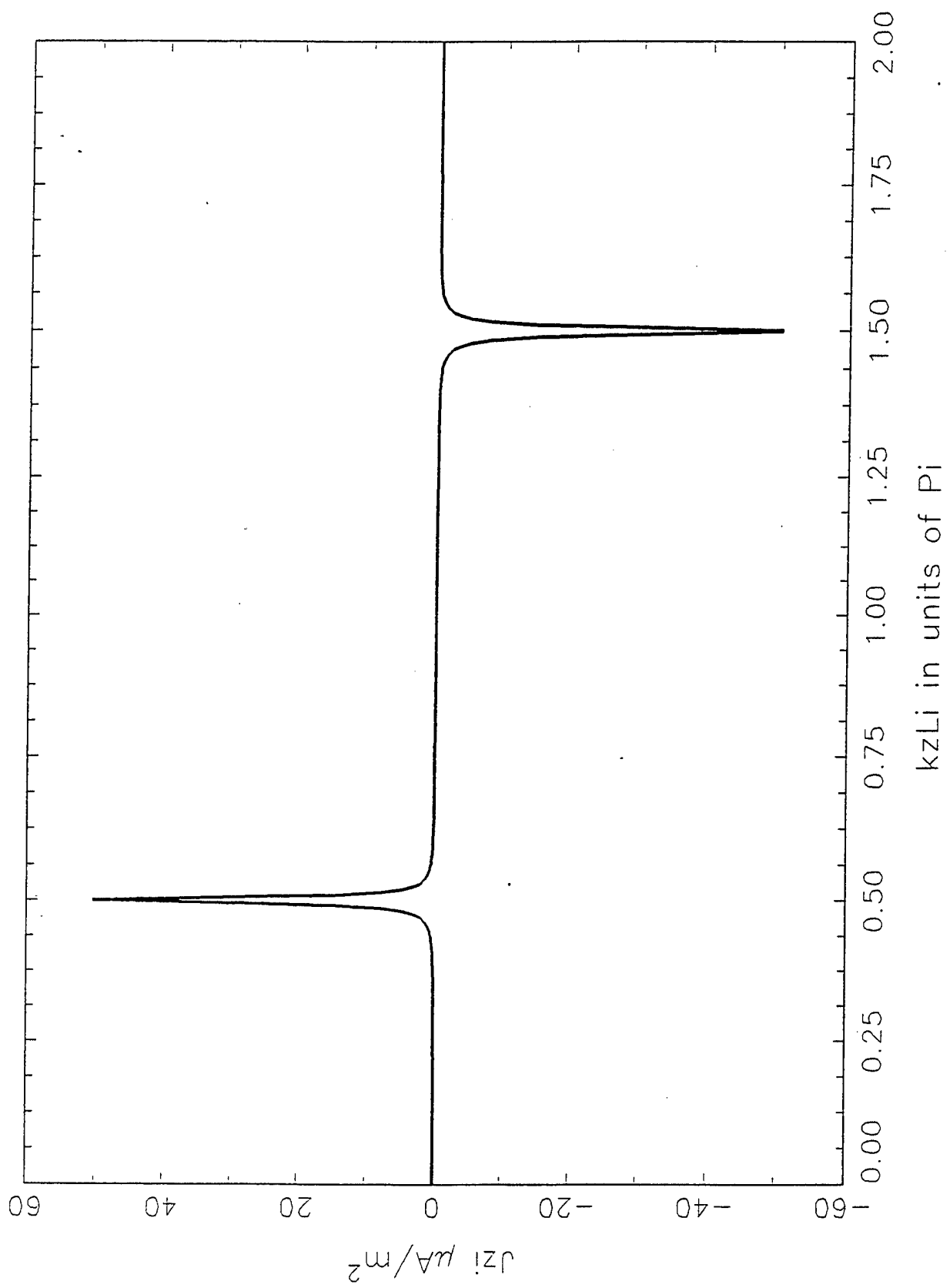


Fig. 5

# Pitch angle scattering of diffuse auroral electrons by whistler mode waves

Elena Villalón

Center for Electromagnetics Research, Northeastern University, Boston, Massachusetts

William J. Burke

Space Science Division, Phillips Laboratory, Hanscom Air Force Base, Massachusetts

**Abstract.** Resonant electron-whistler interactions in the plasma sheet are investigated as possible explanations of the nearly isotropic fluxes of low-energy electrons observed above the diffuse aurora. Whistler mode waves, propagating near the resonance cone with frequencies near or larger than half the equatorial electron cyclotron frequency, can interact with low-energy plasma sheet electrons. A Hamiltonian formulation is developed for test particles interacting with the coherent chorus emission spectra. We consider the second-order resonance condition which requires that inhomogeneities in the Earth's magnetic field be compensated by a finite bandwidth of wave frequencies to maintain resonance for extended distances along field lines. These second-order interactions are very efficient in scattering the electrons toward the atmospheric loss cone. Numerical calculations are presented for the magnetic shell  $L = 5.5$  for wave amplitudes of  $\sim 10^{-6}$  V/m, using different frequency and magnetospheric conditions.

## 1. Introduction

The pitch angle scattering of energetic electrons by whistler waves in the Earth's radiation belts is a long-standing research problem [Lyons and Williams, 1984, and references therein]. Whistler waves are responsible for the precipitation of electrons in both the plasmasphere and the plasma sheet [Bell, 1984]. As electrons scatter toward smaller pitch angles, they give up small quantities of energy, amplifying the waves to the point where the interaction becomes self-sustaining. The limit for stably trapped particle fluxes was first investigated by Kennel and Petschek [1966], and later in self-consistent quasi-linear diffusion models by Bel'spalov and Trakhtengerts [1986], Villalón et al. [1989], and Villalón and Burke [1991].

Past studies have considered whistler waves for which the ratio between the wave and the electron cyclotron frequencies is  $\omega/\Omega_e \ll 1$ . In this case, only electrons whose energies are larger than or of the order of the magnetic energy per particle  $E_c$ , may interact with the waves. Normalized to the electron rest energy,  $E_c = (\Omega_e/\omega_p)^2$ . Here,  $\Omega_e$  and  $\omega_p$  are the electron cyclotron and the plasma frequencies, respectively. As pointed out by Johnstone et al. [1993], in the outer plasma sheet the threshold energy for resonant interactions is estimated to be  $> 10$  keV. In this paper we investigate

the possibility of resonant interactions of whistler mode waves with electrons with energies well below 10 keV. For these interactions to take place, the wave frequency must be close to  $\Omega_e$ .

The diffuse aurora is formed by nearly isotropic fluxes of electrons, mostly with energies of  $< 10$  keV, that precipitate from the plasma sheet [Johnstone, 1983; Inan et al., 1992]. A number of studies have attempted to explain the diffuse aurora by the interaction of the electrons with electrostatic electron cyclotron harmonic (ECH) waves [Swift, 1981]. However, it does not appear that the amplitudes of ECH waves are large enough to account for the electron precipitation [Belmont et al., 1983; Roeder and Koons, 1989]. Johnstone et al. [1993] proposed that the  $< 10$  keV electrons that form the diffuse aurora may be precipitated by whistler mode waves that propagate along the magnetic field with frequencies such that  $\omega \rightarrow \Omega_e$ . They successfully explained how the resonant energy of the electrons could be well below  $E_c$ .

We note that Figure 3 of Burke et al. [1995] gives an example of waves in this frequency band, observed by the CRRES satellite while it passed through the inner plasma sheet during a period of magnetic quieting. Near apogee, where CRRES encountered nearly isotropic plasma sheet electrons, it also measured waves covering the band between  $0.5\Omega_e$  and  $\Omega_e$ . Our experience is that these frequencies are detected by the CRRES plasma wave experiment only in the presence of central plasma sheet electrons. In the case shown by Burke et al. [1995], electric field amplitudes of  $\sim 10^{-6}$  V m $^{-1}$  appear in the frequency band of interest. Dur-

ing disturbed times the intensities of these waves may be several orders of magnitude stronger than in the case presented. Here we wish to demonstrate that even the low amplitudes are sufficient to explain diffuse auroral electron precipitation.

Inan *et al.* [1992] and Inan and Bell [1991] have studied interactions between low-energy electrons and obliquely propagating chorus emissions. They consider first-order resonant interactions with upper band chorus, where the wave frequencies are  $> 0.5\Omega_e$ . The wave magnetic field amplitudes for chorus were reported to be in the range of 1–100 pT. Inan *et al.* [1992] used wave magnetic amplitudes of 1 pT in their calculations. If these waves propagate near the resonance cone, they become quasi-electrostatic. In this way they can even interact with suprathermal electrons [Jasna *et al.*, 1992] and efficiently precipitate low-energy electrons into the atmosphere, leading to the morningside diffuse aurora.

Chorus and triggered emissions are characterized by coherent wave spectra. Triggered emissions are artificially stimulated inside the plasmasphere by ground-based transmitters [Burtis and Helliwell, 1976; Helliwell, 1993]. VLF chorus is frequently associated with microbursts of electron precipitation [Rosenberg *et al.*, 1981; Parks, 1978]. It is believed that chorus is generated through a cyclotron instability which is produced by anisotropic warm electrons in the equatorial plasma sheet [Hashimoto and Kimura, 1981; Ohmi and Hayakawa, 1986]. The nonlinear interactions produce impulsive precipitation of the electrons [Hardy *et al.*, 1990] due to the filling of the loss cone as described by Davidson and Chiu [1987]. The nonlinear interactions between energetic electrons and the waves also produce almost monochromatic wavelets, which generate chorus elements in a manner similar to that of artificially stimulated emissions [Sazhin and Hayakawa, 1992]. Because of the phase coherence of these emissions, the electrons may stay in gyroresonance for long distances along the field lines, leading to second-order resonant interactions [Dysthe, 1971; Nunn, 1974].

Here we consider waves with  $0.45 \leq \omega/\Omega_e < 1$  that propagate obliquely to the background geomagnetic field. These waves may be generated by the linear cyclotron instability of warm electrons interacting with the waves as described by Kennel and Petschek [1966] and Johnstone [1983]. For linear interactions the diffusion of the electrons into the loss cone is weak, and the precipitation does not occur in an impulsive way as in the microbursts [Davidson, 1986a and 1986b]. If wave amplitudes grow to some critical levels, nonlinear effects allow for second-order interactions to take place. Second-order interactions require that the wave amplitudes be large and have a finite frequency spectral spread to compensate for the magnetic field inhomogeneities [Villalón and Burke, 1993]. Second-order interactions are defined in terms of the variation of the relative phase angle between the waves and the electrons, which leads to a specific change of the wave frequency along the field line, as given in section 5. In contrast with the work by Inan *et al.* [1992], we consider second-order interactions for a broad spectrum of VLF chorus.

The wave amplitudes required for efficient electron precipitation are smaller with the second-order resonant interactions than those used by Inan *et al.* [1992]. We assume electric field amplitudes of  $\approx 10^{-6}$  V m $^{-1}$ . For a refractive index  $\eta \leq 30$  this corresponds to wave magnetic field amplitudes of  $\leq 0.1$  pT.

The paper is organized as follows. Section 2 presents the basic equations that describe whistler mode waves propagating in a cold magnetized plasma. Section 3 considers electron-whistler resonant interactions in the Earth's inhomogeneous magnetic field. We establish a mapping between the location of the interactions along the field line and the equatorial pitch angles of electrons resonant at the first cyclotron harmonic. Section 4 contains the basic equations of a test particle Hamiltonian theory. In section 5 we integrate these equations along magnetic field lines. Conditions for second-order resonances are also given. Section 6 contains numerical applications for plasma sheet electrons. We consider second-order resonant interactions of test particles with multiple-frequency waves. The changes in pitch angle and energy are calculated. For wave amplitudes of  $\sim 10^{-6}$  V m $^{-1}$ , we show that the changes in pitch angle may be  $\geq 1^\circ$  for electrons near the edge of the loss cone.

## 2. Whistler Mode Waves

Figure 1 represents the geometry of wave-particle interactions with a whistler mode wave of frequency  $\omega$  and wave vector  $\mathbf{k}$ , propagating in a field-aligned duct. The geomagnetic field  $\mathbf{B}_0$  is along the  $z$  direction, and  $\phi$  is the angle between  $\mathbf{k}$  and  $\mathbf{B}_0$ . For waves propagating near the resonance cone,  $\cos \phi \sim \omega/\Omega_e$ , the refractive indices are very large, and the waves become quasi-electrostatic [Sazhin, 1993]. In terms of  $X = (\omega_p/\omega)^2$ , the refractive index  $\eta = ck/\omega$  satisfies the dispersion relation

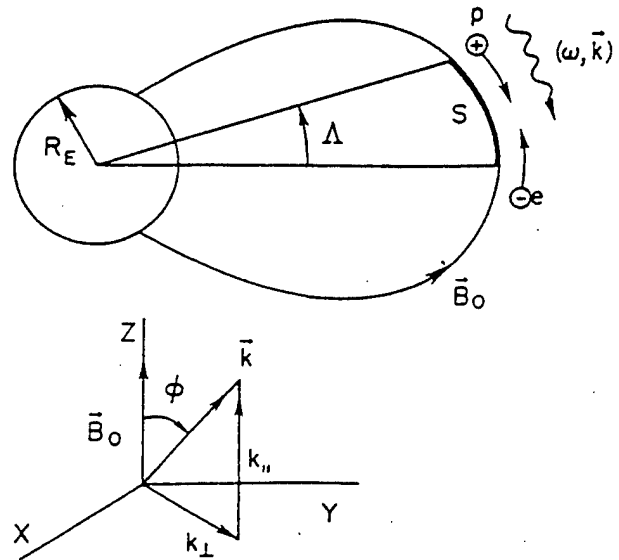


Figure 1. Schematic representation of a whistler mode wave of frequency  $(\omega, \mathbf{k})$ , interacting with electrons and protons. The Earth's dipole magnetic field is  $\mathbf{B}_0$ , the geomagnetic latitude is  $\Lambda$ , and  $s$  is the coordinate along the flux tube.



$$\eta^2 = 1 + \frac{X}{\delta} \quad (1)$$

$$\delta = \frac{\Omega_e}{\omega} |\cos \phi| - 1$$

Near the equator, the angle  $\phi$  is such that  $\cos \phi_r \leq \cos \phi \leq 1$ . The resonance cone angle,  $\phi_r$ , is defined as

$$\cos \phi_r = \frac{\omega}{\Omega_e(L)} \quad (2)$$

We use the argument ( $L$ ) to denote equatorial values of physical quantities. If we call  $\delta(L)$  the value of  $\delta$  at the magnetic equator, we show that when  $\phi = \phi_r$ , then  $\delta(L) = 0$ .

The group velocity in the parallel direction can readily be obtained from (1) considering  $v_{g\parallel} = d\omega/dk_{\parallel}$ . Normalizing  $v_{g\parallel}$  to  $c^{-1}$ , we find that

$$v_{g\parallel} = \frac{1}{\eta_{\parallel}} t(\delta, \phi) \quad (3)$$

$$t(\delta, \phi) = 1 + \cos^2 \phi \left(1 - \frac{2}{\delta + 1}\right)$$

where  $\eta_{\parallel} = \eta \cos \phi$ . Note that as  $\delta \rightarrow 0$ ,  $t(\delta, \phi) \rightarrow \sin^2 \phi$ .

The electric field,  $\mathbf{E}$ , of the wave is represented by

$$\mathbf{E} = \hat{x} \mathcal{E}_1 \cos \Psi - \hat{y} \mathcal{E}_2 \sin \Psi - \hat{z} \mathcal{E}_3 \cos \Psi \quad (4)$$

where  $\hat{x}$ ,  $\hat{y}$ , and  $\hat{z}$  are unit vectors,  $\Psi = k_{\perp} x + k_{\parallel} z - \omega t$ , and  $k_{\parallel}$ ,  $k_{\perp}$  are the components of the wave vector along and perpendicular to  $\mathbf{B}_0$ . The ratios of the electric field components are

$$\begin{aligned} \frac{\mathcal{E}_2}{\mathcal{E}_1} &= \frac{1}{\eta^2} \frac{X}{(\frac{\Omega_e}{\omega} - |\cos \phi|)} \\ \frac{\mathcal{E}_3}{\mathcal{E}_1} &= \frac{1 - X - (\eta \sin \phi)^2}{\eta^2 \sin \phi \cos \phi} \end{aligned} \quad (5)$$

For the case of waves propagating near the resonance cone,  $\omega \sim \Omega_e(L) |\cos \phi|$ , the equatorial refractive index  $\eta^2(L) \gg 1$ . Its electric field is linearly polarized, having components  $|\mathcal{E}_2/\mathcal{E}_1| \ll 1$  and  $|\mathcal{E}_1/\mathcal{E}_3| \sim -(\sin \phi / \cos \phi)$ . In this case the wave becomes quasi-electrostatic, since  $\mathbf{E}$  is almost in the direction of  $\mathbf{k}$ , and the group velocities  $v_g \sim \eta^{-1}$  are very small.

Near the equator, we approximate the Earth's dipole magnetic field as having a parabolic profile

$$h = \frac{\Omega}{\Omega(L)} = 1 + \left(\frac{z}{r_L}\right)^2 \quad (6)$$

where  $z \simeq R_E \Lambda$ ,  $R_E$  is the Earth's radius,  $L$  is the magnetic shell parameter,  $\Lambda$  is the geomagnetic latitude, and  $r_L = (2^{1/2}/3) R_E L$ . The equatorial gyrofrequency is  $\Omega(L)$ , and  $\Omega$  represents the gyrofrequencies of either electrons or protons at locations  $s$  away from the equator along the field line. Equation (6) is obtained

from a Taylor expansion of the dipole field and is an excellent representation of the magnetic geometry within  $\pm 20^\circ$  of the equator.

### 3. Resonant Electron-Whistler Interactions

Here we consider relativistic electrons and normalize their energies to  $(m_e c^2)^{-1}$ , their velocities to  $c^{-1}$ , and their momenta  $p$  to  $(m_e c)^{-1}$ . In what follows we only refer to these normalized quantities. The relativistic factor is  $\gamma_R = [1 - v^2]^{-1/2}$ , where  $v$  is the particle velocity. Resonant whistler-electron interactions must satisfy the condition

$$1 - \eta_{\parallel} v_{\parallel} - \ell \frac{\Omega_e}{\omega} \frac{1}{\gamma_R} = 0 \quad (7)$$

where  $\ell = 0, \pm 1, \pm 2, \dots$  is the harmonic number, and  $\Omega_e = |q| B_0 / m_e c$  is the electron gyrofrequency. Here,  $v_{\parallel}$  and  $\eta_{\parallel} = \eta \cos \phi$  are the parallel components of the particle's velocity and refractive index, respectively.

In terms of the local pitch angle,  $v_{\parallel} = v \cos \theta$ . Here,  $\theta$  is the angle between  $\mathbf{B}_0$  and  $\mathbf{v}$ . We call  $\mu = \sin^2 \theta(L)$ , where  $\theta(L)$  is the equatorial pitch angle. Here,  $\theta(L) > \theta_c$ , where  $\theta_c$  is the pitch angle at the edge of the loss cone, and  $\mu_c$  is the corresponding value of  $\mu$ . In addition, we require that  $\theta(L) < \theta_M$ ; thus the range of resonant equatorial pitch angles is  $\mu_c < \mu < \mu_M$ . The upper limit  $\theta_M$  depends on the extent of the resonant region along the field line, as we shall explain below. As a function of  $L$  shell, the mirror ratio is  $\sigma = \mu_c^{-1} = L^3 (4 - 3/L)^{1/2}$ . To zero order in the electric field amplitudes, a particle's magnetic moment is conserved. Then we may write for the parallel and perpendicular components of the particle velocity  $v$ ,  $v_{\parallel} = v[1 - \mu \Omega / \Omega(L)]^{1/2}$ ,  $v_{\perp} = v[\mu \Omega / \Omega(L)]^{1/2}$ .

As the particles move away from the equator, their parallel velocities  $v_{\parallel}$  decrease. We assume, however, that the waves' phase velocities  $\omega/k_{\parallel}$  remain constant. That is, variations in  $\Omega_e$ ,  $\omega$ , and  $\cos \phi$  are such that  $\eta_{\parallel}$  is constant along the near-equatorial parts of field lines. Given a resonant energy for the  $\ell$  the harmonic,  $\gamma_R = (1 + p_{\parallel}^2)^{1/2}$ , interactions take place at geomagnetic latitudes such that  $1 \leq h \leq h_M$ , where  $h$  is defined in (6). For  $h = 1$  we take  $\theta(L) = \theta_M$ , and for  $h = h_M$  then  $\theta(L) = \theta_c$ . Thus there exists a mapping between  $h$  and  $\mu$ , which may be obtained by solving for the resonance condition in (7).

In terms of the resonant parallel momentum  $p_{\parallel}$ , where  $p_{\parallel} = p_{\parallel} [1 - \mu \Omega / \Omega(L)]^{1/2}$ , (7) becomes

$$p_{\parallel} = \frac{1}{\eta_{\parallel}} \left[ -\frac{\ell \Omega_e}{\omega} + \sqrt{1 + p_{\parallel}^2} \right] \quad (8)$$

The equatorial parallel velocity is obtained from  $v_{\parallel}^2 = p_{\parallel}^2 (1 + p_{\parallel}^2)^{-1}$ .

To find the resonant energy, we consider interactions that take place at the equator  $h = 1$ , such that the resonant pitch angle is  $\theta(L) = \theta_M$ . Next we define

$$\begin{aligned}
A_o &= \eta_{\parallel}^2 \cos^2 \theta_M - 1 \\
D_o &= 2 \frac{\ell \Omega_e(L)}{\omega} \eta_{\parallel} \cos \theta_M \\
C_o &= \left[ \frac{\ell \Omega_e(L)}{\omega} \right]^2 - 1
\end{aligned} \quad (9)$$

Then we show

$$p_{\ell} = -\frac{D_o}{2A_o} \pm \left[ \left( \frac{D_o}{2A_o} \right)^2 - \frac{C_o}{A_o} \right]^{1/2} \quad (10)$$

which solves for the electron momentum. The plus sign must be taken for  $\ell \geq 0$ , and the minus sign for  $\ell < 0$ . Note that for  $\ell > 0$ ,  $\cos \theta(L) < 0$ , and for  $\ell \leq 0$ , then  $\cos \theta(L) > 0$ , so that in all cases  $D_o \leq 0$ . Also note that as  $\cos \phi \rightarrow \cos \phi_r$ ,  $\delta(L) \rightarrow 0$ ,  $\eta_{\parallel} \rightarrow \infty$ , and  $p_{\ell} \rightarrow 0$ , and thus the energy of the resonant electron is very small (i.e.,  $< 1$  keV). When the frequency of the waves  $\omega \rightarrow \Omega_e(L)$ , then  $\cos \phi_r \rightarrow 1$ , and again we have  $\delta(L) \rightarrow 0$ ,  $\eta_{\parallel} \rightarrow \infty$ , and  $p_{\ell} \rightarrow 0$ .

In addition, we also consider interactions that occur at  $h = h_M$  and for pitch angles at the edge of the loss cone  $\theta(L) = \theta_c$ . From (8) we obtain the following relation between  $\mu_M$  and  $h_M$  as a function of the resonant energy  $\gamma_R$  and  $\theta_c$ :

$$\sqrt{1 - \mu_M} = \sqrt{1 - \mu_c} h_M \left[ \frac{1 + f_L \gamma_R}{-h_M + f_L \gamma_R} \right] \quad (11)$$

where we define  $f_L = \omega / \ell \Omega_e(L)$ . The waves exist near the equator, and their extent along the field lines is such that  $h \leq h_M$ , where  $h$  is defined in (6). Because interactions take place near equatorial regions,  $h_M$  is close to one. The upper limit on the resonant equatorial pitch angles  $\theta_M$  is obtained from (11) and depends on the extent of the interaction region as given by  $h_M$ .

Solving (7) for  $h_{\ell}$  as a function of  $\mu$ , we show that for  $\ell \neq 0$ ,

$$h_{\ell} = b_{\ell} + [b_{\ell}^2 + (f_L \eta_{\parallel} p)^2 - \gamma_R^2 f_L^2]^{1/2} \quad (12)$$

$$b_{\ell} = \gamma_R f_L - \frac{\mu}{2} (f_L \eta_{\parallel} p)^2$$

where  $\eta_{\parallel} p f_L = (-1 + \gamma_R f_L) (1 - \mu_M)^{-1/2}$ . For the Landau resonance ( $\ell = 0$ ),

$$h_o = \frac{1}{\mu} \left[ 1 - \frac{1}{(\eta_{\parallel} v)^2} \right] \quad (13)$$

For a given value of the electron energy  $\gamma_R$ , (11) to (13) establish a one-to-one correspondence between the resonant equatorial pitch angles  $\theta(L)$  and the geomagnetic latitudes  $\Lambda$  at which the interactions are taking place.

#### 4. Hamiltonian Theory

The dimensionless electric field amplitudes are

$$e_i = \frac{|q| E_i}{m_e c \omega} \quad (14)$$

We introduce the normalized time  $\tau = t \Omega_e(L)$  and length  $s = z / r_L$ , and define the canonical momenta and action:

$$\begin{aligned}
P_{\parallel} &= p_{\parallel} + e_3 \sin \Psi \\
P_x &= p_x - e_1 \sin \Psi \\
P_y &= p_y - e_2 \cos \Psi - \frac{\Omega_e(s) x}{c}
\end{aligned} \quad (15)$$

$$I = \frac{1}{2} \frac{\Omega(L)}{\Omega(s)} \left[ P_x^2 + (P_y + \frac{\Omega_e(s) x}{c})^2 \right] \quad (16)$$

and call

$$\gamma_o = \left[ 1 + P_{\parallel}^2 + 2I \frac{\Omega(s)}{\Omega(L)} \right]^{1/2} \quad (17)$$

The relative phase angle between the wave and the electron is

$$\xi_{\ell} = \ell \lambda + r_L \int_0^s k_{\parallel} ds' - \frac{\omega}{\Omega_e(L)} \tau \quad (18)$$

$$\lambda = \arctan \left( \frac{P_y + \Omega_e(s) x / c}{P_x} \right)$$

To first order in wave electric field amplitudes, the time-dependent Hamiltonian is [Ginet and Heinemann, 1990; Albert, 1993; Villalón and Burke, 1993]

$$\mathcal{H} = \gamma_o - \frac{P}{\gamma_o} \sum_{\ell=-\infty}^{+\infty} \Upsilon_{\ell}(I, P_{\parallel}, s) \sin \xi_{\ell} \quad (19)$$

where  $P = (\gamma_o^2 - 1)^{1/2}$ , and

$$\begin{aligned}
\Upsilon_{\ell} &= e_3 \frac{P_{\parallel}}{P} \mathcal{J}_{\ell}(a) - \frac{1}{2P} \sqrt{2I \frac{\Omega}{\Omega(L)}} \\
&\quad \cdot [(\epsilon_1 + \epsilon_2) \mathcal{J}_{\ell-1}(a) + (\epsilon_1 - \epsilon_2) \mathcal{J}_{\ell+1}(a)] \quad (20)
\end{aligned}$$

where the  $\mathcal{J}$  values are Bessel functions of argument  $a = k_{\perp} \rho$  and  $\rho = (c / \Omega_e) [2I \Omega / \Omega(L)]^{1/2}$  is the Larmor radius. A constant of motion is

$$C_{\ell} = \ell \mathcal{H} - \left[ \frac{\omega}{\Omega_e(L)} \right] I \quad (21)$$

Next we solve for the equations of motion for a single isolated resonance. To zero order in the electric fields  $ds/d\tau = \kappa P_{\parallel} / \gamma_o$ , where  $\kappa = c / r_L \Omega_e(L) \ll 1$ . For example, at  $L = 5$  we show that  $\kappa = 4.5 \times 10^{-4}$ . Differentiating (18) with respect to  $s$ , the length along the field line, to zero order in the electric field amplitudes, we show

$$\frac{d\xi_{\ell}}{ds} = r_L k_{\parallel} + \frac{\ell \Omega_e - \omega \gamma_o}{\Omega_e(L) \kappa P_{\parallel}} \quad (22)$$

For resonant electrons,  $d\xi_{\ell}/ds = 0$ . Then the equations of motion for the canonical variables reduce to those of the physical variables at the resonance. Referring to the physical action and parallel momentum, in term of the

length  $s$  along the field line, we find that to first order in the electric fields,

$$\frac{dI}{ds} = \frac{\ell}{\kappa} \frac{p}{p_{\parallel}} \Upsilon_{\ell}(I, p_{\parallel}, s) \cos \xi_{\ell} \quad (23)$$

$$\frac{dp_{\parallel}}{ds} = \frac{\kappa \tau_L k_{\parallel}}{\ell} \frac{dI}{ds} - \frac{I}{p_{\parallel}} \frac{1}{\Omega(L)} \frac{d\Omega}{ds} \quad (24)$$

The evolution of the electron resonant energy  $\gamma_R$ , and the equatorial pitch angle  $\mu = \sin^2 \theta_L$ , is

$$\frac{d\gamma_R}{ds} = \frac{\omega}{\ell \Omega_e(L)} \frac{dI}{ds} \quad (25)$$

$$\frac{d\mu}{ds} = \frac{2}{\gamma_R^2 - 1} \left[ \frac{\ell \Omega_e}{\omega} - \gamma_R \mu \right] \frac{d\gamma_R}{ds} \quad (26)$$

Differentiating (22) with respect to  $s$  and assuming that  $d\xi_{\ell}/ds = 0$  yields

$$\frac{d^2 \xi_{\ell}}{ds^2} = \alpha_{\ell} + \beta_{\ell} \left[ \frac{1}{\ell} \frac{dI}{ds} \right] \quad (27)$$

Here,

$$\alpha_{\ell} = \tau_L \frac{dk_{\parallel}}{ds} - \frac{\gamma_R}{\kappa p_{\parallel} \Omega_e(L)} \frac{d\omega}{ds} + \frac{\gamma_R}{\kappa p_{\parallel}} \sqrt{\frac{h-1}{1-\mu h}} \left[ \frac{2\ell}{\gamma_R} \sqrt{1-\mu h} - \Lambda(L, v) \mu \right] \quad (28)$$

$$\beta_{\ell} = \frac{1}{\kappa p_{\parallel}} (\eta_{\parallel}^2 - 1) \left[ \frac{\omega}{\Omega_e(L)} \right]^2 \quad (29)$$

where  $\Lambda(L, v) = \eta_{\parallel} v \omega / \Omega_e(L)$ ; all other variables are defined throughout the paper. For second-order resonant electrons the inhomogeneity of the magnetic field is compensated by the frequency variation, and then  $\alpha_{\ell} = 0$ . In addition, if  $\eta_{\parallel} = 1$ , then  $\beta_{\ell} = 0$ ; this is the case of infinite acceleration studied by Roberts and Buchsbaum [1964].

Combining equations (24) and (25), we obtain

$$\frac{d\gamma_R}{ds} - \frac{1}{\eta_{\parallel}} \left[ \frac{dp_{\parallel}}{ds} + \frac{I}{p_{\parallel}} \frac{1}{\Omega(L)} \frac{d\Omega}{ds} \right] = 0 \quad (30)$$

The diffusion curves, or single-wave characteristics, are obtained by integrating (30) along  $s$ . These are the curves along which the representative point of a particle in the  $p_{\parallel}, p_{\perp}$  plane will move. If we neglect magnetic inhomogeneities, we obtain the diffusion curves for homogeneous, relativistic plasmas  $[1 + p_{\parallel}^2 + p_{\perp}^2]^{1/2} - p_{\parallel}/\eta_{\parallel} = \text{const.}$

## 5. Equations of Motion Near Resonance

At the resonance the parallel component of the momentum,  $p_{\ell\parallel}(R)$ , is given by solving for (8). The physical action is obtained from

$$I_{\ell}(R) = \frac{p_{\ell\parallel}^2(R)}{2} \frac{\mu}{1 - \mu h_{\ell}} \quad (31)$$

where  $h_{\ell}$  is given in (12) and (13).

At the resonance we also obtain  $s_{\ell} = (h_{\ell} - 1)^{1/2}$ . Using a Taylor expansion around  $s = s_{\ell}$ , we obtain for the phase angle [Villalón and Burke, 1993]

$$\xi_{\ell} = \xi_{\ell}(R) + \xi_{\ell}^{(1)}(s - s_{\ell}) + \frac{1}{2} \xi_{\ell}^{(2)}(s - s_{\ell})^2 \quad (32)$$

Here,  $\xi_{\ell}^{(1)} = 0$ , and

$$\xi_{\ell}^{(2)} = \alpha_{\ell}(R) + \beta_{\ell}(R) \left[ \frac{1}{\ell} \frac{dI}{ds} \right]_{(R)} \quad (33)$$

where the subscript  $(R)$  denotes values taken at the resonance, for  $I_{\ell} = I(R)$  and  $p_{\parallel} = p_{\ell\parallel}$ .

We define the length of resonant interaction as

$$\delta s_{\ell} = \int_{-\infty}^{+\infty} \cos \xi_{\ell} ds = \sqrt{\frac{2}{|\xi_{\ell}^{(2)}|}} \Gamma\left(\frac{1}{2}\right) \cos \left( \xi_{\ell}(R) + \frac{\xi_{\ell}^{(2)}}{|\xi_{\ell}^{(2)}|} \frac{\pi}{4} \right) \quad (34)$$

Near resonance the change in action, energy, and pitch angle is given by

$$\Delta I = \left[ \frac{dI}{ds} \right]_{(R)} \delta s_{\ell} \quad (35)$$

$$\Delta \gamma_R = \frac{\omega}{\ell \Omega_e(L)} \Delta I \quad (36)$$

$$\Delta \mu = \frac{2}{\gamma_R^2 - 1} \left[ \frac{\ell \Omega_e}{\omega} - \gamma_R \mu \right] \Delta \gamma_R \quad (37)$$

Here,

$$\left[ \frac{dI}{ds} \right]_{(R)} = \frac{\ell}{\kappa} \frac{p}{p_{\ell\parallel}} \Upsilon_{\ell} [I_{\ell}(R), p_{\ell\parallel}(R), s] \quad (38)$$

where  $\Upsilon_{\ell}$  is defined in (20) for the resonant values of  $I$  and  $p_{\parallel}$ .

If the electric field amplitudes are small compared to the inhomogeneity of the plasma, then we may approximate  $\xi_{\ell}^{(2)} \simeq \alpha_{\ell}(R)$ . For this case the changes in action, energy, and pitch angle are proportional to  $\epsilon_i$ , the electric field amplitudes. In contrast, for second-order resonances,  $\beta_{\ell} [(1/\ell) (dI/ds)]_{(R)} \gg \alpha_{\ell}$ , and then  $\xi_{\ell}^{(2)} \simeq \beta_{\ell}(R) [(1/\ell) (dI/ds)]_{(R)}$ . For second-order interactions the changes in action, energy and pitch angle are proportional to  $\epsilon_i^{1/2}$ .

Second-order resonances require that the inhomogeneity of the magnetic field be compensated by wave frequency variations along the field line [Dysthe, 1971; Nunn, 1974]. By considering (27) and (28), we require that for second-order interactions,  $\alpha_{\ell} \rightarrow 0$ , which leads to the frequency variation along the field line as

$$\frac{1}{\omega} \frac{d\omega}{ds} = \frac{\gamma_R}{\ell h} \sqrt{\frac{h-1}{1-\mu h}} \left[ \frac{2\ell}{\gamma_R} \sqrt{1-\mu h} - \Lambda(L, \nu) \mu \right] \quad (39)$$

where  $\Lambda(L, \nu)$  is defined after (29), and we have taken  $d\eta_{||}/ds = 0$ .

## 6. Numerical Calculations

### 6.1. Resonance Condition

In this section we present some applications of the test particle theory to plasma sheet electrons in the geomagnetic shell  $L = 5.5$ . The dipole magnetic field at the equator is  $B(L) = B_0 L^{-3}$ , where  $B_0 = 3.1 \times 10^4$  nT, and the equatorial electron gyrofrequency is  $\Omega_e(L) = 0.33 \times 10^5$  s<sup>-1</sup>. We take two values for the ratio between the electron plasma and the equatorial cyclotron frequencies,  $\omega_p/\Omega_e(L) = 3$  and 1.5. The width of the resonant cone is  $\theta_c = 3.25^\circ$ . Calculations were conducted for the four frequencies  $\omega/\Omega_e(L) = 0.45, 0.55, 0.75$ , and 0.85. We assume that the waves have a coherent spectrum of finite frequency bandwidth, as occurs in the chorus and triggered emissions [Helliwell, 1967].

Figure 2 plots the energies of resonant electrons in keV versus  $\cos \phi$ , where  $\phi$  is the angle between the wave vector and the geomagnetic field. We take four values for  $\omega/\Omega_e(L)$  as indicated in Figures 2A–2D, and  $\omega_p/\Omega_e(L) = 3$ . The maximum geomagnetic latitude is  $5^\circ$ , which corresponds to  $h_M = 1.035$ . The electron energies represent solutions for the resonance condition as given in (10). The value for  $\theta_M$  is obtained from  $\cos \theta_M = (1 - \mu_c h_M)^{1/2} (1 + f_L) (-h_M + f_L)^{-1}$ . For the frequencies  $\omega/\Omega_e(L) = 0.45$  and 0.55, we consider the two harmonics  $\ell = 0$  and 1; for the frequencies  $\omega/\Omega_e(L) = 0.75$  and 0.85, we represent only the first harmonic,  $\ell = 1$ . We see that for  $\omega/\Omega_e(L) < 0.5$ , the Landau resonance  $\ell = 0$  interacts with lower-energy particles than the first harmonic  $\ell = 1$ . For  $\omega/\Omega_e(L) > 0.5$  the first harmonic reaches lower-energy electrons than the Landau resonance. However, as we

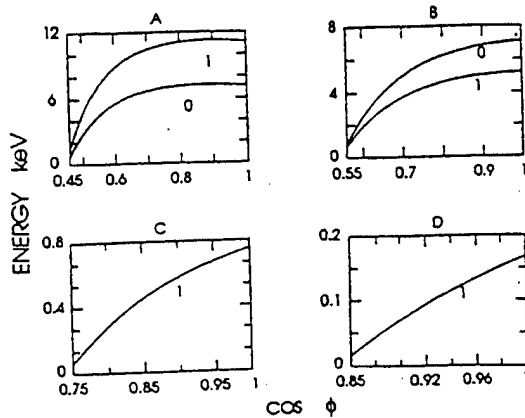


Figure 2. Electron energy in keV versus  $\cos \phi$ , using the ratio  $\omega_p/\Omega_e(L) = 3$ . The frequency ratios  $\omega/\Omega_e(L)$  is equal to (A) 0.45, (B) 0.55, (C) 0.75, and (D) 0.85. Figures 2A and 2B describe the cyclotron harmonics  $\ell = 0$  and 1, as indicated next to the curves. Figures 2C and 2D use only the first harmonic  $\ell = 1$ .

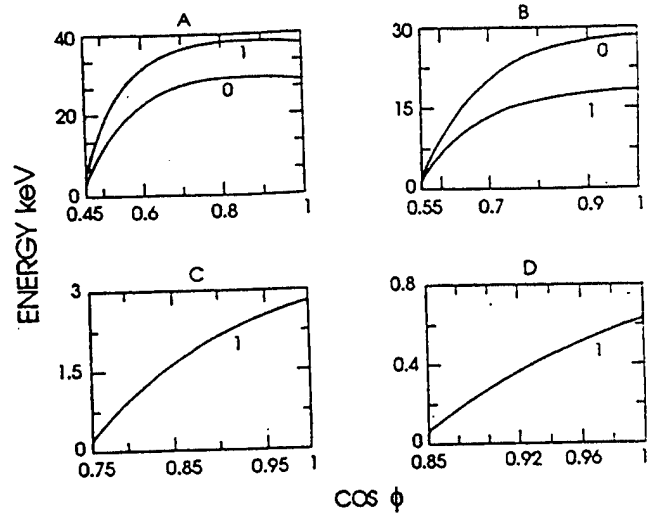


Figure 3. Electron energy in keV versus  $\cos \phi$ , using the ratio  $\omega_p/\Omega_e(L) = 1.5$ . The frequency ratios  $\omega/\Omega_e(L)$  is equal to (A) 0.45, (B) 0.55, (C) 0.75, and (D) 0.85. Figures 3A and 3B describe the cyclotron harmonics  $\ell = 0$  and 1, as indicated next to the curves. Figures 3C and 3D use only the first harmonic  $\ell = 1$ .

show below, only the first harmonic couples efficiently with low energy electrons. We also observe that for waves to interact with electrons of energy of  $< 1$  keV their angles of propagation  $\phi$  must get closer to the resonance angle  $\phi_r$ . Also, if  $\omega \rightarrow \Omega_e(L)$ , then the electron energy decreases below 1 keV.

Figure 3 shows similar calculations considering the ratio  $\omega_p/\Omega_e(L) = 1.5$ . Other parameters do not change. We observe that for all the panels the electron energy is much larger than in the case shown in Figure 2. This is because as  $\omega_p/\Omega_e(L)$  decreases,  $\eta$  also does as given in (1), which leads to larger values of the electron energies.

Next let us consider (11). Given  $\theta_M$ , we solve (11) for  $h_M$  as a function of the electron energy  $\gamma R$  and the loss cone angle  $\mu_c = \sin^2 \theta_c$ . For the  $\ell = 1$  harmonic we obtain

$$h_M = \alpha_M + \left\{ \alpha_M^2 - \hat{f}_L^2 + \frac{(\hat{f}_L - 1)^2}{1 - \mu_M} \right\}^{1/2} \quad (40)$$

$$\alpha_M = \hat{f}_L - \frac{\mu_c}{2(1 - \mu_M)} (\hat{f}_L - 1)^2$$

where  $\hat{f}_L = f_L \gamma_R$  and  $f_L = \omega/\Omega_e(L)$ . This is the same as (12), but now  $\mu = \mu_c$ . Equation (40) defines the range of geomagnetic latitudes at which the electron whistler interactions take place,  $1 \leq h \leq h_M$ , as a function of the resonant equatorial pitch angles whose extension is  $\mu_c \leq \mu \leq \mu_M$ . Note that as  $\hat{f}_L \rightarrow 1$ , the  $h_M \rightarrow \hat{f}_L$ . Thus, as the wave frequency approaches  $\Omega_e$  the electrons and waves interact very near the equator for all values of  $\mu_M$ .

Figure 4 shows the geomagnetic latitude  $\Lambda$  versus resonant equatorial pitch angles  $\theta_M$ . The latitudes are obtained by solving (40) and taking  $\Lambda = (9/2)^{1/2} (h_M$

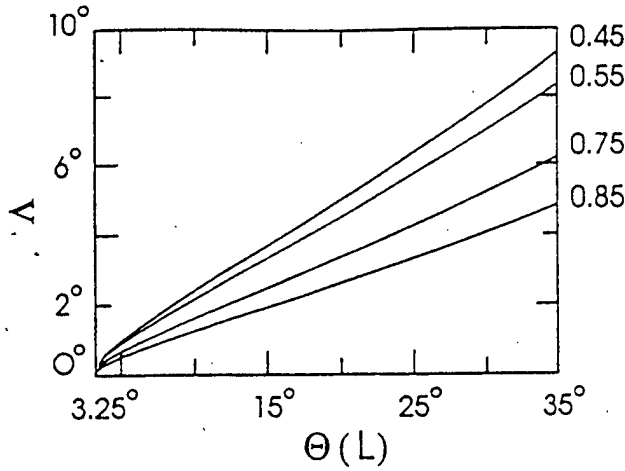


Figure 4. Geomagnetic latitudes  $\Delta$  versus equatorial pitch angles  $\theta(L)$  in degrees. The four curves correspond to the indicated frequency ratios  $\omega/\Omega_e(L)$ .

$1)^{1/2}$ . Because the electron energies are small, we assume that  $\gamma_R = 1$ . We present the four cases  $\omega/\Omega_e(L) = 0.45, 0.55, 0.75$ , and  $0.85$ . As  $\omega \rightarrow \Omega_e(L)$ , the interactions get closer to the equator, and  $h_M \rightarrow 1$ . Figure 4 also shows that for interactions occurring within  $1^\circ$  of the magnetic equator, the range in equatorial pitch angles starting at the loss cone angle is  $\sim 3^\circ$ . Then  $\Delta s = (h_M - 1)^{1/2} = 0.037$ , and the frequency variation as obtained from (39) is small. Note that as  $h \rightarrow 1$ ,  $d\omega/ds \rightarrow 0$ .

## 6.2. Hamiltonian Equations

We now present numerical calculations based on sections 4 and 5 for the geomagnetic shell  $L = 5.5$ . Consider the case  $\omega_p/\Omega_e(L) = 3$ , which gives lower resonant-energy results than if  $\omega_p/\Omega_e(L) = 1.5$ . We again use the four frequencies  $\omega/\Omega_e(L) = 0.45, 0.55, 0.75$ , and  $0.85$ . A wave amplitude of  $10^{-6} \text{ V m}^{-1}$  applies to all examples.

Figure 5 represents the change in equatorial pitch angle  $\Delta\theta_L$  versus the pitch angle in degrees for second-order interactions. The change in pitch angle is obtained by combining (34) through (38), where in (37)  $\Delta\mu = \sin(2\theta_L) \Delta\theta_L$ . We assume that the wave frequency changes along the field line according to (39). Figures 5A–5D correspond to the four frequency ratios. In each panel we represent three values for  $\cos\phi$  as indicated.

Figure 5A, shows the frequency ratio  $\omega/\Omega_e(L) = 0.45$  for the three propagation angles  $\cos\phi = 0.46, 0.5$ , and  $0.999$ ; the corresponding energies of the resonant electrons are 1, 5, and 11 keV. Figure 5B represents the frequency ratio  $\omega/\Omega_e(L) = 0.55$  at three propagation angles  $\cos\phi = 0.56, 0.6$ , and  $0.999$ ; the corresponding resonant energies are 0.4, 1.75, and 5.5 keV. Figure 5C represents the frequency ratio  $\omega/\Omega_e(L) = 0.75$  at three propagation angles  $\cos\phi = 0.78, 0.88$ , and  $0.999$ ; the corresponding resonant energies are 140, 470, and 700 eV. Figure 5D represents the frequency ratio  $\omega/\Omega_e(L) = 0.85$  at three propagation angles  $\cos\phi = 0.86, 0.88$ , and  $0.999$ ; the corresponding resonant energies are 13,

36, and 135 eV. The extensions of the resonant regions along the field line are  $\Delta = 6.3^\circ, 5.7^\circ, 4.3^\circ$ , and  $3.3^\circ$  in Figures 5A, 5B, 5C, and 5D, respectively.

Second-order interactions require frequency variations along the field line given by (39). Thus, for very monochromatic waves the resonance region may extend  $< 1^\circ$  from the magnetic equator. As a matter of fact, if waves are to interact with electrons whose resonant pitch angles are such that  $\theta_c (= 3.25^\circ) \leq \theta_L \leq 6.5^\circ$ , then the interaction region along the field line extends for  $1.4^\circ, 1.25^\circ, 1.0^\circ$ , and  $0.75^\circ$ , corresponding to the frequency ratios  $\omega/\Omega_e(L) = 0.45, 0.55, 0.75$ , and  $0.85$ , respectively.

Calculations have also been conducted for  $\omega_p/\Omega_e(L) = 1.5$ . The changes in pitch angles for all cases are about 30% less efficient than those presented in Figure 5. We have also made calculations for the Landau resonance  $\ell = 0$ , assuming that near the equator  $d\eta_{||}/ds = 0$  to obtain from (28)

$$\alpha_o = -\frac{\gamma_R}{\kappa p_{||}} \sqrt{\frac{h-1}{1-\mu h}} \Delta(L, v) \mu \quad (41)$$

The magnetic inhomogeneity is uncompensated by frequency variations. In addition, because  $\ell = 0$ ,  $\Delta\mu = -2\gamma_R(\gamma_R^2 - 1)^{-1} \mu \Delta\gamma_R$ . Near the loss cone,  $\mu \sim \mu_c$ , and  $\Delta\mu$  is small.

Figure 6 shows the normalized changes in energy as  $\Delta\gamma_R(\gamma_R - 1)^{-1}$  versus resonant equatorial pitch angles. Figures 6A, 6B, 6C, and 6D correspond to the four different frequency ratios indicated. Each panel of Figure 6 shows same three propagation angles as in Figure 5. The corresponding energies for each panel and for each propagation angle are defined in Figure 5. The changes in energy are obtained as in (36), by assuming that the

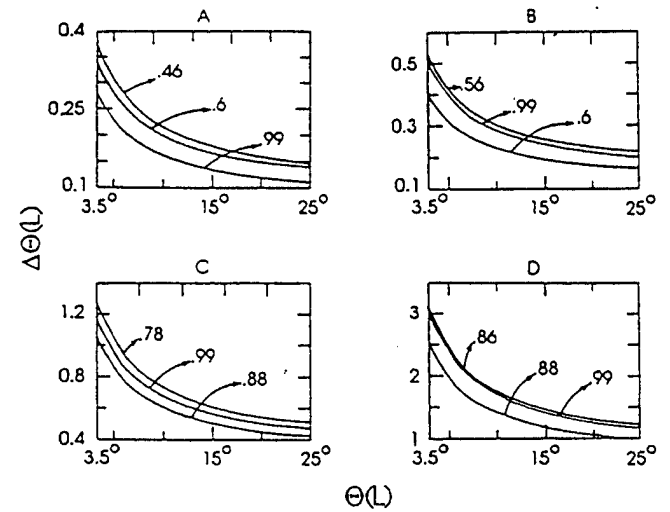


Figure 5. Change in pitch angle  $\Delta\theta(L)$  versus  $\theta(L)$  due to second-order resonant interactions at the first cyclotron harmonic, with  $\omega_p/\Omega_e(L) = 3$ . The frequency ratios  $\omega/\Omega_e(L)$  is equal to (A) 0.45, (B) 0.55, (C) 0.75, and (D) 0.85. Numbers next to the curves correspond to values of  $\cos\phi$ . The resonant energies as functions of  $\cos\phi$  and the frequency ratio are discussed in the text.

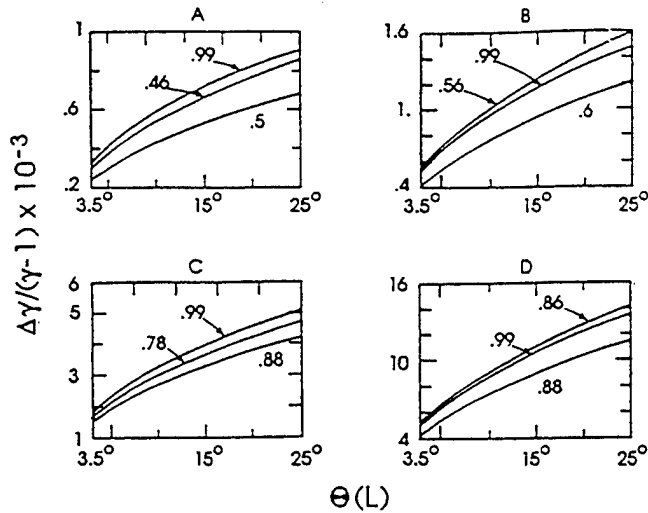


Figure 6. Normalized change in the electron resonant energy  $\Delta\gamma_R (\gamma_R - 1)^{-1}$  versus  $\theta(L)$  for second-order resonant interactions at the first cyclotron harmonic, with  $\omega_p/\Omega_e(L) = 3$ . The ratio  $\omega/\Omega_e(L)$  is equal to (A) 0.45, (B) 0.55, (C) 0.75, and (D) 0.85. Numbers next to the curves refer to different values of  $\cos \phi$ . Resonant energies are given in the text.

second-order resonance condition is satisfied and that the frequency variation along the field line is as given in (39). Note that as  $\omega \rightarrow \Omega_e(L)$ , larger changes in energies are calculated than for smaller values of the ratio  $\omega/\Omega_e(L)$ . For example, for  $\omega/\Omega_e(L) = 0.45$  and  $\Delta\gamma_R (\gamma_R - 1)^{-1} = 10^{-3}$ , there is an energy change of 1 eV for every 1 keV of the electron's initial energy. If  $\omega/\Omega_e(L) = 0.85$  and  $\Delta\gamma_R (\gamma_R - 1)^{-1} = 16 \times 10^{-3}$ , we obtain a change of 16 eV for every 1 keV.

The electrons maintain resonance with the waves over a certain time interval,  $\Delta t$ , over which the phase change of the resonant electron with respect to the wave remains less than, say,  $\pi/2$ . By integrating (27) twice for second-order resonant electrons we obtain,

$$\Delta t = \frac{\pi}{\omega} \left| \gamma_R - \frac{\Omega_e(L)}{\omega} \right| \frac{1}{\eta_{\parallel}^2 - 1} \frac{\gamma_R - 1}{\Delta\gamma_R} \frac{1}{p^2} \quad (42)$$

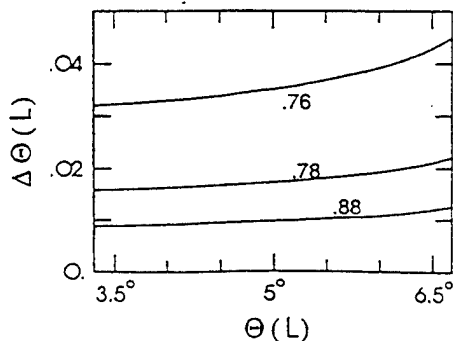


Figure 7. Change in pitch angles  $\Delta\theta(L)$  versus equatorial pitch angles  $\theta(L)$  due to first-order interactions at the first cyclotron harmonic. We use  $\omega/\Omega_e(L) = 0.75$ . Numbers next to the curves refer to values of  $\cos \phi$ .

The time duration as obtained from (42) is consistent with resonance lengths that correspond to  $1^\circ$  to  $3^\circ$  latitude from the equator.

Figure 7 shows the change in pitch angle versus initial pitch angle for first-order resonant electrons. The wave frequency remains constant along the field line. Thus  $\alpha_L$  is finite but at the equator where  $h = 1$ ,  $\alpha_L = 0$ . The changes in pitch angle and energy are linear with the electric field amplitudes. We take the example  $\omega/\Omega_e(L) = 0.75$ . The three angles of propagation are  $\cos \phi = 0.76, 0.78, 0.88$ , and the corresponding resonant energies are 165 eV, 466 eV and 1.5 keV, respectively. The wave amplitude is  $10^{-6} \text{ V m}^{-1}$ . We see that first-order resonant interactions do not give electron scattering as strong as when second-order resonance conditions prevail.

## 7. Summary and Conclusions

We have presented a test particle theory for the interactions of whistler mode waves with  $< 10$ -keV electrons near the equatorial plasma sheet. A Hamiltonian formulation has been developed for interactions with a coherent spectrum of multiple-frequency waves such as those found in the natural chorus emissions. The main results are as follows:

1. Efficient whistler-electron interactions require that the ratios between the wave and the equatorial electron frequencies be such that  $\omega/\Omega_e(L) \geq 0.5$ . For waves propagating near the resonance cone and for  $\omega \rightarrow \Omega_e(L)$ , resonant energies are  $< 1$  keV.

2. We establish a mapping between the resonant, equatorial pitch angles and the geomagnetic latitudes where the resonances take place. For interactions that occur within  $1^\circ$  of the magnetic equator, the range of resonant pitch angles extends about  $3^\circ$  from the edge of the loss cone.

3. Second-order resonant interactions require that inhomogeneities of the magnetic field be compensated by wave frequency variations. In this way, electrons and waves stay in gyroresonance for relatively long distances along the field line. Within a few degrees of the magnetic equator the required frequency variations are small, and the wave spectrum is relatively narrow.

4. Numerical calculations have been conducted for the  $L = 5.5$  shell. As an example we considered wave amplitudes of  $10^{-6} \text{ V m}^{-1}$ , consistent with observations from the CRRES satellite. Changes in pitch angle can be  $> 1^\circ$  for electrons with pitch angles near the edge of the loss cone. This means that the waves can scatter electrons into the atmospheric loss cone very efficiently. Thus whistler-electron interactions are viable explanations of the nearly isotropic precipitation of low-energy electrons from the plasma sheet to form the diffuse aurora.

**Acknowledgments.** This work has been supported by the U.S. Air Force under contract with Northeastern University, F19628-92-K-0007, and the Air Force Office of Scientific Research, task 2311PL03. We are grateful to David A.

Hardy of the Phillips Laboratory, for suggesting this problem.

The Editor thanks D. W. Swift and R. Skoug for their assistance in evaluating this paper.

## References

- Albert, J. M., Cyclotron resonance in an inhomogeneous magnetic field, *Phys. Fluids B*, 5, 2744, 1993.
- Bell, T. F., The nonlinear gyroresonance interaction between energetic electrons and coherent VLF waves propagating at an arbitrary angle with respect to the Earth's magnetic field, *J. Geophys. Res.*, 89, 905, 1984.
- Belmont, G., D. Fontaine, and P. Canu, Are equatorial electron cyclotron waves responsible for diffuse auroral electron precipitation?, *J. Geophys. Res.*, 88, 9163, 1983.
- Bespalov, P. A., and V. Y. Trakhtengerts, Cyclotron instability of Earth radiation belts, *Rev. Plasma Phys.*, 10, 155, 1986.
- Burke, W. J., A. G. Rubin, D. A. Hardy, and E. G. Holeman, Banded electron structures in the plasmasphere, *J. Geophys. Res.*, in press, 1995.
- Burtis, W. J., and R. A. Helliwell, Magnetospheric chorus: Occurrence patterns and normalized frequency, *J. Geophys. Res.*, 80, 1007, 1976.
- Davidson, G. T., Pitch angle diffusion in morningside aurorae, 1, The role of the loss cone in the formation of impulsive bursts precipitation, *J. Geophys. Res.*, 91, 4413, 1986a.
- Davidson, G. T., Pitch angle diffusion in morningside aurorae, 2, The formation of repetitive auroral pulsations, precipitation, *J. Geophys. Res.*, 91, 4429, 1986b.
- Davidson, G. T., and Y. T. Chiu, A nonlinear model of wave-particle interactions in the trapped radiation belts: Auroral pulsation solutions, *Geophys. Res. Lett.*, 14, 1166, 1987.
- Dysthe, K. B., Some studies of triggered whistler emissions, *J. Geophys. Res.*, 76, 6915, 1971.
- Ginet, G. P., and M. Heinemann, Test particle acceleration by small amplitude electromagnetic waves in a uniform magnetic field, *Phys. Fluids B*, 2, 700, 1990.
- Hardy, D. A., W. J. Burke, and E. Villalón, Electron dispersion events in the morningside auroral zone and their relationship with VLF emissions, *J. Geophys. Res.*, 95, 6451, 1990.
- Hashimoto, K., and I. Kimura, A generation mechanism of narrow-band hiss emissions above one half the electron cyclotron frequency in the outer magnetosphere, *J. Geophys. Res.*, 86, 11,148, 1981.
- Helliwell, R. A., A theory of discrete VLF emissions from the magnetosphere, *J. Geophys. Res.*, 72, 4773, 1967.
- Helliwell, R. A., 40 years of whistlers, *Mod. Radio Sci.*, 189, 1993.
- Inan, U. S., and T. F. Bell, Pitch angle scattering of energetic particles by oblique whistler waves, *Geophys. Res. Lett.*, 18, 49, 1991.
- Inan, U. S., Y. T. Chiu, and G. T. Davidson, Whistler-mode chorus and morningside aurorae, *Geophys. Res. Lett.*, 19, 653, 1992.
- Jasna, D., U. S. Inan, and T. F. Bell, Precipitation of suprathermal electrons by oblique whistler waves, *Geophys. Res. Lett.*, 19, 1639, 1992.
- Johnstone, A. D., The mechanism of pulsating aurora, *Ann. Geophys.*, 1, 4, 397, 1983.
- Johnstone, A. D., D. M. Walton, R. Liu, and D. A. Hardy, Pitch angle diffusion of low-energy electrons by whistler-mode waves, *J. Geophys. Res.*, 98, 5959, 1993.
- Kennel, C. F., and H. E. Petschek, Limit on stably trapped particle fluxes, *J. Geophys. Res.*, 71, 1, 1966.
- Lyons, L. R., and D. J. Williams, *Quantitative Aspects of Magnetospheric Physics*, D. Reidel, Norwell, Mass., 1984.
- Nunn, D., A self-consistent theory of triggered VLF emissions, *Planet. Space Sci.*, 22, 349, 1974.
- Ohmi, N., and M. Hayakawa, On the generation of quasi-electrostatic half-electron-gyrofrequency VLF emissions in the magnetosphere, *J. Plasma Phys.*, 35, 351, 1986.
- Parks, G. K., Microburst precipitation phenomena, *J. Geomagn. Geoelectr.*, 30, 327, 1978.
- Roberts C. S., and S. J. Buchsbaum, Motion of a charged particle in a constant magnetic field and a transverse electromagnetic wave propagating along a field, *Phys. Rev. A*, 135, 381, 1964.
- Roeder, J. L., and H. C. Koons, A survey of electron cyclotron waves in the magnetosphere and the diffuse auroral electron precipitation, *J. Geophys. Res.*, 94, 2529, 1989.
- Rosenberg, T. J., J. C. Siren, D. L. Matthews, K. Marthinsen, J. A. Holtet, A. Egeland, D. L. Carpenter, and R. A. Helliwell, Conjugacy of electron microbursts and VLF chorus, *J. Geophys. Res.*, 86, 5819, 1981.
- Sazhin, S. S., *Whistler-Mode Waves in a Hot Plasma*, Cambridge Atmos. and Space Sci. Ser., Cambridge Univ. Press, New York, 1993.
- Sazhin, S. S., and M. Hayakawa, Magnetospheric chorus emissions: A Review, *Planet. Space Sci.*, 40, 681, 1992.
- Swift, D. W., Mechanism for auroral precipitation: A review, *Rev. Geophys.*, 19, 185, 1981.
- Villalón, E., and W. J. Burke, Near-equatorial pitch angle diffusion of energetic electrons by oblique whistler waves, *J. Geophys. Res.*, 96, 9655, 1991.
- Villalón, E., and W. J. Burke, Proton whistler interactions near the equator in the radiation belts, *J. Geophys. Res.*, 98, 13,509, 1993.
- Villalón, E., W. J. Burke, P. L. Rothwell, and M. B. Silevitch, Quasi-linear wave particle interactions in the Earth's radiation belts, *J. Geophys. Res.*, 94, 15,243, 1989.

W. J. Burke, Space Science Division, Phillips Laboratory/ GPSG, Hanscom Air Force Base, MA 01731. (e-mail: burke@zircon.plh.af.mil)

E. Villalón, Center for Electromagnetics Research, Northeastern University, Boston, MA 02115. (e-mail: villalon@zircon.plh.af.mil)

(Received January 27, 1995; revised April 3, 1995; accepted April 4, 1995.)

# Theory of quasi-monochromatic whistler wave generation in the inner plasma sheet

Elena Villalón

Center for Electromagnetics Research, Northeastern University, Boston, Massachusetts

William J. Burke

Phillips Laboratory, Hanscom Air Force Base, Massachusetts

## Abstract.

Nonlinear interactions between plasma sheet electrons and nearly monochromatic whistler wave packets are studied. The theory applies to the generation of chorus emissions from quasi-monochromatic wavelets observed in the plasma sheet at the top of the ELF/VLF hiss band. The hiss-triggered chorus is produced by step-like deformations that develop in distribution functions at the boundaries between resonant and nonresonant electrons. Equations are obtained describing the wave amplitudes and frequency-time characteristics for propagation at small angles with respect to the geomagnetic field. The linear resonant interactions leading to wavelet generation are investigated. The resonant wave frequencies change along the field lines to compensate for geomagnetic field inhomogeneities. If the electric fields exceed the amplitudes of those in the background plasmapheric hiss ( $\gg 10^{-6}$  V/m), electrons become trapped in phase space, and their distribution functions develop plateaus whose extents are proportional to the square roots of electric field amplitudes. Nonlinear currents generated by the trapped electrons are studied to obtain analytical representations of the growth rates and frequency spreads. Numerical examples are presented to illustrate our theoretical analysis.

## 1. Introduction

Magnetospheric plasmas are rich sources of wave-generating processes that reflect linear and nonlinear interactions with the energetic electrons [Sazhin and Hayakawa, 1992]. The purpose of this report is to describe quantitatively the origin of a class of waves that pitch angle scatter electrons from the inner plasma sheet into the high-latitude ionosphere to form the diffuse aurora [Lui et al., 1973; Meng et al., 1979; Schumaker et al., 1989]. Actually, two classes of waves have been suggested to explain the required pitch angle diffusion: electrostatic electron cyclotron harmonic (ECH) waves [e.g., Lyons, 1974] and electromagnetic whistler waves [e.g., Inan et al., 1992; Johnstone et al., 1993]. Although both types of wave can interact resonantly with electrons in the plasma sheet, both explanations have their difficulties. The intensities of ECH waves strongly peak within  $\pm 3^\circ$  of the magnetic equator [Paranicas et al., 1992]. However, most of the time observed amplitudes appear too weak to maintain strong pitch angle diffusion [Belmont et al., 1983; Roeder and Koons, 1989].

For waves whose frequencies  $\omega$  are much smaller than the electron cyclotron frequency and that propagate along the field lines,  $\phi = 0^\circ$ , the resonant energies  $K_R > 10$  keV. Thus initial enthusiasm for adapting the model of Kennel and Petschek [1966] to explain auroral precipitation from the inner plasma sheet was damped by the realization that a critical parameter, the magnetic energy per particle  $K_c$ , was higher than the average energies of plasma sheet electrons. Here  $K_c = m_e c^2 / 2 (\Omega_e / \omega_p \cos \phi)^2$ , where  $m_e c^2$  is the electron rest energy, the  $\omega_p$  and  $\Omega_e$  are the electrons plasma frequencies and gyrofrequencies, respectively. However, recent studies have demonstrated the continued relevance of this mechanism. Johnstone et al. [1993] and Villalón and Burke [1995] argued that whistlers with frequencies greater than half the electron cyclotron frequency  $\Omega_e$  and angle of propagation  $\phi$  oblique to the geomagnetic field can pitch angle scatter low-energy electrons from the plasma sheet. This also results from

$$K_R = K_c \left[ \frac{\Omega_e(L)}{\omega} \cos \phi - 1 \right] \left[ 1 - \frac{\omega \gamma_R}{\Omega_e(L)} \right]^2 \quad (1)$$

since as  $\cos \phi \rightarrow \omega / \Omega_e$ , the resonant energy  $K_R \rightarrow 0$ , regardless of the magnitude of  $K_c$ .

We mainly consider the generation of hiss-triggered chorus in the inner plasma sheet, where the cold plasma population that sustains wave propagation has a den-



sity of a few particles per cubic centimeter [Koons, 1981; Higel and Wu, 1984]. The free energy for chorus generation comes from electrons with energy  $> 10$  keV, and the waves propagate at close angles to the geomagnetic field. After the waves are generated, they may propagate at large angles and interact with the low-energy electrons ( $< 10$  keV) that form the diffuse aurora. The chorus elements appear to grow out of monochromatic, coherent wavelets with frequencies near the upper edge of the hiss band. *Hattori et al.* [1991, Figure 2], reproduced as Figure 1 herein, shows the connection between the chorus emissions and the wavelets in the ELF band of frequencies. It illustrates the causative relationship between the chorus elements arising from by the wavelets immersed in the background, plasma sheet hiss. In the ELF/VLF range of frequencies, hiss-triggered chorus have frequencies larger than  $\sim 0.2 f_{ce}$ . For frequencies below  $\sim 0.5 f_{ce}$ , chorus waves propagate at angles close to the magnetic field direction [Hayakawa et al., 1984]. At frequencies above  $\sim 0.5 f_{ce}$ , chorus propagates close to the direction of the resonance cone [Muto et al., 1987]. Finally, we note that chorus emissions are most commonly detected after substorms in the midnight through morning sectors of the magnetosphere [Tsurutani and Smith, 1974, 1977] and are closely linked with microburst precipitation of electrons with energies  $\geq 20$  keV [Parks, 1978].

Whistler waves that propagate at large angles to the geomagnetic field interact with the warm (500 eV – 20 keV) plasma sheet electrons, causing them to precipitate into the ionosphere where they excite diffuse auroral emissions [Rosenberg et al., 1981]. *Hardy et al.* [1990, Figure 3], show that diffuse auroral electrons in the morning sector frequently have energy-time disper-

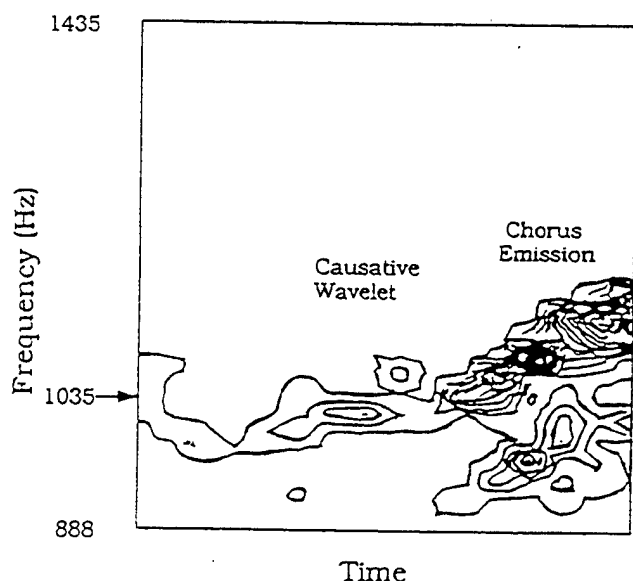


Figure 1. Representation of a frequency-time spectrogram with chorus emissions growing from wavelets at the top of the hiss band. The example is taken from *Hattori et al.* [1991].

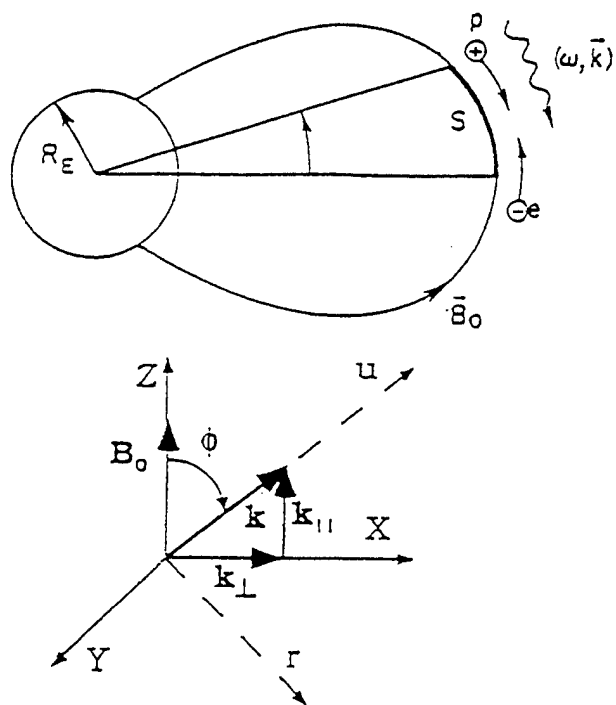


Figure 2. Schematic representation of a whistler wave of frequency  $(\omega, k)$  interacting with the electrons. The Earth's dipole magnetic field is  $B_0$ , and  $Z$  and  $s$  are coordinates along the flux tube.

sion characteristics similar to the frequency-time characteristics of chorus. On the basis of first-order resonance theory, *Inan et al.* [1992] suggested a direct connection between morning sector, diffuse auroral precipitation, and chorus-type whistlers. *Villalón and Burke* [1995] showed that second-order, resonant interactions between the warm electrons and coherent waves propagating at upper band chorus frequencies and large angles to the geomagnetic field produce very efficient pitch-angle scattering. This paper investigates the origin of these waves.

The inner plasma sheet hiss grows through linear interactions with the energetic electrons, causing the resonant electrons to pitch angle scatter. The resonance condition is

$$\omega - \ell \Omega_e / \gamma_R - k_{\parallel} v_{\parallel} = 0 \quad (2)$$

where  $(\omega, k)$  are the wave frequency and propagation vector, respectively, and  $k_{\parallel}$  is the component of  $k$  parallel to the geomagnetic field. The harmonic number is  $\ell = 0, \pm 1, \pm 2, \dots$ ; here we study resonance interaction for the first harmonic  $\ell = 1$ . The component of electron velocity parallel to the magnetic field is  $v_{\parallel}$ , and  $\gamma_R$  is the relativistic factor for resonant electrons. The electron gyrofrequency  $\Omega_e = 2\pi f_{ce}$  varies with normalized distance  $s = Z/r_L$  along the field line, where  $r_L = R_E L \sqrt{2/3}$ . The geometry of the interaction is represented in Figure 2. In the case of hiss generation,  $\Omega_e \gg \omega$ , and the interaction is most effective near the equator where magnetic field inhomogeneities are less

severe than at higher latitudes. In the equatorial region we approximate the geomagnetic field variation as parabolic:

$$h = \frac{\Omega_e(s)}{\Omega_e(L)} = 1 + s^2 \quad (3)$$

where  $L$  denotes value of a parameter at the equator  $s = 0$ . Next, define  $\mu = \sin^2 \theta(L)$ , where  $\theta(L)$  is the equatorial pitch angle. The pitch angles of resonant electrons fall in a range such that  $\mu_c < \mu < \mu_*$ . Here  $\mu_c$  corresponds to the pitch angle at the boundary of the loss cone, which is the same for all electrons, and  $\mu_* = \sin^2 \theta_*$  refers to the upper limit of equatorial pitch angle that satisfies (2). It varies with the energy (momentum) of the resonant electrons.

As a concrete example, we approximate chorus emerging from the top of the hiss band, as having frequencies  $\Omega_e/\omega \leq 2.75$ . For the magnetic shell  $L = 5.5$ , the loss cone is  $\theta_c \sim 3.5^\circ$ . We further assume that a wavelet grows near  $\Omega_e/\omega = 2.75$ , and that the ratio between the plasma and cyclotron frequencies is  $\omega_p/\Omega_e = 3$ . We obtain that  $\theta_* \rightarrow \theta_c$ , for electrons whose energies are  $\sim 20$  keV. For 50 keV electrons, with the plasma parameters defined above,  $\theta_* \simeq 45^\circ$ . As illustrated in Figure 3a, interaction with hiss waves causes a step-like deformation to develop in the electron distribution function near the separatrix between resonant and non-resonant electrons ( $\mu = \mu_*$ ). The location of the step depends on the electron momentum.

Nunn and Sazhin [1991] and later, Trakhtengerts *et al.* [1996], showed that these step-like deformations efficiently produce coherent wavelets at the top of the hiss band. The wavelets are wave packets with small

but finite frequency widths, and their growth rates are obtained in an inhomogeneous plasma. However, Nunn and Sazhin [1991] and Trakhtengerts [1996] do not allow for variations of the resonant wave frequencies with distance along the magnetic field. In this paper we improve on their estimates for growth rates by allowing a resonant electron to interact with different frequencies within a wave packet as it moves away from the equator, as to compensate for magnetic field inhomogeneities. Wave growths turn out to be very large, and the interactions become nonlinear as the electric field amplitudes increase. The nonlinear interactions yield trapping of electrons in the potential wells of the wave electric field amplitudes and subsequent chorus emissions emerging from the wavelets.

In our derivations we conclude that the wave electric fields amplitudes which are required for nonlinear interactions with the electrons are obtained as functions of normalized parameters. These are the normalized electric fields amplitudes  $\varepsilon = |q|E/m_e c \omega$  and  $\kappa = c/\tau_L \Omega_e(L) \ll 1$ . Typically for magnetic shells  $L = 5.5, 6.5$   $\kappa = 4.5 \times 10^{-4}$  and  $6.3 \times 10^{-4}$ , respectively. We show that for nonlinear interactions the electric fields must exceed values such that  $\varepsilon \sim \kappa^2$ . These estimates are consistent with experimental observations [Koons, 1981], which assume electric fields  $\sim 10^{-5}$  V/m. Owing to large electric field amplitudes, the resonant interactions become nonlinear and then the electrons are trapped. We define the relative phase angle  $\xi$  as the angle between the wave electric field  $E_\perp$  and the electron perpendicular velocity  $v_\perp$  in the transverse plane perpendicular to the geomagnetic field  $B_0$ . The electron

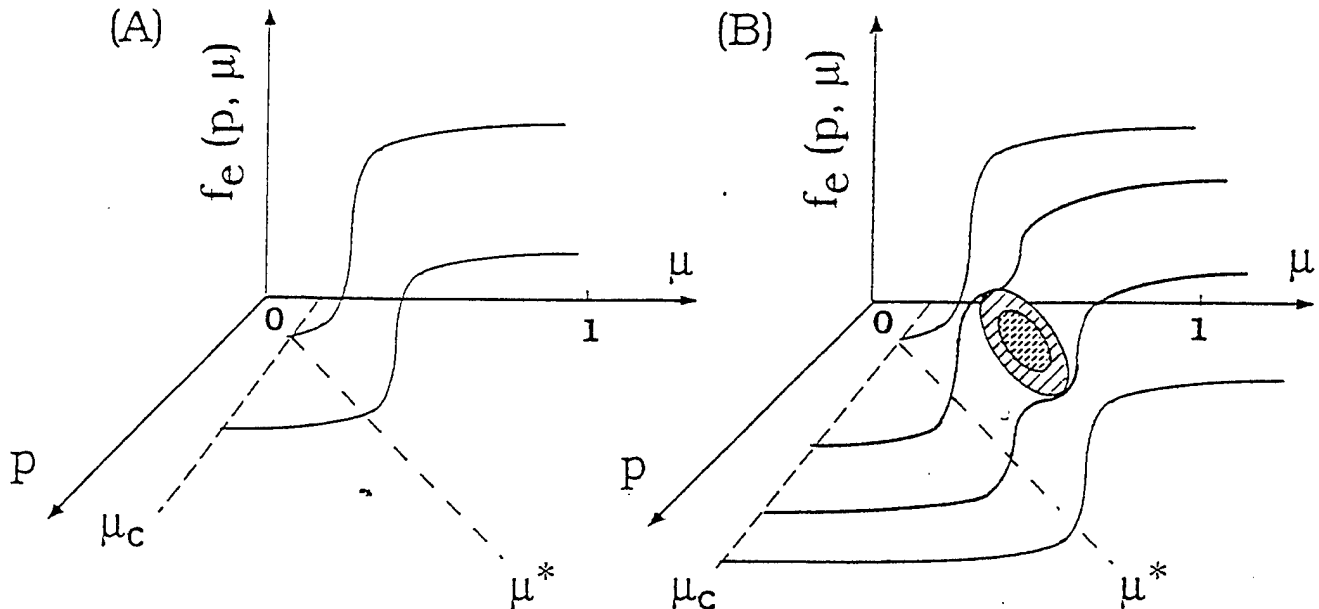


Figure 3. Distribution function of resonant electrons for a given momentum  $p$ , as a function of  $\mu = \sin^2 \theta(L)$ , where  $\theta(L)$  is the equatorial pitch angle. Resonant electrons are confined to the range  $\mu_c \leq \mu \leq \mu_*$ , which depends on  $p$ . (a) The step-like deformation develops an interior plateau owing to (b) particle trapping in the region where the resonant pitch angles are such that  $\mu_* \sim \mu_T$ .

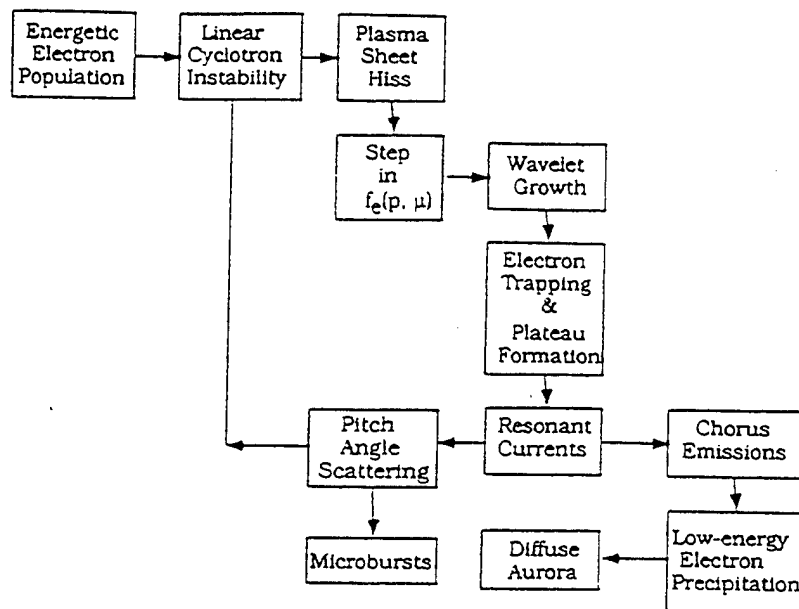


Figure 4. Flowchart representing processes leading to quasi-monochromatic wavelet generation and subsequent chorus radiation and diffuse aurora precipitation.

kinetic energy changes as  $dK/dt = q\mathbf{E} \cdot \mathbf{v}$ , where  $q$  is the electron charge. For the waves to grow from their interactions with the electrons,  $\xi \simeq 0$ . Trapped electrons satisfy the resonance condition in (2), and their angle  $\xi$  is bounded around the second-order resonance angle [Omura *et al.*, 1991], which depends on the plasma inhomogeneities; it is always near  $\xi = \pi/2$ . They remain in resonance with the waves over long distances along the field lines.

The large electric field amplitudes of wavelets preferably trap the electrons which are near the resonance boundary  $\mu = \mu_*$ . We conclude that energies for trapped electrons are those that maximize the growth rates at wavelet frequencies near the top of the hiss band. As a result, plateaus form in the distribution function for those electrons interacting with frequencies of maximum growth [Galeev and Sagdeev, 1979]. From the examples presented here, the plateaus are located near pitch angles such  $\mu_* = \mu_T \sim 0.5$ , so that for frequencies of maximum growth the generated wavelets are at the top of the hiss band. The extent of the plateau is proportional to the square roots of the electric field amplitudes (see Figure 3b). The trapped electrons diffuse toward smaller pitch angles over times which are of the order of the phase correlation between the waves and the electrons. As the plateaus disappear owing to diffusion, the distribution function reverts to its initial, step-like shape. The time for phase correlation is approximately the period of bound oscillations for electrons in the electric field potentials of the wavelets signals [Sudan and Ott, 1971].

The trapped electrons create nonlinear, resonant currents similar to those associated with triggered emissions in the plasmasphere [Dysthe, 1971]. The resonant currents act as antennas to emit chorus waves. The roles of resonant currents for artificially triggering emissions

in the plasmasphere have been studied by a number of authors; see, for example, Helliwell [1967] and Nunn [1974]. Here we adopt these concepts to study chorus emissions, triggered by the electrons trapped in hiss wavelets. Experimental results presented by Hattori *et al.* [1991, Figure 2] and Koons [1981, Figure 2], show that wavelet generation and associated chorus emissions last a few tenths of a second.

Figure 4 contains a flowchart representing the evolution of the cyclotron instabilities which are due to energetic electron populations injected into the inner plasma sheet during substorms. The reservoir of free energy is provided by the energetic electron distribution functions which drive the generation of waves and microburst precipitation. These processes follow the sequence of (1) creation of the plasma sheet ELF/VLF hiss which leads to the formation of a step in the energetic electron distribution function, (2) quasi-monochromatic wavelet generations, (3) particle trapping by the large electric fields of the wavelets which yields nonlinear currents, (4) chorus emissions, (5) microburst precipitation which is a result of these linear and nonlinear interactions with the energetic electrons ( $> 20$  keV), and (6) the diffuse aurora precipitation which is when for large propagation angles the chorus interacts with warm electrons ( $< 10$  keV). The position on the flowchart then reverts to the background plasma sheet waves and the step in the distribution functions created by these waves. The physical processes repeat themselves after a substorm injection for as long as the energetic electron population that sustains the background hiss is present in the magnetosphere. In this paper we investigate wavelets and chorus generation as steps (2–4) of the flowchart.

The paper is organized as follows. Section 2 contains a set of equations describing the temporal and spatial evolution of the electric fields propagating at small an-

gles with respect to the geomagnetic field. Section 3 summarizes the Hamiltonian formulation for a single particle interacting with the waves as developed in a previous article by Villalón and Burke [1995]. Here we represent the evolution of the relative phase angle as a function of the magnetic field inhomogeneities, the frequency variation, and the electric fields of the waves. Conditions for phase trapping are given. Section 4 studies the growth of the wavelets near the top of the hiss band due to step-like deformations of distribution functions at the boundary between resonant and nonresonant electrons. Section 5 investigates the nonlinear currents of trapped electrons that generate the frequency bandwidths. Section 6 shows some numerical examples. Section 7 contains the summary and conclusions. The appendix describes particle trapping and plateau formation.

## 2. The Wave Fields Equations

We take a coordinate system  $(Z, X, Y)$ , in which  $Z$  is along the geomagnetic field and  $X$  and  $Y$  are perpendicular to the field (see Figure 2). We consider a quasi-monochromatic wave packet of central frequency  $\omega$  and wave vector  $k$  which propagates in the  $Z-X$  plane at an angle  $\phi$  with respect to the geomagnetic field. The frequency bandwidth of the wavelet  $\Delta\omega_l$  is such that  $\Delta\omega_l/\omega < 1$ . We define another coordinate system  $(u, r, Y)$ , with  $k$  along  $u$  and  $r$  perpendicular to it.

The electric field of the waves is represented by  $\mathbf{E} = (E_X, E_Y, E_Z)$ , and the magnetic field is represented by:  $\mathbf{B} = (B_X, B_Y, B_Z)$ . We define

$$\begin{aligned} E_{\perp}(u, t) &= -\sin\phi E_Z + \cos\phi E_X + i E_Y \\ &= \mathcal{E}_{\perp} \exp[-i(ku - \omega t)] \\ E_u(u, t) &= \sin\phi E_X + \cos\phi E_Z \\ &= \mathcal{E}_u \exp[-i(ku - \omega t)] \end{aligned} \quad (4)$$

Similar equations may be written for  $B_{\perp}$  in terms of  $B_{X,Y,Z}$  and  $\phi$  and  $B_u$ . We also write  $E_j = \mathcal{E}_j \exp[-i(ku - \omega t)]$ , where the index  $j = X, Y, Z$ .

Maxwell equations are

$$\begin{aligned} \frac{\partial E_{\perp}}{\partial u} &= \frac{i}{c} \frac{\partial B_{\perp}}{\partial t} \\ \frac{\partial B_{\perp}}{\partial u} &= -\frac{i}{c} \frac{\partial E_{\perp}}{\partial t} - i \frac{4\pi}{c} (\mathcal{J}_{res} + \mathcal{J}_c)_{\perp} \end{aligned} \quad (5)$$

The term proportional to  $(\mathcal{J}_{res} + \mathcal{J}_c)_{\perp}$  in (5) corresponds to the perpendicular components of the resonant and cold plasma currents which are defined similarly to  $E_{\perp}$  in (4) as functions of  $\mathcal{J}_X, \mathcal{J}_Y$ , and  $\mathcal{J}_Z$ . The cold plasma current satisfies [Nunn, 1974]:

$$\left[ \frac{\partial}{\partial t} - i\Omega_e \cos\phi \right] \mathcal{J}_{c,\perp} = \frac{\omega_p^2}{4\pi} E_{\perp} + i\Omega_e \sin\phi \mathcal{J}_{c,u} \quad (6)$$

where  $\Omega_e$  and  $\omega_p$  are the electron cyclotron and plasma frequencies, respectively. The contribution of the cold plasma current component  $\mathcal{J}_{c,u} = \cos\phi \mathcal{J}_{c,Z} + \sin\phi \mathcal{J}_{c,X}$

is proportional to  $\sin^2\phi$  and may be ignored for waves that propagate at small angles to the geomagnetic field.

Combining (4) to (6) and assuming propagation close to the magnetic field lines, we obtain the equation for the wave field:

$$\begin{aligned} (\mathcal{A}_R - i\mathcal{A}_I) \mathcal{E}_{\perp} + B \frac{\partial \mathcal{E}_{\perp}}{\partial Z} + \mathcal{K} \frac{\partial \mathcal{E}_{\perp}}{\partial t} \\ = Q \mathcal{J}_{res,\perp} \exp[i(k_{\parallel} Z - \omega t)] \end{aligned} \quad (7)$$

where the resonant current and other parameters are

$$\begin{aligned} \mathcal{J}_{res,\perp} &= q \int_0^{\infty} v_{\perp} dv_{\perp} \int_{-\infty}^{+\infty} dv_{\parallel} \int_0^{2\pi} d\xi V_{\perp} \delta F \\ \mathcal{A}_R &= (\omega - \Omega_e \cos\phi) \frac{dk_{\parallel}}{dZ} \\ \mathcal{A}_I &= (\omega - \Omega_e \cos\phi) (k^2 - \omega^2/c^2) + \omega_p^2 \omega/c^2 \\ B &= 2k_{\parallel} (\omega - \Omega_e \cos\phi) \\ \mathcal{K} &= \frac{2\omega}{c^2} (\omega - \Omega_e \cos\phi) - k^2 - \frac{\omega_p^2 - \omega^2}{c^2} \\ Q &= -\frac{4\pi}{c^2} \omega (\omega - \Omega_e \cos\phi) \end{aligned} \quad (8)$$

Note that the cold plasma whistler dispersion relation is obtained by setting  $\mathcal{A}_I = 0$ . The resonant current is defined in terms of the components  $v_{X,Y,Z}$  of the electron velocity as  $V_{\perp} = -\sin\phi v_Z + \cos\phi v_X + i v_Y$  and the first-order correction to the electron distribution function  $\delta F$  which is linear in the electric field amplitudes.

We write  $\mathcal{E}_{\perp} = |\mathcal{E}_{\perp}| \exp(i\varphi)$  and  $\mathcal{J}_{res,\perp} \exp[i(k_{\parallel} Z - \omega t)] = \mathcal{S}_{\perp} \exp(i\varphi)$ . Here  $\varphi$  is a nonlinear phase spread due to the wavelet's interaction with resonant, trapped electrons. The dimensionless components of the electric field amplitudes are ( $j = X, Y, Z$ ):

$$\varepsilon_j = \frac{|q| |\mathcal{E}_j|}{m_e c \omega} \quad (9)$$

then  $\mathcal{E}_{\perp}$  becomes  $\varepsilon_{\perp}$  and the normalized total wave energy  $\mathcal{W}_k$  is

$$\mathcal{W}_k = -\frac{\mathcal{K}}{Q} \frac{|\varepsilon_{\perp}|^2}{4} = \eta^2 \frac{\Omega_e/\omega \cos\phi}{\Omega_e/\omega \cos\phi - 1} \frac{|\varepsilon_{\perp}|^2}{16\pi} \quad (10)$$

The parallel component of the group velocity is

$$v_{g,\parallel} = \frac{B}{\mathcal{K}} = \frac{c}{\eta_{\parallel}} \frac{\Omega_e/\omega \cos\phi - 1}{\Omega_e/\omega \cos\phi} (\cos^2\phi + 1) \quad (11)$$

where  $\eta = ck/\omega$  is the refractive index and  $\eta_{\parallel} = \eta \cos\phi$ .

From Maxwell equations we obtain for the electric field amplitudes and frequency wave bands

$$\begin{aligned} \frac{\mathcal{A}_R}{\mathcal{K}} + \frac{v_{g,\parallel}}{|\varepsilon_{\perp}|} \frac{\partial |\varepsilon_{\perp}|}{\partial Z} + \frac{1}{|\varepsilon_{\perp}|} \frac{\partial |\varepsilon_{\perp}|}{\partial t} \\ = -2\pi \frac{(j_{\perp} \varepsilon_{\perp}^* + j_{\perp}^* \varepsilon_{\perp})}{16\pi \mathcal{W}_k} \\ -\frac{\mathcal{A}_I}{\mathcal{K}} + v_{g,\parallel} \frac{\partial \varphi}{\partial Z} + \frac{\partial \varphi}{\partial t} \\ = 2\pi \frac{i(j_{\perp} \varepsilon_{\perp}^* - j_{\perp}^* \varepsilon_{\perp})}{16\pi \mathcal{W}_k} \end{aligned} \quad (12)$$

where  $j_{\perp} = |q|S_{\perp}/m_e\omega$ . The frequency bandwidth of the chorus emissions is obtained from the nonlinear phase shift as  $\delta\omega = (\partial\phi/\partial t)$  and the wave vector as  $\delta k_{\parallel} = -(\partial\phi/\partial Z)$ . Let us define

$$\gamma^* = -4\pi \frac{\epsilon_1^* j_{\perp}}{16\pi W_k} \quad (13)$$

The right-hand sides of both equations in (12) are obtained by taking the real and imaginary parts of  $\gamma^*$ , respectively. Here  $\gamma^* = \gamma_G + i(\delta\omega - v_{g,\parallel}\delta k_{\parallel})$  and  $\gamma_G$  is the growth rate.

### 3. Single Particle Interaction

We define the normalized time  $\tau = t\Omega_e(L)$  and length  $s = Z/\tau_L$  as introduced in section 1 and define the relative phase angle between a wave and an electron:

$$\xi_L = \ell \tan^{-1}\left(\frac{P_Y}{P_X}\right) + \int_0^s r_L k_{\parallel} ds' - \frac{\omega \tau}{\Omega_e(L)} \quad (14)$$

where  $P_{X,Y}$  are dimensionless canonical momenta in the  $X, Y$  directions; the canonical action is [Villalón and Burke, 1995]  $I = [\Omega(L)/2\Omega(s)] [P_X^2 + P_Y^2]$ . Differentiating (14) with respect to  $s$ , the length along the field line, to zero order in the electric field amplitudes gives

$$\frac{d\xi_L}{ds} \equiv \frac{d\xi_L}{ds}(\omega, \mu, p) = r_L k_{\parallel} + \frac{\ell\Omega_e(s) - \omega \gamma_R}{\Omega_e(L) \kappa P_{\parallel}} \quad (15)$$

where  $\kappa = c/\tau_L\Omega_e(L) \ll 1$ ,  $\mu = \sin^2\theta(L)$ , and  $\theta(L)$  is the equatorial pitch angle. For resonant electrons  $d\xi_L/ds = 0$ , which leads to the condition (2). We shall consider wave-electron interactions at the  $\ell = 1$  harmonic and then  $\xi_L = \xi$  and assume that the wave frequency spectrum is such that  $\omega_b \leq \omega \leq \omega_T$ . Here  $\omega_T$  is at the top of the hiss band,  $\omega_b$  is a lower frequency in the hiss band, and the bandwidth of the wavelet is obtained as  $\Delta\omega_l = \omega_T - \omega_b$ . The upper frequency  $\omega_T$  is shown in section 4 to be the frequency of maximum growth. We also assume that the resonant wave frequency for a given electron changes along the field line according to the linear approximation:

$$\frac{1}{\omega_T} \frac{d\omega}{ds} = \chi \sqrt{h-1} \quad (16)$$

The resonant interactions extend along the field lines for  $1 \leq h \leq h_m$ . Note that  $\chi$  is defined in terms of the wave frequency spectrum  $\Delta\omega_l$  and the extent of resonant interaction as  $\chi = 2(h_m - 1)^{-1} \Delta\omega_l/\omega_T$ . For a given electron we require that interactions take place with different frequencies within the wave packet so it stays in resonance,  $d\xi/ds = 0$ , over long distances in  $s$ . Thus the resonant wave frequencies change along the field lines within the bandwidth of the wavelet  $\Delta\omega_l$  so as to compensate for magnetic field inhomogeneities.

To first order in the wave electric field amplitudes, the time-dependent Hamiltonian is

$$\mathcal{H} = \gamma_R - \frac{P}{\gamma_R} \sum_{\ell=-\infty}^{+\infty} \Upsilon_{\ell}(I, P_{\parallel}, s) \sin \xi_L \quad (17)$$

where  $P = \sqrt{\gamma_R^2 - 1}$ ,  $\gamma_R$  is the relativistic factor, and

$$\Upsilon_{\ell} = \frac{P_{\parallel}}{P} \epsilon_3 \mathcal{J}_{\ell}(k_{\perp}r) - \frac{1}{2P} \sqrt{2I \frac{\Omega}{\Omega(L)}} \cdot [(\epsilon_1 + \epsilon_2) \mathcal{J}_{\ell-1}(a) + (\epsilon_1 - \epsilon_2) \mathcal{J}_{\ell+1}(a)] \quad (18)$$

where the symbol  $\mathcal{J}$  represent Bessel functions whose arguments  $a = k_{\perp}r$  and  $r$ , the Larmor radius, is given as  $r = (c/\Omega_e) [2I\Omega_e/\Omega_e(L)]^{1/2}$ , where  $I$  is the dimensionless action; for  $\ell = 1$  we write  $\Upsilon_{\ell} = \Upsilon$ .

The equatorial cyclotron resonance condition for the  $\ell = 1$  harmonic is denoted by  $d\xi_L(\omega, \mu, p)/ds = 0$  and may be obtained from (15) by replacing  $\Omega_e(s)$  by  $\Omega_e(L)$ . For resonant electrons the equations of motion for the canonical variables reduce to those of the physical variables at the resonance. Then  $p_{\parallel} \leq p_{\parallel,cr}$ , where  $p_{\parallel,cr}$  satisfies the resonant condition  $d\xi_L/ds = 0$  for  $\omega = \omega_b$ . The range of resonant pitch angles are such that  $\mu_c \leq \mu \leq \mu_T$ , where  $\mu_c$  corresponds to the loss cone boundary. For given particle momentum  $p$  and frequency  $\omega$  we obtain from (2)

$$\mu(p, \omega) = 1 - \left[ \frac{1 - \gamma_R \omega / \Omega_e(L)}{p \eta_{\parallel} \omega / \Omega_e(L)} \right]^2 \quad (19)$$

where  $p = \gamma_R v/c$  is the normalized momentum. The upper boundary  $\mu_T$  is obtained from (19) setting  $\omega = \omega_T$ , a frequency at the top of the hiss band. In addition, if  $\omega_T$  is also the frequency that maximizes the growth rate (see section 4), then electrons satisfying the resonance condition in (19) have pitch angles such that  $\mu_T \sim 0.5$  and their momenta are obtained in terms of  $\omega_T$  and  $\mu_T$ . Owing to the interactions with the plasma sheet hiss, the electron distribution function eventually develops a step-like deformation near  $\theta(L) = \theta_T \sim \pi/4$ , the boundary between resonant and nonresonant electrons for the frequency which is at the top of the hiss and maximizes the growth rate. For given  $p$  and pitch angles  $\mu < \mu_T$ , the equatorial cyclotron resonance condition for the  $\ell = 1$  harmonic  $d\xi_L(\omega, \mu, p)/ds = 0$  is satisfied for resonant frequencies  $\omega < \omega_T$  decreasing with  $\mu$ .

Owing to the formation of the plasma sheet hiss, the distribution function of resonant electrons is depleted for  $\mu \leq \mu_b$ , where  $\mu_c \leq \mu_b \leq \mu_T$ . The distribution function has a step-like deformation at the boundary of resonant and nonresonant electrons. The size of the step is approximately  $\delta\mu = \mu_T - \mu_b$ , which is related to the bandwidth of the wavelet as shown next. Then the lower limit of resonant frequencies  $\omega = \omega_b$  is obtained from (19) by setting  $\mu = \mu_b$ . We define  $f_b, \tau = \omega_b, \tau/\Omega_e(L)$  and  $\Delta f_l \equiv \Delta\omega_l/\Omega_e(L) = f_T - f_b$ . The bandwidth of the wavelet  $\Delta f_l$  may be obtained as a function of momentum  $p$  and  $\omega_T$  solving for

$$\begin{aligned} \delta\mu \beta_*(p) &= [f_b^{-1} \cos \phi - 1] [1 - f_b]^2 \\ &\quad - [f_T^{-1} \cos \phi - 1] [1 - f_T]^2 \\ \beta_*(p) &= \left[ \frac{\omega_p \cos \phi}{\Omega_e(L)} p \right]^2 \end{aligned} \quad (20)$$

Note that  $\Delta f_i$  increases with increasing  $\delta\mu = \mu_T - \mu_b$ ,  $\beta_*$ , which increases with particle energy, and cold plasma density. The maximum value that  $\Delta f_i$  and  $\Delta\omega_i$  may take for fixed  $\mu_T$  is obtained setting  $\mu_b = \mu_c$ , which yields upper limits for the bandwidths of wavelets. As matter of fact, approximately we find that  $\Delta f \sim (\delta\mu) \beta_* f_T^2 / (1 - 3f_T^2)$ . By moving away from the equator,  $\Omega_e(s)$  increases, and for fixed values of  $p$  and  $\omega$ , pitch angles satisfying the local resonance condition must decrease with increasing distance  $s$ . On the other hand, if  $p$  and  $\mu$  are fixed, the parallel momentum  $p_{\parallel} = p(1 - \mu h)^{1/2}$  decreases and  $\Omega_e$  increases with  $s$ , then  $\omega$  must also increase to keep in resonance with the electrons.

Next we differentiate (15) with respect to  $s$  and combine it with the equations of motion presented by Villalón and Burke [1995]. The second derivative of the relative phase of whistlers and resonant electrons represents the deviation from the resonance condition due to the inhomogeneities of the geomagnetic field which we refer to as  $\alpha$  and a finite electric field amplitude contained in the term we call  $\rho$

$$\begin{aligned} \frac{d^2 \xi_L}{ds^2} &= \alpha + \rho \cos \xi_L \\ \rho &= \frac{\beta}{\kappa} \frac{p}{p_{\parallel}} \Upsilon(I, p_{\parallel}, s) \end{aligned} \quad (21)$$

Here

$$\begin{aligned} \alpha &= s \lambda(h, \theta) \\ \lambda(h, \theta) &= \frac{1}{\kappa p_{\parallel}} (-h\chi + 2\ell) \end{aligned} \quad (22)$$

$$+ \frac{1}{\kappa p_{\parallel}} \tan^2 \theta \left[ 1 - \gamma_R \frac{\omega}{\Omega_e(s)} \right] \quad (23)$$

$$\beta = \frac{1}{\kappa p_{\parallel}} (\eta_{\parallel}^2 - 1) \left[ \frac{\omega}{\Omega_e(L)} \right]^2 \quad (24)$$

where we assume that  $d\eta_{\parallel}/ds = 0$ , which establishes a relation between the variation of  $k_{\parallel}$  and  $\omega(s)$  along the field lines. Here  $\theta$  is the particle pitch angle and  $\theta(L)$  is its equatorial value. The normalized electric field amplitudes contribute to  $\rho$  in (21), as  $\Upsilon/\kappa^2$ . Given that  $\kappa^2 \ll 1$ , the normalized electric fields must be of the order of  $\kappa^2 \sim 10^{-7}$  to make significant contributions to the interactions.

From (22) we have that at  $h = 1$ ,  $\alpha = 0$ . In addition, we also require that  $\alpha = 0$  for  $h = h_m$  and for the pitch angle  $\theta_*$  at the boundary between resonant and nonresonant particles, which is a function of frequency and resonant energy as obtained from (19). By taking  $\omega = \omega_T$ , which is a frequency at the top of the hiss band that maximizes the growth rate, then  $\theta_*$  becomes  $\theta_T$ . For interactions occurring near the equator, we obtained the following relation between  $\chi$ ,  $\theta_*$ , and  $h_m$ :

$$\left( 1 - \gamma_R \frac{\omega}{h_m \Omega_e(L)} \right) \tan^2 \theta_* = \chi h_m - 2 \quad (25)$$

Note that as  $\tan \theta_* \gg 1$ , then  $\chi \gg 1$ . Then the mis-

match function  $\lambda$ , which represents the deviation from the second-order resonance condition  $d^2 \xi/ds^2 = 0$  due to the plasma inhomogeneities, approximately is

$$\lambda \simeq \mathcal{D} [\tan^2 \theta - \tan^2 \theta_*] \quad (26)$$

$$\mathcal{D} = \frac{1}{\kappa} \frac{\eta_{\parallel}}{\Omega_e} \simeq \frac{1}{\kappa} \frac{\omega_p/\Omega_e}{[\Omega_e/\omega \cos \phi - 1]^{1/2}} \quad (27)$$

All pitch angles  $\mu_c \leq \mu \leq \mu_T$  contribute to the interactions. Note also that  $\mathcal{D} > \kappa^{-1} \gg 1$ , and then unless  $\theta \rightarrow \theta_*$ , the inhomogeneity factor  $\lambda \gg 1$ . For  $\theta \simeq \theta_*$  and for waves that propagate near the resonance cone angle, we get  $\lambda \rightarrow 0$ .

Now we make a Taylor expansion of the phase angle  $\xi$  around the resonant point  $s - s_R$ ,

$$\xi = \xi^{(0)} + \xi^{(1)}(s - s_R) + \xi^{(2)}(s - s_R)^2/2 + \xi^{(3)}(s - s_R)^3/3 \quad (28)$$

Since  $\xi$  is the angle between the wave electric field and the electron perpendicular velocity, maximum wave growth is achieved near  $\xi = 0^\circ$ . When  $\xi$  is near  $\pi/2$ , the wave magnetic field and the resonant current are aligned [Omura and Matsumoto, 1982] and one expects large modification on the wave frequencies. In sections 4 and 5 we study the two cases  $\xi \simeq 0^\circ$  and  $\xi \simeq \pi/2$ , respectively. This is because for wavelet generation we need maximum growth of the electric fields when  $\xi = 0^\circ$ . In addition, second-order resonant interactions, besides satisfying the resonance condition in (19), the phase angle  $\cos \xi \simeq -\alpha/\rho$ . Near  $\theta \sim \theta_*$ , the inhomogeneity factor  $\lambda \rightarrow 0$ , and we find that for second-order resonant electrons,  $\xi^{(0)} = \pi/2$ . Particle trapping is realized only under conditions of second-order interactions [Omura et al., 1991]. Thus the frequency shifts that lead to the chorus emissions must be found under the conditions of second-order interactions.

In the case of the plasma sheet hiss, the electric fields amplitudes are small (i.e.,  $\Upsilon/\kappa^2 < 1$ ), so we take  $\rho \ll \alpha$ , and the electrons cannot be trapped by the waves. However, there may exist wavelets at the top of the hiss band for which the wave frequency spectrum is very coherent. The wavelets may grow near the equator, owing to the inhomogeneity of the magnetic field, which is compensated by the changes of the resonant frequency along the field lines, and as a result,  $\alpha \simeq 0$ . According to previous results by Villalón and Burke [1995], the maximum exchange of energy between waves and particles take place near the angle  $\xi^{(0)} = 0$ . In this case we may approximate (28) by

$$\xi = \frac{\rho}{2} s^2 + \frac{1}{6} \lambda(h, \theta) s^3 \quad (29)$$

since as  $\lambda(h, \theta) \rightarrow 0$ , (i.e.,  $\theta \rightarrow \theta_*$ ), we need to consider the contribution of the electric fields.

For particles with  $\theta(L)$  near  $\theta_*$ , the inhomogeneity factor  $\alpha$  is very small and is actually zero at  $h = 1$  and  $h_m$ , which means that the waves can efficiently trap the electrons. Electrons trapped by the waves must satisfy the condition  $\rho \gg \alpha$ , where  $\rho$  and  $\alpha$  are given in (21)

and (22). By multiplying both sides of (21) by  $d\xi/ds$  and integrating once we obtain

$$\frac{1}{2} \left( \frac{d\xi}{ds} \right)^2 = C + \int \alpha \frac{d\xi}{ds} ds + \rho \sin \xi \quad (30)$$

where  $C$  is a constant of integration. Since  $s \ll \rho/\lambda$ , particle trapping is easily realized for sufficiently large electric field amplitudes (say,  $\sim 10^{-5}$  V/m) and for smaller values of  $\lambda(h, \theta)$  as defined in (23). For those electrons whose pitch angles are near the jump of the distribution function at  $\theta(L) = \theta_*$ ,  $\lambda$  is very small. Thus we may expect strong particle trapping for the resonant electrons near the jump boundary. For electrons trapped near the phase-stationary point at the bottom of the wave electric field potential wells, we may approximate

$$\xi = \frac{\pi}{2} + \sqrt{2} |\rho|^{1/2} s + \left[ \sqrt{2} |\rho|^{3/2} + \frac{1}{2} \lambda(h, \theta) \right] \frac{s^3}{3} \quad (31)$$

#### 4. Wavelets Growth Rates

In this section we investigate the growth of quasi-monochromatic waves at the top of the hiss band. The resonant frequency bandwidth  $\Delta\omega_r$  is defined in (20) as a function of the step in pitch angle  $\delta\mu = \mu_T - \mu_b$  owing to deformations in electron distribution functions at the boundary between resonant and nonresonant electrons. The hiss waves initially grow owing to their linear interactions with electrons satisfying the resonance condition (19) and eventually cause distribution functions to develop step-like deformations in  $\mu$  which depends on the electron energy and  $f_T$  on the top frequency in the hiss band. The theory of wave growth is described next, considering the inhomogeneity of the Earth magnetic field

We normalized the particle momentum  $p$  to  $(m_e c)^{-1}$ , the velocity  $v$  to  $c^{-1}$ , and the distance  $s$  to  $r_L^{-1}$ . The coupling coefficient between waves and electrons in (13) is obtained in terms of the resonant current which is defined in (8). One shows from the linearized Vlasov's and Maxwell's equations that the first-order correction to the distribution function of resonant particles  $\delta F$  is a function of the zero order distribution function  $F$  as defined below in (34) and (35) and depends linearly on the electric field amplitudes of the waves [Omura and Matsumoto, 1982]. In an inhomogeneous plasma the growth rate as defined by taking the real part of (13) is obtained from the following expression [Bespalov and Trakhtengerts, 1986]

$$\frac{\gamma^*}{\Omega_e(L)} = \frac{\omega_p^2}{\Omega_e(L)^2} \frac{1}{N_e} \int_0^{+\infty} \gamma_R p dp \int_{+\mu_c}^{\mu_T} (hd\mu) \left( \frac{p}{p_{||}} \right)^2 \frac{\Upsilon^2}{16\pi \mathcal{W}_k} \Lambda(p_{||}, \theta) \mathcal{O}F \quad (32)$$

where

$$\mathcal{O}F = \frac{p}{2} \frac{\partial F}{\partial p} + \left[ \frac{\mathcal{L}\Omega_e(L)}{\gamma_R \omega} - \mu \right] \frac{\partial F}{\partial \mu}$$

$$\Lambda = \frac{2\pi}{\kappa} \int_{-\infty}^{+\infty} ds \int_{-\infty}^{+\infty} ds' \exp[-i\Phi(s, s')] \quad (33)$$

where  $\Phi(s, s') = \int_s^{s'} d\bar{s} (d\xi/d\bar{s})$ . In a homogeneous plasma we obtain from the Dirac delta function [Lyons and Williams, 1984],  $\Lambda \rightarrow 2\pi^2 \kappa^{-1} \delta(d\xi/ds)$ , which near resonance gives the contribution  $\Lambda \equiv 4\pi^2 (1 - h\mu) [\Omega_e(L)/\omega \eta_{||}]$ .

Next, call  $z = h\mu$  and, locally, the distribution function is given by

$$F = G(x, \delta\mu) F_0(p_{\perp}, p_{||})$$

$$G = \frac{1}{2} g_1(z) (\tanh z + 1) - \frac{1}{2} g_2(z) (\tanh z - 1) \quad (34)$$

where  $z = 2[\mu_T(p) - \mu]/\delta\mu$  and  $\delta\mu$  is the size of the step deformation. For  $\mu \leq \mu_b$ , then  $G \rightarrow g_1(x)$ , and for  $\mu \geq \mu_T + \delta\mu$ , then  $G \rightarrow g_2(x)$ . If we take the limit  $\mu_b \rightarrow \mu_T$ , i.e.,  $\delta\mu \rightarrow 0$ , then we recover the step function used by Nunn and Sazhin [1991].

Here we approximate  $F_0$  by a bi-Maxwellian distribution of thermal momenta  $\alpha_{\perp}$  and  $\alpha_{||}$ . The anisotropy parameter is denoted by  $A$ , and the mean energy is approached by  $\langle p^2 \rangle = (A + 1) \alpha_{\perp} + \alpha_{||}$ . Following the normalization of Trakhtengerts et al. [1996], we write

$$F_0 = C_A \left( \frac{p_{\perp}^2}{\alpha_{\perp}} \right)^A \exp \left[ -\frac{p_{||}^2}{\alpha_{||}} - \frac{p_{\perp}^2}{\alpha_{\perp}} \right]$$

$$C_A = \frac{n_h}{\pi^{3/2} \Gamma(A + 1) \alpha_{\perp} \alpha_{||}^{1/2}} \quad (35)$$

where  $n_h$  is the density of energetic particle. It reflects the anisotropy and the mean energy that represent the hot electrons population in the plasma sheet. The functions  $g_{1,2}(x)$  are pitch angle eigenfunctions of the diffusion operator. Here  $g_2(x)$  represents the part of the distribution function that does not interact with the waves and then  $g_2 \sim 1$ . The pitch angle eigenfunction  $g_1(x)$  results from considering the effects of the plasma sheet hiss in the resonant part of the distribution function. Eventually, it becomes  $g_2 \ll 1$  as the resonant particles diffuse into the loss cone owing to the interactions.

Next introduce the operator  $\mathcal{O}F = (\mathcal{O}F)_1 + (\mathcal{O}F)_2$ . Here  $(\mathcal{O}F)_1$  represents the part of the distribution function that does not depend on the step deformation and which originates the plasma sheet hiss. The operator  $(\mathcal{O}F)_2$  acts over the step deformation of the distribution function in (34) as described by the functions  $\tanh z$ , and it is responsible for the generation of the wavelets at the top of the hiss band. From (33) we obtain

$$(\mathcal{O}F)_2 = F_0 \frac{1}{\delta\mu} \left( \frac{1}{\cosh z} \right)^2 [g_1(x) - g_2(x)]$$

$$\left[ \frac{\Omega_e(L)}{\gamma_R \omega} h - 1 - h(\mu - \mu_T) \right]$$

$$(OF)_1 = G(OF_0) + \frac{1}{2} F_0 (\tanh z + 1) (OG_1) - \frac{1}{2} F_0 (\tanh z - 1) (OG_2) \quad (36)$$

In what follows we study wavelet generation and then only consider the contribution of the step as represented by  $(OF)_2$  and ignore  $(OF)_1$ . This means we do not investigate the generation of the hiss band. Thus when we refer to frequencies at the top of the hiss bands, we assume they are known from experimental measurements.

After integrating in  $\mu$  we approximate

$$\frac{\gamma^*}{\Omega_e(L)} = \Gamma_L \mathcal{G}(x_T, \delta\mu) \mathcal{K}_A(x_T, x_c) \quad (37)$$

$$\Gamma_L = \frac{\omega_p^2}{\Omega_e(L)^2} \frac{C_A A! \alpha_\perp}{N_c} \left( \frac{p}{p_\perp} \right)^2 \frac{1}{16\pi \mathcal{W}_k} \frac{1}{(\eta_{||} p_R) \exp[-\frac{p_R(h)^2}{\alpha_{||}}]} \quad (38)$$

Here the functions  $\mathcal{G}(x_T, \delta\mu)$  and  $\mathcal{K}_A(x_T, x_c)$  are defined by

$$\mathcal{G} \equiv \int_{x_c}^{x_T} dx \frac{g_1(x) - g_2(x)}{(x_T - x_b)(1 - x)} \Delta(p_{||}, x) \quad (39)$$

$$\mathcal{K}_A \equiv \frac{1}{2A!} \int_{y_c}^{+y_T} dy y^A \exp(-y) \quad (40)$$

By taking the limit  $x_b \rightarrow x_T$  in (39) leads to  $\mathcal{G} \rightarrow [g_1(x_T) - g_2(x_T)] (1 - x_T)^{-1} \Delta(p_{||}, x_T)$ . Also, we have  $y = p^2 z / \alpha_\perp$ , and  $y_{c,m}$  are evaluated for the resonant momenta  $p_{c,m}$ , respectively. For  $p_T$  and  $y_T$  we solve  $d\xi(\omega, \mu, p)/ds = 0$ , with  $\omega = \omega_b$  and  $\mu = \mu_T$  ( $x = x_T$ ). For  $p_c$  and  $y_c$  we solve the resonance condition for  $\omega_T$  and  $\mu_c$  ( $x = x_c$ ), so all possible resonant momenta are considered for interactions such that the frequencies and pitch angles are within the ranges ( $\omega_b \leq \omega \leq \omega_T$ ) and ( $\mu_c \leq \mu \leq \mu_T$ ), respectively.

The function  $\Delta$  is evaluated for  $p_{||} = p_R(h)$  from the resonance condition, and all other quantities appearing in (37) and (38) should be obtained for  $\mu \sim \mu_T$  near the jump boundary, which corresponds to the frequency of maximum growth  $\omega_T$ . In an inhomogeneous magnetic field the resonance condition, together with the dispersion relation for whistlers, yields the resonant momentum of the energetic particles as obtained by Kennel and Petcheski [1966]

$$p_R(h)^2 = \left[ \frac{\Omega_e(L)}{\omega_{pL} \cos \phi} \right]^2 \left[ \frac{\Omega_e(L)}{\omega} h \cos \phi - 1 \right] \left[ h - \frac{\omega \gamma_R}{\Omega_e(L)} \right]^2 \quad (41)$$

Note that (41) is the same as (1) rewritten in terms of momentum.

To obtain the growth of wavelets near the top of the hiss band, we must take the real part of (33). Next introduce the notation  $\Delta = \Delta_R + i\Delta_I$ , where  $\Delta_{R,I}$  denotes the real and imaginary parts of  $\Delta$ . If the amplitudes of the electric fields  $\mathcal{E}_\perp \rightarrow 0$ , one may ignore particle trapping, and then to achieve maximum growth, we require that  $\xi^{(0)} = 0$  in the Taylor expansion that leads to (29). Under the limit  $\rho \rightarrow 0$  we show

$$\Delta_R = \frac{\pi}{\kappa} \left| \int_{-\infty}^{+\infty} \exp[i\xi(s)] ds \right|^2 = \frac{\pi}{3\kappa} \Gamma\left(\frac{1}{3}\right)^2 \left(\frac{6}{\lambda}\right)^{2/3} \quad (42)$$

which is proportional to  $\kappa^{-1/3}$  as shown also by Trakhtengerts et al. [1996]. Following the definition in (26), we obtain

$$\Delta_R \simeq \pi \Gamma\left(\frac{1}{3}\right)^2 \mathcal{D}^{1/3} \frac{\Omega_e}{\eta_{||} \omega} \left[ \frac{1}{|\tan^2 \theta - \tan^2 \theta_T|} \right]^{2/3} \quad (43)$$

where  $\mathcal{D}$  is defined in (27) and we have taken  $\theta_* = \theta_T$ . This expression for  $\Delta_R$  assumes large values for pitch angles near the jump of the distribution function. This singularity in  $\theta = \theta_T$  is not present in the theoretical analysis of Trakhtengerts et al. [1996]. This is because we allow for the frequency of resonance to change as in (25) to compensate for the magnetic field inhomogeneities so that  $\lambda$  as approximated by (26) is very small for  $\theta \rightarrow \theta_T$ . To estimate more accurately the value of  $\Delta_R$  near  $\theta = \theta_T$ , we consider that  $\xi = \rho s^2/2$ . In this case as  $\theta \rightarrow \theta_T$ , then  $\Delta_R \rightarrow 2\pi^2/\kappa\rho$ .

The frequency of maximum growth  $f_T$  may be obtained combining (37) and (41) as a function of  $\beta_*$ , after defining  $\beta_* \equiv \beta_*(\alpha_{||})$  as in (20), and  $f = \omega/\Omega_e(L)$ . If we take  $\gamma_R \cos \phi \sim 1$  for maximum growth,  $f_T$  is approximately given by

$$f_T \equiv \frac{\omega_T}{\Omega_e(L)} \sim \frac{3 + \beta_*/2}{6\gamma_R} - \left[ \left( \frac{3 + \beta_*/2}{6\gamma_R} \right)^2 - \frac{1}{3\gamma_R^2} \right]^{1/2} \quad (44)$$

Note that for  $\beta_* \gg 1$  and for waves propagating along the field lines, then  $f_T \sim (3 + 0.5\beta_*)^{-1} \ll 1$ . When  $\beta_* \rightarrow 0$ , then  $f_T \rightarrow \cos \phi$ . As the particle momentum or plasma density increases ( $\beta_* \gg 1$ ) and the frequency of maximum growth decreases.

Next we assume that the frequency of maximum growth is given by the upper limit of the wavelet bandwidth, which is known from experimental measurements. To maximize the growth rates for frequencies at the top of the hiss band, we must obtain  $\beta_*$  in terms of  $f_T$  as follows:

$$\beta_* = \frac{2\varphi}{f_T} [\cos \phi - f_T] [1 - \gamma_R f_T]^2 \quad (45)$$

We introduce an empirical factor  $\varphi \geq 1/2$  for the purpose of the discussion that follows. Combining (45) and the resonance condition in (41) with  $h = 1$ , we find that  $\varphi = 1$  corresponds to  $\mu_T = 0.5$  and  $\varphi = 1/2$  to  $\mu_T = 0$ . Note that (45) leads to the result in (44) by



approximately solving for  $f_T < 0.5$  and setting  $\varphi = 1$ . Recall that  $\beta_*$  as in (20) is a function of the electron resonant momentum and the magnetic energy per particle. Since  $\omega_p/\Omega_e$  is given by external plasma conditions, the values that  $\beta_*$  take from (45) with  $\varphi = 1$  define a range of electron energies (momenta) that interact with waves at the top of the hiss band for pitch angles near  $\mu = 0.5$ . If the mean energy of the distribution function in (35) is smaller than the energies obtained from (45) with  $\varphi = 1$ , then one must consider other interactions as having significant contributions to maximum growth. The other interactions with less energetic particles have  $1/2 \leq \varphi < 1$  and their corresponding resonant pitch angles  $\mu < 0.5$ .

The imaginary part of  $\Lambda$  is defined as

$$\begin{aligned} \Lambda_I &= \frac{2\pi}{\kappa} \int_{-\infty}^{+\infty} ds \cos \xi(s) \int_{-\infty}^s \sin \xi(s') ds' \\ &\quad - \frac{2\pi}{\kappa} \int_{-\infty}^{+\infty} ds \sin \xi(s) \int_{-\infty}^s \cos \xi(s') ds' \\ &\simeq -\frac{2\pi}{\kappa} \int_{-\infty}^{+\infty} ds \frac{1}{(d\xi/ds)} \end{aligned} \quad (46)$$

Now we take the phase angle  $\xi = x^3 + bx^2$ , where  $x = (\lambda/6)^{1/3}s$  and  $b = (\rho/2)(6/\lambda)^{2/3}$ . This phase angle does not represent particle trapping as explained in section 3, and after substituting in (46), we obtain  $\Lambda_I = 0$ . Next we study particle trapping and chorus emissions. We have already argued that particle trapping is easily realized when the inhomogeneity factor  $\lambda \rightarrow 0$  and the stationary point for the phase angle is near  $\xi = \pi/2$ , as in the Taylor expansion (31).

The electric fields must become large enough near the boundary of the step deformation to satisfy  $\rho > (\sqrt{2}\lambda/3)^{2/3}$ . The inhomogeneity factor  $\lambda$  is estimated from (26) as function of the step in pitch angle  $\delta\mu$ , then  $\lambda(\delta\mu) = [\tan^2 \theta_* - \tan^2 \theta_b] \mathcal{D}$ . By defining  $\varepsilon_1 = 2\mu^{-1/2} \Upsilon$ , we show

$$\varepsilon_1 = \left[ \frac{4}{3} \lambda(\delta\mu) \right]^{2/3} \frac{1}{\mathcal{D}^2} \frac{1 - \gamma_R \omega / \Omega_e}{\eta_{\parallel} \omega / \Omega_e} \frac{1}{\tan \theta_*} \quad (47)$$

If normalized electric fields  $\sim \varepsilon_1$ , then particles may be trapped, which yield chorus emissions.

## 5. Nonlinear Frequency Bandwidths of Chorus Emissions

Chorus emissions are triggered by wavelets whose electric fields have reached large amplitudes to trap the electrons as in (47). The resonant interactions between trapped electrons and the wavelets are nonlinear, and they originate frequency spread that are described in this section. Owing to the interactions with the waves, the distribution function evolves toward a plateau in the region of phase space that corresponds to trapped particles [Galeev and Sagdeev, 1979]. Qualitatively, this

is shown in Figure 3 and is illustrated in the appendix. Particles are more easily trapped near the jump boundary  $\mu_*$  of the step-like distribution function because there, the electric fields are larger and the mismatch function  $\lambda(h, \theta) \simeq 0$ . Note that if we consider the wavelets near the top of the hiss band and whose frequencies  $\omega_T$  are obtained by maximizing the growth rates in terms of  $\beta_*$  as in section 4, then  $\mu_*$  becomes  $\mu_T \sim 0.5$ . Subsequently, we have that near  $x_*$ ,  $g_{1,2}$  are given in the appendix and then we approximate

$$\mathcal{G}(x_*, \Delta\mu) \rightarrow \Delta\mu [g'_1(x_*) + g'_2(x_*)] \frac{1}{(1-x_*)} \Lambda(p_{\parallel}, x_*) \quad (48)$$

where  $g'_{1,2}(x_*)$  represents the derivative of the functions  $g_{1,2}$  with respect to  $x$  and are evaluated at the jump boundary  $x_*$ . The width in pitch angle of the plateau may be estimated from (30) by taking  $C = 0$  and the length of the interaction small enough, which yields

$$\frac{\Delta\mu}{1-\mu_*} = \pm 2\sqrt{2} \frac{\kappa}{\eta_{\parallel}} \frac{\Omega_e(L)}{\omega} \rho^{1/2} \quad (49)$$

The nonlinear coupling coefficient is obtained from (37) through (40), which yields

$$\begin{aligned} \frac{\gamma^*}{\Omega_e(L)} &= \Gamma_L \Delta\mu [g'_1(x_*) + g'_2(x_*)] (1-x_*)^{-1} \\ &\quad \mathcal{K}_A(x_*, \Delta\omega_l) \Lambda(p_{\parallel}, x_*) \end{aligned} \quad (50)$$

where  $\Delta\omega_l$  is the frequency width of the wavelet that triggers the chorus emissions. In addition, we find

$$\mathcal{K}_A(x_*, \Delta\omega_l) = \frac{1}{2A!} \int_{x_*}^{y_T} dy y^A \exp(-y) \simeq \frac{\Delta\omega_l}{\omega_T} \mathcal{T}_*(x_*) \quad (51)$$

where  $y_{T,b}^* = p_*(\omega_{T,b})^2/\alpha_{\perp}$ . Here  $p_*(\omega_b)$  and  $p_*(\omega_T)$  are obtained by solving the equatorial resonant condition  $d\xi_L(\omega, \mu_*, p)/ds = 0$  for  $p$  and setting  $\omega = \omega_b$  and  $\omega_T$ , respectively.

To find the frequency spread we need to take the imaginary part of the function  $\Lambda(p_{\parallel})$  as defined in (33). We substitute the phase shift  $\xi$  by its expression in (31), i.e.,  $\xi = \sqrt{2}(x + x^3 d/3)$ , where  $x = \rho^{1/2}s$  and  $d = 1 + \lambda(2\rho)^{-3/2}$ . Then we approximate  $\Lambda = \Lambda_R + i\Lambda_I$ , as

$$\Lambda \simeq \frac{\pi}{\rho\kappa} \left[ \frac{4}{3d} K_{1/3}(\vartheta)^2 - i\pi \left( \frac{2}{d} \right)^{1/2} \right] \quad (52)$$

where  $\vartheta = (8/9d)^{1/2}$  is the argument of the Bessel function  $K_{1/3}$ ; we have that for  $d = 1$ ,  $K_{1/3} \sim 0.43$ . If  $\lambda \ll (2\rho)^{3/2}$ , where  $\rho$  is defined in (21), then  $\gamma^*/\Omega_e(L) \sim \rho^{-1/2}$ , and is proportional to the square root of the inverse electric field amplitudes. For  $\lambda \gg (2\rho)^{3/2}$  we obtain  $d \gg 1$  and  $\Lambda_I \rightarrow 0$ , thus large inhomogeneities cannot trigger emissions.

The chorus emissions are triggered by the wavelets, and their frequency spreads are represented by  $\delta\omega$ . We obtain  $\delta\omega$  as function of the bandwidth of the wavelets  $\Delta\omega_l$  as

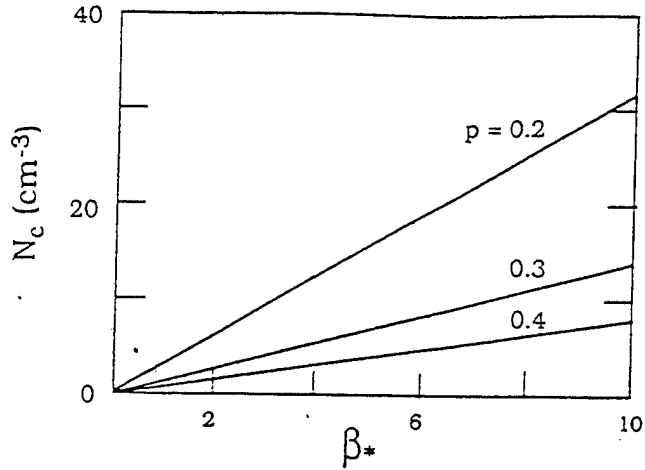


Figure 5. Density of cold plasma particles versus  $\beta_*$  as defined in (20) for three values of the normalized electron momentum.

$$\frac{\delta\omega}{\Delta\omega_l} = [2\pi \frac{\Omega_e(L)}{\omega}]^2 \Gamma_L \frac{1}{\eta_{||}} [g'_1(x_*) + g'_2(x_*)] \frac{T_*(x_*)}{(\rho d)^{1/2}} \quad (53)$$

As shown by *Omura et al.* [1991], if we take  $\lambda = 0$ ,  $d = 1$ , then  $\delta\omega \sim \rho^{-1/2} \sim |\mathcal{E}_\perp|^{-1/2}$ . As the electric fields become small, i.e.,  $\lambda > (2\rho)^{3/2}$ , then  $(\rho d)^{-1/2} \rightarrow (\sqrt{\rho}/\lambda)^{1/2}$  and  $\delta\omega \sim \rho^{+1/4}$ , and since  $\rho < 1$ , the frequency shifts can be quite small, as shown by *Shklyar et al.* [1992]. Considering the stationary case, the electric fields reach the value

$$v_{g,||} \frac{\partial |\mathcal{E}_\perp|^{1/2}}{\partial Z} = \frac{\delta\omega}{2\pi} \vartheta K_{1/3}^2(\vartheta) |\mathcal{E}_\perp|^{1/2} \quad (54)$$

For  $\lambda \rightarrow 0$ ,  $d = 1$ , and since  $\rho \sim |\mathcal{E}_\perp|$ , then the right-hand side of (54) is independent of the electric fields.

## 6. Numerical Examples

As an example, we study electron-whistler interactions at the  $L = 6.5$  shell, where the equatorial elec-

tron gyrofrequency is  $\Omega_e(L) = 2 \times 10^4$  rad/s. The loss cone width is about  $3^\circ$ , and as indicated before,  $\kappa = c/\Omega_e(L)r_L = 6.3 \times 10^{-4}$ . We consider electrons whose normalized momenta are  $p = 0.2, 0.3$ , and  $0.4$ , which correspond to energies between  $\sim 10$  and  $40$  keV. We shall calculate our physical variables in terms of  $\beta_*$ , as given in (20), which is proportional to the inverse of the square of the normalized magnetic energy per particle,  $[\Omega_e(L)/\omega_p]^2$ , and to the square of the electron momentum. For all the examples presented here we assume waves that propagate along the field lines so that  $\cos \phi = 1$ .

Figure 5 shows the density of cold plasma particles that sustain the waves versus  $\beta_*$  for the three different momenta indicated. By increasing the electron energy (momentum), the number of cold plasma particles that produce the same value of  $\beta_*$  decreases. If these calculations were done, say at  $L = 5.5$ , the number of cold plasma electrons are larger than at  $L = 6.5$  for the same values of  $\beta_*$  and momenta as in Figure 5.

Figure 6 shows two relevant physical parameters in the theory of wavelets generation indicated by  $\omega_T/\Omega_e(L)$  and  $\Delta\omega_l/\omega_T$ , and by taking three different values for the size of the step in the electron distribution function, i.e.,  $\delta\mu = 0.5, 0.25$ , and  $0.1$ . Here  $\omega_T$  is the frequency of maximum growth and is obtained from (44) as a function of  $\beta_*$ , and  $\Delta\omega_l$  is the normalized frequency bandwidths of the wavelets which is calculated by solving (20) also versus  $\beta_*$ . Note that as  $\beta_* \rightarrow 0$  then  $\omega_T \rightarrow \Omega_e(L)$ , and as  $\beta_*$  increases then  $\omega_T$  becomes smaller. The frequency bandwidths saturate at about  $\Delta\omega_l/\omega_T \simeq 0.4$  for large  $\beta_*$ , assuming  $\delta\mu = 0.5$ . Experimental observations show that frequencies at the top of the hiss spectrum are about  $1/3$  of the electron gyrofrequency. Thus according to our estimates for the frequency of maximum growth,  $\beta_* > 1$  for the physical parameters to be realized. Next we consider two examples taken from experimental papers to illustrate better the relevance of our calculations for the frequen-

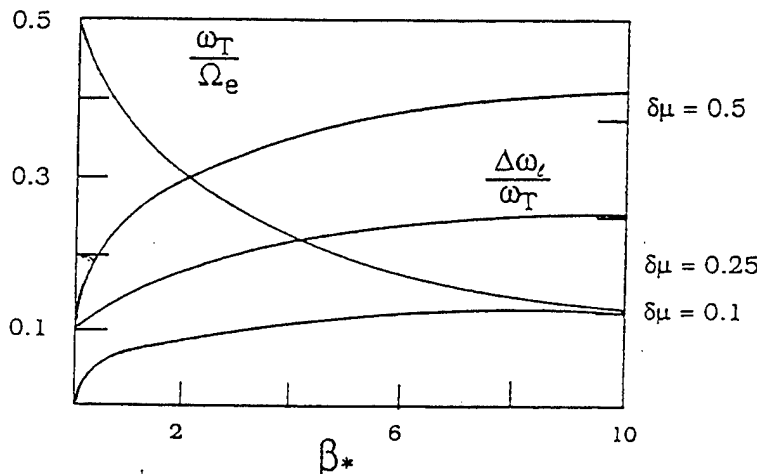


Figure 6. Frequency of maximum growth  $\omega_T$  normalized to electron gyrofrequency  $\Omega_e$  versus  $\beta_*$ . Frequency spread of the wavelet  $\Delta\omega_l$  divided by  $\omega_T$  for three values of the size of the step  $\delta\mu$  versus  $\beta_*$  as obtained from (20).

cies and bandwidths of wavelets in terms of normalized parameters presented in Figure 6.

Figure 1 contains results from *Hattori et al.* [1991], which may be compared with the calculations in Figure 6. In Figure 1 the ratio  $f_T = \omega_T/\Omega_e \simeq 0.34$  and the interaction occurs near the equator where the experimentally measured cyclotron frequency,  $f_{ce} = 3.039$  kHz, is compatible with the dipole model for the geomagnetic field. According to our results in Figure 6, the ratio  $f_T = 0.34$  corresponds to  $\beta_* \sim 2$ . For resonant energies between 10 and 50 KeV, the plasma density is just a few particles  $\text{cm}^{-3}$ , in agreement with results by *Higel and Wu* [1984]. The bandwidth of the wavelets is also estimated from Figure 1,  $\Delta\omega_1/\omega_T \sim 0.1$  and then  $0.1 \leq \delta\mu < 0.25$ , which corresponds to a distribution function whose step deformation is  $\sim 6^\circ$ .

We also compare calculations in Figure 6 with the example given by *Koons* [1981]. At the magnetic shell  $L = 6$ , the ratio is taken  $f_T \sim 0.1$ , the plasma density was assumed 29 particles  $\text{cm}^{-3}$ , and the interacting electron energies 10–15 keV. According to our calculations, the ratio  $f_T = 0.13$  corresponds to  $\beta_* = 10$ , which for energies of  $\sim 15$  keV yields a cold plasma population  $\sim 30 \text{ cm}^{-3}$ , in agreement with the above assumptions. As acknowledged by *Koons* [1981], this cold plasma density is large compared to experimental measurements under normal conditions. Next consider a plasma whose density is  $\sim 5$  particles  $\text{cm}^{-3}$  so that at  $L = 6$ ,  $\omega_p/\Omega_e = 5$ . Assuming  $\beta_* \sim 10$ , we obtain the electron momentum  $p = 0.6$ , which corresponds to an energy of  $\sim 85$  keV, and according to the resonance condition in (19), the pitch angle is  $\sim 22^\circ$ . This energy is larger than that taken by *Koons* [1981] for producing waves  $f_T \sim 0.1$  in a cold plasma of low density. This example serves to illustrate the main points of our calculations in Figure 6 in terms of normalized plasma and particles parameters as defined through  $\beta_*$  to obtain frequencies that maximize the growth rates.

To investigate the effects that inhomogeneities and multiple resonances have on the linear growth of the waves, we introduce the ratio between the growth rates  $\gamma_G$  and  $\gamma_H$ . Here  $\gamma_G$  is calculated by taking the real part of (37), recalling that  $\gamma^* = \gamma_G + i(\delta\omega - v_{g,\parallel} \delta k_{\parallel})$  and substituting  $\Lambda_R$  by the expressions in (42) or (43). In a weakly inhomogeneous plasma and smooth distribution functions, the electron-whistler interactions take place with single-frequency waves. Then the stationary phase points obtained solving for  $d\xi/ds = 0$  as functions of  $s$  are not degenerate, which means that near the equatorial cross section there is only one root. In this case of weak inhomogeneity the growth rate  $\gamma_H$  is obtained similarly to  $\gamma_G$  from the real part of (37) and by approaching  $\Lambda_R$  by the Dirac delta function as given after (33). We also define an angular dependent growth rate,  $\gamma_{G,H}(\mu)$ , such that the actual growth rates are  $\gamma_{G,H} = \int_0^{\mu_T} \gamma_{G,H}(\mu) d\mu/\mu_T$ . We calculate in Figure 7 the following

$$\frac{\gamma_G(\mu)}{\gamma_H(\mu)} = \frac{1}{4\pi^2} \eta_{\parallel} \frac{\omega}{\Omega_e} \Lambda_R \quad (55)$$

versus  $\mu = \sin^2 \theta(L)$ ,  $\theta(L)$  is the equatorial pitch angle. The linear growth rates are enhanced by at least a factor of 15 owing to the inhomogeneities and distribution functions with jump boundaries. We represent the case  $\beta_* = 5$  for the normalized electron velocities as indicated in Figure 7. The two lines that are almost parallel below  $\gamma_G/\gamma_H = 10$  are obtained by setting  $\chi = 0$  in the definition of  $\lambda$  in (23). The top two lines next to the numbers in Figure 7 that indicate the electron velocities become very large near  $\mu = 0.50$ . They are calculated assuming that the frequency of resonance varies along the field line according to (16), where  $\chi > 2$  is given in (25) so the magnetic field inhomogeneities are compensated by the frequency variation. In this case,  $\Lambda_R$  goes to infinity owing to the singularity near  $\theta = \theta_T$ . We have estimated the value of  $\Lambda_R$  at  $\theta_T$  by including the effects of finite electric fields. Then we substitute  $\xi$  by (29) in the integral defining  $\Lambda_R$  in (42). Notice that the singularity near  $\theta_T$  is not present in the analysis of *Trakhtengerts et al.* [1996]. The growth rates can be very large at the boundary between resonant and non-resonant electrons. This is because for a given electron the frequencies of resonance have been changed along the field lines according to (25) to match the magnetic field inhomogeneities near the jump boundary.

Figure 8 represents the electric field amplitudes thresholds versus  $\beta_*$  for the transition to the nonlinear regime of particle trapping and chorus emissions. The electric fields are given by (47) taking  $\delta\mu \sim 0.5$ ,  $\theta_s = \theta_c$  as the loss cone boundary and considering the frequency

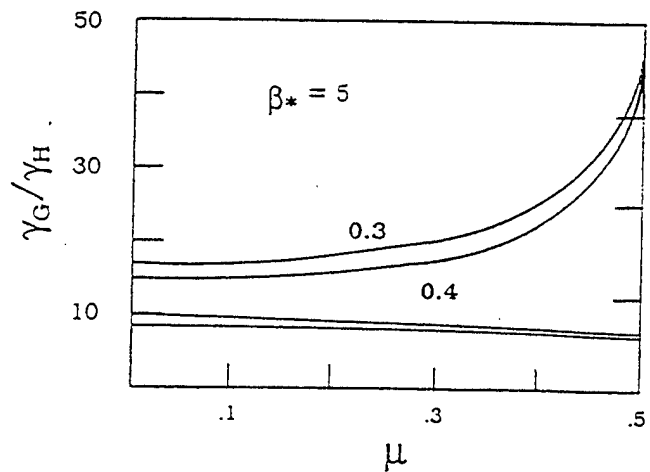


Figure 7. The ratio  $\gamma_G/\gamma_H$  as in (55) plotted versus  $\mu = \sin^2 \theta(L)$ . We take  $\beta_* = 5$  as in (20), and the numbers next to the lines are normalized electron momenta. The linear growth rates are enhanced by a factor equal to this ratio owing to the magnetic field inhomogeneities and step-like distribution functions. The two parallel lines below  $\gamma_G/\gamma_H = 10$  are obtained by taking the frequency of the wave constant along the field lines.

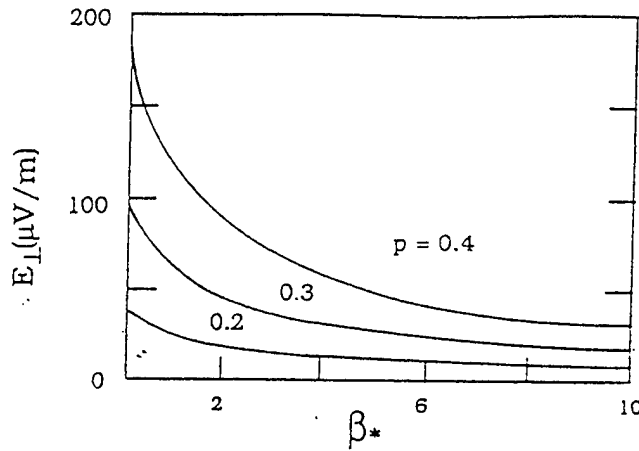


Figure 8. The electric field amplitude thresholds for nonlinear interactions, in  $10^{-6}$  V/m, obtained from (47), versus  $\beta_*$ , given in (20). The minimum electric field is  $6.6 \mu\text{V/m}$  for  $p = 0.2$  and  $\beta_* = 10$ . The frequency of the wave is  $\omega_T$ , and numbers next to the curves are normalized electron velocities.

of maximum growth  $\omega_T$ . The numbers next to the lines are the normalized velocities. The minimum electric field is  $6.6 \times 10^{-6}$  V/m, which corresponds to  $\beta_* = 10$  and  $p = 0.2$ . These electric field amplitudes are compatible with the values observed experimentally since according to the article by *Koons* [1981], electric fields are at least of the order of  $10^{-5}$  V/m for the triggering waves.

The electric fields represented in Figure 8 build near the boundary between resonant and nonresonant electrons, as explained in section 5, and they create plateaus in the distribution function as a result of the electron trapping. Figure 9 represents the extent of the plateaus for the equatorial pitch angle  $\Delta\theta(L)$  in degrees near  $\theta_T \sim 45^\circ$  versus  $\beta_*$  as calculated from (49). Similar to Figure 8, the numbers next to the lines are the nor-

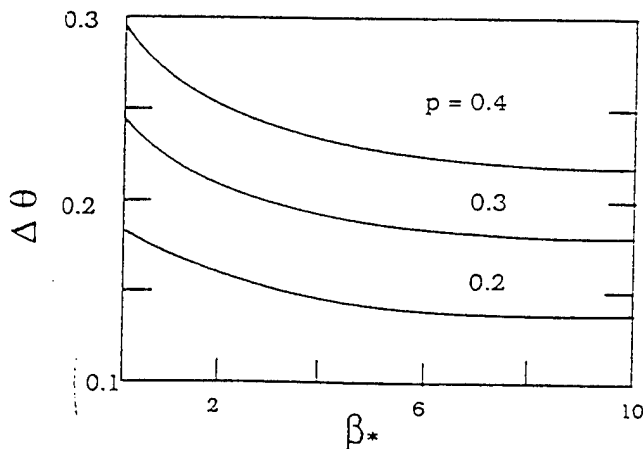


Figure 9. Sizes of the plateaus, in degrees, for the electron pitch angle distribution function as function of  $\beta_*$  for  $p = 0.2, 0.3$ , and  $0.4$ . The electric fields that produce these plateaus are calculated in Figure 8.

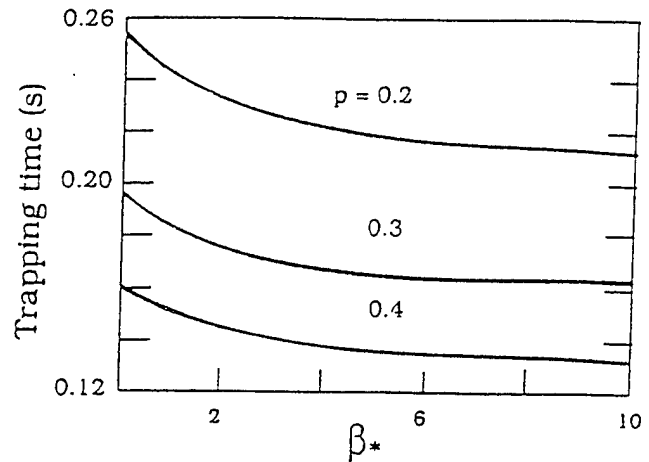


Figure 10. Bound oscillation time, in seconds, of the electrons in the potential wells of the wavelets as given by (56) versus  $\beta_*$ . These oscillation times approximately correspond to the duration of the plateaus represented in Figure 8. We show  $p = 0.2, 0.3$ , and  $0.4$ .

malized electrons velocities. These plateaus trap the electrons that form the nonlinear resonant currents triggering the chorus emissions.

The duration of the plateau or the nonlinear trapping time is approximately the oscillation time of the electrons around the equilibrium position  $\xi = \pi/2$  as obtained from (21). Following the definition given by *Sudan and Ott* [1971], time correlation is one oscillation period of the resonant electrons as they advance into the potential well of the wavelets. In units of  $\Omega_e^{-1}(L)$  we find that the correlation time  $\sigma$  is given by

$$\sigma = \frac{2\pi}{\eta_{\parallel} f_T} \left[ \frac{1}{2\gamma_R} \tan \theta(L) \frac{\gamma_R^{-1} - f_T}{\eta_{\parallel} f_T} \right]^{-1/2} \bar{\varepsilon}_{\perp}^{-1/2} \quad (56)$$

where  $f_T = \omega_T/\Omega_e(L)$  is the frequency at the top of the hiss band and  $\bar{\varepsilon}_{\perp}$  is defined in (47). Figure 10 represents  $\sigma \times \Omega_e^{-1}(L)$  in seconds versus  $\beta_*$  for the three  $p = 0.2, 0.3, 0.4$ , as indicated. We see that the correlation time is a few tenths of a second and that it is smaller for larger values of  $p$  because the electric fields are larger for increasing electron energy as shown in Figure 8. Experimental observations by *Koons* [1981] and *Hattori et al.* [1991] show that chorus emissions last for a few tenths of seconds, which roughly agrees with the correlation times presented here.

## 7. Summary and Conclusions

We have presented a theory of chorus generation in the magnetosphere, according to which chorus is emitted by electrons trapped in wavelets propagating at the top of the hiss band. The distribution functions of the electrons develop step-like deformations near the boundary between resonant and nonresonant electrons owing to their linear interactions with the inner plasma

sheet hiss. The physical processes leading to chorus radiation and plateau formation are explained in Figure 4. The main results of our theory are described as follows.

1. The electric field amplitudes of waves propagating at small angles to the magnetic field grow owing to their interactions with energetic electrons. This leads to the generation of resonant currents.

2. Quasi-monochromatic waves packets (wavelets) whose frequency bandwidths are represented by  $\Delta\omega_l$  grow at the top of the hiss band. This is due to the linear interactions with electrons whose distribution functions show step-like deformations. We have obtained analytical expressions for  $\Delta\omega_l$  and the growth rates of the wavelets. We assume that a resonant electron interacts with different frequencies within the bandwidth of the wave packet, at different locations along the field lines to compensate for the magnetic field inhomogeneities. Because of this, our estimates of growth rates are larger than those previously obtained by *Nunn and Sazhin [1991]* and *Trakhtengerts et al. [1996]*.

3. As the wavelet electric fields increase, electrons become trapped. The electron distribution functions develop plateaus near the jump boundary in phase space, whose extent is proportional to the square roots of the electric fields. The plateau duration is approximately the time of phase correlation between the waves and the electrons. The relative phase angles between the electrons and the waves were obtained near the equator for trapped particles.

4. Chorus emissions are triggered by wavelets and nonlinear resonant currents carried by trapped electrons. We show that their frequency spreads  $\delta\omega$  are proportional to  $|\mathcal{E}_\perp|^{-1/2}$  and to the frequency bandwidth of the wavelet  $\Delta\omega_l$ .

5. Thus the frequency dispersions come from two sources. The first is linear dispersion due to step-like distribution function, and the magnetic field inhomogeneities that originate the wavelet bandwidth. The second source is nonlinear dispersion owing to plateau formation and trapped electrons, which originate currents and the chorus frequency spread.

6. Numerical calculations that apply to different magnetospheric regimes give the frequency of maximum growth and the frequency bandwidths of the wavelets as function of  $\beta_*$ , i.e., the square of the inverse normalized magnetic energy per particle times the electron velocity. The electric field amplitudes are obtained for the transition to the nonlinear trapping and chorus emissions. Further analysis, using measured energetic particle fluxes to obtain actual chorus growth rates and frequency spreads, will be presented in a future paper.

## Appendix: Plateau Formation

For a fixed position  $s$  along the field line, the distribution functions  $f$  for resonant particles depend on time  $t$ , pitch angle  $\mu = \sin^2 \theta(L)$ , and momentum  $p$ .

For a fixed value of the electron energy, we assume that distribution functions show step-like deformations in the equatorial pitch angle for  $\mu = \mu_*$ , where  $\mu_*$  is the boundary between resonant and nonresonant particles. By taking a Taylor expansion of the distribution function for a fixed value of the electron momentum near the jump boundary, we write

$$f(t, \mu, p) = f_* + \left(\frac{df}{d\mu}\right)_{\mu=\mu_*} \Delta\mu \quad (57)$$

where  $f_*$  stands for  $f[t, \mu_*(p), p]$ .

We define  $\tau = \Omega_e(L)t$ ,  $\hat{\xi} = \pi/4 - \xi/2$ , and  $\rho_C^2 = 2\rho/(C + \rho)$ , and  $C$  is a constant. For particles that are near the boundary,  $\lambda(h, \theta_*) \simeq 0$ , we rewrite (30) as

$$\frac{d\hat{\xi}}{d\tau} = \frac{2\pi}{\sigma \rho_C} [1 - \rho_C^2 \sin^2 \hat{\xi}]^{1/2} \quad (58)$$

where  $2\pi\sigma^{-1} = \kappa v_{\parallel} \sqrt{\rho(s)}$ . Here  $\sigma$  is the bound oscillation time of the particle in the potential well of the wave normalized to  $\Omega_e(L)$ . It was already introduced in section 6 for the transition electric fields defined in (47).

The solution of (58) is expressed in terms of elliptic functions as  $F(\hat{\xi}, \rho_C) = \int_0^{\hat{\xi}} d\varphi [1 - \rho_C^2 \sin^2 \hat{\xi}]^{-1/2}$ ,

$$F(\hat{\xi}, \rho_C) - F(\hat{\xi}_0, \rho_C) = \tau \frac{\kappa v_{\parallel} \sqrt{\rho}}{\rho_C} \quad (59)$$

For trapped particles,  $|\rho_C| > 1$ , and for untrapped,  $|\rho_C| < 1$  [*Bud'ko et al., 1972*]. Thus if  $C < \rho$ , electrons may be trapped.

We also show that

$$\frac{d\hat{\xi}}{d\tau} = \frac{1}{4} v_{\parallel} \eta_{\parallel} \frac{\omega}{\Omega_e(L)} \frac{\Delta\mu}{1 - \mu_*} \quad (60)$$

Combining (58) to (60), we obtain

$$f - f_* = \pm 4 f'(\mu_*) \frac{1 - \mu_*}{k_{\parallel} \tau_L} \frac{\sqrt{\rho}}{\rho_C} dn[F(\hat{\xi}, \rho_C) - \frac{2\pi\tau}{\sigma \rho_C}, \rho_C] \quad (61)$$

where  $f'$  denotes the derivative of  $f$  and  $dn[u, \rho_C]$  is the Jacobi elliptical function. The time average of the Jacobi function is for  $|\rho_C| < 1$   $(\pi/2) F(\pi/2, \rho_C)$ , the total elliptical integral of the first kind. For trapped particles,  $|\rho_C| > 1$ , the time average is zero, and then the first derivative of the distribution function is also zero near  $\mu = \mu_*$ . By imposing the condition of plateau formation on the distribution function, we obtain that the functions  $g_{1,2}$  must satisfy

$$g_1(\mu) - g_2(\mu) \simeq \Delta\mu [g'_1(\mu_*) + g'_2(\mu_*)] \quad (62)$$

for  $\mu$  near  $\mu_*$  and  $\Delta\mu \ll 1$  as given in (48).

### Acknowledgments.

This work has been supported by the U.S. Air Force under contract with Northeastern University, F19628-95-C-0212, and the Air Force Office of Scientific Research, task 2311GP.

The Editor thanks two referees for their assistance in evaluating this paper.

### References

- Belmont, G., D. Fontaine, and P. Cann, Are equatorial electron cyclotron waves responsible for diffuse auroral electron precipitation?, *J. Geophys. Res.*, **88**, 9163, 1983.
- Bespalov, P. A., and V. Y. Trakhtengerts, Cyclotron instability of Earth radiation belts, *Reviews of Plasma Physics*, vol. 10, p. 155. Consult. Bur., New York, 1986.
- Bud'ko, N. I., V. I. Karpman, and D. R. Shklyar, Stability of a plasma in the field of a longitudinal monochromatic wave, *Sov. Phys. JETP, Engl. Trans.*, **34**, 778, 1972.
- Dysthe, K. B., Some studies of triggered whistler emissions, *J. Geophys. Res.*, **76**, 6915, 1971.
- Galeev, A. A., and R. S. Sagdeev, Nonlinear plasma theory, *Reviews of Plasma Physics*, vol. 7, p. 1, Consult. Bur., New York, 1979.
- Hardy, D. A., W. J. Burke, and E. Villalón, Electron dispersion events in the morningside auroral zone and their relationship with VLF emissions, *J. Geophys. Res.*, **95**, 6451, 1990.
- Hattori, K., M. Hayakawa, D. Lagoutte, M. Parrot, and F. Lefevre, Further evidence of triggering chorus emissions from wavelets, *Planet. Space Sci.*, **39**, 1465, 1991.
- Hayakawa, M., Y. Yamanaka, M. Parrot, and F. Lefevre, The wave normals of magnetospheric chorus emissions observed on board GEOS 2, *J. Geophys. Res.*, **89**, 2811, 1984.
- Helliwell, R. A., A theory of discrete VLF emissions from the magnetosphere, *J. Geophys. Res.*, **72**, 4773, 1967.
- Higel, B., and L. Wu, Electron density and plasmopause characteristics at 6.6  $R_E$ : A statistical study of the GEOS 2 relaxation sounder data, *J. Geophys. Res.*, **89**, 1583, 1984.
- Inan, U. S., Y. T. Chiu, and G. T. Davidson, Whistler-mode chorus and morningside aurora, *Geophys. Res. Lett.*, **19**, 653, 1992.
- Johnstone, A. D., D. M. Walton, R. Liu, and D. A. Hardy, Pitch angle diffusion of low-energy electrons by whistler mode waves, *J. Geophys. Res.*, **98**, 5959, 1993.
- Kennel, C. F., and H. E. Petschek, A limit on stably trapped particle fluxes, *J. Geophys. Res.*, **71**, 1, 1966.
- Koons, H. C., The role of hiss in magnetospheric chorus emissions, *J. Geophys. Res.*, **86**, 6745, 1981.
- Lui, A. T. Y., P. Perrault, S.-I. Akasofu, and C. D. Anger, The diffuse aurora, *Planet. Space Sci.*, **21**, 857, 1973.
- Lyons, L. R., Electron diffusion driven by magnetospheric electrostatic waves, *J. Geophys. Res.*, **79**, 575, 1974.
- Lyons, L. R., and D. J. Williams, *Quantitative Aspects of Magnetospheric Physics*, D. Reidel, Norwell, Mass., 1984.
- Meng, C. I., B. Mauk, and C. E. McIlwain, Electron precipitation of evening diffuse aurora and its conjugate electron fluxes near the magnetospheric equator, *J. Geophys. Res.*, **84**, 2545, 1979.
- Muto, H., M. Hayakawa, M. Parrot, and F. Lefevre, Direction finding of half-gyrofrequency VLF emissions in the off-equatorial region of the magnetosphere and their generation and propagation, *J. Geophys. Res.*, **92**, 7538, 1987.
- Nunn, D., A self-consistent theory of triggered VLF emissions, *Planet. Space Sci.*, **22**, 349, 1974.
- Nunn, D., and S. S. Sazhin, On the generation mechanism of hiss-triggered chorus, *Ann. Geophys.*, **9**, 603, 1991.
- Omura, Y., and H. Matsumoto, Computer simulations of basic processes of coherent whistler wave-particle interactions in the magnetosphere, *J. Geophys. Res.*, **87**, 4435, 1982.
- Omura, Y., D. Nunn, H. Matsumoto, and M. J. Rycroft, A review of observational, theoretical and numerical studies of VLF triggered emissions, *J. Atmos. Terr. Phys.*, **53**, 351, 1991.
- Paranicas, C., W. J. Hughes, H. J. Singer, and R. R. Anderson, Banded electrostatic emissions observed by the CRRES plasma wave experiment, *J. Geophys. Res.*, **97**, 13889, 1992.
- Parks, G. K., Microburst precipitation phenomena, *J. Geomagn. Geoelectr.*, **30**, 327, 1978.
- Roeder, J. L., and H. C. Koons, A survey of electron cyclotron waves in the magnetosphere and the diffuse auroral electron precipitation, *J. Geophys. Res.*, **94**, 2529, 1989.
- Rosenberg, T. J., J. C. Siren, D. L. Matthews, K. Marthinsen, J. A. Holtet, A. Egeland, D. L. Carpenter, and R. A. Helliwell, Conjugacy of electron microbursts and VLF chorus, *J. Geophys. Res.*, **86**, 5819, 1981.
- Sazhin, S. S., and M. Hayakawa, Magnetospheric chorus emissions: A review, *Planet. Space Sci.*, **40**, 681, 1992.
- Schumaker, T. L., M. S. Gussenhoven, D. A. Hardy, and R. L. Caravillano, The relationship between diffuse auroral and plasma sheet electron distributions near local midnight, *J. Geophys. Res.*, **94**, 10061, 1989.
- Shklyar, D. R., D. Nunn, A. J. Smith, and S. S. Sazhin, An investigation into the nonlinear frequency shift in magnetospherically propagated VLF pulses, *J. Geophys. Res.*, **97**, 19,389, 1992.
- Sudan, R. N., and E. Ott, Theory of triggered VLF emissions, *J. Geophys. Res.*, **76**, 4463, 1971.
- Trakhtengerts, V. Y., M. J. Rycroft, and A. G. Demekhov, Interrelation of noise-like and discrete ELF/VLF emissions generated by cyclotron interactions, *J. Geophys. Res.*, **101**, 13,293, 1996.
- Tsurutani, B. T., and E. J. Smith, Postmidnight chorus: A substorm phenomenon, *J. Geophys. Res.*, **79**, 118, 1974.
- Tsurutani, B. T., and E. J. Smith, Two types of magnetospheric ELF chorus and their substorm dependence, *J. Geophys. Res.*, **82**, 5112, 1977.
- Villalón, E., and W. J. Burke, Pitch angle scattering of diffuse auroral electrons by whistler mode waves, *J. Geophys. Res.*, **100**, 19,361, 1995.

W. J. Burke, Phillips Laboratory, Hanscom Air Force Base, MA 01731.

E. Villalón, Center for Electromagnetics Research, Northeastern University, Boston, MA 02115. (e-mail: villalon@sricon.plh.af.mil)

(Received August 7, 1996; revised March 3, 1997; accepted March 4, 1997.)

## Electron acceleration by MHz waves during OEDIPUS C

C. Y. Huang,<sup>1</sup> W. J. Burke,<sup>2</sup> D. A. Hardy,<sup>2</sup> M. P. Gough,<sup>3</sup> H. G. James,<sup>4</sup> E. Villalón,<sup>5</sup>  
and L. C. Gentile<sup>1</sup>

Short title: ELECTRON ACCELERATION ON OEDIPUS C

**Abstract.** OEDIPUS C was a tethered mother-son experiment that was launched northward from the Poker Flat rocket range at 0638 UT on November 7, 1995, across a sequence of auroral structures. During the flight's upleg the magnetically-aligned tether was deployed to a separation of  $\sim 1.2$  km then cut at both ends. The Forward payload contained a 50 kHz to 8 MHz stepped-frequency transmitter. Receivers were carried on both Forward and Aft payloads. The transmitter swept through the frequency range every 0.5 s. During each of the 3 ms steps the transmitter emitted only for the first 0.3 ms. The scientific complement also included multiangular electrostatic analyzers on both payloads that were sensitive to fluxes of electrons with energies from 20 eV to 20 keV. The durations of sampling and frequency steps were matched. During the flight the electron gyrofrequency was approximately twice the plasma frequency. When the transmitter swept through the local gyrofrequency the particle detectors on both payloads detected sounder accelerated electrons (SAEs) independent of the energy steps being sampled. In addition, SAEs were detected at the Aft payload out to separations of several hundred meters for wave emissions at harmonics of the electron gyrofrequency as well as in the upper hybrid and whistler bands. As the vehicle separation increased, significant time differences developed between the wave-emission pulses and the onsets/durations of SAE detections. The data indicate that electrons are heated through strong wave-particle interactions. However, a simple resonant-interaction explanation appears inadequate. We outline requirements for any model(s) purporting to explain OEDIPUS C measurements.



## Introduction

This paper presents the first example of bistatic measurements of sounder accelerated electrons (SAEs) detected during the OEDIPUS C (O-C) sounding rocket experiment flown in November 1995. Previous rocket-borne experiments in which sounders were used to probe the ionospheric plasma were limited to low- to mid-latitudes, and only monostatic measurements were made. In the Intercosmos 19 [Gal'perin *et al.*, 1981; Serov *et al.*, 1985; Shuiskaya *et al.*, 1990] and ISIS I and II [James, 1983] experiments electrons were accelerated from a cold background to hundreds of eV, with a maximum of 1 keV being reported. At low altitudes where  $f_{pe} > f_{ce}$  the Intercosmos 19 experiments demonstrated that the sounder produced a wide variety of plasma modes interacting with measureable fluxes of energized electrons [Serov *et al.*, 1985]. At higher altitudes where  $f_{pe} < f_{ce}$  ISIS II reported energetic fluxes of electrons when the transmitted frequency ranged from  $f_{pe}$  to  $f_{uh}$ , where  $f_{uh} = \sqrt{f_{pe}^2 + f_{ce}^2}$  is the upper hybrid frequency, and a second maximum at  $2 f_{ce}$  [James, 1983]. Figure 11 of James [1983] shows that the fluxes of electrons with energies  $\sim 300$  eV peak at pitch angles near  $90^\circ$ . However, the peak fluxes of electrons with lesser energies are displaced from  $90^\circ$  pitch angles.

One purpose in active sounding experiments is to investigate the wave-particle interactions which result from sounder transmission. By transmitting a signal at a known frequency and observing the effect on the ambient plasma we can establish cause and effect. In naturally occurring wave-particle interactions this ambiguity cannot always be eliminated. A secondary goal is to examine mechanisms for ionospheric heating for which sounders provide one means of energetic input.

In this paper we report results obtained simultaneously from two particle detectors when a radio transmitter actively transmitted through a range of frequencies via crossed dipole antennas. One detector was co-located with the sounder on one payload. A second detector was located on a separate payload connected to the first by a

magnetically-aligned conducting tether. The separation distance between the payloads increased as the tether was extended. The only role played by the tether in our study is to maintain the two payloads along the magnetic field. We do not treat any of the results which arise from power put into the tether itself. Of particular interest to us is the response of the electron population surrounding the sounder when it was actively transmitting in certain frequency ranges. We find that electrons were accelerated up to the maximum detectable energy of 20 keV when these frequency ranges were sounded. In addition we note several anomalies in the appearance, duration and pitch angle distribution in the sounder-accelerated electron (SAE) population which remain unexplained by current theory.

## Instrumentation and Experimental Background

The O-C experiment was launched from the Poker Flat range ( $65.5^\circ$  N,  $212.5^\circ$  E) in the premidnight sector at 0638:17.26 UT on November 7, 1995, aboard a Black Brant 12 sounding rocket. The rocket's trajectory was almost due north, achieving an apogee of 824 km at 517 s time after launch (TAL). Scientific instruments were distributed between two platforms, referred to as Forward and Aft, that were separated by an electrically conducting tether that was closely aligned with the Earth's magnetic field **B**. Separation between the payloads was initiated at 174 s TAL by means of an argon gas thruster. The tether achieved full extension of 1173 m at 450 s TAL. It was cut at both ends at 623 s TAL.

The Forward payload carried a digitally controlled radio transmitter called the high frequency exciter (HEX) whose signals could be fed into two pairs of 19 m tip to tip "V" shaped dipoles or into the tether [James and Calvert, 1998]. The "V" shape was adapted to produce linearly polarized fields in the antenna plane perpendicular to **B**. The antenna's output was divided into six repeating sequences, each of 0.5 s duration. The 3 s intervals required for the full sequence are referred to as major frames (MAF)

and the 0.5 s intervals as minor frames (MIF). Each emission sequence was divided into 165 steps each of 3.03 ms duration. Emission sequences used during the upleg portion of the flight are listed in Table 1 and the modes of transmission are illustrated in Figure 1. During the upleg part of the flight, sounder accelerated electrons were detected only while the dipoles were connected to the transmitter and SH3 sequences were exercised. From Table 1 it can be seen that this occurs on MIFs 2, 3, and 4, or 3 times during each major frame. We will restrict our discussion to these minor frames only. During SH3 sequences input frequencies ranged from 25 kHz to 8 MHz in 160 steps, separated in frequency by 50 kHz. No power was fed into the dipoles during 5 of the SH3 steps early and at the end of the sequence. The total time taken to cycle through 165 steps is 0.5 s. During times when the HEX output is listed as 100 V, 10 W of power was fed into the dipoles. The modes in which power is fed into the tether are not discussed in this paper. A synchronized wave receiver called REX, located on the Aft payload, monitored the transmission characteristics of waves emitted from HEX [James and Calvert, 1998].

Two energetic particle instruments (EPI) were placed on the Forward (EPI-F) and Aft (EPI-A) payloads. They consisted of triquadraser spherical electrostatic analyzers with fields of view of  $140^\circ \times 8^\circ$ . This acceptance fan was divided into eight zones of  $17.5^\circ \times 8^\circ$ . Figure 2 shows that the sensors were placed so that zone 2 for Forward and Aft payloads looked down and up along **B**, respectively. Zone 7 of both EPIs looked nearly perpendicular to **B**. To clarify the following discussion we will use the zone numbers (1 through 8) and central look angle relative to the magnetic field, i.e. pitch angle as follows: zone 1 ( $-17.5^\circ$ ), zone 2 ( $0^\circ$ ), etc. up to zone 7 ( $87.5^\circ$ ), zone 8 ( $105^\circ$ ) with the understanding that the acceptance angle of each zone is  $17.5^\circ$  and the angle after each zone number refers to the central angle of each zone. The EPIs covered the energy range 10 eV to 20 keV in 32 logarithmically spaced increments, with  $\Delta E/E \approx 10\%$  and a geometric factor of  $5 \times 10^{-2}$ . Full energy spectra for each of the zones were compiled at a rate of  $10 \text{ s}^{-1}$ .

In Figure 3 we show a schematic illustrating operation of the HEX transmitter and the EPI during a single major frame. The 3 s interval is divided into 6 minor frames each of which lasts 0.5 s which is the time necessary to complete a single sweep of each of the frequency steps. These frequency sweeps are labelled SH 3, SH 4, and FF, details of which are given in Table 1. The EPI sweeps through its 32 energy steps, each of duration 3.03 ms in 0.1 s. Thus in Figure 3 the EPI sweep is represented by a sawtooth wave. The cycle times of the transmitter and the EPI are slightly different. This is represented by a small displacement in the EPI sweep relative to the HEX minor frame.

The lower part of Figure 3 shows the relative stepping sequences for the two instruments. The transmitter steps actually consist of a series of pulses which have an active interval of 300  $\mu$ s followed by a passive interval of 2.7 ms before stepping up to the next frequency. Note that the displacement of the EPI cycle relative to the HEX sounder means that as each set of frequencies is repeated the EPI is detecting a different energy. Part of the argument we make is that although electrons of all energies are accelerated when specific frequencies are sounded, the nature of the instrument operation allows us to observe only those electrons corresponding to the particular energy step sampled by the EPI at that time.

To avoid internal arcing the high voltage supplies of the EPIs were turned on at  $\sim 200$  s TAL. In parallel with normal counting, the EPIs further process data in two ways: 0-8 MHz electron autocorrelation functions (ACFs) and sub-millisecond superposed epoch analysis of the energy (frequency) steps. For the autocorrelations, times between electron arrivals are measured in units of a clock running at 16 MHz. Using a buncher technique, histograms of time separations between electron detections are accumulated for each of the 32 energy levels sampled by the EPIs [Gough 1980; Gough *et al.*, 1995]. The histograms are equivalent to the summation of many one-bit ACFs. Normally electron counts are accumulated by the EPI for the full 3.03 ms duration of an energy step to determine individual spectra (directional differential

fluxes). An alternative method to analyze electron fluxes involves using the correlator capability of the sensor to determine the arrival times of individual electrons into adjacent pairs of sensors (zones 1 and 2, 3 and 4, 5 and 6, 7 and 8). Summed time series of counts for two frequency emission steps are presented as superposed epochs relative to the initial time of the frequency pulses by the HEX transmitter. In these cases the temporal resolution or accumulation period is 90  $\mu$ s.

It should be noted that we are not using the correlator technique to find resonant wave frequencies as was done for the Tethered Satellite System missions [Gough *et al.*, 1995]. We use the correlator only to give us a high-time-resolution breakdown of the 3.03 ms cycle time of the EPI. We have checked the output of the ACFs and compared the counting levels with the fluxes returned directly from the EPI, and after making the conversion necessary for the summed pitch angles and times, we arrive at identical numbers.

At the time of the O-C launch, a series of bright auroral arcs was located to the north of Poker Flat. By the time of EPI turn on, the payloads were at an altitude of  $\sim 440$  km and approaching field lines connected to the most equatorward auroral arc. The top plot of Figure 4 provides the electron cyclotron  $f_{ce}$  and the plasma  $f_{pe}$  frequencies plotted as functions of time for the upleg portion of the flight. The IGRF 1995 model of the Earth's magnetic field was used to calculate  $f_{ce}$  at the spacecraft locations. Values of  $f_{pe}$  were determined from X and Z mode cutoffs observed in ionograms measured at the Aft payload [James and Calvert, 1998]. The plots in Figure 4 show that: (1)  $f_{ce}$  smoothly decreased with altitude from 1.32 to 1.12 MHz between 200 and 500 s TAL, and (2)  $f_{pe}$  decreased from 0.7 MHz at 200 s to 0.6 MHz at 240 s. After that it decreased rapidly to  $< 0.2$  MHz. The bottom plot of Figure 4 gives the length of the tether and the spacecraft altitude as functions of time. The shaded areas in the figure between 200 and 260 s TAL mark the approximate duration of SAE detections by EPI-A.

## Observations

Plate 1 shows the uncorrected counts from zones 4 ( $35^\circ$ ) and 7 ( $87.5^\circ$ ) of the electrostatic analyzer on the Forward payload for the interval from 200–260 s after launch. The background auroral electrons can be seen in both zones but are more readily apparent in zone 7 ( $87.5^\circ$ ) which detects the backscattered or reflected population with large ( $\sim 90^\circ$ ) pitch angles. The SAEs appear in sets of three corresponding to the minor frames 2, 3, and 4 when the transmitter is in swept frequency mode and the dipole antenna is connected as mentioned in the preceding section (see Table 1).

There are differences between the responses in zone 4 which detects electrons arriving with pitch angles of  $35^\circ \pm 9^\circ$  and zone 7 which is approximately perpendicular to the magnetic field. The response level in zone 4 is higher than that in zone 7. We have taken into account the difference in sensitivity when generating distributions and fluxes from the raw counts. The SAEs in zone 4 ( $35^\circ$ ) appear at all energies. This can be seen as sets of three pulses that appear at steadily decreasing energies until the lowest values are reached and the sequence begins again at the highest energies. An example of such a transition can be seen around 221 s. In contrast the SAEs in zone 7 ( $87.5^\circ$ ) are restricted to the lower energies. As the SAEs are detected at decreasing energies up to  $\sim 239$  s, the corresponding transition to the highest energies does not occur until the end of the sequence shown in Plate 1.

On the Forward payload the strongest signal occurs at the electron gyrofrequency  $f_{ce}$  when the HEX radio transmitter sweeps through this part of its range and the dipole antenna is connected. For brevity we do not show results from the Aft payload which are qualitatively similar to those of Plate 1. The main difference is an overall increase in counting rate. The auroral electrons are detected most intensely in zone 2 ( $0^\circ$ ) which looks up the magnetic field, and weakly at large pitch angles.

The sets of 3 pulses seen in Plate 1 correspond to the times when the electron gyrofrequency is transmitted by the HEX in each of the 3 minor frames 2, 3 and 4. It

is difficult to separate the gyrofrequency from the upper hybrid resonance frequency as  $f_p \ll f_{ce}$  (see Figure 4), but as higher order resonant frequencies are detected at weak levels, we assume these to be higher-order harmonics of  $f_{ce}$ .

On the Forward payload which is co-located with the HEX transmitter, transmission from the antenna at the electron gyrofrequency caused electron acceleration throughout the duration of the rocket flight. This contrasts with the Aft payload which was  $\sim 150$  to 575 m distant from the transmitter during the 200–260 s interval under discussion. SAEs at the gyrofrequency and higher harmonics are observed on the Aft payload for the first 60 s of flight but were not detectable after 260 s TAL until shortly before re-entry when a large array of wave emissions is detected.

A second emission is observed at the Aft payload which is not apparent on the Forward payload. This occurs at  $\sim 0.2$  to 0.7 MHz. We refer to these emissions as the whistler band [Stix, 1962] based on the frequency relative to the natural gyro- and plasma frequencies. This emission is only observed for the same 60 s as the gyrofrequency emissions on the Aft payload [James *et al.*, 1999].

The electron analyzer data can be displayed at higher time resolution provided by the superposed epoch time analysis [Gough *et al.*, 1995]. The accumulated counts for adjacent zones are combined so that zones 1 and 2 ( $\pm 17.5^\circ$ ), 3 and 4 ( $17.5^\circ$  and  $35^\circ$ ), 5 and 6 ( $52.5^\circ$  and  $70^\circ$ ), 7 and 8 ( $87.5^\circ$  and  $105^\circ$ ) are summed in pairs and the results plotted for the 3.03 ms required for a single electron analyzer energy step. In Figure 5A we show the raw counts versus lag times for the summed counts in zones 3 ( $17.5^\circ$ ) and 4 ( $35^\circ$ ) for energy 28 – 36 eV and when the transmitted frequency is 1.275 – 1.325 MHz. These data are observed on the Forward payload. The time is 239 s TAL, minor frame 2. Recall that individual HEX transmitter steps during this emission sequence (SH 3 - see Figure 3) last 3 ms with the transmitter active for 0.3 ms and passive for 2.7 ms. This plot shows arrival of electrons in a narrow energy band during the 3 ms duration of the HEX pulse. No other energies are excited and no heated electrons are observed

at any other transmitted frequency.

In Figure 5 individual lag intervals are of  $90 \mu\text{s}$  duration. The pulse width of the enhanced electron counts lasts 4 lag intervals, or  $\sim 360 \mu\text{s}$ . This corresponds to the time that the transmitter is active. Note that there is no time delay between the start of transmission and observation of enhanced electron counts. Simultaneous with the observation of high electron counts at intermediate pitch angles ( $17.5^\circ - 35^\circ$ ), the EPI detects electrons in all other zones, from 1 ( $-17.5^\circ$ ) through 8 ( $105^\circ$ ), at the same energy ( $28 - 36 \text{ eV}$ ) and corresponding to the same transmitted frequency ( $1.275 - 1.325 \text{ MHz}$ ).

This example is typical of the measurements made on the Forward payload with one significant exception. In Figure 5A the electrons are in the  $28 - 36 \text{ eV}$  energy range. At energies  $< 200 \text{ eV}$  enhanced counts are observed at all pitch angles. Above  $200 \text{ eV}$  only electrons at intermediate pitch angles from  $18 - 82^\circ$ , corresponding to zones 3 - 6, are observed at enhanced counting levels. However at these intermediate pitch angles, we detect SAEs through the entire energy range. These features are discussed in more detail when we present the distribution functions for the SAEs.

In Figure 5B we show count rates from the Aft payload versus lag times for the summed counts in zones 3 and 4 ( $17.5^\circ - 35^\circ$ ), energy =  $400 - 500 \text{ eV}$ , transmitted frequency =  $1.325 - 1.375 \text{ MHz}$ . The time is again  $239 \text{ s TAL}$  ( $L \approx 400 \text{ m}$ ), minor frame 2, the same time as is shown in Figure 5A for the Forward payload. The SAEs observed on the Aft payload show several distinct differences. (1) There is a noticeable time lag between the start of HEX transmission in this frequency range and the first appearance of significant count rates above the auroral background,  $\sim 270 \mu\text{s}$ . This time delay increases with tether length, or equivalently, with distance from the HEX transmitter on the Forward payload. (2) The peak count rates also remain elevated for a longer time than on the Forward payload. At this time the SAE pulse duration lasts about 6 lag intervals or  $540 \mu\text{s}$ . Note that the HEX transmitter is off from  $300 \mu\text{s}$  into the sweep, so these high electron counts are mostly detected after the transmitter is



turned off. (3) The count rates decline more gradually, going through an interval lasting  $\sim 300 \mu\text{s}$  during which count rates decrease below the maximum but remain above the auroral background. (4) The background count rates are  $\sim 20\%$  of the peak values. In comparison the background on the Forward payload is  $< 10\%$  of the peak rate.

Other features of the SAEs observed on the Aft payload are identical with those seen on the Forward payload, i.e. the enhanced electron counts are in the same energy range over all pitch angles when the electron energy is  $< 200 \text{ eV}$ . At higher energies SAEs are confined to intermediate pitch angles ( $18^\circ - 70^\circ$ ).

Note that one significant difference between the simultaneous observations of enhanced counts on the separated payloads is the energy of the electrons which interact with the transmitted wave. On the Forward payload the SAE energy is  $28 - 36 \text{ eV}$ , while at the Aft payload it is  $400 - 500 \text{ eV}$ . The EPIs on the payloads are not synchronized. This difference illustrates an important result: whenever the transmitted frequency is at the electron gyrofrequency ( $\sim 1.3 \text{ MHz}$ ) ambient electrons at all energies are accelerated. The acceleration in the near-field region is immediate and coincides precisely with the duration of the transmitted signal. At the distant payload, the first detection of SAEs depends on the distance from the transmitter, and the duration of the SAEs far exceeds the time over which power is applied to the sounder.

In Figure 5C the low-frequency SAEs observed on the Aft payload are shown. These also occur at 239 TAL, minor frame 2, but at a different part of the frequency sweep. The HEX transmitter frequency at this time is  $425\text{-}475 \text{ kHz}$ , and the electron energy is  $1.5 - 1.8 \text{ keV}$ . The counts rise after 1 lag interval and remain elevated for 5 periods, or  $450 \mu\text{s}$ . The decrease in count rate is sharper than for the gyrofrequency emission on the Aft payload shown in Figure 5B but less precipitous than the Forward payload SAEs shown in Figure 5A. The background in Figure 5C is also intermediate between that of Figures 5A and 5B. As in the gyrofrequency SAEs the whistler SAEs are observed whenever the frequency is in the appropriate range, regardless of the electron

energy. The pitch angle range is also related to electron energy with all pitch angles observed below 70 eV, and only at the intermediate pitch angles above this energy.

The Liouville theorem suggests a means for estimating the amount by which electrons were accelerated through their interactions with HEX emissions in the whistler and/or upper hybrid frequency bands. In its simplest form the Liouville theorem states that for an ensemble of particles their phase space densities (distribution functions) remain constant along dynamical trajectories. For distributions of electrons in the ionosphere this is equivalent to saying that they obey the collisionless Boltzmann equation. In the case at hand, it is necessary to determine the distribution function of the SAEs and the auroral electron population from which they were accelerated. This is not an easy task. As seen above, encounters with SAEs are discrete events subject to the beating between the EPI energy and the HEX emission cycles. Also, data indicate that during the interval 200 – 260 s TAL, background auroral electron fluxes were quite variable. Subsequent paragraphs summarize results of our efforts to describe the distribution functions of both the auroral and SAE populations.

Figures 6A and 6B provide representative examples of electron distribution functions  $f(E)$  plotted as functions of energy. They were measured by EPI-F at 239 s TAL and EPI-A at 227 s TAL at pitch angles of  $0^\circ$ ,  $35^\circ$ , and  $87.5^\circ$  to the Earth's magnetic field. Both of these distribution functions were acquired while HEX was operating in the SH3 mode feeding energy to the dipoles. For convenience in our description of the data we somewhat arbitrarily divide the distribution function into two parts, referring to electrons with  $E > 1$  keV as auroral primaries and those with  $E < 1$  keV as auroral secondaries. The secondary population is composed of energy-degraded and backscattered primaries as well as energetic electrons created in ionizing collisions. From the plots in Figure 6 three empirical points may be made: (1) The primary auroral distribution function did not decrease monotonically with energy. A peak in  $f(E)$  was detected by EPI-F at  $E \approx 4.2$  keV and pitch angles near  $90^\circ$  (zone 7). At this energy

$f_7(E)$  was a full order of magnitude higher than that of backscattered electrons,  $f_2(E)$ . A peak in  $f(E)$  at  $\sim 3$  keV, measured by EPI-A at 227s TAL, was isotropic over the downcoming hemisphere. (2) EPI-F measured peaks in  $f(E)$  for the secondary electron populations between 25 and 40 eV. Likewise, EPI-A detected peaks in  $f(E)$  and near 400 eV by EPI-A. These are examples of SAE events excited as HEX swept through the upper hybrid and whistler frequency bands. (3) The SAE distribution function measured by EPI-F increased more at  $90^\circ$  pitch angles than at intermediate pitch angles, which increased more than at a pitch angle of  $0^\circ$ . A similar feature appears at 400 eV in EPI-A measurements. However, at EPI-A the next two energy steps show the largest increase at intermediate pitch angles. These observations suggest that the acceleration is exerted perpendicular to  $\mathbf{B}$  rather than along it.

To estimate the electron acceleration, we have superposed straight lines on Figures 6A and 6B that approximate the unperturbed distributions of the secondary electrons as isotropic and following a power law over the energy range  $10 \text{ eV} \leq E \leq 300 \text{ eV}$ . The secondary distribution function is represented as

$$f(E) = 2 \times 10^{-24} \left[ \frac{10}{E} \right]^3 \quad (1)$$

where  $f(E)$  is in  $\text{s}^3/\text{cm}^6$  and  $E$  in eV. For the energy range  $300 \text{ eV} \leq E \leq 20 \text{ keV}$  the primary auroral distribution can be represented as

$$f(E) = 1 \times 10^{-28} \left[ \frac{300}{E} \right]^2 \quad (2)$$

where  $f(E)$  is in  $\text{s}^3/\text{cm}^6$  and  $E$  is in eV.

Figure 7 presents all SAE distribution functions observed by EPI-F between 200 and 260 s TAL calculated using high-time resolution count rates available through the EPI correlator function. Data points represent sums over two adjacent EPI zones and energy steps acquired in  $\sim 90 \mu\text{s}$ . To calculate  $f_{i,j}(E)$  we approximated effective geometric factors and central energies as geometric means ( $\sqrt{X_i X_j}$ ) of values determined prior to

flight. In some cases EPI sampled the same zone/energy step pairs twice during the 60 s interval of interest. Data in Figure 7 show that (1) SAEs were detected in zone pairs at  $0^\circ$  and  $90^\circ$  pitch angles only at electron energies  $\leq 60$  eV and 400 eV, respectively. (2) Statistically, for  $E < 400$  eV,  $f_{3,4}(E)$  ( $\sim 26^\circ$  pitch angle) had the highest values. Note that for  $E > 400$  eV, symbols representing  $f_{5,6}(E)$  ( $\sim 61^\circ$  pitch angle) in Figure 7 overlay and hide those representing  $f_{3,4}(E)$  ( $\sim 26^\circ$  pitch angle). In fact,  $f_{3,4}(E) \approx f_{5,6}(E)$ . (3) To a good approximation,  $f_{3,4}(E)$  can be represented as following power laws with spectral indices of -3 and -2 at energies below and above 300 eV, respectively. For reference, Figure 7 also shows the approximated auroral electron distributions as in Figure 5A measured by EPI-F at 239 s. A comparison of the measurements shows that  $f_4(E)$  roughly parallels  $f_{3,4}(E)$ . This suggests that the energy gained by an electron  $\Delta E$  in an encounter with a HEX wave emission is nearly proportional to its initial energy.

All SAE measurements made by EPI-A during times when HEX was emitting in the upper hybrid and whistler frequency bands are given in Figures 8A and 8B, respectively. Again, distribution functions were derived from count rates acquired using the EPI correlator function. Many of the features found in the EPI-F measurements also appear in Figure 8. From 300 eV to 20 keV the distributions can be approximated as  $f(E) \propto \left[\frac{1}{E}\right]^2$ . The intercept varies slightly between frequency ranges. In addition to the fact that whistler band emissions accelerated electrons reaching the Aft but not the Forward payload, the main differences between data in Figures 7 and 8 are: (1) signatures of  $f_{1,2}(E)$  at  $0^\circ$  pitch angle are discernible in Figure 8A out to energies of  $\sim 450$  eV, (2) at any given energy, the distribution functions of SAEs reaching EPI-A are systematically lower than those observed by EPI-F, and (3) the acceleration observed at the Forward payload is more uniform over the observed energy range than that at the Aft payload.

Table 2 presents examples of the SAE energies recorded during HEX transmissions. The effect at the Forward payload where the transmitter is located is dramatic. The 10 W output from the transmitter accelerates electrons up to a factor of 5 in energy as the

upper hybrid band is swept. At the Aft payload acceleration in the upper hybrid and whistler bands is less marked. Electrons are energized up to 3 times their initial energy at higher initial energies. At the Aft payload the energized electrons persist for several microseconds after the transmitter is turned off.

From the SAE distributions shown in Figures 7 and 8 it appears that the precipitating auroral electrons which peak at 3 – 5 keV have been smoothed out. The SAEs show no maxima over this energy range and no appreciable pitch-angle anisotropy. Counts are significant at intermediate pitch angles of  $9^\circ - 70^\circ$ , but peak primarily at  $45^\circ$  to the magnetic field. The SAE spectra are obtained over the complete 60 s interval from 200 -- 260 s TAL which includes the background auroral distributions shown in Figure 6. As can be seen in Plate 1 there is a continuous source of precipitating electrons during this interval.

## Summary and Discussion

The operation of the 10 W HEX transmitter had significant effects on the ambient electrons as the paired dipole antennas swept in frequency. At the Forward payload electron acceleration occurred across the upper hybrid frequency band regardless of the initial energy of the electrons. Further, electrons were accelerated at all energies in such a way that, except for auroral electron peaks, the initial spectral shape was preserved. At the Aft payload accelerated electrons were detected when the HEX swept through the whistler and upper hybrid frequency bands. Occasionally acceleration effects were also seen at harmonics of the electron frequency. The degree of electron acceleration increased with the initial energy from ~50% at 50 eV to a factor of 3 at 1 keV. Unlike the Forward payload where SAEs were detected only while the transmitter was on, at the Aft payload SAEs were observed after a brief delay and persisted for a short interval after the transmitter turned off. These effects became more pronounced as the tether length increased.

It should be remembered that our estimates of the SAE distribution function assume that the raw count rate is evenly divided between adjacent detector zones with total acceptance angle of  $35^\circ$  and combined energy levels. The actual count rates may be higher than our conservative estimates. The distribution functions for the SAEs are smoothly fitted by power law expressions. Maxima or minima in the background auroral distribution are smoothed out. In addition pitch angle anisotropies as shown in Figure 6A and 6B seem to be erased. Other than the averaging effect of the sum over adjacent energy steps and detector zones no processing of the data has been carried out. Flux levels of the SAEs are higher at the Forward payload. Apart from this, there are few differences between the SAE distributions measured on the separate payloads or between the high- and low-frequency SAEs.

Prior detections of SAEs were made at lower latitudes and involved acceleration of cold ionospheric plasma [James *et al.*, 1999]. By launching into a quiet auroral arc the O-C experiment experienced a background superthermal population superimposed on the cold ambient ionosphere. In a previous study of SAEs observed on the ISIS II satellite at 1400 km and subauroral latitudes the results were similar to ours [James, 1983]. Electrons were observed to be accelerated as the transmitter swept through the gyrofrequency and its harmonics. However, the maximum energy was a few hundred eV, and it was postulated that this was caused by the induced spacecraft potential. While a potential may be induced around the spacecraft it is difficult to reconcile this with the observation of electron correlations only when the HEX transmitter is sweeping through the upper hybrid and whistler bands.

Previous measurements have shown that spacecraft crossing intense auroral electron fluxes in darkness with low background plasma densities charge negatively [Gussenhoven *et al.*, 1985]. Thus if the Aft payload charged, it would be negatively charged, decreasing rather than increasing the flux of electrons reaching EPI-A. We conclude that the observed SAEs must result from strong interactions between the local auroral electron

population and certain HEX emitted waves.

To investigate the nature of the acceleration process it is useful to fit the observed directional differential flux  $J$  ( $(\text{cm}^3 \text{ s sr eV})^{-1}$ ) using kappa functions [Vasyliunas, 1968].  $J$  for the background auroral electrons observed at the Aft payload at 227 s is shown in Figure 9A. These data correspond to the distribution function plotted in Figure 6B except that 7 zones are shown in Figure 9. Also shown in Figure 9A are four possible functional fits. In each case the density has been kept constant such that  $\int f(v) d^3v = N$ , the measured electron density at this time. It can be seen that the auroral electrons are not well described by a Maxwellian with an assumed temperature of 0.1 eV. The best fit is given by a combination of two kappa functions, one at lower energy ( $10 \text{ eV} < E \leq 1 \text{ keV}$ ) with  $\kappa = 2$  and a temperature of 0.1–0.2 eV and one at high energy ( $1 \text{ keV} < E < 20 \text{ keV}$ ) with  $\kappa = 3$ .

In Figure 9B we show the SAE directional differential flux corresponding to the distribution shown in Figure 8B. As we have noted above, the SAE fluxes in the two frequency bands observed on the Aft payload and the SAEs observed on the Forward payload are all quite similar, so the data shown in Figure 9B are representative of all three sets of SAE observations. The functional fits from Figure 9A are repeated in Figure 9B. The change in the differential flux shows the effect of the sounder on the initial electron population. The final flux is not a simple heating of the initial population which would appear as a translation of the initial fitted curves to higher energies. The lower-energy portion of the curve is best fitted by a  $\kappa = 2$  fit with a temperature of 1 eV. However the higher energy portion ( $E > 300 \text{ eV}$ ) shows an increase in flux levels indicating that electrons from the low-energy part of the range have been accelerated into this energy range. This appears as a hardening of the spectrum as also noted in Figures 7 and 8 and Table 2. It can also be seen that the transition between the two kappa distributions now occurs at  $\sim 300 \text{ eV}$  compared with  $\sim 1 \text{ keV}$  for the unaccelerated electrons.

The main purpose of this paper has been to report EPI measurements during SAE detections. Although providing theoretical explanations of the OEDIPUS C measurements is well beyond its scope, some comments on model requirements for such explanations seem appropriate. We have already concluded that accelerated electrons observed during sounder operations result from wave-particle rather than vehicle-particle interactions. It is clear, however, that the acceleration does not proceed from simple resonant interactions. No particular initial electron velocity component along the magnetic field was preferentially selected as required to satisfy a resonance condition

$$\omega - k_{\parallel}v_{\parallel} + n\Omega_{ce} = 0$$

The standard notation is used  $\omega = 2\pi f$ ,  $\Omega_{ce} = 2\pi f_{ce}$ ,  $k_{\parallel}$  is the component of the wave vector along  $\mathbf{B}$  and  $n$  is an integer. Rather, acceleration occurs over a wide range of energies and pitch angles. At intermediate pitch angles (zones 3-6, corresponding to pitch angle  $18^{\circ}$ - $70^{\circ}$ ) SAEs were observed at both payloads up to the maximum energy of 20 keV. This would not be predicted in standard linear wave-particle theory. A theoretical study of the whistler mode wave-particle interaction was carried out by *James et al.* [1999]. They show that while acceleration over the entire energy range can be demonstrated the maximum increase in energy at high energies ( $E \geq 1$  keV) is a few hundred eV, not the several keV observed (see Table 2).

The second requirement is that the model utilize a finite heating region. SAEs were not detected at the Aft payload after 260 s TAL but continued at the Forward payload throughout the flight. This indicates that magnetic connection between finite acceleration volumes and the Aft payload was lost. Since the disconnection occurred at about the same time for both whistler and upper hybrid bands, the magnetic cross sections of the heated regions are comparable. Without better information concerning the cross magnetic field separation between the two payloads, it is impossible to specify the exact dimensions of the acceleration volume. If the nominal separation of a few



meters is correct, then the cross section of the interaction region was on the order of an auroral electron gyrodiameter.

A third requirement of a physical model is that it be able to explain the observed acceleration of electrons both up and down magnetic field lines whenever the HEX swept through the upper hybrid band. Clearly such a model would include the low density conditions prevailing during the actual flight of OEDIPUS C. For verification purposes, the model should be adapted to predict plasma responses when  $f_{pe} \geq f_{ce}$ .

Finally a complete model must also explain the detection of intense SAEs at the Aft payload but relatively weak SAEs on the Forward payload during HEX emissions at whistler band frequencies. What is the nature of the acceleration interaction? The electric fields of whistler-mode waves are perpendicular to the magnetic field. Why is it that SAEs with the highest energies, detected at pitch angles from  $17.5^\circ - 70^\circ$ , have large velocity components along **B**?

The results of the OEDIPUS C experiment show that relatively low-power transmitters emitting in sweep-frequency modes can accelerate ambient electrons to high energies. This effect has now been observed at a wide range of spacecraft altitudes and magnetic latitudes. Direct wave injection has promise as a highly efficient method for studying the electrodynamics of local ionospheric heating in spatially limited electromagnetic fields. It can be speculated that the acceleration process is intimately related to the near-field effects around the crossed dipole antenna during HEX transmissions. We would expect large localized electric fields to be generated in some complex pattern in the vicinity of the antenna which could accelerate ambient electrons to high energies. Without a detailed study of the electric field generated by the antenna we cannot pursue this speculation further.

**Acknowledgments.** OEDIPUS C was a collaborative project of the Canadian Space Agency and the National Aeronautics and Space Administration. This work was supported

by the U.S. Air Force Office of Scientific Research task 2311PL04, by Air Force contracts F19628-96-K-0030 and F49620-98-1-0012 with Boston College and F19628-95-C-0212 with Northeastern University, and by the Particle Physics and Astronomy Research Council of the UK.

## References

- Gal'perin, Yu. I., R. Z. Sagdeev, F. K. Shuiskaya, Yu. V. Lisakov, V. V. Migulin, Y. V. Kushnereveskii, M. D. Fligel, and G. V. Vasil'ev, Detection of electron acceleration in the ionospheric plasma under the influence of high power radio radiation near the local plasma frequency aboard the space vehicle Interkosmos 19, *Cosmic Res.*, 19, 22, 1981.
- Goldstein, H., *Classical Mechanics*, Addison Wesley, Reading, Mass, pp. 266-268, 1950.
- Gough, M. P., A technique for rocket borne detection of electron bunching at megahertz frequencies, *Nucl. Instrum. Methods*, 177, 581, 1980.
- Gough, M. P., M. R. Oberhardt, D. A. Hardy, W. J. Burke, L. C. Gentile, B. McNeil, K. Bounar, D. C. Thompson, and W. J. Raitt, Correlator measurements of MHz wave-particle interactions during electron beam operations on STS-46, *J. Geophys. Res.*, 100, 21561, 1995.
- Gussenhoven, M. S., D. A. Hardy, F. J. Rich, W. J. Burke, and H.-C. Yeh, High-level spacecraft charging in the low altitude polar auroral environment, *J. Geophys. Res.*, 90, 11,009, 1985.
- James, H. G., Souder-accelerated particles observed on ISIS, *J. Geophys. Res.*, 88, 4027, 1983.
- James, H. G., and W. Calvert, Interference fringes detected during OEDIPUS C, *Radio Sci.*, 33, 617, 1998.
- James, H. G., V. I. Sotnikov, W. J. Burke, and C. Y. Huang, OEDIPUS C observations of electrons accelerated by radio frequency fields at whistler-mode frequencies, *Phys. of Plasmas*, in press, 1999.
- Serov, A. A., Yu. I. Gal'perin, Yu. V. Lisakov and F. K. Shuiskaya, Local acceleration of electrons of the near satellite plasma by the radio emission of a powerful on board transmitter, *Cosmic Res.*, 23, 361, 1985.
- Shuiskaya, F. K., Yu. I. Gal'perin, A. A. Serov, N. V. Barants, Yu. V. Kushnerevesky, G. V. Vasil'ev, S. A. Pulinet, M. D. Fligel, and V. V. Selegev, Resonant heating of the

ionospheric plasma by powerful radiopulses aboard the Intercosmos 19 and Cosmos 1809 satellites, *Planet. Space Sci.*, 38, 173, 1990.

Stix, T. H., *The Theory of Plasma Waves*, McGraw-Hill, New York, pp. 29-30, 1962.

Vasyliunas, V. M., A survey of low-energy electrons in the evening sector of the magnetosphere with OGO1 and OGO3, *J Geophys. Res.*, 73, 2839, 1968.

---

W. J. Burke and D. A. Hardy, Air Force Research Laboratory, 29 Randolph Road, Hanscom AFB, MA, 01731-3010. (william.burke2@hanscom.af.mil; david.hardy@hanscom.af.mil)

L. C. Gentile and C. Y. Huang, Boston College Institute for Scientific Research, 402 St. Clement's Hall, 140 Commonwealth Avenue, Chestnut Hill, MA 02467-3862. (louise.gentile@hanscom.af.mil, cheryl.huang@hanscom.af.mil)

M. P. Gough, Space Science Centre, University of Sussex, Brighton, BN1 9QT, UK. (m.p.gough@sussex.ac.uk)

H. G. James, Communications Research Centre, Department of Communications, Ottawa, Ontario, Canada K2H 8S7. (james@cancrc.dgrc.doc.ca)

E. Villalón, Center for Electromagnetics Research, Northeastern University, Boston, MA 02115.

Received Month xx, 1999; revised Month xx, 2000; accepted Month xx, 2000.

---

<sup>1</sup>Boston College Institute for Scientific Research, Chestnut Hill, Massachusetts

<sup>2</sup>Air Force Research Laboratory, Hanscom Air Force Base, Massachusetts

<sup>3</sup>Space Science Centre, University of Sussex, Brighton, England

<sup>4</sup>Communications Research Centre, Ottawa, Ontario, Canada

<sup>5</sup>Center for Electromagnetics Research, Northeastern University, Boston, Massachusetts

**Table 1.** HEX Operations during OEDIPUS C Upleg

MIF	Time	Mode	Voltage	Dipole	Tether
1	0.0 – 0.5	SH3	2.51 V	grounded	connected
2	0.5 – 1.0	SH3	100 V	connected	grounded
3	1.0 – 1.5	SH3	100 V	connected	grounded
4	1.5 – 2.0	SH3	100 V	connected	grounded
5	2.0 – 2.5	SH4	2.51 V	grounded	connected
6	2.5 – 3.0	FF	100 V	connected	grounded

**Table 2.** SAE energies recorded during HEX transmissions

	$E_i$	$E_f$ Forward	$E_f$ Aft, HF	$E_f$ Aft, LF
1	50 eV	160 eV	76 eV	71 eV
2	100 eV	340 eV	170 eV	170 eV
3	1000 eV	5500 eV	3400 eV	2900 ev

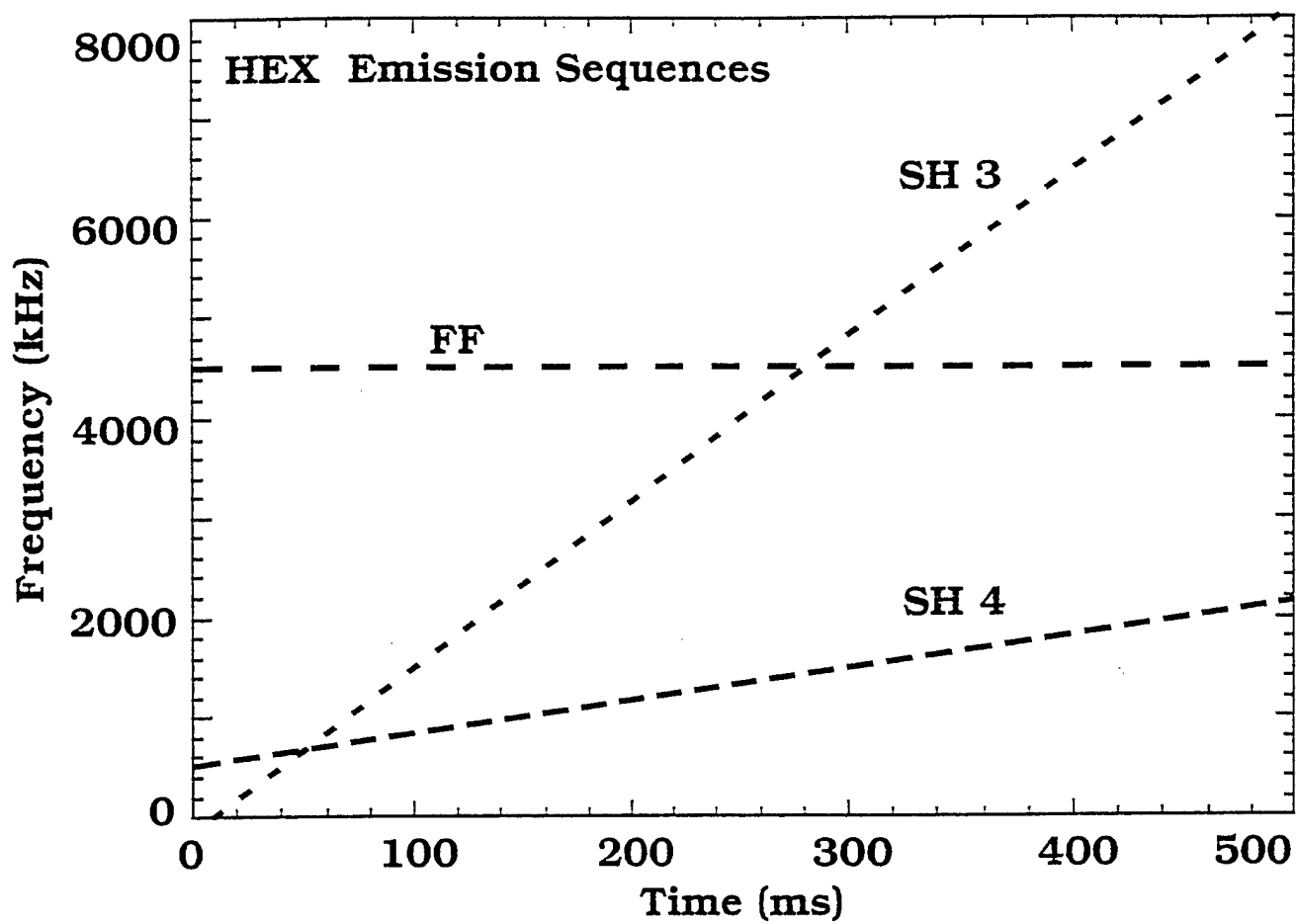


Figure 1. HEX emission sequences during the upleg of OEDIPUS C.

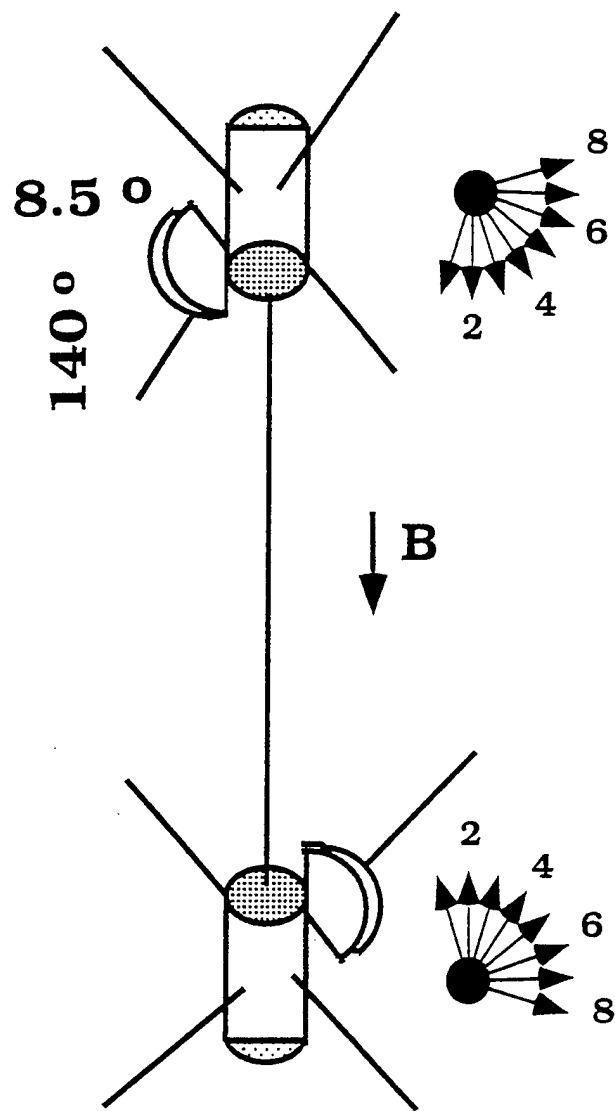


Figure 2. Schematic representations of OEDIPUS C payload and look directions of EPIs.



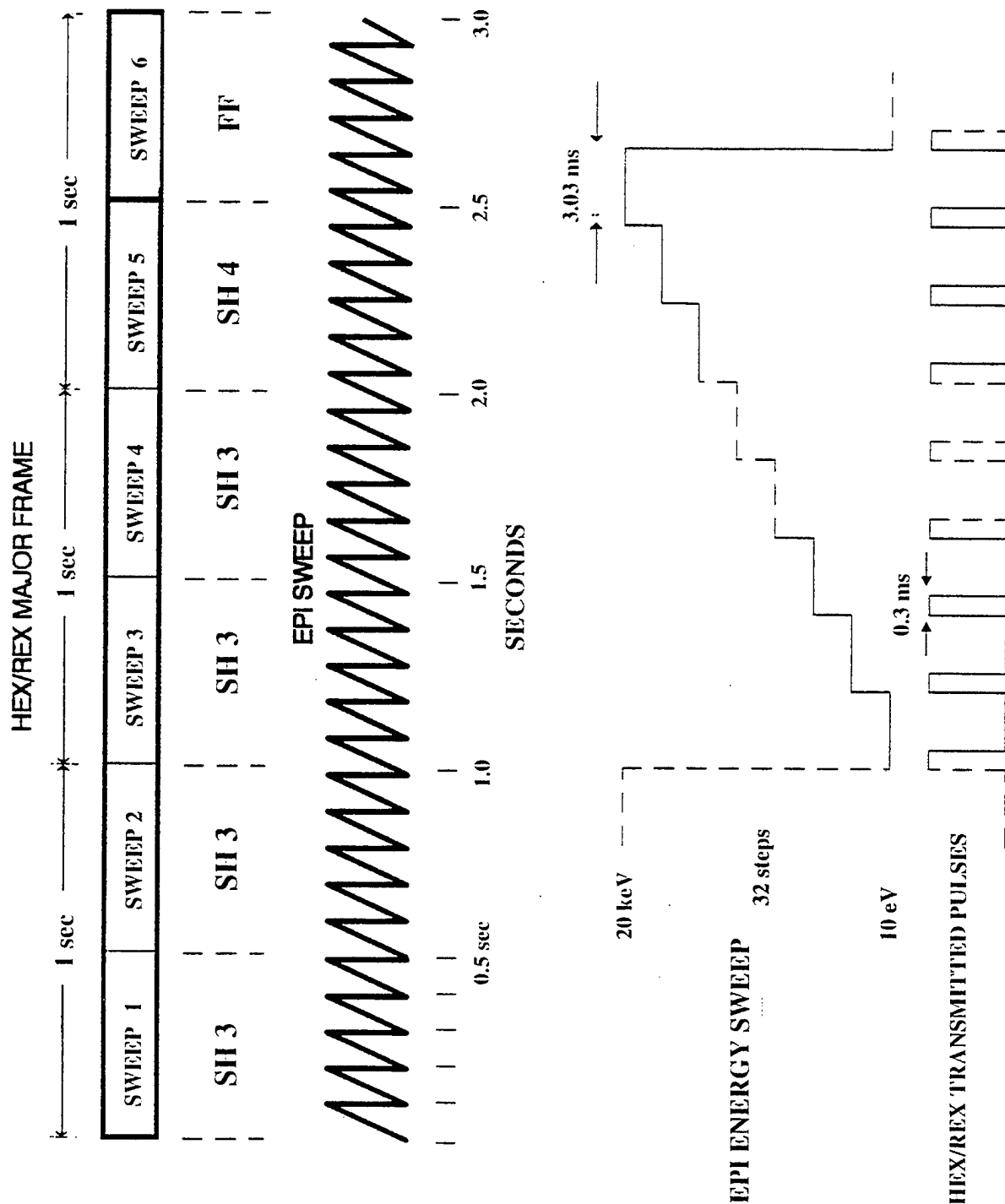


Figure 3. Schematic illustrating operation of the HEX transmitter and EPI detector during a single major frame.

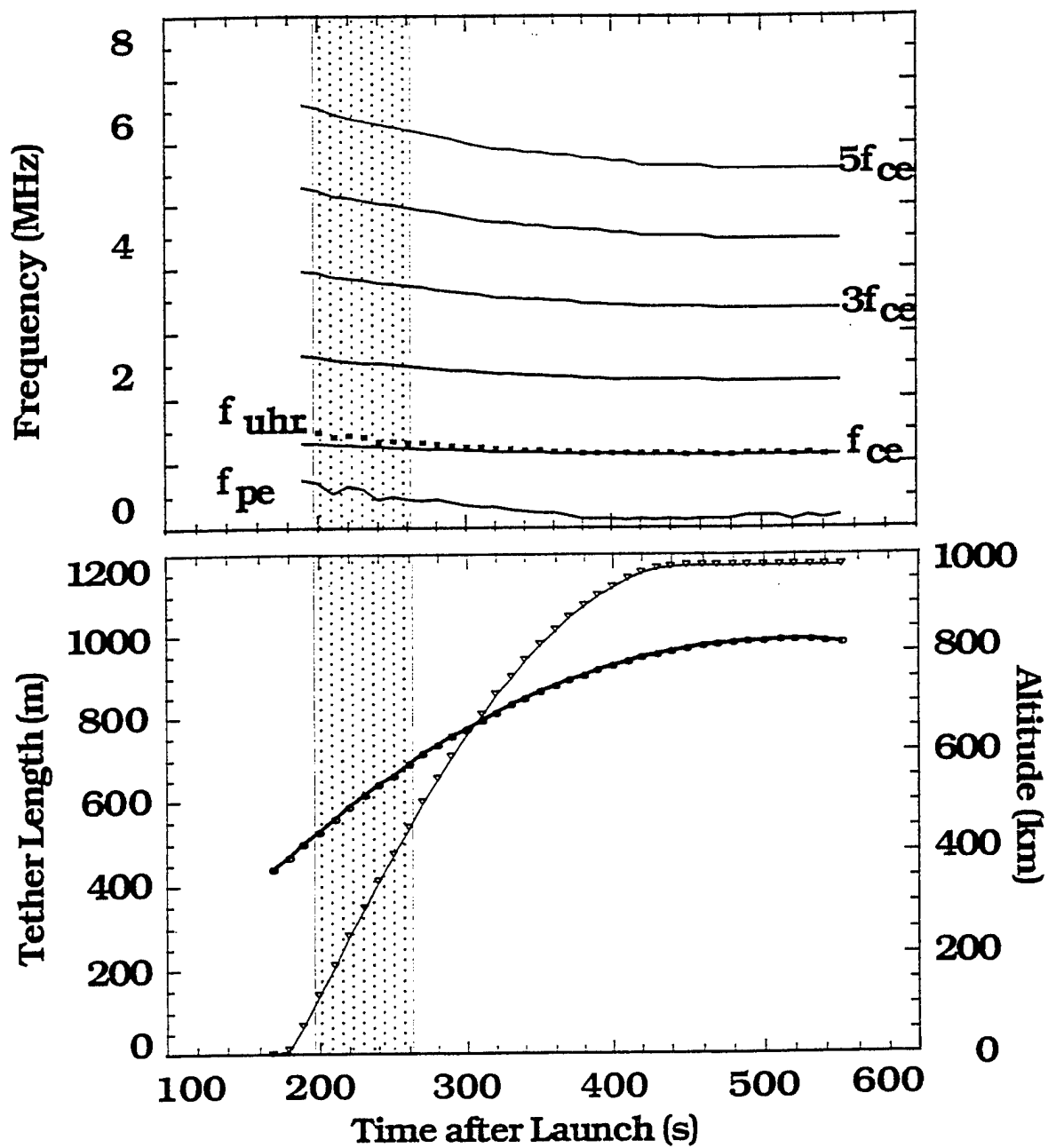
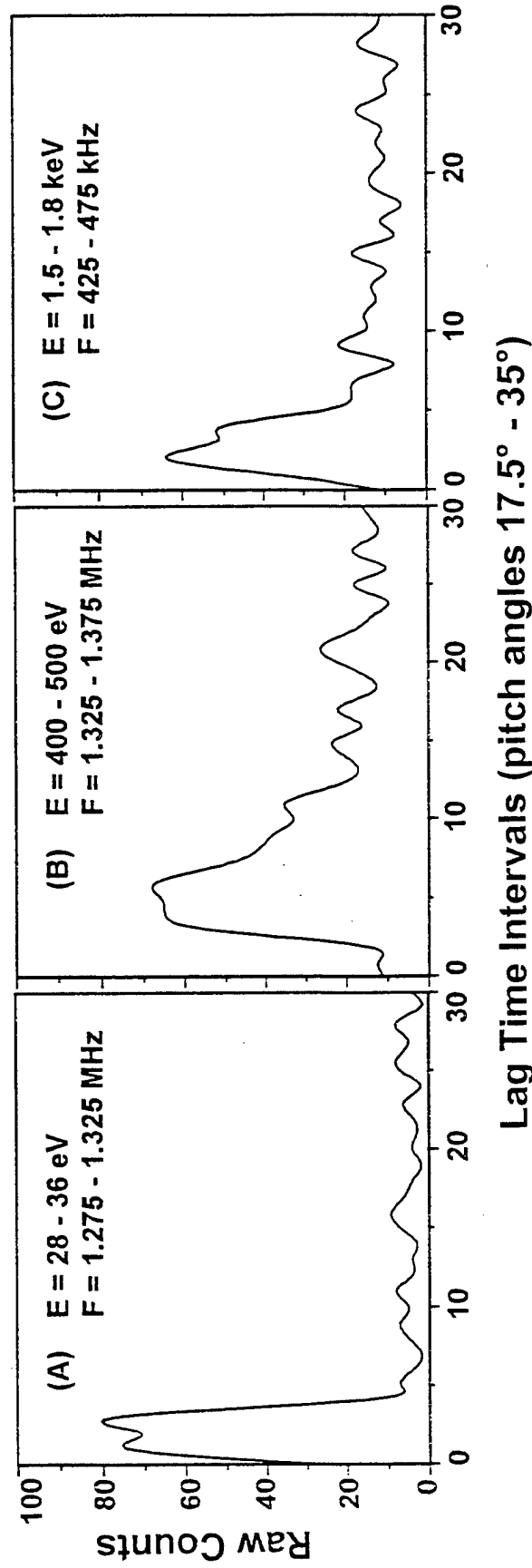


Figure 4. Electron cyclotron and plasma frequencies (top) as well as payload altitude in kilometers and tether length in meters (bottom) during OEDIPUS C upleg.



**Figure 5.** Examples of sounder accelerated electrons (SAEs) observed at both payloads during a single sounder sweep at intermediate pitch angles (17.5° - 35°). The plots show count rates as a function of lag time during a single energy and frequency step. These typical SAEs were observed simultaneously (A) at the Forward payload when  $\omega \approx \Omega_e$ , (B) at the Aft payload at the same time as that shown in A, and (C) at the Aft payload at  $\omega \approx \omega_{UH}$  during the same transmitter sweep as that in A and B.

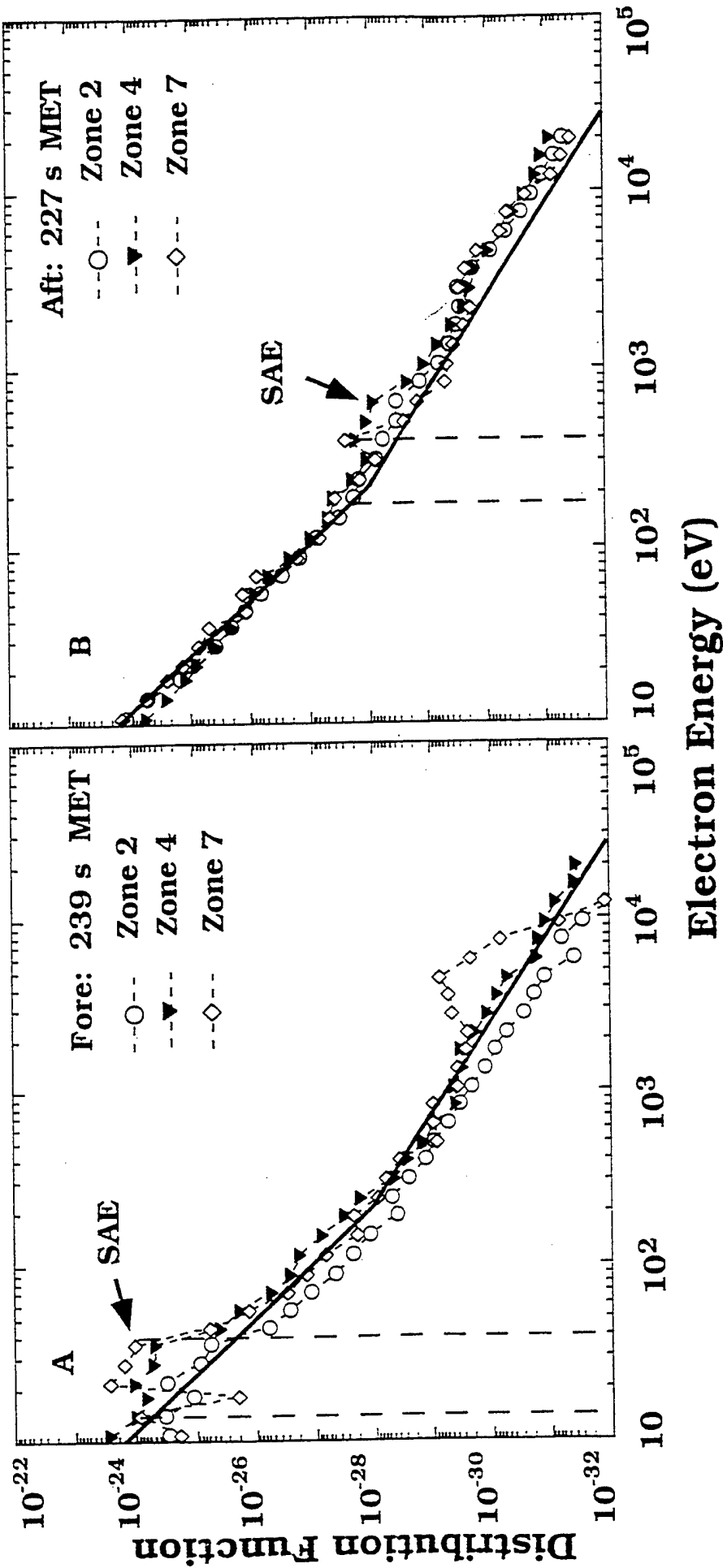


Figure 6. Electron distribution functions measured in zones 2 ( $0^\circ$ ), 4 ( $35^\circ$ ), and 7 ( $87.5^\circ$ ) of (A) EPI-F at 239 s TAL, and (B) EPI-A at 227 s TAL. Distribution functions of SAEs rise above those of background secondary auroral electrons. Solid lines denote the approximate fit we apply to the data.

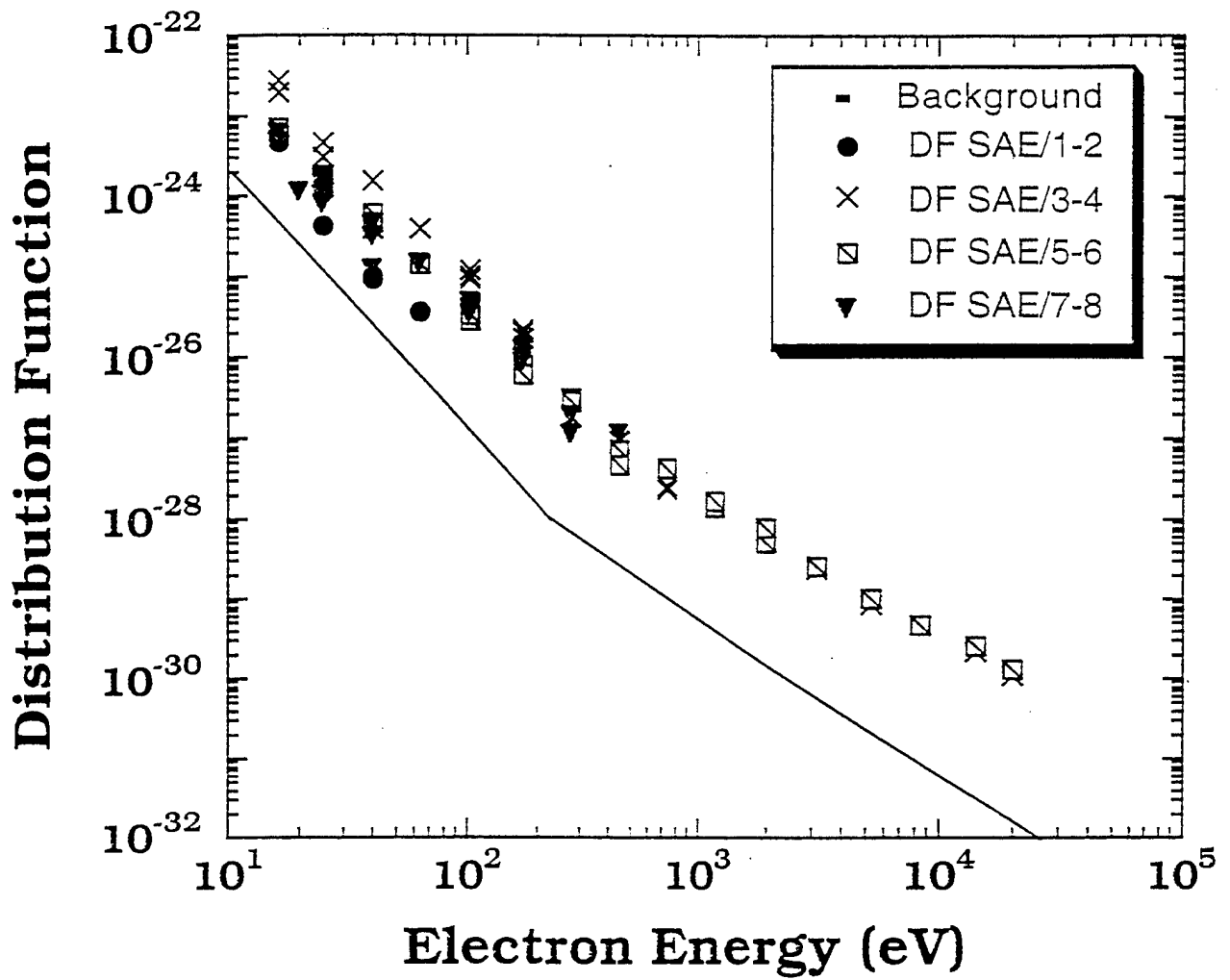
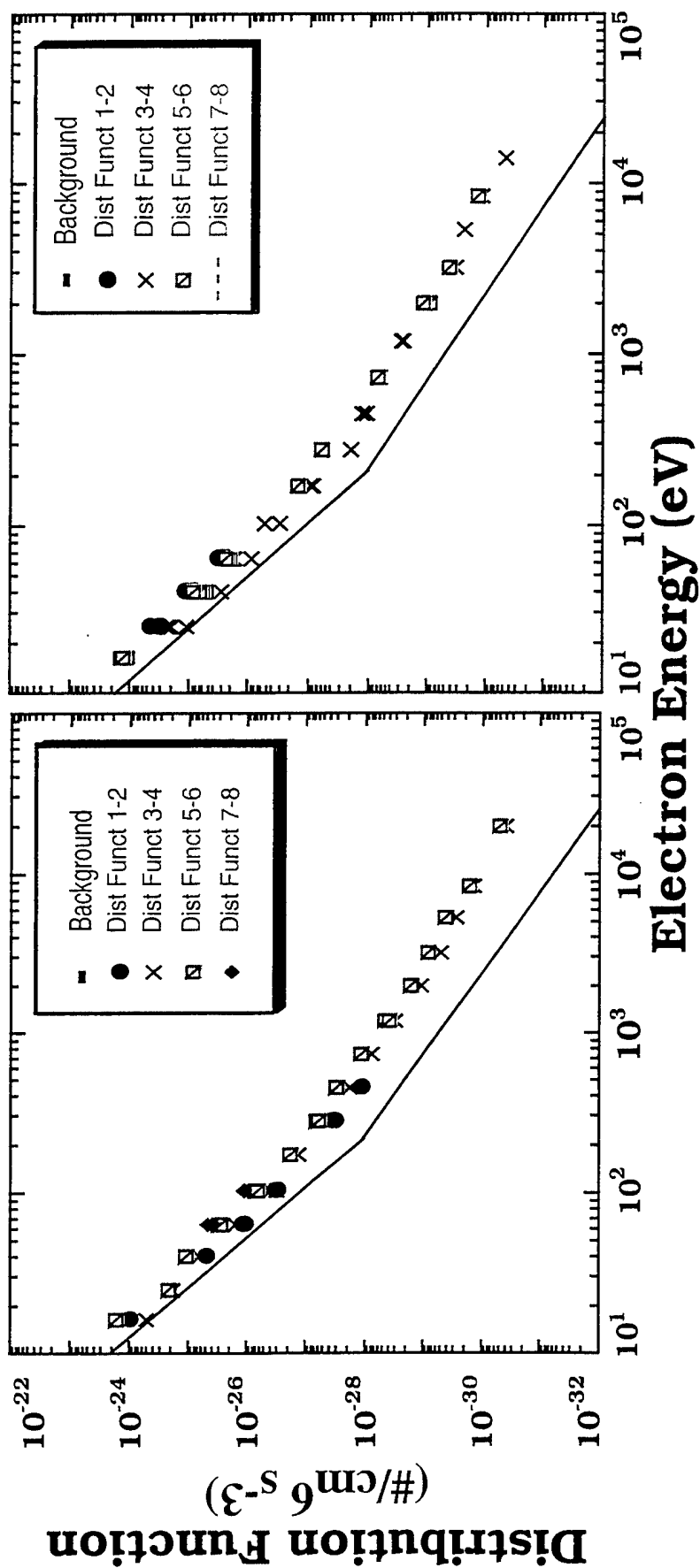


Figure 7. Distribution functions of SAEs observed by EPI-F between 200 and 260 s TAL. Calculated values were based on high time resolution measurements derived from correlator zone pairs while HEX emitted in the upper hybrid frequency band. The fitted line derived from the distributions shown in Figure 6 is repeated.



**Figure 8.** Distribution functions of SAEs observed by EPI-A between 200 and 260 s TAL using high time resolution measurements while HEX emitted in(A) upper hybrid and (B) whistler frequency bands. The fitted line derived from the distributions shown in Figure 6 is repeated.

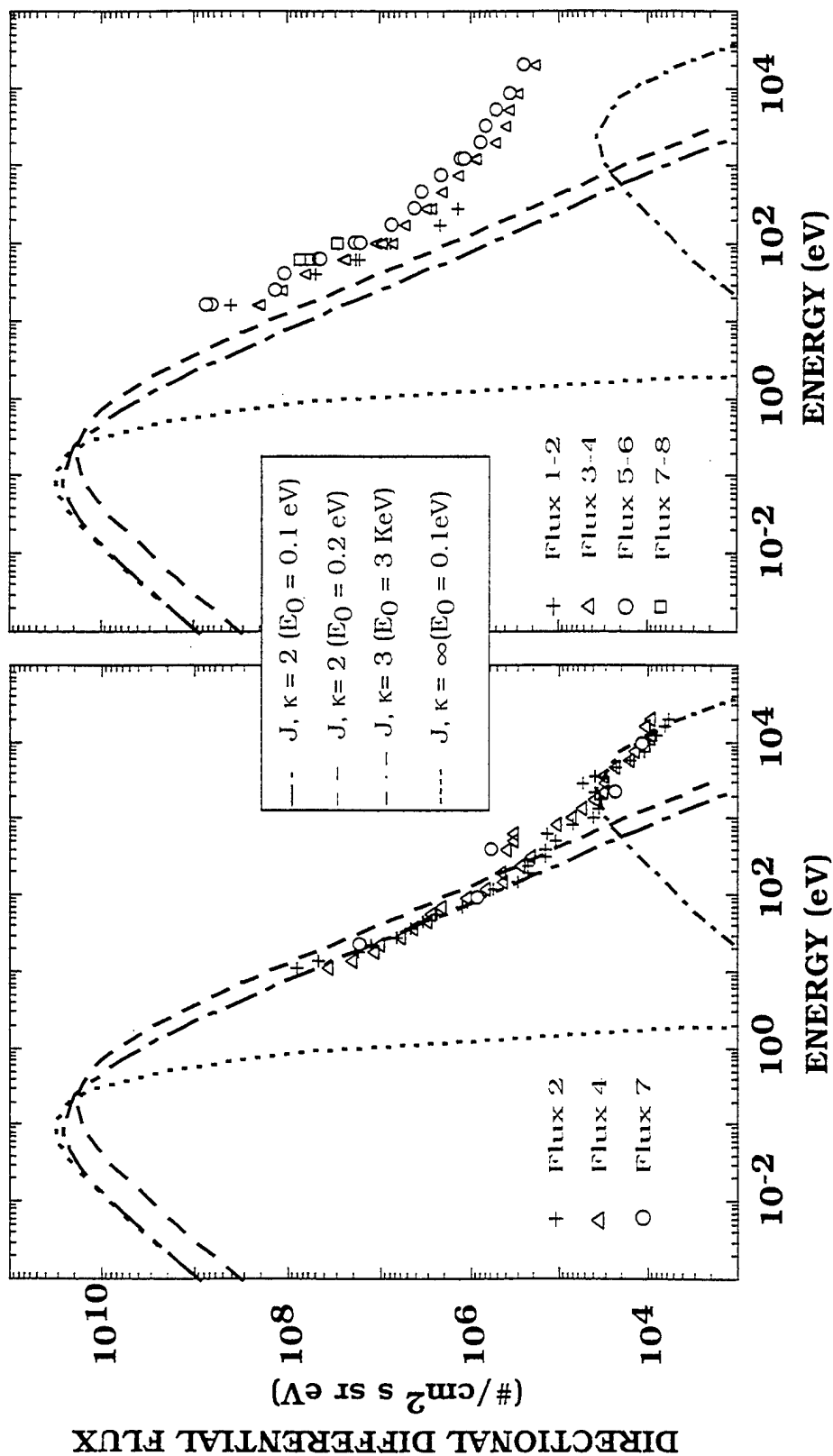
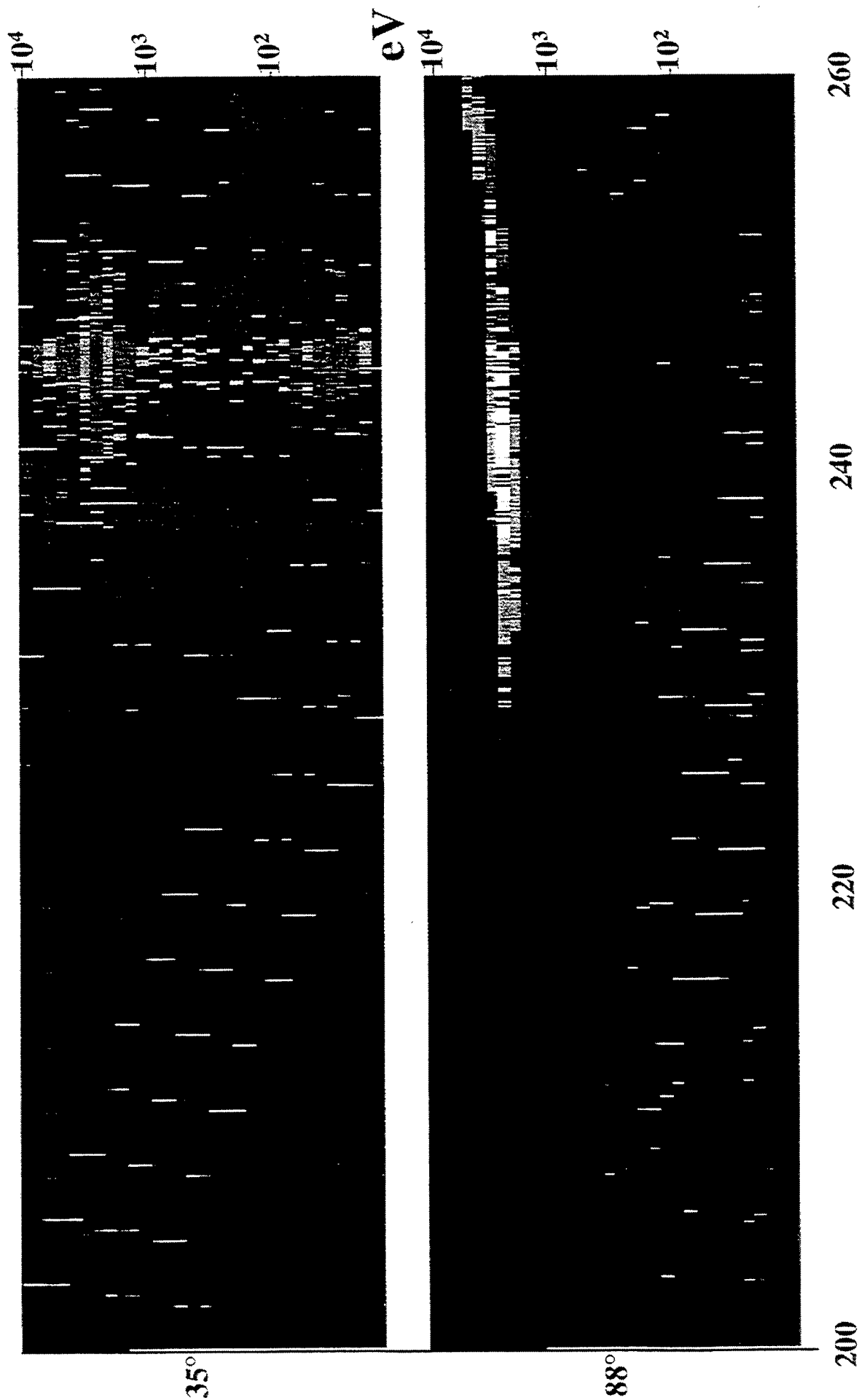


Figure 9. Directional differential flux for background auroral electrons and SAEs including (A) Maxwellian and kappa functions representing different electron energies plotted with observed auroral electron flux from the Aft payload and (B) differential fluxes for the SAEs in Figure 8A, together with the Maxwellian and kappa functions from 9A. The background electron distribution function is shown in Figure 6B.

# FORWARD PAYLOAD



TAL (Sec)

Plate 1. Energy versus time spectrograms for zones 4 (35°) and 7(87.5°) of EPI-F between 200 and 260 s TAL. Count rates are represented by different colors. Electron energies are presented on logarithmic scales extending from 10 eV to 20 keV. The maximum on this color bar is 75 counts in 3.03 ms.



# Theory of Plasma Waves Propagation and Electron Heating in a Tenuous Ionospheric Plasma

Elena Villalón<sup>1</sup>

Center for Electromagnetics Research, Northeastern University, Boston, Massachusetts

Short title:

---

<sup>1</sup>Also, at Air Force Research Laboratory, Hanscom AFB, Massachusetts

### Abstract.

Radiowave propagation and plasma heating are investigated for ionospheric plasmas under conditions such that the ratio between the plasma and gyrofrequencies  $Q = \omega_p/\Omega_e < 1$ . The situation is of interest to in situ rocket experiments, whereby the electric energy of the quasi-electrostatic wave fields is generally larger than the plasma kinetic energy and the non-linearity can modify the plasma density. The quasi-electrostatic W- and Z-modes are studied by including thermal corrections for frequencies near or below the unperturbed  $\omega_p$  and within the range  $\Omega_e$  through the upper hybrid  $\omega_{UH}$ , respectively. The refractive indices vary rapidly with the wave normal angles and with the plasma frequency which changes its value due to the ponderomotive force. Thus, there can exist a large number of eigenmodes which cannot be explained by the linear theory and whose frequencies fall within propagation regions of the linear W- and Z- plasma waves. These eigenmodes which are generated in density gradients and for all possible propagation angles, can efficiently interact with a wide range of electron energies and pitch angles. The isotropic distributions of secondary electrons ( $< 500$  eV) absorb their electric energy through Doppler-shifted resonant interactions at some harmonic of  $\Omega_e$ .

## 1. Introduction

Radio wave propagation and plasma heating are two intricately connected plasma problems of great interest to ionospheric and magnetospheric research. Here we address these problems for an auroral ionospheric plasma of low background plasma density. In fact if  $\omega_p$  and  $\Omega_e$  are respectively the electron plasma and gyrofrequencies, then we assume all through this paper that  $Q = \omega_p/\Omega_e < 1$ . Our research is partially motivated by certain experimental observations of the Oedipus C (OC) sounding rocket *Huang et al.* [1999]. We are interested in studying the resonant plasma eigenmodes which might be responsible for the acceleration of the electrons. In addition, we investigate the linear and non-linear theories that may explain the electron acceleration.

Briefly, the OC rocket consisted of double subpayloads which were formed by the transmitter and receiver, and whose antennas were aligned along the geomagnetic field. The unperturbed plasma frequency  $\omega_p$  fell monotonically from 0.6 to 0.1 MHz, and the gyrofrequency went from 1.1 to 1.3 MHz. The OC sounder emits RF pulses with a repetition rate of at least 300  $\mu$ s, over the frequency range of 25 kHz to 8 MHz. The electric fields were  $> 20$  V/m within short distances near the transmitter. The energetic particle instruments placed on the forward and aft subpayloads covered the energy range from 10 eV to 20 keV and measured pitch angles over a wide range of directions with respect to the geomagnetic field. Sounder accelerated electrons (SAE's) are fluxes of electrons which were accelerated by the electromagnetic energy of the RF pulses. As a matter of fact, SAE's get energized through the absorption of wave energy from the slowly propagating sounder-stimulated resonant plasma modes. This is because when the transmitter emitted frequencies that were near the major electron resonant frequencies, the RF pulses were capable of stimulating the resonant plasma waves. The radiated electric fields of the quasi-electrostatic waves interact efficiently with the electrons, which remain energized for several milliseconds even after the end of the pulse.

Under the cold plasma approximation a wave of frequency  $\omega$  and wave vector  $k$  becomes quasi-electrostatic if the refractive index  $\eta = ck/\omega \rightarrow \infty$  *Oya* [1971]. The slowly propagating quasi-electrostatic modes can interact very efficiently with the electrons and accelerate them. The frequencies of these

waves and their propagation characteristics, differ depending on the value of the plasma parameter  $Q = \omega_p/\Omega_e < 1$  [Stiz, 1992]. As a matter of fact the observations for ionospheric experiments such as in ISIS [James, 1983] and others [Oya, 1970; Benson, 1982] differ on the values of the plasma frequency. Because plasma wave resonances are determined by the values of  $Q$ , SAE's are critically dependent on the parameters  $Q$  and  $P \equiv \omega/\Omega_e$  as shown by Serov *et al.* [1985] and by Shuiskaya *et al.* [1990].

The OC observations for electron acceleration took place when the sounder emitted frequencies within the range of propagation of the quasi-electrostatic W- and Z- plasma eigenmodes [Budden 1985]. Therefore for the Z-mode waves whose frequencies are near  $\Omega_e$  and the upper hybrid frequency  $\omega_{UH}$ , the electrons were accelerated over a large range of energies and pitch angles. In addition, acceleration by the W-mode waves at the subcyclotron frequencies  $\omega \leq \omega_p < \Omega_e$ , was observed only in the aft subpayload over a broad range extending a large fraction of a megahertz. There exists a minimum value of  $\omega_p \sim 0.4 \Omega_e$ , below which SAE's observations were not detected. Fundamentally, the electron distributions in the auroral plasma are formed by two different populations [Lyons and Williams, 1984]: (i) the low energy ( $< 500$  eV) secondary isotropic electrons, and (ii) the more energetic (from 1 up to 20 KeV) less populated primary electron distribution which might be anisotropic in pitch-angle [Arnoldy *et al.*, 1974]. In this paper we investigate secondary electrons acceleration which, according to the observations, gain an approximately constant fraction of their initial kinetic energy when interacting with the wave fields.

The paper is organized as follows: Section 2 contains the cold plasma Appleton-Hartree dispersion relation, and the frequencies of propagation are calculated for quasi-electrostatic waves as functions of the parameter  $Q = \omega_p/\Omega_e$  and the angle  $\theta$  between the wave vector  $k$  and geomagnetic field  $\mathbf{B}_0$ . In Section 3, we include first-order thermal corrections to the equations describing the quasi-electrostatic W- and Z-eigenmodes as done by Aubry *et al.* [1970], Sazhin [1993] and by Villalón [1989]. Because of the large electric fields we devote Section 4 to the study of the ponderomotive force, its effects on the background plasma density [Al'pert, 1983] and on the generation of other eigenmodes. Section 5 describes the heating of secondary electrons due to resonant interactions with a large number of

the quasi-electrostatic eigenmodes. Section 6 presents numerical calculations for wave propagation considering the thermal corrections and for the heating of secondary electrons. Section 7 contains the summary and discussion.

## 2. The Cold Plasma Equations

Let us consider a magnetized plasma with the  $z$ -axis which is vertically upwards and oppositely directed to the geomagnetic field  $\mathbf{B}_0$ . A wave of frequency  $\omega$  and wave vector  $k$  propagates in the plane  $x-z$ , at an angle  $\theta$  with respect to  $z$ . The group velocity which is in the direction of the ray forms an angle  $\beta$  with respect to  $z$ , and  $\alpha$  is the angle between the ray and wave normal; see Fig. 1 for the geometrical details. The wave propagates in a cold magnetized plasma, where the thermal speed  $v_{TH}$  is very small, i. e.  $v_{TH}/c \ll 1$ , and the density of the cold plasma is such that  $Q = \omega_p/\Omega_e < 1$ . The refractive index  $\eta = ck/\omega$ , is described by the Appleton-Hartree dispersion relation

$$A_o \eta^4 - B_c \eta^2 + C_c = 0 \quad (1)$$

For a cold plasma  $A_o = A_c$  and the other coefficients  $B_c$ , and  $C_c$ , are

$$\begin{aligned} A_c &= 1 - X \frac{1 - Y^2 \cos^2 \theta}{1 - Y^2} \\ B_c &= \frac{1}{1 - Y^2} [2(1 - X)^2 - 2Y^2 + XY^2 (\cos^2 \theta + 1)] \\ C_c &= \frac{1 - X}{1 - Y^2} (1 + Y - X) (1 - Y - X) \end{aligned} \quad (2)$$

where  $X = (\omega_p/\omega)^2$ . Let us define the unit vector  $\mathbf{b}_o = \mathbf{B}_0/B_o$ , then  $\mathbf{Y} = -\mathbf{b}_o \Omega_e/\omega$  is in the direction of  $z$  and  $\Omega_e > 0$  is the electron cyclotron frequency. We may approximate the solutions to (1) as the electromagnetic wave with  $\eta^2 = C_c/B_c \sim 1$ , and the quasi-electrostatic plasma wave with  $\eta^2 = B_c/A_c \rightarrow \infty$ . Here we study the latter case,  $\eta \gg 1$ , for which we must require that  $A_c \rightarrow 0$ . The quasi-electrostatic waves have frequencies which are given as functions of  $Q = X^{1/2}/Y$  and the angle  $\theta$  by solving for  $A_c = 0$  as Budden [1985]

$$\left(\frac{\omega}{\Omega_e}\right)^2 = \frac{1}{2} (1 + Q^2) \pm \frac{1}{2} \left[ (1 + Q^2)^2 - \frac{4Q^2}{\tan^2 \theta + 1} \right]^{1/2} \quad (3)$$

The ordinary and extraordinary plasma resonances correspond to the  $-$  and  $+$  signs in (3), and they fall within the regions of propagation for the W- and Z-modes, respectively. The W- and Z-eigenmodes have frequencies whose extent are  $0 \leq \omega \leq \omega_p$ , and  $\omega_{UH} \geq \omega \geq \Omega_e$ , which correspond to angles of propagation  $0 \leq \cos^2 \theta \leq 1$ , respectively. Here  $\omega_{UH} = (\omega_p^2 + \Omega_e^2)^{1/2}$  is the upper hybrid frequency, which for  $Q \leq 2/3$  is close to  $\Omega_e$ . Figure 2 depicts curves for the ordinary and extraordinary modes branches as related to the W- and Z-mode propagation regions, by assuming  $Q = \omega_p/\Omega_e = 0.66$ . The extraordinary modes propagate beyond the Z- and X-modes cut-offs as shown in the figure for  $X = 1 \pm Y$ . The Z-mode becomes quasi-electrostatic (shaded region) for the frequencies given in (3). The ordinary modes propagation regions extend to both the left and right of  $X = 1$ . The ordinary mode becomes quasi-electrostatic  $\eta \rightarrow \infty$ , in the region of propagation of the W-mode for  $X \leq 1$  (also shaded).

### 3. Thermal Corrections

The frequencies of quasi-electrostatic plasma waves for the W- and Z-modes are defined in (3) after solving for  $A_c = 0$  and then, in cold plasma theory,  $\eta \rightarrow \infty$ . Near plasma resonances the waves have short wavelengths which can be calculated by considering first order thermal corrections to the cold plasma dispersion relation. As a matter of fact the finite values of  $\eta$  are obtained by including contributions first order in  $\epsilon^2$  to the elements of the dielectric function, where  $\epsilon = v_{TH}/c$ . This leads to a finite value of the fourth order coefficient  $A_o$  which multiplies  $\eta^4$  in the Appleton-Hartree relation in (1). Then following the works of Villalon [1989] and Sazhin [1993], we get that the fourth order coefficient  $A_o$  becomes

$$\begin{aligned}
 A_o &= A_c - \eta^2 \left( \frac{v_{TH}}{c} \right)^2 A_{TH} + \eta^4 \left( \frac{v_{TH}}{c} \right)^4 \chi_{TH} \\
 A_{TH} &= \frac{X}{Y^2} \left[ \sin^4 \theta \left( \frac{-1}{1-Y^2} + \frac{1}{1-4Y^2} \right) + 3Y^2 \cos^4 \theta \right] \\
 &\quad + \frac{X}{2Y^2} \cos^2 \theta \sin^2 \theta \left[ -2 + \frac{1}{Y^2(1-Y)} V_{+1} + \frac{1}{Y^2(1+Y)} V_{-1} \right]
 \end{aligned} \tag{4}$$

where  $\chi_{TH}$  is given in (9) and

$$V_{\pm 1} = -Z_{\pm}^2 \frac{Y^2}{(-1 \pm Y)^2} W(Z_{\pm}) \quad (5)$$

where  $Z_{\pm} = (\omega \pm \Omega_c)/k_{\parallel} v_{TH}$  and  $W(Z_{\pm})$  is the plasma dispersion function, (see *Ichimaru* [1973]), which for  $|Z_{\pm}| \gg 1$  then  $W \rightarrow -1/Z_{\pm}^2$ . Because of the proximity to plasma resonances, to neglect the contribution of the imaginary part of  $W(Z_{\pm})$  in (5) and in the subsequent equations (6) to (8), we will assume that  $|Z_{\pm}| > 3$ ; in the numerical calculations of Sec. 6 we always check the validity of this assumption. For  $A_c \simeq 0$  and  $\eta^2 \gg 1$  the solutions to the dispersion relation (1) that correspond to the quasi-electrostatic plasma waves, are found from

$$A_{TH} \left( \frac{v_{TH}}{c} \right)^2 \eta^4 + B_c - \frac{C_c}{\eta^2} = 0 \quad (6)$$

Then if  $B_c$  is finite we put  $\eta \simeq \eta_{TH}$  where  $\eta_{TH}^2 = (-B_c/A_{TH})^{1/2} (c/v_{TH})$ , which is very large. If  $B_c \rightarrow 0$  and if  $|C_c/\eta_{TH}^2| \geq -B_c$ , then we need to solve a cubic equation for  $\eta$ . If the frequency  $\omega$  is slightly out of resonance because  $A_c$  has a finite but small value, we may approximate the solution to the dispersion relation as

$$\eta^2 \simeq \eta_{TH}^2 \left[ 1 + \frac{A_c}{(-B_c A_{TH})^{1/2}} \frac{c}{v_{TH}} + \frac{1}{\eta_{TH}^2} \frac{C_c A_{TH}}{-B_c} \right]^{1/2} \quad (7)$$

This approximation describes in a warm plasma, the refractive indices of the quasi-electrostatic W- and Z-waves, which otherwise will be infinite in the cold approximation. Since  $\eta_{TH}$  takes a finite but small value the group velocity along the wave vector,  $v_{g,k}$ , is not necessarily zero. This is to be contrasted with the cold plasma approximation for which  $\eta \rightarrow \infty$ , and then  $v_{g,k} \rightarrow 0$ .

If the group velocity becomes zero the wave electric fields may grow in time from the electrostatic energy of the RF-pulses radiated by the antennas. In fact, the quasi-electrostatic wave fields build up locally near the transmitter antennas and cannot propagate away to other parts of the plasma. This is also the situation found in absolute instabilities which grow as function of time locally within restricted plasma regions. On the other hand, it is usually assumed that absolute instabilities absorb the free energy that exists in the plasma instead of getting its growth energy from the antennas. In a warm plasma, due to the finite but small values of  $\eta_{TH}$ , the radiated wave fields may convect away as

functions of time from the source locations where the sounder-stimulated resonant plasma modes were created. The cases of absolute and convective sounder-stimulated plasma waves are studied in more details next by considering the contributions of the thermal corrections to the refractive indices and group velocities.

We investigate the limit  $\eta_{TH} \rightarrow 0$ , because of its relevance for the absolute growth of the radiated electric fields, as explained above. We call thermal instabilities when the coefficient  $A_{TH} \rightarrow 0$ . Then the thermal refractive index in (6) becomes infinite  $\eta_{TH}^2 \rightarrow \infty$  and the wave amplitudes can grow only in time without propagating away from the emitting antennas. Under the plasma conditions  $\omega_p < \Omega_e$ , we find that only the Z-mode for  $\omega$  near  $\omega_{UH}$ , satisfies the conditions  $A_c = 0$  and  $A_{TH} \ll 1$  necessary for thermal singularities. As a matter of fact consider the upper branch of the resonance curves in (3), which relates to the extraordinary waves whose frequencies are such that  $\omega_{UH} \geq \omega \geq \Omega_e$ . For  $\omega$  near  $\omega_{UH}$  and for  $\cos \theta \rightarrow 0$ , we may approximate

$$\begin{aligned} \tan^2 \theta &\simeq \frac{1}{3} (6 - 3Y^2 + Y^4) \frac{4Y^2 - 1}{(1 - Y^2)^2} \\ A_{TH} &\simeq 3X \cos^4 \theta \end{aligned} \quad (8)$$

For the thermal plasma resonances  $A_{TH}$  becomes very small as  $\cos \theta \rightarrow 0$ , and  $\eta_{TH} \rightarrow \infty$  for  $\omega$  near  $\omega_{UH}$ . However the component  $\eta_{||}$  of the thermal refractive index may still be small ( $\ll \eta$ ) since then  $\theta \simeq \pi/2$ . The refractive index for the thermal plasma resonances must be calculated considering corrections second order in  $\epsilon^2$ , and then  $\eta^2 \sim \epsilon^{-4/3} (B_c/\chi_{TH})^{1/3} \gg \eta_{TH}^2$ . Here

$$\begin{aligned} \chi &= \sin^2 \theta \cos^3 \theta \frac{(-15Y^2 + 17Y^4 - 6Y^6)}{(1 - Y^2)^3} \\ &+ \sin^2 \theta \cos \theta \frac{(-15Y^2 + 7Y^4 - 4Y^6)}{(1 - Y^2)(1 - 4Y^2)} \end{aligned} \quad (9)$$

The group velocity is obtained in terms of the cold plasma coefficients,  $A_{TH}$ , and their derivatives with respect to the wave frequency  $\omega$ . By considering the following

$$\eta' \simeq \frac{1}{2B_c + 4\eta^4 (v_{TH}/c)^2 A_{TH}} \eta^3 \omega \frac{\partial A_c}{\partial \omega} \quad (10)$$

The group velocity component along the wave normal  $k$  is  $v_{g,k} = c/\eta'$ . Note that as  $\eta' \gg 1$  then



$\vartheta_{g,k}/c \sim 1/\eta^3 \ll 1$ . Also as  $A_{TH} \rightarrow 0$  one gets  $\eta' \rightarrow \infty$  and then  $\vartheta_{g,k} \rightarrow 0$ .

The ray group velocity along the direction of propagation is  $\vartheta_g = \vartheta_{g,k}/\cos \alpha$ . The angle  $\cos \alpha$  is given in function of the derivative of the refractive index with respect to the wave angle  $\theta$  as [Budden, 1985] :  $\tan \alpha = (\partial\eta/\partial\theta) \eta^{-1}$ . For  $\cos \theta \sin \theta > 0$  we find that  $\vartheta_g/c \sim \cos \theta \sin \theta \eta^{-1}$  which is also small for  $\eta$  large. In fact for thermal plasma resonances, if  $\eta_{TH} \rightarrow \infty$  then  $\vartheta_g$  becomes very small and accordingly, the waves electric field can increase their amplitudes locally near the emitting antennas as function of time.

## 4. The Ponderomotive Force

Let us consider the normalized electric field amplitudes

$$\mathcal{E} = \frac{q}{m_e \Omega_e c} |\mathbf{E}|, \quad (11)$$

The same normalization applies for the three components of the electric field  $\mathbf{E}$ , along  $x$ ,  $y$ , and  $z$  directions as denoted by  $\mathcal{E}_i$ ,  $i = 1, 2, 3$ , respectively. Now consider that  $P$  is the power flux density (Watts / m<sup>2</sup>), and  $\mathcal{W}_k$  the energy density of waves. We consider the energy transfer to the quasi-electrostatic fields in the direction of the wave normal  $\mathcal{W}_k = P/\vartheta_{g,k}$ . From the thermal dispersion relation we find

$$\begin{aligned} \frac{P}{c} &= -\Upsilon |E|^2 \\ \Upsilon &= \frac{1}{8\pi} \left[ 2 \left( \frac{v_{TH}}{c} \right)^2 \eta A_{TH} - A_c \frac{1}{\eta} + C_c \frac{1}{\eta^5} \right] \end{aligned} \quad (12)$$

Note that for  $A_c \rightarrow 0$  and  $\eta \gg 1$ , the electric fields become very large near  $\omega_{UH}$  since then  $A_{TH}$  and  $\Upsilon \rightarrow 0$ . Furthermore, the cold plasma theory shows that near  $\omega_p$ ,  $B_c \rightarrow 0$ , which is due to the occurrence of a cut-off and a plasma resonant mode simultaneously. The thermal refractive index, which is very large, sharply turns  $\eta_{TH} \rightarrow 0$  as  $\omega$  approaches the plasma frequency. As a result, the electric fields can also be very large near  $\omega_p$  if  $\Upsilon \sim 0$ .

Because of the radiation pressure of the large electric fields, the resulting ponderomotive potential,  $\Phi_p$ , effectively yields a change in the background plasma density. Here  $\Phi_p$  is normalized to  $T_e^{-1}$  so that

the changes in the cold plasma density are given by

$$n_e = n_i = N_c \exp \left( -\frac{\Phi_p}{1 + T_i/T_e} \right) \quad (13)$$

where  $T_{e,i}$  refers to the background electron and ion temperatures. The modified plasma frequency  $\tilde{\omega}_p$  can be obtained after substituting the plasma density by the expression in (13); as  $n_e \rightarrow N_c$  then  $\tilde{\omega}_p \rightarrow \omega_p$  which is the unperturbed plasma frequency. The ponderomotive potential is calculated as function of the tensor  $\underline{\delta}$  which is related to the mobility tensor. In terms of the dielectric tensor,  $\underline{\epsilon}$ , we find that  $\underline{\delta} = -i(Y^2/X)(\underline{\epsilon} - \underline{1})$ , Ichimaru [1973]; the tensor components are denoted by  $\delta_{i,j}$ , where  $i, j = 1, 2, 3$ . We find

$$\Phi_p = \frac{1}{4} \left( \frac{c}{v_{TH}} \right)^2 \sum_{i=1,3} \delta_{i,i} |\mathcal{E}_i|^2 + \frac{1}{4} \left( \frac{c}{v_{TH}} \right)^2 \sum_{i=1,3} \sum_{j>i} \delta_{i,j} [\mathcal{E}_i^* \mathcal{E}_j + (-1)^{i+j} \mathcal{E}_i \mathcal{E}_j^*] \quad (14)$$

with  $i, j = 1, 2, 3$  corresponding to the  $x, y$ , and  $z$  components. For a cold plasma the dielectric components are  $\epsilon_{1,1} = \epsilon_{2,2} = 1 - X/(1 - Y^2)$ ;  $\epsilon_{3,3} = 1 - X$ ;  $\epsilon_{1,2} = \epsilon_{2,1} = iXY/(1 - Y^2)$ ; and the rest of them are zero [Al'pert, 1983]. As an example, we assume that the electric field is 20 V/m and that  $v_{TH}/c = 0.001$ . Under these conditions  $\mathcal{E}(\mathcal{T}\mathcal{H}) \equiv 0.5(c/v_{TH})\mathcal{E} = 1$ , and the changes in the background plasma density are very significant.

As a matter of fact the electric fields which are created by in situ rocket experiments and which are detected by the antennas, can be very large ( $> 20$  V/m) near the plasma surrounding the transmitter. Thus at a few wavelengths near the transmitter the plasma could be very inhomogeneous with rapid changes in the density. The theory of plasma eigenmodes presented in the last section must be complemented by incorporating the density gradients created by the ponderomotive force. Because of a decreasing density the values that the non-linearly modified factor,  $Q = \tilde{\omega}_p/\Omega_e$ , can take near the launching antennas may change rapidly within short distances. As a result, the quasi-electrostatic waves which are excited non-linearly due to decreasing values of  $Q$  have frequencies which are always within the range of propagation for the linear W- and Z-eigenmodes. Henceforth we understand the refractive indices of the linear W- and Z-eigenmodes as well as  $\omega_p$  and  $X$ , represent values which are calculated for the unperturbed plasma density which does not account for ponderomotive effects.

## 5. Electron Heating

In an ionospheric plasma we have two distinct electron populations of the auroral (primary) and the backscatter (secondary) electrons. They can interact with the nearby electric fields that have been described by the theory of eigenmodes in the previous three sections. The majority of electrons belong to the secondary population whose energies range from 10 eV to about 500 eV. The primary or auroral electrons have energies from approximately 1 keV up to above 10 keV, and their distribution functions can be anisotropic in pitch angle. Here we restrict our investigations to electron heating by the W- and Z-eigenmodes for the less energetic but more numerous populated secondary electrons.

In all cases particles and waves must satisfy the resonance condition

$$\omega - n\Omega_e/\gamma_R = k_{\parallel}v_{\parallel} \quad (15)$$

where  $n$  is the harmonic number, and  $\gamma_R$  is the relativistic factor. Here  $k_{\parallel}$  and  $v_{\parallel}$  are the components along  $z$  which is oppositely directed to the geomagnetic field, of the wave normal and the particle velocity, respectively. Efficient interactions between the low energy secondary electrons and the quasi-electrostatic W- and Z- plasma eigenmodes require that  $n = 0$  or  $1$ , for  $k_{\perp}\rho \ll 1$  where  $\rho$  is the Larmor radius. Note that wave vectors  $k_{\parallel}$ 's which contribute to the resonance condition in (15), can be derived from either linear or non-linear wave theory. For linear theory the background plasma density is unperturbed. Nevertheless, as explained in Sec. 4, the non-linearities introduce plasma density gradients and a larger number of resonant eigenmodes that depend on the local values of  $Q$ . Non-linear eigenmodes can be obtained by solving (3) through (6) with  $Q$  varying as function of the non-linearly modified plasma frequency  $\tilde{\omega}_p$  which decreases with the plasma density as explained in Sec. 4.

The distribution functions of secondary electrons are mainly isotropic in pitch angle, and decrease with energy as a power law. We consider the following model for the distribution functions of secondary electrons which is consistent with experiments,

$$f(v) = \frac{K_s}{w_{\kappa}^{3/2}} \frac{1}{(1 + v^2/w_{\kappa})^{\kappa+1}}$$

$$K_s = \frac{N_s}{\pi^{3/2}} \frac{\Gamma(\kappa + 1)}{\Gamma(\kappa - 1/2)} \quad (16)$$

where  $\kappa > 2$  is the exponent of the differential flux which also contributes in the Gamma functions  $\Gamma$ . Here  $\sqrt{w_\kappa}$  is the most probable speed of resonant electrons. The conservation of total energy in the plasma due to interactions between waves and particles, require that over time the following equation is satisfied *Stix* [1992]

$$\frac{d}{dt} \left[ 2\pi m_e c^2 \int_{v_m}^{\infty} f(v) (\gamma_R - 1) v^2 dv + \mathcal{W}_k \right] = 0 \quad (17)$$

where  $\mathcal{W}_k$  is the energy density of waves; here,  $v_m$  is the smallest resonant velocity which is obtained from (15) for  $\cos \theta = 1$  and for a spectrum of waves centered around  $k$  and  $\omega$ . In fact, the experimental observations of the OC rocket, shows that the amount of energy an electron can gain is proportional to the electron's initial kinetic energy. In order to explain these observations we consider the effects that the distribution functions have upon the energy increment of a single electron. Actually, equation (17) effectively demonstrates that the wave energy must be divided over time among the total population of secondary electrons. In addition, since  $f(v)$  is isotropic, electrons with the same initial kinetic energies will increment their energies by similar amounts. The energy density of waves changes in time as  $\mathcal{W}_k \sim \exp(-2\gamma_D t) |E|^2$ , where  $\gamma_D$  is the linear damping rate *Kennel and Wong* [1967]. See the Appendix for an approximate expression of the damping rate which depends on the derivative of  $f(v)$ .

Next, we want to investigate the energy gain by a single electron interacting with the quasi-electrostatic fields. Because of the collective effects mentioned above, we assume that the electric field amplitudes are not constant independent of time yet, that instead, they decrease their values with time. This is due to multiple resonant interactions with the overall population of secondary electrons which damp the waves out. A consequence of this multiple interactions is to restrict the amount of energy an electron can gain. We normalized the linear damping rates as  $\hat{\gamma}_D = 2\pi|\gamma_D|/\Omega_e$ . The normalized electric field amplitudes are given in (11) and we define the perpendicular and parallel components as:  $\mathcal{E}_\perp = \sqrt{2} \mathcal{E} \sin \theta$  and  $\mathcal{E}_\parallel = 2 \mathcal{E} \cos \theta$ , respectively. The amplitudes of the electric field components are

reduced as function of time due to the resonant interactions, we put

$$\Sigma_{\perp, \parallel}(\tau) = \exp(-\hat{\gamma}_D \tau) \mathcal{E}_{\perp, \parallel} \quad (18)$$

where time is normalized so that  $\tau = t \Omega_e / 2\pi$ . Here,  $\mathcal{E}$  is the constant normalized electric field defined in (11) for  $\tau = 0$ .

The theory of Hamiltonian potential wells was developed by *Villalón and Burke* [1987], *Villalón* [1989], and *Ginet and Heinemann* [1990]. It gives an estimate of the energy a single electron can gain by resonant interactions with the quasi-electrostatic fields. Here we modify the theory of Hamiltonian potential wells to include the temporal dependences of the electric fields due to linear damping from the distribution functions in (16). We call  $U = (\gamma_R - \gamma_o)/\gamma_o$  the normalized electron energy where  $\gamma_R$  and  $\gamma_o$  are the relativistic factors at anytime during the interaction and for  $\tau = 0$ , respectively. For a given isolated harmonic  $n$  the evolution of the electron energy with time is obtained solving for

$$(U + 1)^2 \left( \frac{dU}{d\tau} \right)^2 + V_n(U, \tau) = 0 \quad (19)$$

with  $n = 0, \pm 1, \pm 2, \dots$ . The potential wells are discussed extensively in the references given above. By solving for  $V_n(U, \tau \rightarrow 0) = 0$ , we find the maximum values that the energy of the resonant electron can reach in terms of the initial electric fields amplitudes and the initial particles' conditions. For quasi-electrostatic fields we find

$$\begin{aligned} \frac{1}{\pi^2} V_n(U, \tau) &= U^4 - \Sigma_{\parallel}^2(\tau) K_n(U) - \Sigma_{\perp}^2(\tau) [K_{n+1}(U) + K_{n-1}(U)] \\ K_n(U) &= \int_0^U J_n^2(k_{\perp} \rho') (1 + U') dU' \end{aligned} \quad (20)$$

where the Bessel functions are evaluated for the Larmor radius  $\rho' \equiv \rho(U')$ . We can further estimate for the gyroharmonics  $n = 0, 1$ , the potentials  $V_n(U, \tau)$  by assuming that the arguments of the Bessel functions are small which leads

$$V_{0,1} = \pi^2 U \left[ U^3 - \Sigma_{\parallel, \perp}^2(\tau) \right] \quad (21)$$

Next, we discuss the implications that the assumption in (18) of time-dependent electric fields has on the theory of Hamiltonian potential wells as given by (19) and (20). For reasons of comparison, let

us study the case  $\hat{\gamma}_D \rightarrow 0$  so that the electric field amplitudes are now constant independent of time, i. e.  $\Sigma(\tau) \rightarrow \mathcal{E}$ . From (21) we obtain the maximum energy an electron can gain as  $\tilde{U}_o = \mathcal{E}_p^{2/3}$  with  $p = \perp, \parallel$  for the resonances  $n = 1, 0$ , respectively. The time it takes to reach the maximum energy gain  $\tilde{U}_o$  is calculated from the analysis by *Ginet and Heinemann* [1990]:

$$\tau_c = \frac{1}{\pi \mathcal{E}^{2/3}} \int_0^1 \frac{d\hat{Z}}{[\hat{Z}(1 - \hat{Z}^3)]^{1/2}} \quad (22)$$

where  $\hat{Z} = U/\mathcal{E}_p^{2/3}$ . Hence we get  $\tau_c \sim 0.75 \mathcal{E}_p^{-2/3}$ , with  $\mathcal{E}_p$  standing either for the perpendicular,  $p = \perp$ , or parallel,  $p = \parallel$ , components. Thus particles of different initial kinetic energies can be accelerated up to the maximum energy  $\sim \mathcal{E}^{2/3}$  over a period of time equal to  $\tau_c$ .

As an example we assume that the electric field is  $|E| = 20$  V/m, and then from (11) one gets  $\mathcal{E} = 2 \times 10^{-3}$  for  $\Omega_e = 1$  MHz. By assuming constant electric fields, i. e.  $\gamma_D = 0$ , the total energy gain by an electron is  $\tilde{U}_o = 0.016$ . This corresponds to 8.15 KeV, and requires a total interaction time of about  $\tau_c = 50$  gyroperiods. However, the OC observations show that electrons can only increase their energies by an amount which is proportional to their kinetic energy and which is always smaller than the maximum energy,  $\tilde{U}_o$ , allowed for constant electric fields. In addition, it also shows that this happens over interactions times of about less than a few gyroperiods. In order to understand these experimental results we assume that, during their interactions with the waves, an electron increases its energy by the limited amount  $\Delta K$ . The energy increment  $\Delta K$  which is normalized to  $(mc^2)^{-1}$  and derived from the experimental results, is such that  $\Delta K \ll \tilde{U}_o$ . Since for secondary electrons  $\hat{Z} \ll 1$ , the time it takes to increase the energy by  $\Delta K$  is approximately given by  $\tau_l \sim 2/(\pi\mathcal{E}) \sqrt{\Delta K}$ . The latter approach can reasonably be used to predict the increment in electron energies if the number of gyroperiods is small  $\tau_l \ll \tau_c$  in agreement with observations.

Our previous discussions effectively demonstrate that the theory which is described by the Hamiltonian potentials with  $\gamma_D = 0$  is incomplete. As shown above, the approximation of constant electric fields gives reasonably good estimates of acceleration times under assumptions of limited energy gain  $\Delta K$  for the electrons, i. e.  $\Delta K \ll \tilde{U}_o$ . Yet it does not account for the restrictions that the electrons can only increment their energy by this relatively small amounts. This is because under the

limit  $\gamma_D \rightarrow 0$ , the collective effects of the overall electron population upon the wave amplitudes are essentially ignored. To include those effects we have developed model equations in (19) and (20), in terms of electric fields amplitudes which are depleted in time. This approximation is unique because it requires knowledge of the background distribution functions of electrons and its derivative with respect to  $v$ , to find out the actual energy gain by a single electron. For small values of  $\gamma_D$ , the approximation yields that the actual energy gain by an electron is

$$\tilde{U}_D \simeq \frac{2}{3} \frac{\mathcal{E}^{4/3}}{\hat{\gamma}_D} \left[ 1 - \exp\left(-\frac{3}{2} \frac{\hat{\gamma}_D}{\mathcal{E}^{2/3}}\right) \right] \quad (23)$$

Thus, due to the reduced amplitudes of the electric fields, an electron gain less energy than that predicted by the original unperturbed Hamiltonian theory of *Villalón and Burke* [1987]. In fact, for small damping  $\hat{\gamma}_D \rightarrow 0$ , we recover the results of the unperturbed theory  $\tilde{U}_D \rightarrow \tilde{U}_0 \sim \mathcal{E}^{2/3}$ . For strong damping  $\hat{\gamma}_D \gg \mathcal{E}^{2/3}$ , we obtain  $\tilde{U}_D \rightarrow 2/3 (\mathcal{E}^{4/3}/\hat{\gamma}_D)$ , and then  $\tilde{U}_D \ll \mathcal{E}^{2/3}$ . Since damping rates are proportional to the number of electrons the most populated parts of the distributions can in overall increase their energy more than less populated ones. However the energy increment per electron can be small for the large population because that energy must be divided among more particles.

## 6. Numerical examples

To illustrate the theoretical analysis of previous sections, we consider wave eigenmodes that propagate in a tenuous ionospheric auroral plasma, where the plasma frequency is always smaller than the electron gyrofrequency, such that  $\Omega_e \sim 1.2$  Mhz. In our calculations we take three different values for the ratio  $Q = \omega_p/\Omega_e = 0.33, 0.66$ , and  $0.85$ , and as an example we assume that  $v_{TH}/c = 0.001$ . The frequencies of resonant plasma modes which can heat the ambient electrons are described by (3) and depicted in Fig. 2.

Figure 3 represents the frequencies  $\omega/\Omega_e$  of the quasi-electrostatic W- and Z-modes ( $\eta \rightarrow \infty$ ) as functions of  $\cos \theta$ ; where  $\theta$  is the angle between  $\mathbf{k}$  and  $z$  (oppositely directed to  $\mathbf{B}_0$ ). They are the solutions to equation (3) for the three different values of  $Q$  as indicated. The curves below  $\omega/\Omega_e = 1$

are the ordinary plasma wave resonances (W-modes) for three values of  $\omega_p/\Omega_e$  as indicated. Note that as  $\omega \rightarrow \omega_p$ ,  $\cos \theta \rightarrow 1$  and as  $\omega \rightarrow 0$  then  $\cos \theta \rightarrow 0$ . For the extraordinary branch of Z-mode plasma resonances we have that when  $\omega \rightarrow \Omega_e$ ,  $\cos \theta \rightarrow 1$  and when  $\omega \rightarrow \omega_{UH}$  then  $\cos \theta \rightarrow 0$ .

The refractive indices  $\eta$  for these eigenmodes are infinite in cold plasma theory, and we need to consider the thermal corrections to find out the finite values for  $\eta$ ; we take  $v_{TH}/c = 0.001$  which corresponds to  $\sim 2900^\circ$  K. The values of  $\eta^2 \sim c/v_{TH}$  are obtained by solving for (6). Figure 4 represents the parallel components  $\eta_{\parallel}^2 = (\eta \cos \theta)^2$  of the W-eigenmodes versus frequency  $\omega/\Omega_e$ , for  $\omega \leq \omega_p$  and three values of  $Q = \omega_p/\Omega_e$ . Once the refractive indices are known in a warm plasma approximation, we can solve for the resonance condition in (15) which furnishes the energies and  $v_{\parallel}$  of the resonant electrons. For the first gyroharmonic  $n = 1$ , Fig. 5 represents the resonant parallel velocities of electrons interacting with the W-eigenmodes,  $v_{\parallel} = v \cos a$  normalized to  $c^{-1}$  versus  $\omega/\Omega_e$ , where  $a$  is the particle's pitch-angle. Note that  $v_{\parallel}$  may be in the range of energies of the auroral beam population if  $Q \geq 0.66$ , implying  $\omega$  close to  $\omega_p$ . When the plasma density is low so that  $Q \leq 0.33$ , then  $v_{\parallel}$  is so large that interactions are not possible with the available electron populations. This situation may be created by density depletions as produced by the large electric fields due to the ponderomotive force, which may not allow for electron acceleration near the transmitter. Other gyroharmonics will not be represented here but the Landau resonance leads to  $v_{\parallel}/c = \eta_{\parallel}^{-1} \sim (c/v_{TH})^{1/2}$ , and values for  $v_{\parallel}/c$ , can be obtained from the results in Fig. 4.

Within the extraordinary branch the Z-eigenmodes are such that their frequencies extent is  $\Omega_e \leq \omega \leq \omega_{UH}$ . For the Z-modes, Fig. 6 represents the refractive indices versus  $\omega/\Omega_e$  considering the three values of  $Q = 0.33, 0.66$ , and  $0.85$ . The upper panel contains  $\eta^2$  as obtained solving for (6). The lower panel  $\eta_{\parallel}^2 = \eta^2 \cos^2 \theta$ , where  $\cos \theta = 1$  and  $0$  for  $\omega = \Omega_e$ , and  $\omega_{UH}$ , respectively. In all cases presented in this paper we require that the waves were not heavily damped and then that the argument of the plasma function in (5) was such that  $|Z_{\pm}| > 3$ . Those modes near the electron gyrofrequency are strongly Landau damped,  $|Z_{\pm}| < 3$ , which leads to the kind of spiky behaviour near the gyrofrequency as shown in the figures. Near the upper hybrid the refractive indices are very large because  $A_{TH} \rightarrow 0$ .



However the parallel components  $\eta_{\parallel}$ , are not so large since those waves propagate almost perpendicular to  $\mathbf{B}_0$ .

Figure 7 represents the resonant parallel velocities of electrons which interact with the Z-eigenmodes versus  $\omega/\Omega_e$ . The  $v_{\parallel}$ 's are obtained from (15) by assuming interactions with the first gyroharmonic  $n = 1$ . We see that they are smaller than those found for the W-eigenmodes. We can also obtain for other gyroharmonics the resonant velocities  $v_{\parallel}$ , but these are not represented here.

The propagation of the W- and Z- eigenmodes are described by the group velocities  $\mathbf{v}_g$  and the angle  $\beta$  with respect to  $z$  which is oppositely directed to the geomagnetic field. Here  $\alpha$  is the angle between  $\mathbf{k}$  and  $\mathbf{v}_g$ . Figure 8 represents the cosines of the angles  $\theta$ ,  $\alpha$ , and  $\beta$ . The upper and lower panels correspond to the W- and Z-modes, respectively. In both panels we take  $\omega_p/\Omega_e = 0.66$ , similar behaviour is found for the others values of  $Q$ . For the W-mode we always find that for  $X < 1$ ,  $\cos \alpha \simeq 0$ . In addition, near  $\omega_p$  the W-modes have group velocities almost perpendicular to the geomagnetic fields and then, electron acceleration may be observed near the transmitter. For the Z-mode, as shown in the lower panel, the group velocity angle  $\beta$  with respect to  $z$  is very close to the field line which allows acceleration to be detected by both subpayloads.

Figure 9 describes some calculations for the secondary electron population, whose energies  $< 500$  eV. The experimental OC observations show that electrons effectively increased their energy by about a factor of two. Accordingly, we estimate the time (in number of gyroperiods) that it takes for an electron to double its initial kinetic energy,  $K$  given in eV, versus  $\ln(K)$ . To calculate the interaction time we use the Hamiltonian equations in (19) through (22). As an example, we assume a constant value of  $E = 20$  V/m. In general, if the electric fields were not depleted by their interactions with the plasma, an electron could gain approximately 8 keV over many gyroperiods as discussed in Sec. 5. Nevertheless it takes less than a few gyroperiods to double the kinetic energy of secondary electrons.

The numerical calculations just presented illustrate that generally the theory of warm plasma eigenmodes for the W- and Z- plasma waves is consistent with OC experimental observations. The large refractive indices extend over a broad range of propagation angles and can interact with many electrons

of different energies and pitch angles. The analysis for secondary electron acceleration was presented in Section 5 and compare with the experimental observations. Although in the numerical applications we only treat constant electric fields, we came out with interactions times which were small (i. e. a few gyroperiods), and which allowed to increment the electron energies by the amounts predicted by the experiments. We leave for future work the more detailed investigations that consider the particle distribution functions and that apply some of the concepts introduced in Section 5. By using the damping rates that deplete the electric fields in time we incorporate the contribution of distribution functions of electrons. These distributions functions can determine intrinsically the energy increments of a single electron in terms of their parameters and those of the plasma.

## 7. Summary and Discussion

We have presented a theory to explain the propagation of radiowaves and plasma heating in a tenuous auroral plasma. The ratio between the plasma and electron cyclotron frequencies was  $Q = \omega_p/\Omega_e \leq 0.5$ . From cold plasma theory, the quasi-electrostatic waves of the ordinary and extraordinary branches fall within the propagation regions for the whistler (W-) and Z- eigenmodes, and their frequency ranges are  $\omega \leq \omega_p$  and  $\Omega_e \leq \omega_{UH}$ , respectively. Our main contributions are:

1) We include first order thermal corrections ( $v_{TH}/c \ll 1$ ) to obtain the refractive indices  $\eta$ , and wave amplitudes of quasi-electrostatic W- and Z- eigenmodes. This gives that  $\eta \sim (c/v_{TH})^{1/2} (-B_c/A_{TH})^{1/4}$ , which depends on frequency and wave vector through the coefficients  $B_c$  and  $A_{TH}$  as defined in (2) and (4).

2) The theory shows a thermal resonant plasma wave near  $\omega_{UH}$ , which happens when the cold and warm plasma coefficients  $A_c = 0$  and  $A_{TH} \rightarrow 0$  simultaneously. The electric field amplitudes become very large for the upper hybrid eigenmode and the electric energy is highly concentrated since the group velocity  $v_g \rightarrow 0$ .

3) The ponderomotive force of large amplitude quasi-electrostatic fields, effectively can create plasma density cavities near the transmitting antenna. Therefore a large number of eigenmodes are also

non-linearly excited whose refractive indices can change rapidly with wave normal angles and plasma density gradients. The non-linear refractive indices can satisfy the resonance condition for interactions with many electrons of different energies and pitch-angles.

4) We have modified the Hamiltonian potential wells theory for the wave-particle interactions to include the depletion of the electric fields as function of time. Approximate expressions are given for the amount of energy an electron can gain by including the damping rates of the electric fields.

5) Plasma heating results from interactions between the W- and Z-eigenmodes and the secondary ( $< 500$  eV) electron distribution. The energy gain by a single electron is a fraction of its initial kinetic energy. The time it takes to gain the energy is calculated for some numerical examples.

As a matter of fact, the non-linear heating deserved further attention. The electric fields and power distributions, which lead to electron acceleration, must be calculated. The radiated fields far removed from the antennas are mainly cast into electromagnetic waves with finite group velocities [*Jordan and Balmain, 1968*]. The nearby-radiated fields formed a sheath close to the antennas which, in the near stationary case, are composed mostly of quasi-electrostatic eigenmodes. The nearby sheath fields have group velocities which are so small that do not easily convect away from the antennas radiation regions. The distributions of the sheath fields in space need to be investigated to give a more precise estimate of non-linear effects and plasma acceleration.

## Appendix

The linear damping (growth) rates of wave fields interacting with electrons that satisfy the resonance condition in (15), are given by *Lyons and Williams* [1984]. Here we study for the secondary electrons whose distribution functions are described by (16), the linear damping rates of quasi-electrostatic wave eigenmodes.

The waves are damped out due to their interactions with low energy isotropic distribution functions of electrons. The linear damping rates are approximately obtained for the distribution functions in

(16), and by integrating in velocity space  $0 \leq v \leq \infty$ . We get

$$\frac{\gamma D}{\omega} \simeq -X \mu_R \frac{\pi}{4(\kappa+2)} \frac{c}{\sqrt{w_\kappa}} \frac{K_s}{N_c} \frac{1}{|\eta_{||}|} \frac{\Theta_{n,k}}{\mathcal{W}_k} \quad (24)$$

where  $\mu_R = \sin^2 a_R$ , the most probable electron pitch-angle that satisfy the resonance condition. It can be approximated as  $\cos a_R \simeq (c/w_\kappa) (1 - nY)/\eta_{||} u_m$ , and  $u_m^2 = 3\kappa/2(\kappa - 3/2)$ . Here  $\Theta_{n,k}$  is a function of wave amplitudes as

$$\Theta_{n,k} = \frac{1}{2} \left| E_{k,L} \mathcal{J}_{n-1} + E_{k,R} \mathcal{J}_{n+1} - \sqrt{2} E_{k,||} \mathcal{J}_n \right|^2 \quad (25)$$

where the polarizations are expressed by  $L, R, ||$  referring to the left, right, or along the geomagnetic field components. Here the argument of the Bessel functions,  $\mathcal{J}_\nu$ , is  $k_\perp \rho$  and  $\nu = n \pm 1$  and  $n$ .

### Acknowledgments.

This work has been supported by the U.S. Air Force under contract with Northeastern University, F19628-95-C-0212. The author is deeply grateful to Drs. W. J. Burke and C. Y. Huang for useful discussions. Special thanks are given to Dr. G. James for providing all the available experimental results.

## References

- Al'pert Ya. L., *Space Plasma*, Vol. 1, Cambridge Atmospheric and Space Science Series, Cambridge University Press, UK (1990).
- Arnoldy R. L., P. B. Lewis and P. O. Isaacson, Field-aligned auroral electron fluxes, *J. Geophys. Res.* 79, 4208, 1974.
- Aubry M., J. Bitouin and Ph. Graff, Propagation and group velocity in a warm magnetoplasma, *Radio Sci.*, 5, 635, 1970.
- Benson R. F., Stimulated Plasma instability and non-linear phenomena in the ionosphere, *Radio Sci.*, 17, 1637, 1982.
- Budden K. G., *The Propagation of Radio Waves: The theory of radio waves of low power in the ionosphere and magnetosphere*, Cambridge University Press, Great Britain, 1985.
- Cary J. R. and A. N. Kaufman, Ponderomotive force and linear susceptibility in Vlasov plasma, *Phys. Rev. Lett.*, 39, 403, 1977.
- Gendrin R., General relationships between wave amplification and particle diffusion in a magnetosphere, *Rev. Geophys. and Space Phys.*, 19, 171, 1981.
- Ginet G., and M. Heinemann, Test particle acceleration by small amplitude electromagnetic waves in a uniform magnetic field, *Phys. Fluids B*, 2, 700, 1990.
- Huang C. Y., W. J. Burke, D. A. Hardy, M. P. Gough, H. G. James, E. Villalón, and L. C. Gentile, Electron acceleration by MHz waves during OEDIPUS C, submitted to *J. Geophys. Res.*, 1999.
- Ichimaru S., *Basic Principles of Plasma Physics: A Statistical Approach*, Series in frontier of Physics, W. A. Benjamin Inc., Advanced book program, Reading Mass., 1973.
- James H. G., Souder accelerated particles observed on ISIS, *J. Geophys. Res. A*, 5, 4027,

1983.

Jordan E. C., and K. G. Balmain, *Electromagnetic Waves and Radiating Systems*, Prentice-Hall Electrical Engineering Series, Englewood Cliffs, N. J., 1968.

Kennel C. F. and H. V. Wong, Resonant particle instabilities in a uniform magnetized field, *J. Plasma Phys.*, *1*, 75, 1967.

Lyons L. R. and D. J. Williams, *Quantitative Aspects of Magnetospheric Physics*, Geophysics and Astrophysics monographs, D. Reidel Publishing Co., Boston, 1984.

Oya H., Sequence of diffuse plasma resonances observed on Aloute 2 ionograms, *J. Geophys. Res.*, *75*, 4279, 1970.

Oya H., Conversion of electrostatic plasma waves into electromagnetic waves: numerical calculations of the dispersion relation for all wavelengths, *Radio Sci.*, *6*, 1131, 1971.

Sazhin S., *Whistler-mode Waves in a Hot Plasma*, Cambridge atmospheric and space science series, Cambridge University Press, 1993.

Serov A. A., Yu. I. Galperin, Yu. V. Lisakov, and F. K. Shuiskaya, Local acceleration of electrons of the near-satellite plasma by the radio emission of a powerful on board transmitter, *Cosmic Res.*, *23*, 361, 1985.

Shuiskaya F. K., Yu. I. Galperin, A. A. Serov, N. V. Baranets, Yu. V. Kushnerevsky, G. V. Vasil'ev, S. A. Pulinets, M. D. Flegel, and V. V. Selegey, Resonant heating of the ionospheric plasma by powerful radiopulses aboard the INtercosmos-19 and Cosmos-1809 Satellites, *Space Sci.*, *38*, 173, 1990.

Stix T. H., *Waves in Plasmas*, American Institute of Physics, New York, N. Y., 1992.

Villalón E. and W. J. Burke, Relativistic particle acceleration by obliquely propagating electromagnetic fields, *Phys. Fluids*, *30*, 3695, 1987.

Villalón E., Ionospheric electron acceleration by electromagnetic waves near regions of plasma resonances, *J. Geophys. Res. A*, 94, 2717, 1989.

---

E. Villalón, Center for Electromagnetics Research, Northeastern University, Boston, MA 02115.

(e-mail: villalon@plh.af.mil)

Received A 7, 199; revised M 3, 199; accepted M 4, 199.

**Figure 1.** Geometrical representation of the waves and electrons parameters. The relevant angles between  $z$  and  $k$ , and  $\vartheta_g$ , are represented by  $\theta$  and  $\beta$ , respectively. The electron velocity  $v$ , and the pitch angle  $\alpha$  are also represented.

**Figure 2.** The refractive indices  $\eta^2$  are depicted versus  $\omega/\Omega_e$  as obtained from the Appleton-Hartree equation, by assuming that  $\omega_p/\Omega_e = 0.666$ . The ordinary and extraordinary modes branches are shown. The plasma resonances where  $\eta^2 \rightarrow \infty$ , in the shaded regions for the propagation of the W- and Z- modes are also indicated.

**Figure 3.** Frequencies of the resonant modes  $\omega/\Omega_e$  versus  $\cos \theta$ , the angle between the wave vector and geomagnetic field. The Z- and W- eigenmodes are above and below  $\omega = \Omega_e$  and  $\omega = \omega_p$ , respectively. We represent three values of  $\omega_p/\Omega_e = 0.33, 0.66$  and  $0.85$  as indicated.

**Figure 4.** Parallel refractive indices  $\eta_{\parallel}^2$ , versus  $\omega/\Omega_e$  for the W-eigenmode and three values of  $\omega_p/\Omega_e$  as indicated. They are obtained by introducing first-order thermal corrections with  $v_{TH}/c = 0.001$ .

**Figure 5.** Parallel velocity of resonant electrons versus  $\omega/\Omega_e$  for the W-eigenmodes whose refractive indices are represented in Fig. 4 and for the harmonic  $n = 1$ ; the values of  $\omega_p/\Omega_e$  are also indicated.

**Figure 6.** Parallel refractive indices versus  $\omega/\Omega_e$  for the Z-mode, and the three values of  $\omega_p/\Omega_e$  and for  $v_{TH}/c = 0.001$ . The upper panel A) represents  $\eta^2$  which is the largest near the upper-hybrid frequency. The lower panel B) represent the parallel component  $\eta_{\parallel}^2$ .

**Figure 7.** Parallel velocity of resonant electrons versus  $\omega/\Omega_e$  for the Z-eigenmodes whose refractive indices are represented in Fig. 6; the values of  $\omega_p/\Omega_e$  are also indicated.

**Figure 8.** Cosine of propagation angles  $\alpha$ ,  $\beta$ , and  $\theta$  as defined in Fig. 1 versus  $\omega/\Omega_e$  for  $\omega_p/\Omega_e = 0.66$ . The upper A) and lower B) panels contain the W- and Z- modes, respectively.



**Figure 9.** Time in number of gyroperiods versus  $\ln(K)$ , where  $K$  is the electron energy. We consider resonant interactions with secondary electrons. We assume that the initial kinetic energy doubles over the period of time shown in the figure.

## Table of symbols

$\omega_p$ .....	plasma frequency.
$\Omega_e$ .....	electron cyclotron frequency.
$\omega_{UH}$ .....	upper-hybrid frequency.
$\omega$ .....	wave frequency.
$Q = \omega_p/\Omega_e$ , $X = (\omega_p/\omega)^2$ , $Y = \Omega_e/\omega$ .....	frequencies ratios.
$B_o$ .....	geomagnetic field.
$k$ , $k_{  , \perp}$ .....	wave vector and its components.
$\eta = ck/\omega$ .....	wave refractive index.
$\eta_{TH}$ .....	thermal refractive index.
$\theta$ .....	wave vector angle with $B_o$ .
$\beta$ .....	group velocity (ray) angle with $B_o$ .
$\alpha$ .....	angle between wave vector and ray direction.
$a$ .....	electron pitch angle.
$W-$ and $Z-$ eigenmodes .....	whistler and extraordinary waves.
$v_{TH}$ .....	electron thermal velocity.
$\epsilon = v_{TH}/c$ .....	the thermal velocity divided by speed of light.
$A_c$ , $B_c$ , $C_c$ .....	cold plasma dispersion relation coefficients.
$A_o$ .....	total fourth order coefficient including thermal corrections.
$A_{TH}$ and $\chi_{TH}$ .....	thermal corrections.
$W(Z_{\pm})$ , $Z_{\pm} = (\omega \pm \Omega_e)/k_{  }v_{  }$ .....	Plasma dispersion function and its argument.
$\vartheta_g$ , $\vartheta_{g,k}$ .....	group velocity and its component along the wave vector.
$P$ .....	power flux density.

$\mathcal{W}_k$ .....	energy density of waves.
$E$ .....	electric field amplitude.
$\mathcal{E}$ .....	normalized electric field as in (11).
$\Sigma(\tau)$ .....	time-dependent normalized electric field as in (18).
$\phi_p$ .....	normalized ponderomotive force.
$n_e, n_i$ .....	electron and ion modified plasma densities.
$N_e$ .....	cold unperturbed plasma density.
$\tilde{\omega}_p$ .....	non-linearly modified plasma frequency.
$T_{e,i}$ .....	electron and ion temperatures.
$\underline{\delta}, \underline{\varepsilon}$ .....	mobility and dielectric tensors.
$v, v_{  ,\perp}$ .....	electron velocity and its components.
$\rho = v_{\perp}/\Omega_e$ .....	Larmor radius.
$\gamma_R, \gamma_o$ .....	relativistic factors at different times.
$\gamma_D, \hat{\gamma}_D = 2\pi\gamma_D/\Omega_e$ .....	linear damping rates.
$f(v)$ .....	electron distribution function.
$\sqrt{w_k}$ .....	electron most probable speed.
$v_m$ .....	smallest resonant velocity.
$\tau = 2\pi t/\Omega_e$ .....	normalized time.
$U = \gamma_R/\gamma_o - 1$ .....	effective energy gain .
$V_n(U, \tau)$ .....	time-dependent Hamiltonian potential wells.
$n$ .....	gyroharmonic number.
$\tilde{U}_o$ .....	maximum allowed energy gain from theory.
$\tau_c$ .....	total interaction time for $\tilde{U}_o$ .

$K$ .....	empirical electron kinetic energy in eV.
$\Delta K$ .....	limited energy gain (empirical value).
$\tau_l$ .....	corresponding interaction time for $\Delta K$ .
$\tilde{U}_D$ .....	limited energy gain from theory.

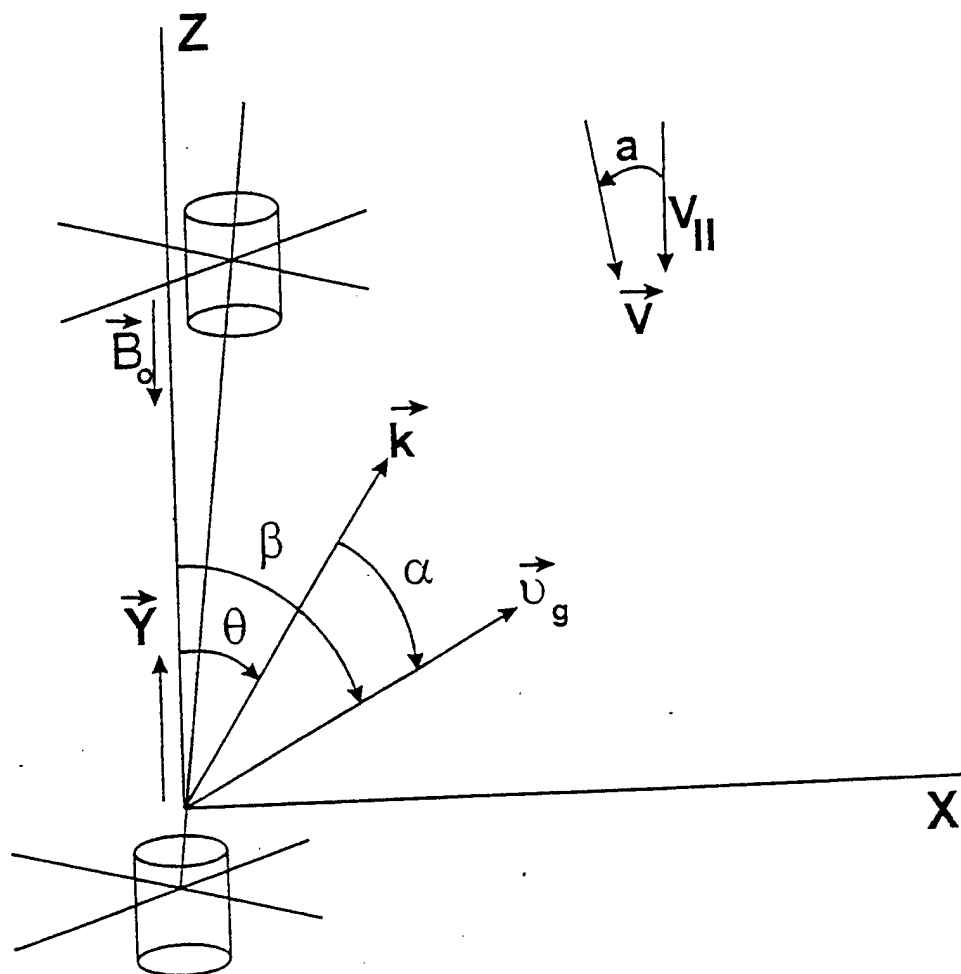


Figure 1

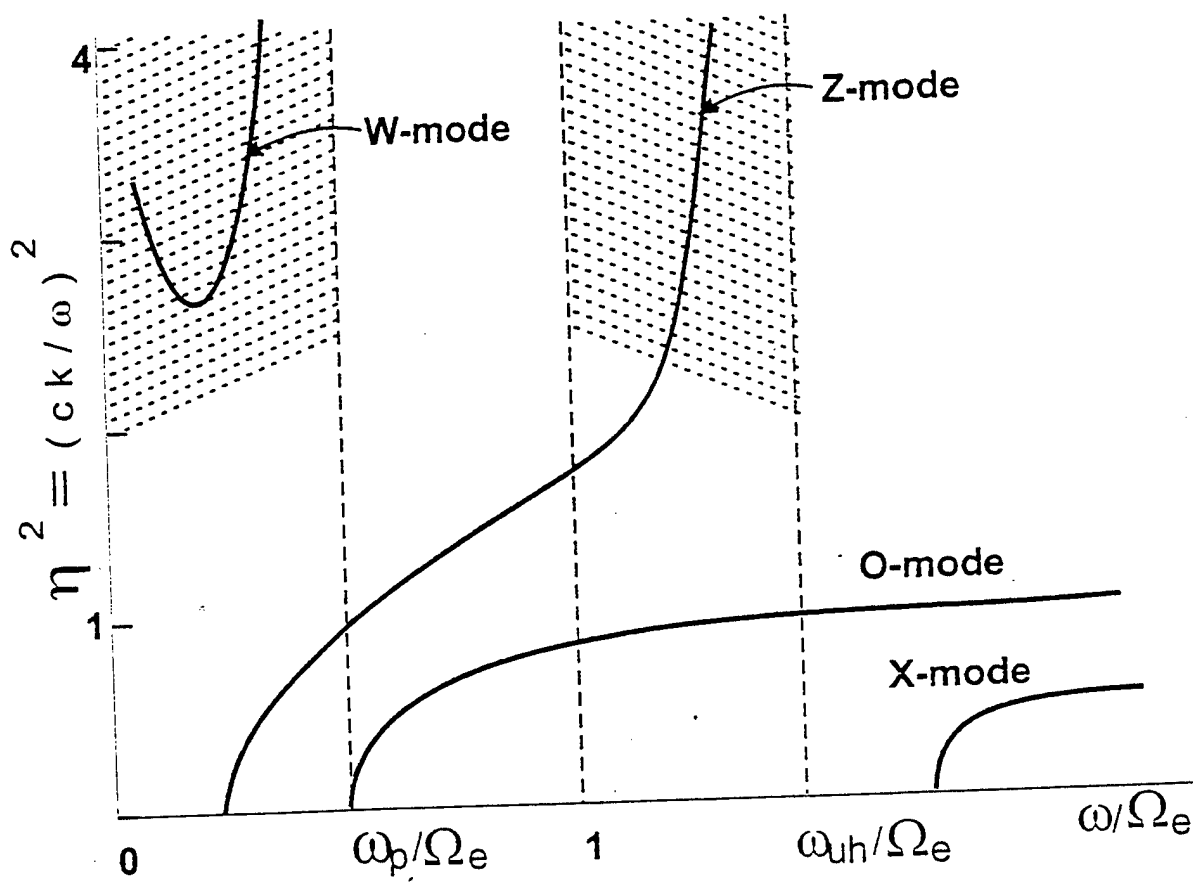
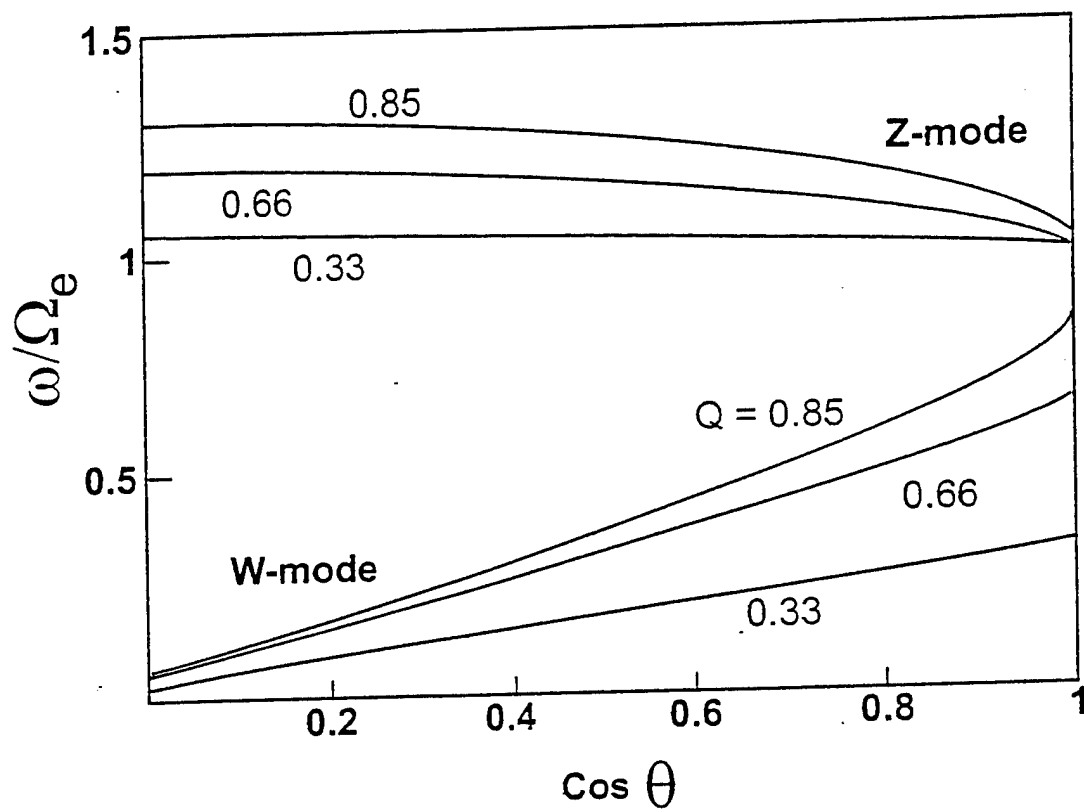
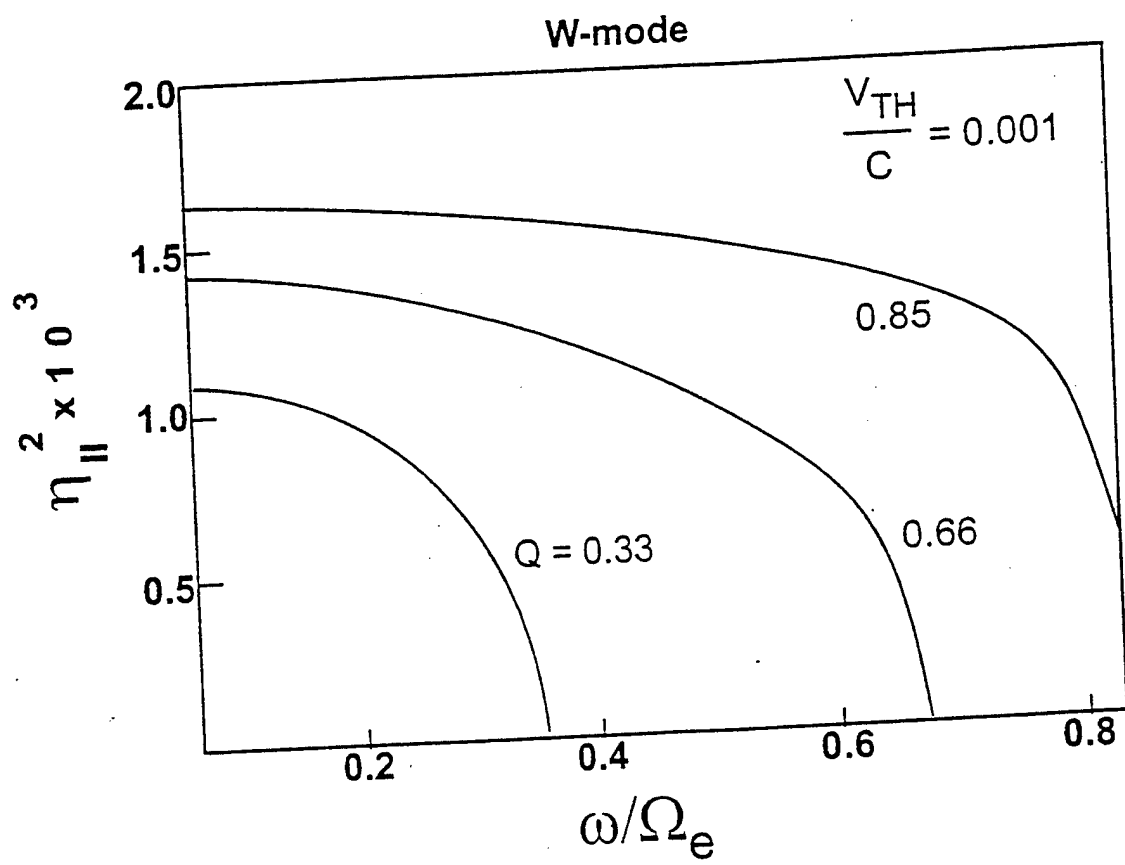
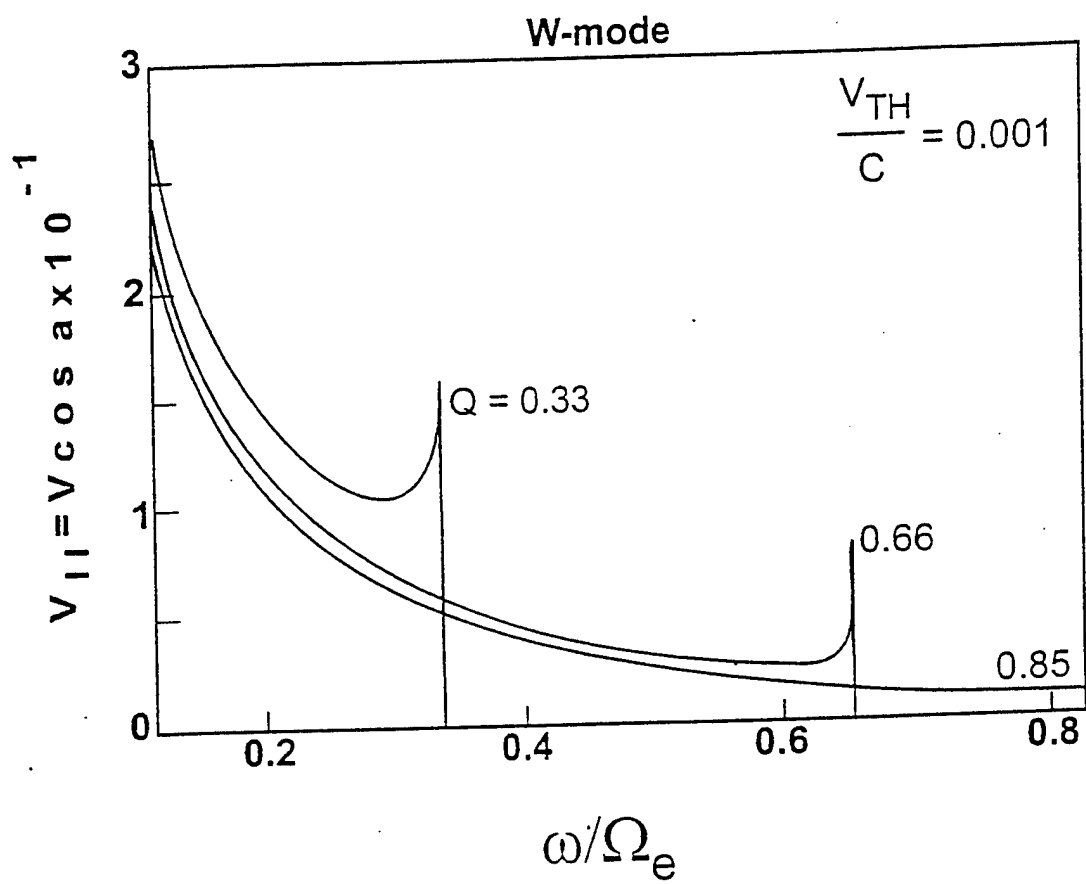


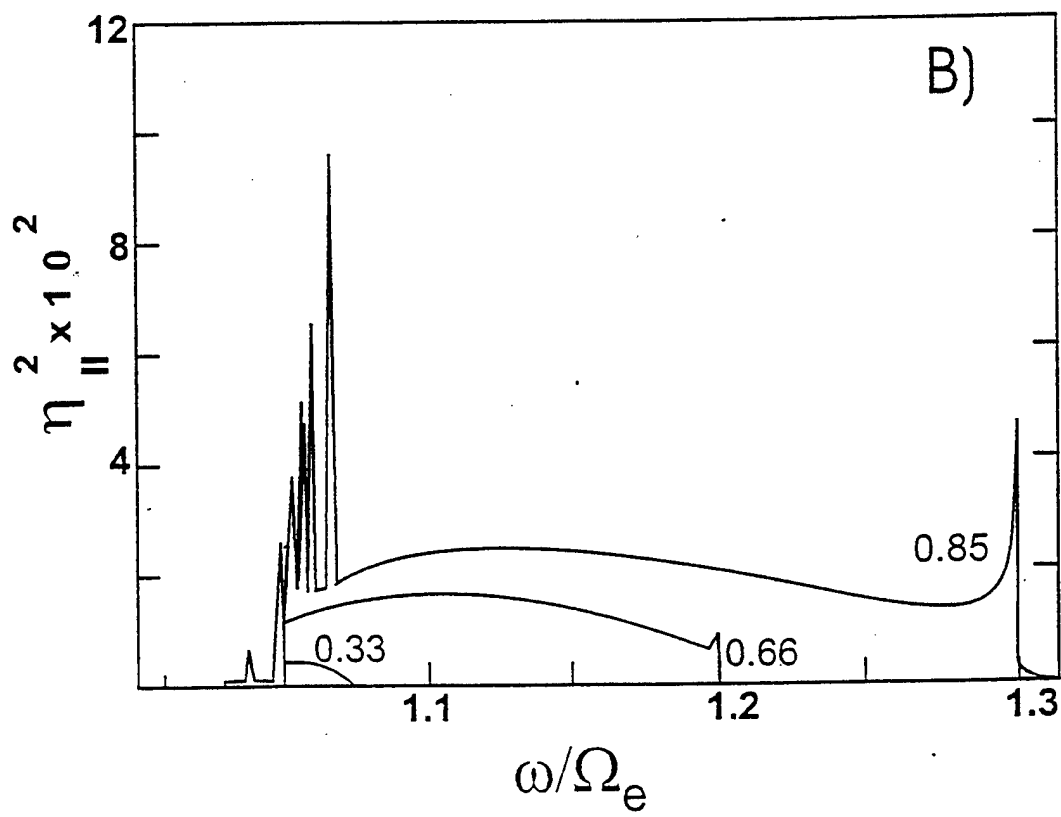
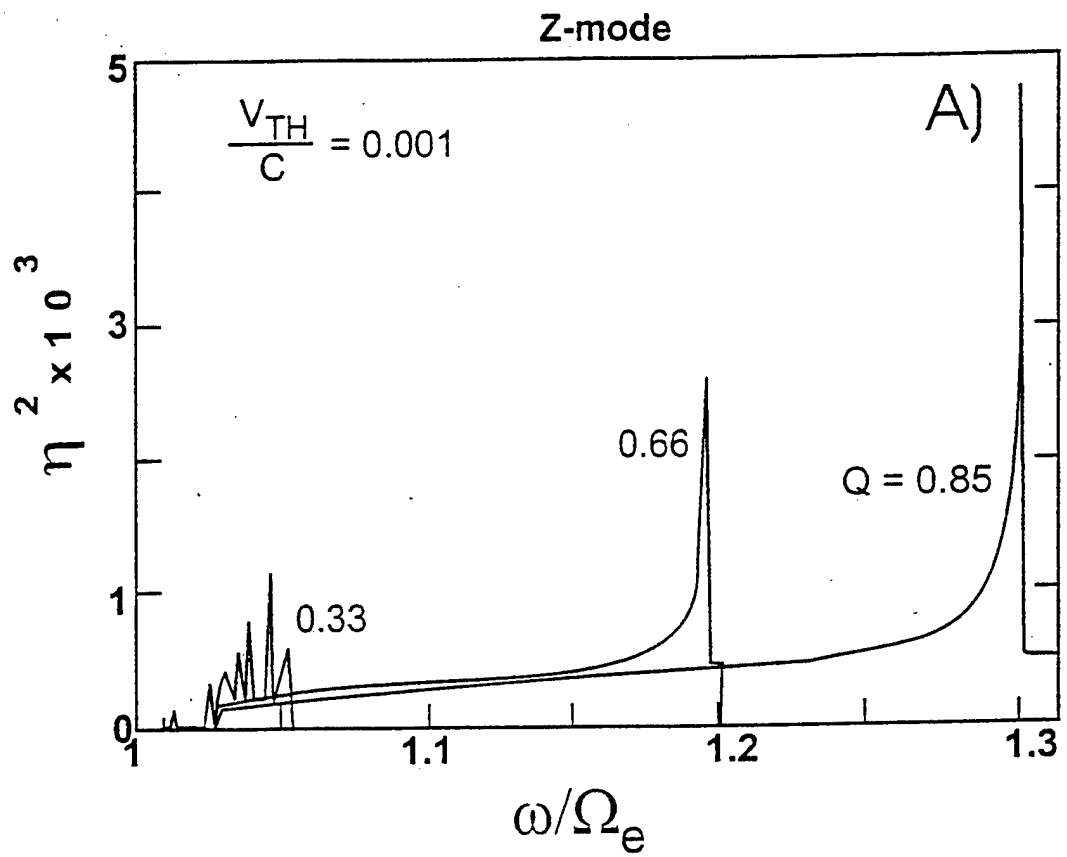
Figure 2











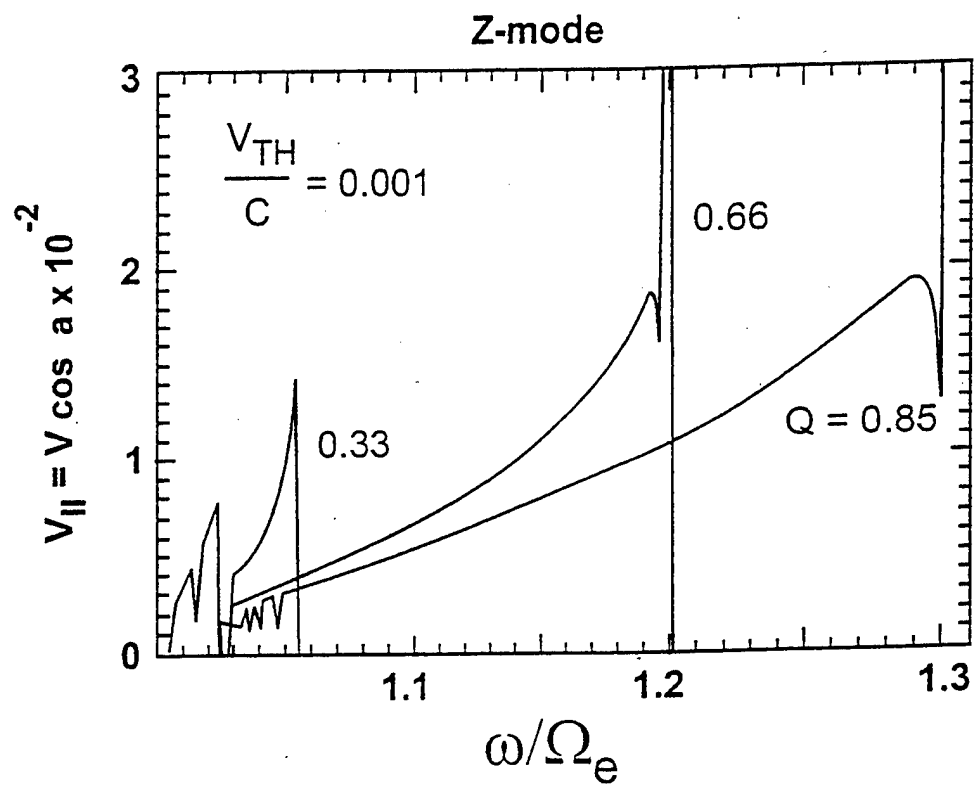


**Figure 7**

